SCANNING TUNNELING SPECTROSCOPY AT THE SINGLE ATOM SCALE

THÈSE N^{O} 3465 (2006)

PRÉSENTÉE À LA FACULTÉ SCIENCES DE BASE

Laboratoire de physique des surfaces

SÉCTION DE PHYSIQUE

ÉCOLE POLYTECHNIQUE FÉDÉRALE DE LAUSANNE

POUR L'OBTENTION DU GRADE DE DOCTEUR ÈS SCIENCES

PAR

Markus TERNES

Diplom-Physiker, Technische Universität Berlin, Allemagne
et de nationalité allemande

acceptée sur proposition du jury:

Prof. J.-Ph. Ansermet, président du jury
Prof. W.-D. Schneider, directeur de thèse
Dr A. Heinrich, rapporteur
Prof. F. Mila, rapporteur
Prof. C. Renner, rapporteur

ÉCOLE POLYTECHNIQUE
FÉDÉRALE DE LAUSANNE

Lausanne, EPFL
2006

Abstract

This thesis reports measurements at the single atom scale by using low-temperature scanning tunneling microscopy (STM) and spectroscopy (STS). Different sample systems where analyzed with normal conducting and superconducting tips.

Chapter 2 presents the theoretical aspects which have to be taken into account for a detailed analysis and a consistent interpretation of the STS measurements.

In chapter 3 the creation of a hexagonally ordered superlattice of single Ce adatoms on Ag(111) is reported and understood within a scattering model of the surface state electrons with the adatoms. Furthermore, the change in the local density of states of the surface state in ordered and slightly disordered superlattices is measured and theoretically explained within a tight-binding model which allows to understand the creation and stability of the superlattice by an energy gain of the participating surface-state electrons.

Because Ce atoms have a non-vanishing magnetic moment which is expected to interact with the continuous states of the supporting surface leading to a Kondo resonance, chapter 4 presents measurements on single Ce adatoms on different Ag surfaces. This chapter shows the difficulties to interpret the obtained data. For instance, bistable Ce adatoms are detected on Ag(100) which show drastical changes in their apparent height and spectral signature depending on the tunneling conditions. The possible physical processes behind these phenomena are discussed.

While the results presented in the first chapters were obtained with a normal conducting tip, chapter 5 intensively discusses the opportunities superconducting tips offer in low-temperature STS measurements. Novel insight in and thorough understanding of Andreev reflection processes are obtained by using the unique possibility of having different superconducting gaps in the tip and the sample. Detailed analyses of the supercurrent at low tunneling resistances reveal tunneling currents which are not described within the standard resistivity shunted junction model, and are presumably due to self-induced tunneling or due to an additional quasiparticle tunneling channel which only exist in asymmetric junctions. Furthermore, the influence of single magnetic Co atoms inbetween the superconducting tunnel junction on the obtained spectrum is discussed.

Keywords: Scanning tunneling microscopy (STM), scanning tunneling spectroscopy (STS), superlattice, surface state, Kondo effect, superconductivity, Andreev reflections, supercurrent

Résumé

Cette thèse rapporte des mesures faites à l'échelle de l'atome en utilisant la microscopie et la spectroscopie à balayage par effet tunnel (STM et STS). Différents systèmes d'échantillons ont été analysés avec des pointes conductrices normale et supraconductrices.

Le chapitre 2 présente les aspects théoriques donc nous devons tenir compte afin d'avoir une analyse détaillée et une interprétation consistente des mesures de la STS.

Dans le chapitre 3 la création d'un superréseau de configuration hexagonale d'adatomes de Ce sur une surface d'Ag(111) est rapportée et comprise grâce à un modèle de dispersion des électrons de la surface avec les adatomes de Ce. De plus nous avons mesuré le changement de la fonction de densité des états locale de l'état de la surface pour des réseaux ordonnés et désordonnés et tenté de l'expliquer théoriquement à l'aide d'un modèle de 'tight-binding' permettant de comprendre la création et la stabilité du super-réseau grâce à un gain d'énergie des électrons de surface participant au processus.

Parce que les atomes de Ce ont un moment magnétique non-négligeable censé interagir avec le continuum d'états de la surface de support et par conséquent induire une résonance de Kondo, le chapitre 4 expose des mesures faites sur des atomes de Ce isolés sur différentes surfaces d'Ag. Ce chapitre expose les difficultés à expliquer les données obtenues. Par exemple, des adatomes de Ce bistables détectés sur de l'Ag(100) et démontrent des changements drastiques dans leur hauteur apparente et leur signature spectroscopique dépendamment des conditions de tunneling. Nous discutons les processus physiques possibles derrière ce phénomène.

Alors que les résultats présentés dans les premiers chapitres sont obtenus avec une pointe conductrice normale, le chapitre 5 discute dans le détail des opportunités qu'offrent les pointes supraconductrices pour des mesures STS à basse température. Une compréhension nouvelle et approfondie des processus de réflexion d'Andreev ont été obtenus en utilisant la possibilité unique d'avoir différents gaps supraconducteurs dans la pointe ainsi que dans l'échantillon. Des analyses détaillées du courant supraconducteur avec de basses résistances d'effet tunnel révèlent des courants d'effet tunnel qui ne sont pas décrits par le modèle standard de jonction shuntée avec une résistance. Ils sont vraisemblablement dus à un effet tunnel self-induit ou à un canal de tunneling de quasiparticules supplémentaire qui n'existe que dans des jonctions asymétriques. Nous discutons aussi de l'influence d'atomes de Co magnétique isolés placés entre les jonctions d'effet tunnel supraconducteurs sur le spectre obtenu.

Mots clés: Microscopie à effet tunnel (STM), spectroscopie à effet tunnel (STS), superréseau, état de surface, effet Kondo, supraconductivité, réflexion d'Andreev, courant supraconducteur

Zusammenfassung

In dieser Arbeit werden Messungen vorgestellt, die mit Hilfe der Tieftemperatur-Rastertunnelmikroskopie (STM) und -spektroskopie (STS) auf atomarer Ebene gewonnen wurden. Dabei sind verschiedene Probensysteme mit normalleitenden und supraleitenden Tunnelspitzen untersucht worden.

Die theoretischen Überlegungen, die für eine detaillierte Analyse und konsistente Auswertung der spektroskopischen Daten unabdingbar sind, werden in Kapitel 2 präsentiert.

Kapital 3 berichtet über die Entstehung von hexagonal geordneten Übergittern aus einzelnen Ce Adatomen auf der Ag(111) Oberfläche, welche mittels der Streuung von Oberflächenelektronen an den Ce Adatomen erklärt werden kann. Weiterhin wird die Änderung der lokalen Zustandsdichte des Oberflächenzustandes in geordneten und leicht ungeordneten Übergittern gemessen und innerhalb eines „tight binding" Modells theoretisch beschrieben. In diesem Model kann die Entstehung und Stabilität des Übergitters als Folge des Energiezuwachses der beteiligten Oberflächenelektronen verstanden werden.

Da die Ce Atome ein nichtverschwindendes magnetisches Moment besitzen, werden Kondo-Resonanzen erwartet, die durch Wechselwirkung mit den kontinuierlichen Zuständen der unterliegenden Oberfläche entstehen. Kapitel 4 präsentiert daher spektroskopische Messungen an einzelnen Ce Adatomen auf unterschiedlichen Ag-Oberflächen. Dabei werden die Schwierigkeiten bei der Interpretation dieser Daten aufgezeigt. So werden zum Beispiel bistabile Ce Atome auf Ag(100) detektiert, deren spektrale Eigenschaften und scheinbare Höhe drastisch von den Tunnelparametern abhängen.

Während alle Ergebnisse aus den Kapiteln 3 und 4 mittels normalleitender Spitzen gewonnen wurden, werden in Kapitel 5 die Möglichkeiten intensiv diskutiert, die sich mit supraleitenden Spitzen in Tieftemperatur-STS Messungen eröffnen. Die einzigartige Möglichkeit, unterschiedliche Bandlücken in Spitze und Probe zu präparieren, ermöglicht ein neuartiges und umfassenderes Verständnis von Andreev-Reflektionen. Die detaillierte Analyse der Superströme bei niedrigen Tunnelwiderständen enthüllt, daß die Tunnelströme nicht innerhalb des Standardmodells von einem Tunnelübergang mit Parallelwiderstand (resistivity shunted junction model) beschrieben werden können. Wir vermuten, daß entweder selbstinduziertes Tunneln von Elektronenpaaren oder zusätzliche Tunnelkanäle für Quasiteilchen, welche nur in asymmetrischen Übergängen existieren, die Ursache sind. Des Weiteren wird der Einfluss von einzelnen magnetischen Co Atomen in dem supraleitenden Tunnelübergang auf das Spektrum diskutiert.

Contents

Chapter 1

Introduction

At the beginning of the 20^{th} century, the origin of the electrical transport mechanism in metals was only partly understood. At that time, one of the main questions was the low temperature behavior of the electrical resistivity of pure metals and metals containing some impurities. While it was known that the specific electrical resistivity depends linearly on the temperature as long as the measurements were performed close to ambient temperatures, the low temperature range could not yet be measured and led to the open question if the resistivity reaches a finite value, approaches asymptotically zero resistance, or even increases at temperatures close to the absolute zero.

The idea of having no resistance in metals at zero temperature was based on a model of elementary vibrations in a solid published by *Albert Einstein* [1]. In this model, the vibrational energy of the atoms depends exponentially on the temperature and should be zero at $T = 0$. Thus, it was believed that the electron transport should no longer be hindered by movements of the atoms in the metal.

It was *H. K. Onnes* who first reached a new temperature regime by successfully liquefying helium, a noble gas with a boiling temperature of only 4.2 K. Cooling down mercury to such low temperatures, he found a completely unexpected behavior of the conductivity; the mercury sample lost suddenly all its resistivity below a temperature of 4.2 K [2] (figure 1.1 (a)). Since then, this effect is called superconductivity and was found in several metallic elements, alloys and since 1986 additionally in ceramic cuprates [4].

Ferromagnetic metals, such as iron or cobalt, do not show superconductivity. But if they are diluted as impurities in non-magnetic metals, they remarkably change the low-temperature resistance of the hosting metal. For instance, a low concentration of Fe diluted in Cu reveals a temperature dependence of the resistivity which increases instead of decreases below a certain temperature (figure 1.1 (b)).

The origin of both effects remained unsolved for a long-time because they are the result of complex collective phenomena between the many electrons of the atoms in a solid. Nowadays, we have understood these phenomena due to the pioneering work of *J. Bardeen*, *L. N. Cooper*, and *J. R. Schrieffer* who explained the superconducting state as a long-range attractive interaction between the conducting electrons (chapter 5.1.2) [5], and *J. Kondo* who showed that the increase in resistivity, as seen in figure 1.1 (b), can be explained with spin-flip processes between the localized magnetic moment of the impurities and the electrons of the host (chapter 4.1.1) [6]. Today, this effect is called the Kondo-effect.

In this thesis we discuss these phenomena and their interactions on the single atom scale

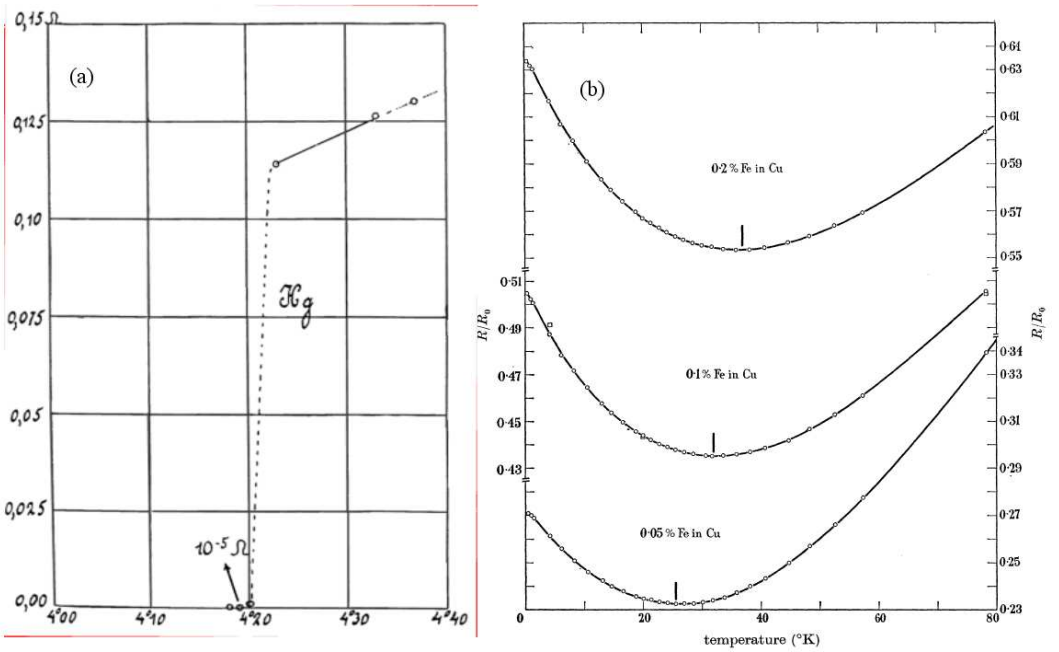

Figure 1.1: (a): The resistivity of mercury (Hg) measured at very low temperatures by H. K. Onnes shows a sudden drop at the critical temperature $T = 4.2$ K [2]. (b): Samples containing magnetic impurities (Fe) diluted in a non-magnetic metal (Cu) show an increase in resistivity below a concentration-dependent temperature [3].

with the help of a powerful tool, the scanning tunneling microscope (STM). The STM, which soon celebrates its 25 anniversary, has the unique capability to image surfaces and to characterize the electronic properties with atomic resolution (chapter 2).

We show that single cerium (Ce) adatoms can interact with each other indirectly by scattering processes of electrons at the adatoms. The electrons originate from a two-dimensional electron gas which exists on the Ag(111) surface and moderates the long-rage interaction which leads to the creation of hexagonal ordered structures of adatoms on the surface at low temperatures (chapter 3).

The Kondo effect and the difficulties of its clear detection on single Ce adatom is the subject of chapter 4. Measurements using superconducting tips are shown in chapter 5. In this last chapter, not only new aspects of the current transport between two superconductors are observed and discussed (chapter 5.4 and 5.6), but first results are additionally presented which show the interplay between a single magnetic adatom and the superconductivity of sample and tip. (chapter 5.5).

Not all results presented in this thesis are in their complexity well understood. They remain open with the strong belief to be answered in further experimental investigations.

Chapter 2

Scanning tunneling microscopy and spectroscopy

When in 1981 *G. Binnig*, *H. Rohrer*, *Ch. Gerber*, and *E. Weibel* presented for the first time their idea of a scanning tunneling microscope (STM) [7], they opened a door to a new and powerful tool for the analysis of surfaces. Shortly after, they demonstrated the capability of the STM to image metal surfaces with atomic resolution [8] and showed that this new tool is able to answer complex physical questions. In particular they could resolve the famous 7×7 reconstruction of the Si(111) surface in real space [9].

Following these revolutionizing results, a rapid development started that led to a multitude of investigations using the STM. Furthemore, several related methods have since been developed, such as for example the atomic force microscope (AFM) [10], the scanning-nearfield optical microscope (SNOM) [11], the magnetic force microscope (MFM) [12], and the ballistic-electron-emission microscope (BEEM) [13].

All of these techniques have in common that they use a *probe* to observe locally physical properties down to atomic lateral resolution. The data is thereby obtained by *scanning* a grid of points on the surface and combining the detected physical properties into an image using the data to code each point of the image. Because of this scanning mechanism, all these techniques are summarized as scanning probe microscopes (SPM).

The purpose of this chapter is to give a short introduction to the STM, focusing mainly on its spectroscopic capabilities.

2.1 Principles

The STM uses the tunneling effect to obtain a current between a sharp tip and the sample by applying a voltage between both of them. Although classically forbidden, but already considered since the early days of quantum mechanics [14] and observed in the beginning of the 1960's in planar junctions [15, 16], a current can be detected before tip and sample come into contact. This tunneling current is held constant by processing it in an electrical feedback loop that compares it to a preset current and then varies the distance between tip and sample accordingly, i. e. moving the tip towards or away from the sample. When the tip is scanned over the surface, the tip height is determined by the local geometric and electronic structure of the surface and thus produces a surface map in real space (see figure 2.1 (a)).

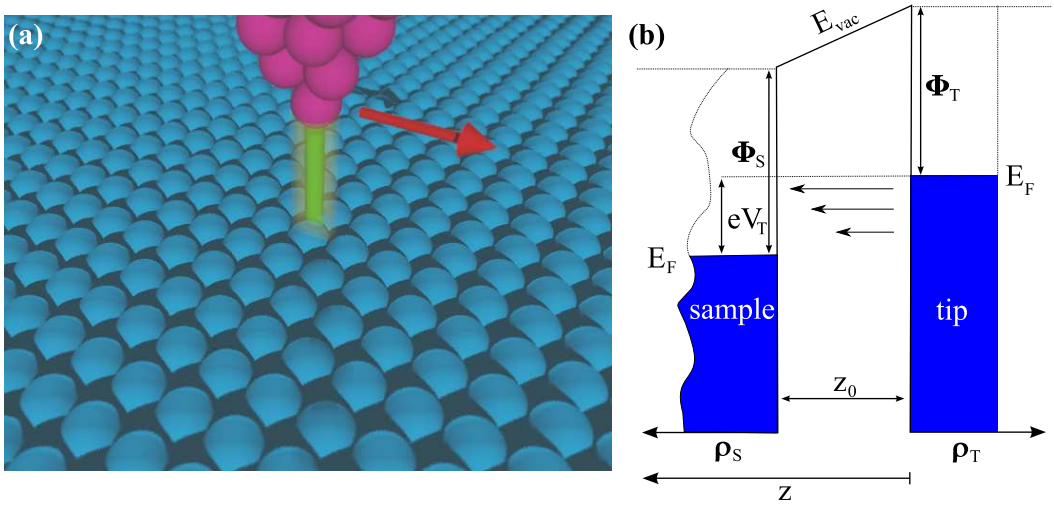

Figure 2.1: (a): Schematic representation of the tunnel junction. An atomically sharp tip scans over a surface. Only the last atom of the tip significantly contributes to the tunneling process. (b): Schematic view of the tunneling process between an ideal tip with flat ρ_t and a sample with a LDOS of $\rho_s(E)$. When a positive voltage V_T is applied to the sample with respect to the tip, electrons from occupied tip states (right-hand side) are able to tunnel into unoccupied sample states (left-hand side). Therefore they must overcome an approximately trapezoidal tunnel barrier formed by the two work functions of tip and sample and eV_T.

Quantum mechanically, the system can be rationalized with the help of a one-dimensional simplification, where the sample as well as the tip are described by an ideal metal in which the electron states are filled up to the Fermi energy E_F. The two electrodes are separated by a small vacuum gap z_0. An applied voltage V_T shifts the two Fermi energies by eV_T relatively to each other. We will use the convention that a positive tunneling voltage V_T increases the energy in the tip. The distance z, the two work functions Φ_s and Φ_t from tip and sample, and eV_T represent a trapezoidal tunnel barrier for the electrons (figure 2.1 (b)). From elementary quantum mechanics (see for example [17]), an electron in the tip ($z = 0$) at Fermi energy, represented by its wavefunction $\psi(z)$, has a finite probability of being localized in the sample at the position z:

$$|\psi(z)|^2 = |\psi(0)|^2 e^{-2\kappa z}, \quad \kappa = \sqrt{\frac{m_0}{\hbar^2}(\Phi_t + \Phi_s - eV_T)}. \tag{2.1}$$

Using the free electron mass for m_0, and realistic values for the work functions $\Phi \approx 4-5$ eV [18], 2κ becomes of the order of $20\,\mathrm{nm}^{-1}$, i. e. a variation in z of 0.1 nm results in an order of magnitude difference in the tunneling probability. This sensitivity in the tip-sample distance is the reason for the extremely high vertical resolution of the STM which can reach the sub-picometer regime.

Introducing the concept of the *local density of states* (LDOS), i. e. the density of states per energy interval at a specific position:

$$\rho(\vec{r}, E) = \sum_{\upsilon} |\psi_\upsilon(\vec{r})|^2 \delta(E_\upsilon - E), \tag{2.2}$$

one can express the tunneling current from tip to sample by [19]:[1]

$$I_{t\to s} = \frac{4\pi e}{\hbar} \int_{-\infty}^{\infty} \rho_t(\epsilon - eV_T)\rho_s(\epsilon) f_t(\epsilon - eV_T)\left(1 - f_s(\epsilon)\right) \left|M(\epsilon - eV_T, \epsilon)\right|^2 d\epsilon. \quad (2.3)$$

In this formula $f(\epsilon)$ denotes the temperature dependent Fermi-Dirac distribution $f(\epsilon) = (1 + \exp[\epsilon/k_B T])^{-1}$ for the electrons, and $M(\epsilon_t, \epsilon_s)$ the tunneling matrix element, i. e the coupling between the electron wavefunctions at the energy ϵ_t in the tip with the sample wavefunctions at ϵ_s. In the one-dimensional simplification as in equation 2.1, $|M|^2$ is given by:

$$\left|M(\epsilon - eV_T, \epsilon)\right|^2 = \exp\left[-2z\sqrt{\frac{m_e}{\hbar^2}\left(\Phi_t + \Phi_s - eV_T + 2\epsilon\right)}\right]. \quad (2.4)$$

As it can be seen, the current depends linearly on the LDOS of tip and sample, whereby the Fermi-Dirac distributions ensure that only occupied states in the tip $(f_t(\epsilon - eV_T))$ and unoccupied states in the sample $(1 - f_s(\epsilon))$ are counted for the tunneling from tip to sample. Of course, for the whole tunneling current I_T, one has to take into account the current in both directions from tip to sample as well as from sample to tip. After trivial summation, the result is:

$$I_T = \frac{4\pi e}{\hbar} \int_{-\infty}^{\infty} \rho_t(\epsilon - eV_T)\rho_s(\epsilon)\left(f_t(\epsilon - eV_T) - f_s(\epsilon)\right) \left|M(\epsilon - eV_T, \epsilon)\right|^2 d\epsilon. \quad (2.5)$$

Notice that due to equation 2.4 the highest contribution in the current comes from electronic states close to the Fermi energies of the tip ($V_T > 0$) or the sample ($V_T < 0$) (see schematic representation in figure 2.1).

Although equation 2.5 is easy to understand, the main problem is the determination of the tunneling matrix element M in a more realistic approximation than in the simple one dimensional model. The matrix element depends on the geometric position in space of the atoms in the sample and in the tip as well as the wave functions at the given energies. Since the main task for the STM is to produce an image of the sample surface, one is looking for a configuration where the tip DOS can be neglected. But, unfortunately, in most cases the actual geometric and chemical structure of the tip is unknown (despite some efforts to determine the structure of the tip by field-ion microscopy before using them in STM [20]) leading to an unknown tip DOS.

Shortly after the invention of the STM, *J. Tersoff* and *D. R. Hamann* presented a calculation using first-order perturbation theory [21] which gave an analytical result for the matrix element [22, 23] in a heavily simplified tunneling system as a representation for the STM. In particular, they solved the problem for an atomically sharp tip, where only the last atom, i. e. the atom that is closest to the sample surface, contributes to the tunneling process. The wavefunction of this atom (the interacting one) is therefore described by a spherical, s-like orbital. The density of states over the energy interval of interest is assumed to be constant. Taking only elastic tunneling processes into account, i. e. energy conservation during tunneling (for inelastic processes see chapter 2.3.3), the tunneling matrix element is written

[1] Here and in the following the energies are referred relative to the Fermi-energy of sample and tip.

in low voltage approximation as:

$$M_{\mu\nu} = -\frac{2\pi C\hbar^2}{\kappa m_e} \cdot \Psi_\mu^S(\vec{r}), \quad \text{with:} \quad \begin{aligned} C &= \text{constant} \\ \kappa &= \text{as in equ. 2.1.} \end{aligned} \tag{2.6}$$

This Tersoff-Hamann tunneling matrix element only depends on the position of the outermost atom of the tip at $\vec{r}$, and not on the wavefunction of the tip. Using equation 2.5, setting the temperature $T \to 0$, and restricting ourself to voltages $|V| \ll \Phi/e$ we resolve the widely used expression for the tunneling current in STM:

$$I_T = \frac{16\pi^3 C^2 \hbar^3 e}{\kappa^2 m_e^2} \rho_t \int_0^{eV_T} \rho_s(\epsilon) d\epsilon. \tag{2.7}$$

2.2 Imaging in constant-current mode

As shown in the last section, the tunneling current depends exponentially on the tip-sample distance. Thus, scanning the tip laterally over the sample results in a modulation of the current, corresponding to the surface corrugation. But with a tip-sample distance of usually ≤ 1 nm even small mechanical instabilities in the STM or steps on the surface would result in a crash of the tip into the surface. Thereby, imaging in the so-called constant-height mode is only applicable on flat surfaces and for small scan areas. To overcome these limitations in most STM experiments the constant-current mode is used to obtain the structure of the surface.

In this imaging mode the tunneling current is held constant by changing the tip-sample distance z. In that way, the recorded changes in the z value give a direct image of the surface. The image depends, therefore, on the applied tunneling voltage V_T and the preset tunneling current I_T. The tip scans a constant-value surface determined by I_T: the LDOS of the sample integrated over the energy window $E_F \leq E \leq E_F + eV_T$ according to equation 2.7 and figure 2.1 (b). Both the bias voltage V_T and the preset tunneling current I_T are independent parameters in the experiment. Depending on the polarity of V_T, occupied ($V_T < 0$) or unoccupied states ($V_T > 0$) in the sample are recorded [24], while I_T for constant V_T determines the tip height. On metallic samples, with their approximately constant density of states around E_F, the obtained images correspond to the geometric surface topography [25], but the correct analysis of the STM image is not always an easy task even on well known clean metallic surfaces, because the LDOS might be affected by, for example, surface state modulations [26]. Additionally the Tersoff-Hamann approximations might fail as illustrated in figure 2.2. Here the tip has changed during the experiment in such a way that not only the last atom contributes to the tunneling current. Therefore, in the right panel the STM resolves the geometric structure of the tip observed by the adatoms of the sample, i. e. the convolution of the tip geometry with the surface structure.

To conclude, even if the beauty of STM topographic images lies in the direct observation of the atomic structure of the sample, one has to be aware that the underlying physical description is rather complex and even after 25 years not accessible in all of its details. Thus, we are compelled to use strong simplifications to extract physical meanings out of our experiments.

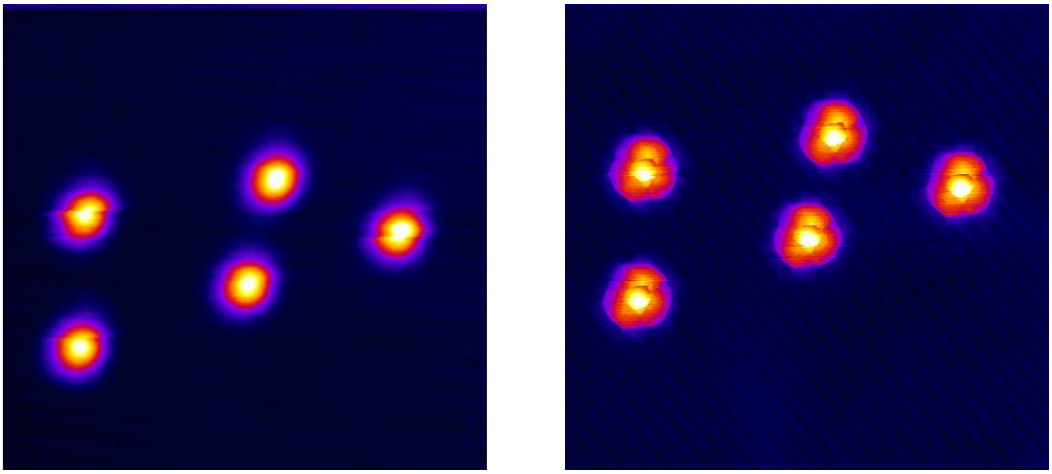

Figure 2.2: Topographic images (8.1×7.8 nm^2) measured at a temperature of 5 K with $V_T = -37$ mV and $I_T = 400$ pA showing the influence of the tip on the observations. Left side: 5 Co atoms on a clean Ag(100) surface. Right side: Since the tip has changed between the two measurements, the same atoms appear now with a shape similar to a 3-fold flower due to a convolution between the geometric structure of tip and sample.

2.3 Spectroscopy

One of the most fascinating potentials of the STM is its capability to obtain spectroscopic data with its atomic resolution. As we will see in this section, the STM allows us to measure directly the LDOS and, additionally, inelastic processes where the tunneling electrons excite states in the sample during the tunneling process by loosing partly their kinetic energy.

Since the main results presented in this thesis are obtained with the help of spectroscopic measurements, the description of this technique and the physical interpretation will be discussed in detail.

Taking the tunneling current as expressed in equation 2.5 but with the restriction that the tunneling matrix element stays constant (i. e. the energy eV_T is small compared to the work functions Φ in tip and sample, so that the tunneling matrix M in equation 2.4 changes only negligibly)[2] we get:

$$I_T \propto \int_{-\infty}^{\infty} \rho_s(\epsilon)\rho_t(\epsilon - eV_T)\left(f_t(\epsilon - eV_T) - f_s(\epsilon)\right) d\epsilon. \tag{2.8}$$

We calculate the first derivative of the tunneling current I_T with respect to the applied bias

[2] In addition, any changes in the attributes of the electrons in tip and sample, such as spin and orbital state, are neglected.

voltage V:

$$\left.\frac{\partial I_T}{\partial V}\right|_{V_T} \propto \int_{-\infty}^{\infty} d\epsilon \Big[-\rho_s(\epsilon)\rho_t'(\epsilon - eV_T) f_t(\epsilon - eV_T) \\ -\rho_s(\epsilon)\rho_t(\epsilon - eV_T) f_t'(\epsilon - eV_T) \\ +\rho_s(\epsilon)\rho_t'(\epsilon - eV_T) f_t(\epsilon - eV_T) f_s(\epsilon) \Big]. \tag{2.9}$$

The ρ_t' means the first derivative of the LDOS in the tip with respect to the energy:

$$\rho_t'(\epsilon) = \frac{\partial \rho_t(\epsilon)}{\partial \epsilon}, \tag{2.10}$$

while

$$f'(\epsilon) = \frac{\partial f(\epsilon)}{\partial \epsilon} = \frac{-\exp(\epsilon/k_BT)}{k_BT\left(1+\exp(\epsilon/k_BT)\right)^2} = \frac{-1}{2k_BT}\,\mathrm{sech}^2(\epsilon/k_BT) \tag{2.11}$$

is the first derivative of the Fermi-Dirac distribution function.[3]

While equation 2.9 is quite complicated, it can be simplified assuming a constant LDOS of the tip, i. e. $\rho_t' \equiv 0$, and a temperature of the junction of zero, so that $f'(\epsilon)_{k_BT\to 0} = -\delta(\epsilon)$ becomes the delta distribution. With these assumptions, the first and third sum in 2.9 vanish and the derivative of the tunneling current becomes:

$$\left.\frac{\partial I_T}{\partial V}\right|_{V_T} \propto \rho_t \int_{-\infty}^{\infty} \rho_s(\epsilon)\delta(\epsilon - eV_T)d\epsilon = \rho_t\rho_s(eV_T). \tag{2.12}$$

Thus, the derivative $\partial I_T/\partial V$ provides a value that is proportional to the LDOS in the sample at the energy eV_T. Technically, the tip is placed over the point of interest on the sample surface with chosen V_T and I_T which determine the tip-sample distance z. Then the tunneling voltage is ramped while the feedback loop is opened, i. e. z stays constant, and the current is recorded. With this $I_T(V)$ data the LDOS can be calculated numerically.

Unfortunately, the tunneling current is often too noisy to obtain reasonable data with this numerical method. In most tunneling spectroscopy experiments a dI_T/dV signal is detected with the help of a Lock-In technique.

2.3.1 Using the Lock-In technique

To obtain spectroscopic data with high signal to noise ratio, the tunneling voltage V_T is modulated with a small sinusoidal voltage $V_m \sin(\omega_m t)$. The modulation frequency $f_m = \omega_m/2\pi$ is thereby set to much higher values as the regulation speed of the feedback loop that holds the tunneling current constant in closed-loop mode, thus it is guaranteed that the modulation does not influence the recording of constant-current images. Now when a spectrum is taken – meaning that the tip is stabilized over a point of interest, the feedback

[3] Notice that, due to the symmetry of equation 2.8, the indices for tip and sample are interchangeable in equation 2.9 when inverting V_T.

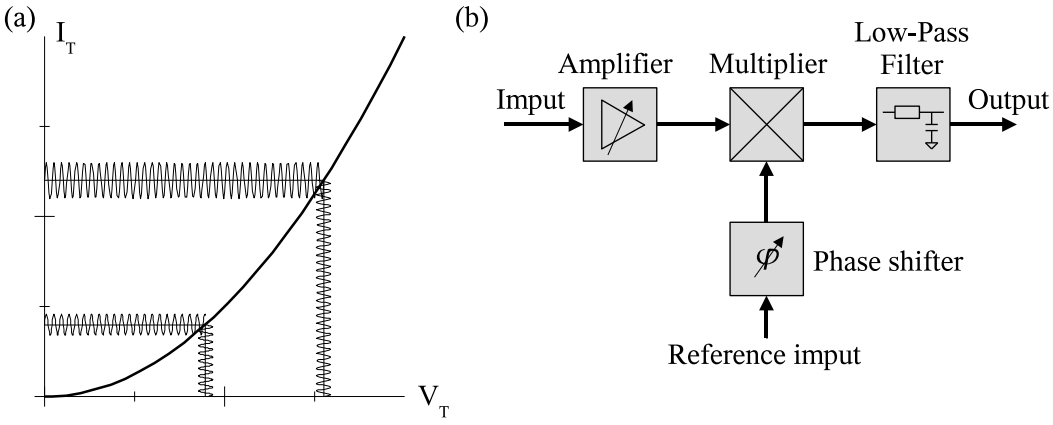

Figure 2.3: (a): A small modulation of the tunneling voltage results in an alternating current (AC) modulation of I_T. The amplitude of this modulation depends therefore on the slope of the $I(V)$ curve. Thus it is proportional to the first derivative dI/dV of the tunneling current. (b): Schematic representation of a phase and frequency sensitive Lock-In amplifier.

loop is opened, and the tunneling voltage V_T is ramped – we get a tunneling current using the Tersoff-Hamann approximation (equation 2.7) of:

$$I_T \propto \int_0^{eV_T + eV_m \sin(\omega_m t)} \rho_s(\epsilon) d\epsilon. \tag{2.13}$$

Expanding the current in a Taylor series:

$$I_T \propto \underbrace{\int_0^{eV_T} \rho_s(\epsilon) d\epsilon}_{\propto I_T(V_T)} + \underbrace{\rho_s(eV_T)}_{\propto I'_T(V_T)} eV_m \sin(\omega_m t) + \underbrace{\rho'_s(eV_T)}_{\propto I''_T(V_T)} \frac{e^2 V_m^2}{2} \sin^2(\omega_m t) \ldots, \tag{2.14}$$

we see that in a first approximation the amplitude of the current modulation with a frequency $f_m = \omega_m / 2\pi$ at the tunneling voltage V_T is proportional to the first derivative of the $I(V)$ curve at V_T and therefore proportional to the LDOS in the sample (see figure 2.3 (a)).

Usually, the tunneling current is disturbed by a wide-band current noise originating from mechanical vibrations in the tunnel junction and thermal noise generated in the first amplifier, the current-voltage converter. Thus, a *Lock-In* amplifier is used to measure the modulation of I_T. Schematically represented in figure 2.3 (b), it contains as the essential part a multiplier. The amplified current signal is multiplied with a reference signal taken directly from the modulation generator and phase shifted by φ. Taking into account the noise, the output of the multiplier results in:

$$\begin{aligned} \underbrace{\sin(\omega_m t + \varphi)}_{\text{reference}} \times \left(\underbrace{\rho_s(\epsilon) eV_m \sin(\omega_m t + \varphi_0)}_{\text{signal}} + \underbrace{\int_0^\infty a_\omega \sin(\omega t + \varphi_\omega) d\omega}_{\text{noise}} \right) \\ = \frac{1}{2} \rho_s(\epsilon) eV_m \Big[\cos(\varphi - \varphi_0) + \cos(2\omega_m t + \varphi + \varphi_0) \Big] + \ldots, \end{aligned} \tag{2.15}$$

with a_ω and φ_ω as the the amplitude and phase of the noise at the frequency $f = \omega/2\pi$. As it can be seen, only the contribution of the input signal that has exactly the same frequency as the reference is mixed down to a direct-current signal depending only on the phase angle $\varphi - \varphi_o$. All overlying noises with broad frequencies and uncorrelated phases with respect to the reference are filtered out by the frequency low-pass. Thus, the output of the Lock-In is directly linear to the modulation amplitude and the LDOS of the surface.

To summarize, the main goal of the modulation technique together with the detection by a Lock-In amplifier is to measure electronically the first derivative dI/dV of the tunneling current and to transpose the signal of interest from zero frequency to the frequency of the modulation f_m. With this method the $1/f$ (*Schottky*) noise is obviously strongly suppressed, while it is the main source of noise in numerically calculated dI/dV curves.

Unfortunately, this method has also its drawbacks. In real experiments, the wires that connect the sample and the tip with the electrical setup and the tip-sample geometry form a capacitance C_p which lets a parasitical AC current $I_p = C_p \frac{dV}{dt}$ flow across the junction independently of the tunneling process. Due to the capacitance, this current is phase shifted by 90° with respect to the modulation of the tunneling current over the junction which behaves like an ohmic resistor $R_T = V_T/I_T$. Even though this current should not affect the output signal of the Lock-In because of the phase sensitivity of equation 2.15, in measurements where the tunnel junction resistivity R_T is high compared to the apparent resistance $X_C = (\omega_m C)^{-1}$ of the capacitance the amplitude of the crosstalk signal can overcome the signal of interest by several orders of magnitude. Assuming, for example, a setpoint current of 20 pA at a tunneling voltage of 100 mV remaining in a junction resistance of $R_T = V_T/I_T = 5\,\mathrm{G\Omega}$, and a modulation amplitude of $V_m = 10$ mV at 2 kHz, a crosstalk capacity of 2 pF, i. e. $X_C = 40\,\mathrm{M\Omega}$, would lead to a parasitical AC current of $V_m/X_C = 25$ pA, while the signal of interest is only of the order of $V_m/R_T = 2$ pA.

Obtaining accurate spectroscopic data under such conditions depends crucially on the correct phase adjustment between reference input and signal input, because even a small misalignment would result in a strong background in the output signal of the Lock-In. Additionally, the crosstalk signal reduces the usable dynamic range of the Lock-In so that a compensation circuit, which annihilates the capacity crosstalk signal before it is amplified and detected by the Lock-In is recommended. For that, a variable 180° phase-shifted signal of the modulation voltage is applied via a small capacitance $C_{comp} \gtrsim C_p$ and added to the tunneling current as seen in figure 2.4. With the variable gain $\alpha < 0$ the compensation current $I_{comp} = \alpha C_{comp} \frac{dV}{dt}$ is adjusted to annihilate the crosstalk current, i. e. $-I_{comp} = I_p$. Thus, all crosstalk induced disturbances are removed before the tunneling current enters the current-voltage converter and before it is processed in the Lock-In.

Furthermore, the use of the Lock-In and the modulation technique has an additional disadvantage. Due to the modulation of the tunneling voltage, the energy resolution is limited. The component I_ω, i. e. the first Fourier coefficient of the current function $I = I(V_T + V_m \sin(\omega_m t))$ developed in terms of ω_m:

$$I_\omega = \frac{1}{\pi} \int_{-\pi}^{\pi} I(V_T + V_m \sin(\tau)) \cos(\tau) d\tau, \tag{2.16}$$

averaged over time is the output of the Lock-In. Partially integrating I_ω leads to the *instrumental resolution function* $F_m = \frac{2}{\pi} \Re \sqrt{V_m^2 - \epsilon^2}/V_m^2$ of the Lock-In [27]. In other words,

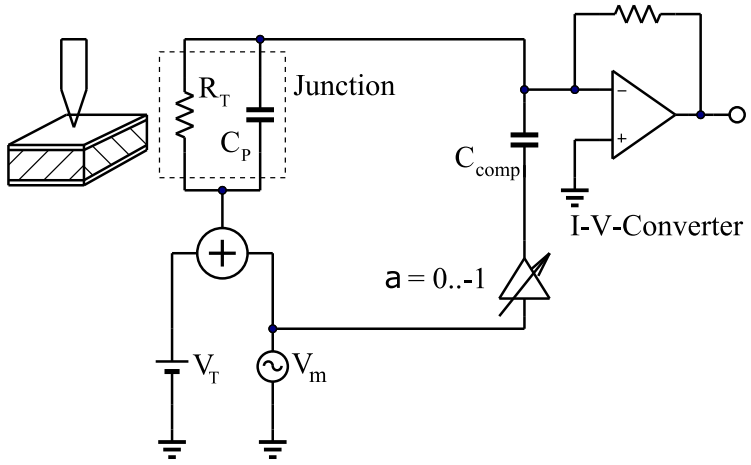

Figure 2.4: Crosstalk compensation during spectroscopic measurements. Due to the unavoidable coupling between the modulated tunneling voltage and the current I_T by the parasitic capacity C_p, a compensation by a 180° phase shifted signal over C_{comp} is helpful to detect small current signals.

our detected dI/dV signal is a convolution of the LDOS ρ_S in the sample and the instrumental resolution function:

$$\frac{dI}{dV}(V_T) \propto (\rho_s * F_m)(V_T) = \frac{2}{\pi V_m} \int_{-V_m}^{V_m} \rho_s(e(V_T+\epsilon))\sqrt{V_m^2-\epsilon^2}\, d\epsilon. \tag{2.17}$$

To give an idea of this broadening, we assume a perfectly flat ρ_s with the exception of one infinitely sharp δ-like peak at a certain energy. As it can be seen in figure 2.5 the δ-like peak is broadened to a half-sphere with a width of $2eV_m$.

To summarize, as long as the modulation voltage V_m is significantly smaller than the characteristic spectral feature, the broadening can be neglected. Otherwise one has to perform a deconvolution of the modulation and the LDOS to obtain the correct physical properties [28].

2.3.2 Influence of the finite temperature

Up to now we have assumed a junction temperature of zero to simplify the deduction of a model for tunneling spectroscopy. But often the resolution limit is determined by the finite temperature in the experiment. Using equation 2.9 from page 8 with the constraint of constant LDOS in the tip we get for the first derivative $\partial I/\partial V$:

$$\left.\frac{\partial I}{\partial V}\right|_{V_T} \propto \rho_t \int_{-\infty}^{\infty} \rho_s(eV_T+\epsilon)\,\mathrm{sech}^2\!\left(\frac{\epsilon}{k_BT}\right) d\epsilon. \tag{2.18}$$

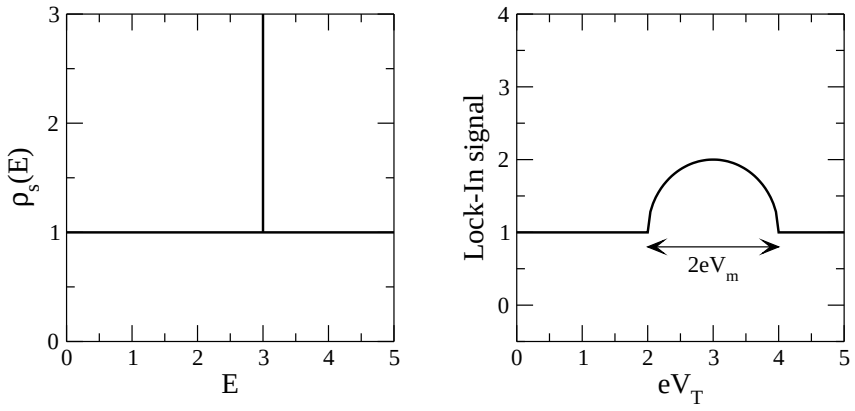

Figure 2.5: Visualization of the influence of the modulation on the resolution of obtained spectroscopic data. Assuming a perfectly flat LDOS in the sample with only one infinitely sharp peak (left panel) the modulation broadens this peak to a half-sphere with a width of $2eV_m$ (right panel).

The LDOS of the sample is convoluted with a hyperbolic secant function, which smears out all spectroscopic features.[4] In figure 2.6, the $\partial I/\partial V$ curve for an infinitely sharp δ-like peak in the LDOS is calculated. It shows a Gaussian-like broadening with a full width at half maximum (FWHM) of $3.2k_BT$. At ambient conditions of $T = 300$ K, the energy resolution would be limited to only $\Delta E \approx 80$ meV, while in low-temperature STS measurements the resolution is strongly enhanced and can reach the sub-millielectronvolt region.

In realistic high resolution spectroscopic experiments with Lock-In detection (see previous section 2.3.1), the signal is not only broadened by the temperature but additionally by the modulation voltage. Thus, the detected Lock-In signal has to be calculated by convoluting the temperature broadening function $F_T = \text{sech}^2(\epsilon/k_BT)$ as well as the instrumental resolution function F_m (equation 2.17) with the LDOS ρ_s of the sample:

$$\frac{dI}{dV}(V_T) \propto (\rho_s * F_T * F_m)(eV_T). \tag{2.19}$$

Using the temperature as fitting parameter in well known spectra (for example the BCS quasi-particle gap (see chapter 5)) can result in surprisingly high temperatures, higher than the base temperature of the STM. The reason is that even equation 2.19 does not include broadening due to noise in the power supply of V_T and offset-voltage noises in the current-voltage converter. As long as these noises are random they can be included in 2.19 by using an *effective temperature*: $T_{eff} := \sqrt{T^2 + T_n^2}$, with T_n as *noise temperature* originating from the electrical setup. Often these noises are the main source of broadening especially if periodical signals (for example multiples of the line frequency due to ground loops or high frequency signals from telecommunication transmitters (broadcast, cellular, etc.)) couple into the tunneling current or voltage.

[4] Remarkably, only the temperature of the tip and not of the sample influences the resolution when assuming constant LDOS in the tip, although tip and sample are usually in thermal equilibrium. Otherwise the temperature difference would lead to a thermo-voltage between tip and sample [29] which can be experimentally used to detect very sensitively the derivative of the LDOS at E_F [30].

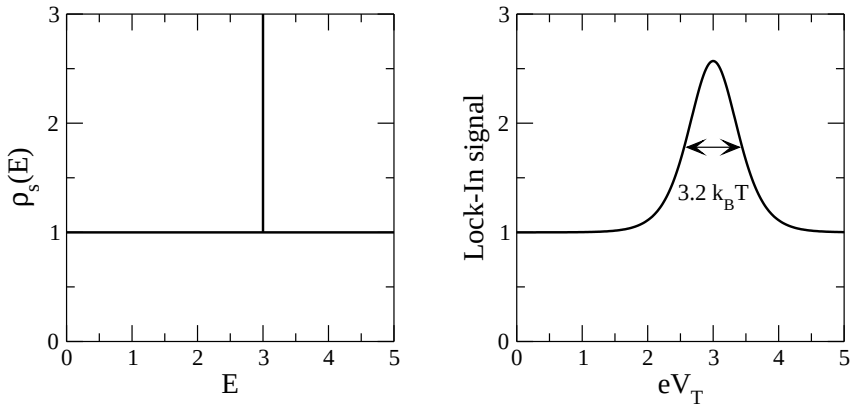

Figure 2.6: Visualization of the influence of the temperature on the resolution of obtained spectroscopic data. Assuming a perfectly flat LDOS in the sample with only one infinite sharp peak (left panel) the temperature T broadens this peak to a Gaussian-like peak with a FWHM of $3.2k_BT$ (right panel).

2.3.3 Inelastic electron tunneling spectroscopy

The goal of inelastic electron tunneling spectroscopy (IETS) is the detection of processes in which the tunneling electron looses partly its kinetic energy during the tunneling process between tip and sample. As schematically represented in figure 2.7, electrons with a sufficient kinetic energy have the possibility to excite internal states in, for example, adsorbates on the surface. After losing partly their kinetic energy, the electrons still must have enough energy to enter the electrode to be detected.

In planar tunnel junctions, IETS measurements were already performed approximately 40 years ago to detect vibrational excitation modes [31, 32, 33]. Because of the high lateral resolution in STM experiments which makes it possible to address individual atoms or molecules on surfaces, it is very appealing to perform measurements to detect inelastic processes. Additionally, in STM the characteristics of the adsorbate are much better defined and can be checked easily with the STM in contrast to planar tunnel junctions where the molecule is embedded in an ill-defined environment not accessible for direct studies. Indeed, there are also other techniques which have the capability to observe vibrational spectra – such as high resolution electron energy-loss spectroscopy (HREELS), infrared reflection-adsorption (IRRAS) or (micro) *Raman* spectroscopy – but only IETS has the advantage of imaging directly within the same experiment the atom or molecule under test.

Even if in the early days of STM collective vibrational excitations at the surface of graphite where detected [34], it is only recently that measurements have been performed on a single molecular level to detect molecular vibrations [35, 36, 37, 38, 39] and even the spin flip of single atoms [40]. To understand the influence of additional inelastic tunneling channels on the obtained spectra, we will present in short a model that mainly follows the idea of [41] and its application to STM [42]:

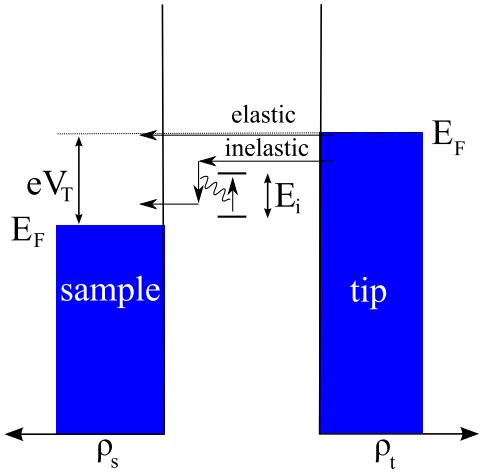

Figure 2.7: Schematic view of the inelastic tunneling process: In addition to the elastic tunneling current, an additional inelastic channel may exist where an electron crosses the barrier losing partly its energy by exciting an internal state in, for example, an adsorbate on the surface.

IETS without saturation:

The additional inelastic tunneling channel arises due to the fact that an electron with a kinetic energy $|eV_T| \geq E_i$ excites, for example, a vibrational mode in a molecule adsorbed on the sample surface. As we have seen in section 2.3, the contribution of the elastic tunneling current I_e is linear to the applied tunneling voltage V_T. Above the threshhold of E_i/e, the additional inelastic current I_i flows in first approximation linearly to the reduced voltage $V_T - E_i/e$ when assuming a lifetime τ_{ex} of the excited state much smaller than the average time between two tunneling processes[5], i. e. $\tau_{ex} \ll e/I_T$,. For the overall tunneling current $I_T = I_e + I_i$ we get:

$$I_T = \sigma_e V_T + \frac{\sigma_i}{e} \int_{-\infty}^{\infty} \big(\underbrace{f(\epsilon - eV_T + E_i)(1 - f(\epsilon))}_{t \to s} + \underbrace{f(\epsilon)(1 - f(\epsilon - eV_T - E_i))}_{s \to t} \big) d\epsilon. \tag{2.20}$$

The conductances σ_e and σ_i stand for the elastic and inelastic linear conductance, respectively, while $f(\epsilon)$ is the Fermi-Dirac distribution function as defined on page 5. Here we can not use the simplification as in equation 2.5. Instead we have to take into account tunneling in both directions from tip to sample ($t \to s$) as well as from sample to tip ($s \to t$) using the Fermi-Dirac distributions. The integral in 2.20 can be solved analytically [41]:

$$I_T = \sigma_e V_T + \sigma_i \left(\frac{\left(V_T - \frac{E_i}{e}\right) \tilde{f}(eV_T - E_i)}{\tilde{f}(eV_T - E_i) - 1} + \frac{\left(V_T + \frac{E_i}{e}\right) \tilde{f}(-eV_T - E_i)}{\tilde{f}(-eV_T - E_i) - 1} \right), \tag{2.21}$$

with the shorthand $\tilde{f}(\epsilon) = \exp(\epsilon/k_B T)$. The current-voltage curve in the zero temperature limit is shown in figure 2.8 (a). Calculating the first derivative with respect to the tunneling

[5] With this restriction, we assure that the tunneling electrons always find the system in its ground state.

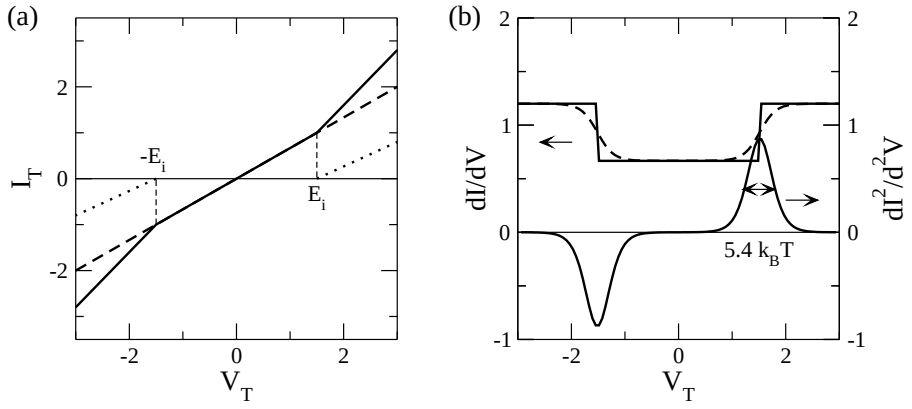

Figure 2.8: (a): Current-voltage relation of an inelastic tunneling process. An additional tunneling channel opens when the tunneling voltage exceeds the threshhold $|eV_T| \geq E_i$. The current (full line) consists of an elastic (dashed line) and an inelastic (dotted line) contribution. (b): dI/dV (upper curve) and dI^2/d^2V (lower curve) spectra of an inelastic tunneling process. Symmetrically around E_F a step like structure is detected in the dI/dV curve, smeared out due to the finite temperature (dashed line). In the dI^2/d^2V curve peaks with a width of $5.4k_BT$ occur.

voltage results in:

$$\left.\frac{\partial I_T}{\partial V}\right|_{V_T} = \sigma_e + \sigma_i \int_{-\infty}^{\infty} \left(f'(\epsilon - eV_T + E_i)(f(\epsilon) - 1) + f(\epsilon) f'(\epsilon + eV_T + E_i) \right) d\epsilon, \tag{2.22}$$

and

$$\left.\frac{\partial I_T}{\partial V}\right|_{V_T} = \sigma_e + \sigma_i \left(\frac{\tilde{f}(eV_T - E_i)\left(\tilde{f}(eV_T - E_i) - 1 - \frac{eV_T - E_i}{k_BT}\right)}{\left(\tilde{f}(eV_T - E_i) - 1\right)^2} + \frac{\tilde{f}(-eV_T - E_i)\left(\tilde{f}(-eV_T - E_i) + 1 + \frac{eV_T + E_i}{k_BT}\right)}{\left(\tilde{f}(-eV_T - E_i) - 1\right)^2} \right). \tag{2.23}$$

Surprisingly, equation 2.23 can be simplified with an acceptable error ($< 0.5\%$) to a more handy function:

$$\left.\frac{\partial I_T}{\partial V}\right|_{V_T} = \sigma_e + \sigma_i \left(\hat{f}(-eV_T + E_i) + \hat{f}(eV_T + E_i) \right), \tag{2.24}$$

with $\hat{f}$ as a modified Fermi-Dirac distribution: $\hat{f}(\epsilon) = (1 + \exp[\epsilon/1.46k_BT])^{-1}$. The resulting dI/dV curve shows a step-like increase in the conductivity symmetrically around E_F at $\pm E_i$ (see figure 2.8 (b)).

Furthermore, performing the second derivation results in peaks at $\pm E_i$:

$$\left.\frac{\partial^2 I_T}{\partial V^2}\right|_{V_T} = e\sigma_i\big(\hat{f}'((-eV_T + E_i)) + \hat{f}'((eV_T + E_i))\big), \tag{2.25}$$

which are schematically sketched in figure 2.8 (b). The broadening due to the finite temperature is therefore $5.4k_BT$ [41].

The d^2I/dV^2 signal can be easily detected with the Lock-In technique (see section 2.3.1) as shown in equation 2.14 on page 9 when using as reference for the Lock-In $2 \times \omega_m$. As for the dI/dV-measurement, the modulation of the voltage additionally broadens the detected signal by an instrumental resolution function of [27]:

$$F_m \propto \Re(e^2V_m^2 - \epsilon^2)^{3/2}. \tag{2.26}$$

IETS with saturation:

If the assumption we made in the beginning of this section is not fulfilled, i. e. the lifetime of the excited state is comparable or longer than the average time between two tunneling processes $\tau_{ex} \gtrapprox e/I_T$, the obtained spectra can change drastically.

As it was shown in reference [43], the conductance of the system for $|eV_T| > E_i$ can be described with an average conductance:

$$\overline{\sigma} = n_g\sigma_g + n_{ex}\sigma_{ex}, \quad n_g + n_{ex} = 1, \tag{2.27}$$

with the two conductances σ_g and σ_{ex} of the ground and excited state, respectively, and the average fractional occupations of the system n_g (ground state) and n_{ex} (excited state). The current-voltage relation, which we will treat for simplification only for positive voltages, can now be written in the zero-temperature limit as the following:

$$\begin{aligned} I_T(V_T) &= \sigma_g V_T && \text{for } eV_T < E_i, \\ I_T(V_T) &= \underbrace{(n_g\sigma_g + n_{ex}\sigma_{ex})V_T}_{elastic} + \underbrace{n_g\sigma_{up}(V_T - E_i/e) + n_{ex}\sigma_{down}V_T}_{inelastic} && \text{for } eV_T \geq E_i. \end{aligned} \tag{2.28}$$

The first part of the sum contains elastic contributions to the tunneling current, while inelastic current contributions are added in the second part originating from the transfer of the system from ground to excited state ($n_g\sigma_{up}(V_T - E_i/e)$) and from relaxation of the excited state by inelastic scattering ($n_{ex}\sigma_{down}V_T$). The fractional occupation in the excited state n_{ex} calculated as:

$$\begin{aligned} n_{ex} &= 0 && \text{for } eV_T < E_i, \\ n_{ex} &= \frac{\tau_g^{-1}}{\tau_g^{-1} + \tau_{ex}^{-1}} = \frac{\sigma_{up}(eV_T - E_i)}{\sigma_{up}(eV_T - E_i) + \sigma_{down}eV_T + e^2S} && \text{for } eV_T \geq E_i, \end{aligned} \tag{2.29}$$

with τ_g and τ_{ex} as the average lifetime of the ground and excited state, respectively. Spontaneous relaxation of the system from excited to ground state is thereby included into the lifetime τ_{ex} by the relaxation rate S.

After substitution of equations 2.27 and 2.29 into equation 2.28, one obtains for the differential conductance [43]:

$$\left.\frac{\partial I_T}{\partial V}\right|_{V_T} = \sigma_g \qquad \text{for } eV_T < E_i,$$
$$\left.\frac{\partial I_T}{\partial V}\right|_{V_T} = A + \frac{B}{\left(1+\frac{V_T - E_i/e}{\Gamma}\right)^2}, \qquad \text{for } eV_T \geq E_i, \tag{2.30}$$

with the parameters A, B, and Γ as:

$$A = \frac{\sigma_{up}(\sigma_{ex}+\sigma_{down}) + \sigma_{down}(\sigma_g + \sigma_{up})}{\sigma_{up}+\sigma_{down}}, \tag{2.31}$$

$$B = \sigma_{up}\frac{(\sigma_{up}E_i - e^2S)(\sigma_{ex}-\sigma_g) + 2\sigma_{up}\sigma_{down}E_i + e^2S(\sigma_{up}-\sigma_{down})}{(\sigma_{down}E_i + e^2S)(\sigma_{up}+\sigma_{down})}, \tag{2.32}$$

$$\Gamma = \frac{\sigma_{down}E_i + e^2S}{e(\sigma_{up}+\sigma_{down})}. \tag{2.33}$$

The resulting spectra depend strongly on the parameters of the system. The inelastic tunneling spectrum without saturation, as discussed in the previous paragraph, can be recovered from the presented model when assuming $\tau_g \gg \tau_{ex}$, i. e. $I_{down} + eS \gg I_{up}$, whereby $I_{down} = \sigma_{down}V_T$ and $I_{up} = \sigma_{up}(V_T - E_i/e)$ are the current contributions to relax and excite the state, respectively. While the currents $I_{up,down}$ have to be smaller than I_T, this is equivalent to $eS \gg I_T$. Under these assumptions equation 2.29 results in $n_g \approx 1$ and $n_{ex} \approx 0$ and equation 2.28 has the same form as equation 2.20 (in the $T = 0$ limit) with the commutation $\sigma_g \equiv \sigma_e$ and $\sigma_{up} \equiv \sigma_i$.

When the system has a sufficiently small relaxation rate S, the spectrum becomes asymmetric around $\pm E_i$. As schematically shown in figure 2.9 strong peaks or dips occur in the spectra when crossing the threshold $|eV_T| = E_i$. Assuming a conductivity of the excited state equal or larger than the conductivity of the ground state, i. e. $\sigma_{ex} \geq \sigma_g$, the spectra reminds us of the quasiparticle excitation spectrum in a superconductor (see chapter 5) as drawn in figure 2.9 (a) for $\sigma_{ex}/\sigma_g = 3$.

On the other hand, dips occur when assuming a sufficiently smaller conductance in the excited state then in the ground state which might even result in negative differential resistance (NDR). This is schematically presented in figure 2.9 (b).

A smaller conductance in the excited state of the system compared to the ground state might surprise, but can be understood by, for example, a change in the geometrical configuration of an adsorbed molecule [44]. Thus, the presented model has the additional advantage of being applicable on two-state systems with switching times, i. e. lifetimes of the ground and excited state much higher than the normal self-relaxation time S which lies in the ns and fs region. Under conditions where τ_g and τ_{ex} reach accessible timescales (μs-ms) for STM, the switching can be directly recorded and thus n_g, n_{ex} are calculable with equation 2.29 [44, 43].

Additionally, even timescales much shorter than in $I_T(t)$ measurements directly accessible can be analyzed by varying the setpoint current I_T and thus the number of tunneling electrons per second. IETS is applicable within a tunneling current of approximatively $20\,\text{pA} < I_T < 100\,\text{nA}$, corresponding to $1 \times 10^8 - 5 \times 10^{11}$ electrons per second or an

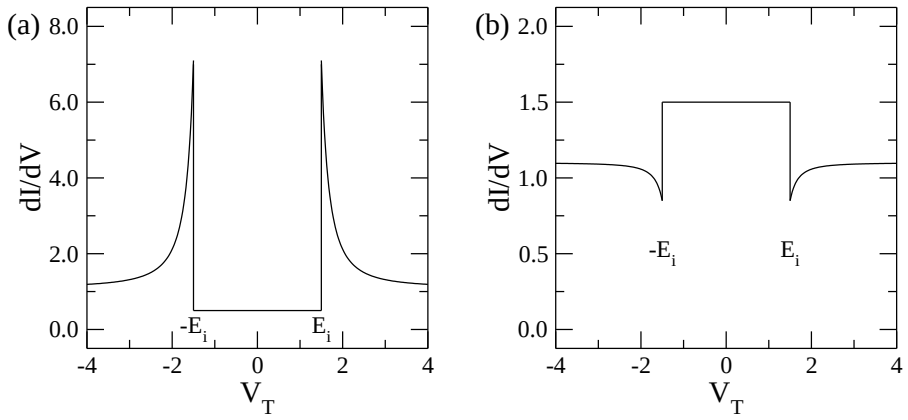

Figure 2.9: Simulated dI/dV spectra for inelastic tunneling with saturation. (a): A BCS-like spectrum with peaks at $eV_T = \pm E_i$ can occur when $\sigma_{ex} > \sigma_g$. The graphic shows a simulation using equation 2.30 with the parameters $A = 1.1$, $B = 6.0$, and $\Gamma = 0.35$ [arb. units], calculated for $\sigma_{ex}/\sigma_g = 3$, $\sigma_{up} = \sigma_{down} = 0.2 \times \sigma_g$, and $S = 0$. (b): Dips rather than peaks at $eV_T = \pm E_i$ occur when $\sigma_{ex} < \sigma_g$. Here it is simulated with $A = 1.1$, $B = -0.25$, and $\Gamma = 0.35$ [arb. units], calculated for $\sigma_g/\sigma_{ex} = 3$, $\sigma_{up} = \sigma_{down} = 0.2 \times \sigma_{ex}$, and $S = 0$.

adjustable average time between two tunneling electrons of $\tau \approx 2$ fs $- 10$ ns. While the conductances σ scale linearly with the tunneling current I_T, the spontaneous relaxation rate S is constant and thus discoverable by performing IETS measurements in a wide current range.

2.3.4 Spectroscopic maps

Up to now we have discussed the possibility of measuring the LDOS on single points. These methods use the high resolution of the STM to obtain locally a $\rho(eV_T)$ curve, i. e. the energy dependent LDOS.

Sometimes it is more useful to map the LDOS of a specific area at a certain energy. This is done by using the constant-current imaging mode (section 2.2) while modulating the applied voltage V_T and detecting the dI/dV signal continuously to create a map of the LDOS at the energy eV_T.

The main problem for analyzing dI/dV maps arises from the fact that we can no longer assume that the tip-sample distance stays constant. During the scan not only does the geometric surface topography change the tip height, but also variations in the LDOS integral $\int_0^{eV_T} \rho(\epsilon) d\epsilon$ influences the tip height as explained in section 2.2. To minimize these influences, the tip-sample distance can be taken into account to correct the dI/dV map by [45]:

$$\Delta\left(\frac{dI}{dV}\right) \approx -2\kappa \left(\frac{dI}{dV}\right)_0 \Delta z, \tag{2.34}$$

with $(dI/dV)_0$ as average dI/dV signal, $\Delta(dI/dV)$ and Δz as the change in the dI/dV and the z-signal, respectively, and $\kappa(z)$, as in equation 2.1 on page 4, with the estimated average tip-height z.

2.3.5 Beyond the limit of resolution

As we have discussed in detail in this section, STS offers a fascinating potential to obtain detailed spectroscopic information of the probed system. Unfortunately, the resolution is limited due to broadening effects. While in most cases the influence of electronic noise sources and the modulation voltage (section 2.3.1) to this broadening can be acceptably reduced by carefully designing the experiment and equipment, the influence of the finite temperature (section 2.3.2) is only reducible to a certain degree and therefore often the limiting factor of the approachable maximum resolution.

It might be useful to imagine for a moment a situation in which we are able to design the LDOS for a "perfect" tip. For spectroscopic measurements, a tip with flat LDOS over the energy range of interest might not be the best choice because of the broadening of the occupation of electronic states around E_F, which is a direct consequence of the fermionic nature of electrons and described by the Fermi-Dirac distribution. An imaginary tip with only a sharp peak in the LDOS at E_F would not be limited in resolution by the finite temperature as seen by calculating $\partial I_T/\partial V$ with equation 2.9. With such a tip the first and third sum vanish. Integration of the second part yields $\rho_s(eV_T)$:

$$\begin{aligned}\left.\frac{\partial I_T}{\partial V}\right|_{V_T} \propto \int_{-\infty}^{\infty} d\epsilon \Big[&\underbrace{-\rho_s(\epsilon)\delta'(\epsilon - eV_T) f_t(\epsilon - eV_T)}_{=0} \\ &-\rho_s(\epsilon)\delta(\epsilon - eV_T) f_t'(\epsilon - eV_T) \\ &+\underbrace{\rho_s(\epsilon)\delta'(\epsilon - eV_T) f_t(\epsilon - eV_T) f_s(\epsilon)}_{=0}\Big] \\ &= \rho_s(eV_T).\end{aligned} \tag{2.35}$$

Unfortunately, such a tip does not exist. But as it will be shown in chapter 5.3, superconducting tips with their sharp increase in the quasi-particle excitation spectra at $eV_T = \pm\Delta$ and their gap between $E_F \pm \Delta$ can be successfully used to significantly increase the resolution in STS measurements. With these tips it is indeed possible to obtain resolutions below $3.2k_BT$ (elastic tunneling) or $5.4k_BT$ (inelastic tunneling) even if one has to perform a deconvolution of the sample spectrum from the quasi-particle excitation spectrum of the superconducting tip.

Chapter 3

Creating a superlattice of Ce adatoms on Ag(111)

3.1 Introduction

The control of the geometric, electronic, and magnetic properties of ordered structures at the nanoscale is necessary for the understanding and fabrication of new materials and devices with structures as small as single atoms or molecules. In principle, there are two routes that lead to the construction of nano objects: (i) the "top-down" approach which is the extention of current methods of microelectronic production. In the (ii) "bottom-up" approach single atoms or molecules are manipulated using the STM to create complex structures [46, 47, 48, 49, 50], or, alternatively, atomic or molecular patterns are formed by self-assembly [51, 52, 53, 54].

In this chapter, the creation of a hexagonal superlattice of single Ce adatoms on the Ag(111) surface will be discussed. As proposed more than 25 years ago [55], long-range surface-state-mediated adatom interactions, which have been found on different metal surfaces [56, 57, 58, 59], can be the driving force to create such a superlattice when the adatom concentration, the sample temperature, and the adatom diffusing barrier are in a subtle balance [60, 61, 62].

Furthermore, the influence of such an artificially produced adatom superlattice on the surface state electrons will be discussed. A simple, intuitive model based on a periodical two-dimensional lattice and additionally performed tight-binding simulations will reveal site-dependent characteristic features in the LDOS which we compare with spectroscopic measurements showing good agreements between model and data [63].

The opening of an energy gap in the surface state band will be crucial for the understanding of the lattice stability and is reminiscent of the gap opening in systems with charge-density waves [64] or of metal-insulator *Mott*-transitions [65, 66]. Due to the high lateral resolution of STM, the local distribution of the electrons in the bonding and antibonding bands of the split surface state was measured [63]. Remarkably, the model based on surface state mediated adatom interaction, as well as the band calculations obtained with the tight-binding approach, resulted for the lowest energy configuration in the same adatom-adatom distance as experimentally observed. These reveal the fascinating duality in nature, where physical problems in the nanoworld can be solved using an approach in real space (as in the

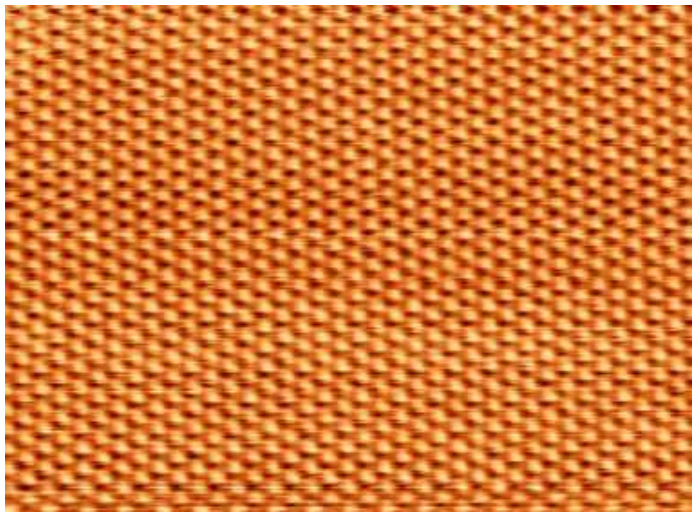

Figure 3.1: The clean Ag(111) surface observed with STM at a base temperature of $T = 50$ K with a tunneling voltage of $V_T = -20$ mV and a setpoint current $I_T = 1$ nA. The size of the image is approximately 9.5×7 nm^2.

first), or in reciprocal space (as in the latter).

Additionally, the influence of imperfections and disorder on the LDOS was measured and rationalized within the tight-binding model [63]. These results are of considerable interest, as disorder is expected to lead to *Anderson* localization in 2D [67, 68] with dramatic consequences on several properties, including the conductivity and the LDOS of the electrons in the sample.

3.1.1 The surface state of Ag(111)

Silver has a face-centered-cubic (fcc) crystal structure with a unit cell side-length of 409 pm [69]. The hexagonal closed-packed (111) surface reveals six-fold symmetry with an interatomic distance of $409 \text{ pm}/\sqrt{2} = 289$ pm, which can be made visible with STM as shown in figure 3.1.

The Ag(111) surface has a *Shockley*-like surface state [70, 71] which appears at the Γ-point of the projected band structure and has a band edge below the Fermi energy at -63 meV [26]. The surface state exists due to the fact that the periodicity of the crystal potential is interrupted at a surface. Normally "forbidden" electron wave-functions with an imaginary k-vector inside the crystal have on some surfaces a nonvanishing real part [72]. The amplitude of the surface states wave-function decreases exponentially in the crystal as well as in the vacuum. Nevertheless, on the Ag(111) surface the surface state electrons form a nearly free two-dimensional (2D) electron gas with an effective electron mass of $m^* = 0.42\, m_0$ (m_0: free electron mass) [73] and an almost parabolic energy momentum relation for low energies ($E \lesssim 250$ meV) as discussed in the following. Thus, it can be described by the expression

$$E(\vec{k}) = \frac{\hbar^2 \vec{k}^2}{2m^*} - E_0, \tag{3.1}$$

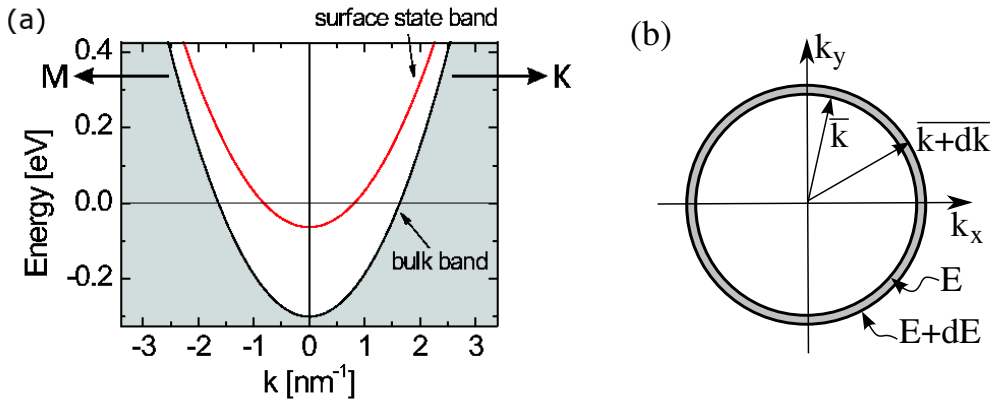

Figure 3.2: (a): Schematic representation of the projected band structure of the Ag(111) surface around the Γ point ($\vec{k} = \vec{0}$) plotted in direction of the M and K point. The parabolic curve describes the dispersion of the surface state. (b): For a 2D free-electron gas, the momentum $\vec{k}$ has two components and all $\vec{k}$ with the same energy lie on a circle. The difference between two circles of constant energy is the gray hatched ring.

which is schematically represented in figure 3.2 (a). The density of states (DOS) $n(E)$, i. e. the number of states in an energy interval $(E, E + dE)$, is thereby given as [72]:

$$n(E)dE = \frac{1}{(2\pi)^m} \left(\int_{\vec{k}(E)} \frac{df_E}{|grad_{\vec{k}} E(\vec{k})|} \right) dE, \quad m = \text{dimension} = 2 \text{ in this case,} \quad (3.2)$$

with f_E as the constant energy surface in $\vec{k}$-space and $grad_{\vec{k}} E(\vec{k})$ as the gradient of $E(\vec{k})$ with respect to $\vec{k}$.

For the free 2D electron gas, equation 3.2 can be understood with the help of figure 3.2 (b). All possible electron states with energy E are located on a circle in the k_x, k_y momentum space with constant absolute momentum value $k = \sqrt{k_x^2 + k_y^2}$. Changing k to $k + dk$ leads to $n(k)dk = 2\pi k dk$ new states (gray area). With the substitution $dk = m^*(\hbar^2 k)^{-1} dE$ obtained from the differentiation of equation 3.1, one can calculate the DOS of the 2D electron gas as an energy independent constant of:

$$E > E_0: \quad n(E)dE = \frac{m^*}{2\pi\hbar^2} dE; \qquad E < E_0: \quad n(E)dE = 0. \qquad (3.3)$$

As seen in chapter 2.3, scanning tunneling spectroscopy measures the LDOS of the sample. On clean Ag(111) terraces, a step-like increase in the differential conductance at $E_0 = -63$ meV can be observed which is due to the opening of new tunneling states of the surface state DOS, as shown in figure 3.3.

Additionally, mapping the LDOS (see chapter 2.3.4) at different tunneling voltages $eV_T > E_0$ close to surface steps or impurities allows the direct measurement of the energy momentum relation of equation 3.1 [74]. The electron waves are reflected at steps and

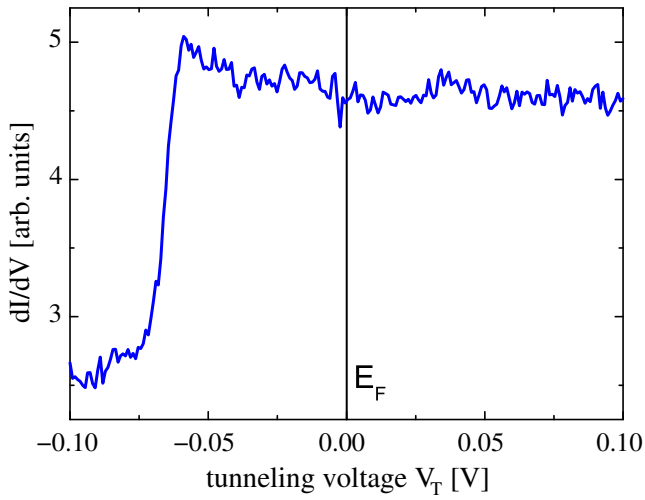

Figure 3.3: The surface state observed with STS on a clean Ag(111) terrace at a temperature of $T = 5$ K. Clearly visible is the step-like increase in the LDOS at energies above the surface-state onset at ≈ -63 meV. $V_T = -100$ mV, $I_T = 1$ nA, and $V_m = 5$ mV.

impurities producing an oscillating interference pattern (Fig. 3.4). Since these interference patterns are oscillations in $|\psi(\vec{r})|^2$ with $\psi(\vec{r})$ as the surface state electron eigenfunction, the spatial frequency of the pattern is given by $2k(E)$ with $k(E)$ as the inverse of the dispersion $E(k)$ of equation 3.1. This method has been successfully applied to measure the dispersion relation of the surface state of different metal surfaces [75, 76, 73].

3.1.2 Electron density oscillations

As shown in figure 3.4, impurities and adsorbates on the Ag(111) surface act as scatterers for the electron waves. They break the symmetry of a clean surface by inducing an additional local potential to the periodic potential of the surface atoms. The electrons around this perturbation attempt to screen the potential by density oscillations, so called *Friedel-oscillations* after J. Friedel who first described these oscillations theoretically [77]. The wave length of this oscillation at the Fermi energy E_F is thereby determined by half of the wave length $\lambda_F = 2\pi/k_F$ of the screening electrons.

In silver, the *Thomas-Fermi* wave vector for bulk electrons ($k_{TF} = 12$ nm^{-1}) [78] is relatively large compared to that of the (111) surface state electrons of $k_F = \sqrt{2m^* E_0}/\hbar = 0.82$ nm^{-1}. The shorter wave vector of the surface state electrons produces about a 15-times larger oscillation wavelength, which makes the observation in STM much easier. Additionally, the screening amplitude decays in the bulk with r^{-2}, while it decays on the surface for surface state electrons only with r^{-1} due to the dimensional restriction in two dimension.

A single Ce atom observed on a clean Ag(111) surface reveals this Friedel-like oscillatory modulation of the surface state electron density, as shown in figure 3.5 (a). The pseudo 3D representation results from a constant current STM image which was measured at a base temperature of $T = 3.9$ K to ensure that the Ce adatom is immobile during the measurement. It shows concentric rings of increased tip-height around the atom in the center of the

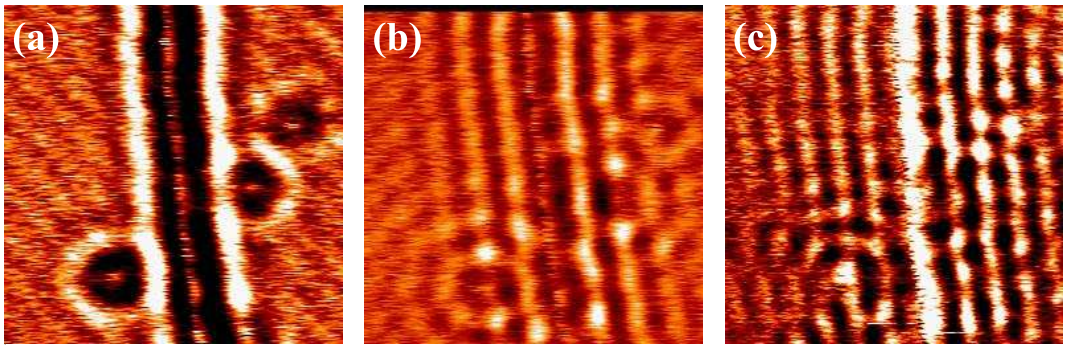

Figure 3.4: dI/dV maps of Ag(111) at (a): $V_T = -50$ mV, (b): $V_T = -25$ mV, (c): $V_T = +10$ mV. Oscillations perpendicular to the step edge, which run vertically through the middle of the images and circular around impurities, form a standing wave pattern with an energy dependent wave length. The size of the image is 40×40 nm^2 recorded with a base temperature of $T = 50$ K, a setpoint current of $I_T = 0.5$ nA, and a voltage modulation of $V_m = 5$ mV.

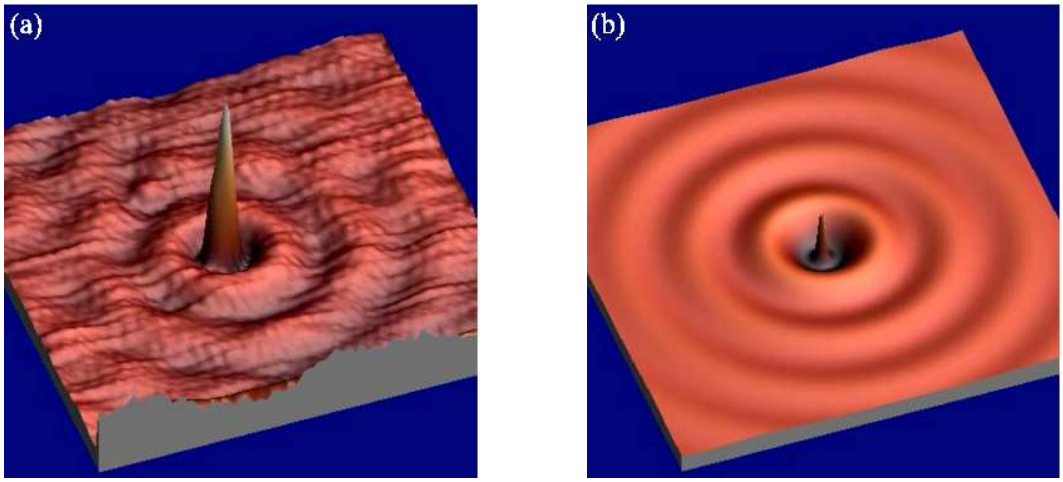

Figure 3.5: (a): Friedel oscillation of a single Ce adatom on a clean Ag(111) surface observed at a base temperature of $T = 3.9$ K, a tunneling voltage of $V_T = -3$ mV, and a setpoint current $I_T = 20$ pA. Image size: 25×25 nm^2. (b): Simulation using equation 3.4 with a scattering phase shift of $\theta_0 = 0.37\,\pi$ and a wave vector at E_F of $k = 0.82$ nm^{-1}.

image. The tunneling voltage V_T was set to -3 mV, very close to E_F, so that only the small interval between $E_F - 3$ mV and E_F of the LDOS contributes to the tunneling current (see equation 2.7 and chapter 2.2) and thus, the topographic image reflects mainly the LDOS at E_F. A first maximum exists at a radius of ≈ 3.2 nm, while the following rings are at a distance of $\approx \lambda_F/2 = 3.8$ nm from each other, with λ_F as the in-surface Fermi-wavelength $\lambda_F = 2\pi/k_F$. The deviations from a perfect circular shape are due to interferences with reflections from other adatoms located further away and therefore not seen in the figure.

For the LDOS at E_F, the variation can be described as the sum of the amplitude of an incoming and a reflected electron wave [75]:

$$\Delta\rho(r) \propto \frac{1}{k_F r}\left(\cos^2\left(k_F r - \frac{\pi}{4} + \theta_0\right) - \cos^2\left(k_F r - \frac{\pi}{4}\right)\right). \tag{3.4}$$

The Fermi-level phase shift θ_0 of the reflected wave is thereby due to the interaction with the adsorbate. Simulating equation 3.4 and comparing it with the measured pattern results in a phase shift for Ce on Ag(111) of $\theta_0 = (0.37 \pm 0.05)\pi$, as shown in figure 3.5 (b). The simulation is in good agreement with figure 3.5 (a) except for the shape of the atom in the center of the image which is not included in the simulation.

3.2 An adsorbate superstructure

Dosing approximately 0.2% of a monatomic layer (ML)[1] of Ce adatoms from a thoroughly degassed tungsten filament onto a well-prepared Ag(111) surface leads to a non-random distribution of Ce adatoms. Figure 3.6 shows an image taken at a temperature of 3.9 K by pumping on the bath of the He cryostat [79]. The tunneling voltage $V_T = -100$ mV and current setpoint $I_T = -20$ pA lead to a high tunneling resistance to prevent influences of the cut Pt-Ir tip on the adatoms. The adatoms form rows and small islands with a typical adatom-adatom separation of 3.2 ± 0.05 nm.

After having increased the sample temperature to 4.7 K the Ce adatoms look "fuzzy" due to the jumps of the adatoms to adjacent lattice positions on the underlying Ag(111) lattice seen in figure 3.7. The few stable objects which remain immobile in the image were identified as dimers which have been formed after Ce evaporation on the sample at a temperature of about 8 K. Even at the low setpoint current ($I_T = 20$ pA), some of the Ce adatoms show tip-induced motions. The atoms move in the direction of the scan as seen in multiple imaging of the same atom in several subsequent scanlines.

The observed adatom-adatom distance of 3.2 nm matches the first maximum in real space of the electron density oscillation at E_F around a single Ce adatom, as discussed in section 3.1.2. While *J. Friedel* already suggested an interaction between embedded atoms in a crystal due to electron density oscillations [77], *K. H. Lau* and *W. Kohn* showed that for interactions between adsorbates on a surface with a partly filled surface state band the interaction energy decays only with $1/r^2$ instead of $1/r^5$ as for interactions mediated by bulk states [55]. The explicit theoretical analysis based on the *Harris* functional expression [80] was performed by *P. Hyldgaard* and *M. Persson* [81] in particular to be easily applicable

[1] In the context described here, a monatomic layer of Ce means the complete coverage of the Ag(111) surface with Ce atoms having the same spacing as in their crystal lattice. ($\approx 4 \times 10^{14}\text{cm}^{-2}$)

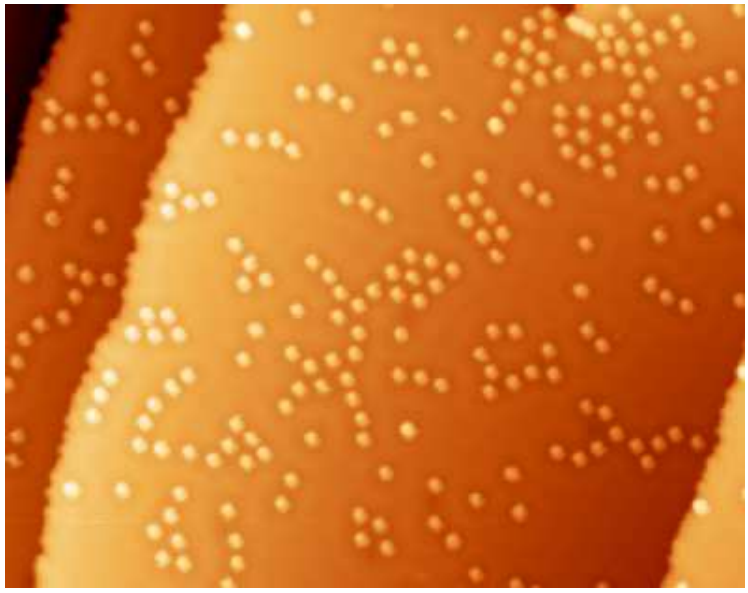

Figure 3.6: STM constant-current image of the Ag(111) surface covered by approximately 0.2% of a ML of Ce obtained at a temperature of 3.9 K (image-size 100×80 nm^2, $V_T = -100$ mV, $I_T = 20$ pA). The Ce adatoms have a preferred next-neighbor distance of 3.2 nm.

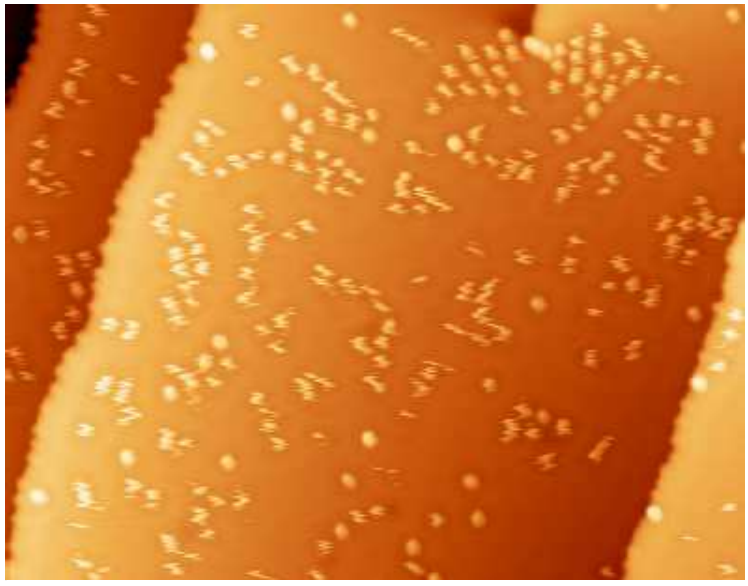

Figure 3.7: STM constant-current image as in figure 3.6 but at a temperature of 4.7 K. The Ce adatoms are mobile and appear "fuzzy" while some dimers which have been formed are immobile.

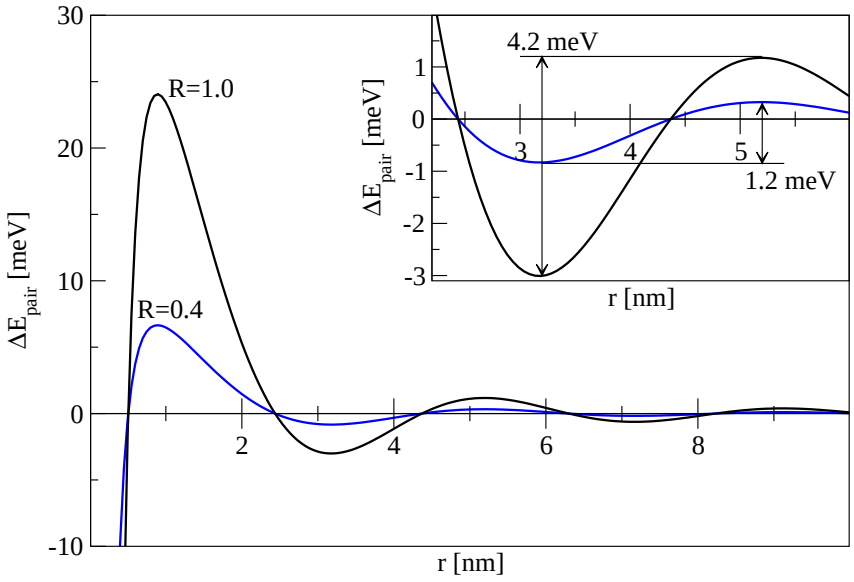

Figure 3.8: Calculated interaction energy between two Ce adatoms on Ag(111) for $\theta_0 = 0.37\pi$. Depending on the reflectivity R the trapping barrier for an adatom-adatom distance of 3.2 nm is between $1.2 - 4.2$ meV.

to STM measurements. Their results lead to the following surface state mediated interaction energy between two adatoms which is in good agreement with *ab initio* calculations [82]:

$$\Delta E_{pair}(r) \simeq -E_0 \left(\frac{(R-1)^2}{4} + R\sin^2(\delta_0') \right) \times \left(\frac{2}{\pi} \right)^2 \frac{\sin(2k_F r + 2\theta_0)}{(k_F r)^2}. \qquad (3.5)$$

The interaction energy depends on the distance r between the adsorbates, the reflectivity R, the surface state band edge onset energy E_0 with respect to E_F, and the associated surface Fermi wavevector k_F. Scattering into bulk states is taken into account by a complex phase shift: $\delta_0 = \delta_0' + i\delta_0''$. With this definition, the reflectivity is written as $R = \exp[-2\delta_0'']$ and the Friedel-like phase shift at E_F for an isolated adsorbate can be written [81]:

$$\theta_0 = \tan^{-1}\left(\frac{1 - R\cos(2\delta_0')}{R\delta_0'} \right). \qquad (3.6)$$

Using the observed phase shift $\theta_0 = (0.37 \pm 0.05)\pi$ (see section 3.1.2 and figure 3.5), equation 3.5 has its first minimum at $r = 3.2 \pm 0.2$ nm and a weak local maximum at $r = 5.2 \pm 0.2$ nm (Figure 3.8). The amplitude of the interaction energy depends therefore on the reflectivity R which can only be between 0.40 and 1.0 due to the restrictions implied by equation 3.6. For $R = 1$ the Ce adatoms act as perfect scatterers, i. e. no surface state electron waves are scattered into bulk states, and the trapping barrier for an adjacent adatom at the position of minimal energy ($r = 3.2$ nm) is about 4.2 meV, while for $R = 0.4$ the trapping barrier decreases to about 1.2 meV. To conclude, the deposited Ce must have sufficient thermal energy to overcome the small potential barrier at an adatom-adatom distance of $r = 5.2$ nm by random diffusion, but get trapped afterwards at the energetically preferred distance of $r = 3.2$ nm, as observed in figure 3.6.

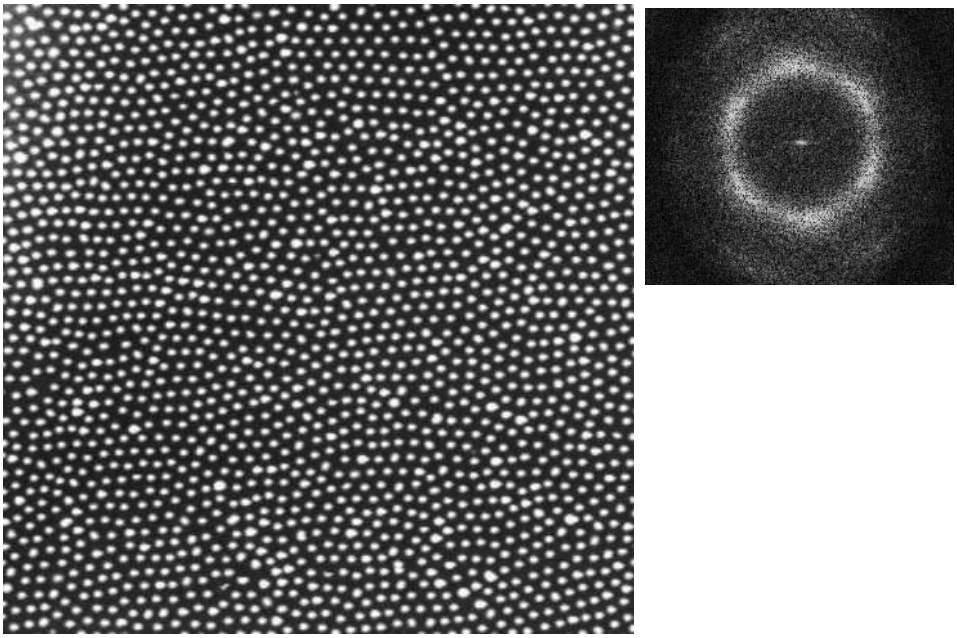

Figure 3.9: Left: Constant-current STM image (108×108 nm^2, $V_T = -90$ mV, $I_T = 40$ pA) of the Ag(111) surface covered by approximately 0.01 ML of Ce at a base temperature of 3.9 K. Right: Fourier transformation of the image.

Increasing at low temperature ($T = 3.9$ K) the coverage to about 1% of a ML of Ce adatoms leads to an ordered hexagonal arrangement as shown in figure 3.9 (left). The Ce adatoms are clearly visible as bright spots forming a hexagonal superlattice with a distance between two neighboring adatoms of 3.2 ± 0.2 nm which is manifested in the Fourier transformation (3.9 (right)) as a ring-like structure at the corresponding space-frequencies. As a consequence of the only short range angular correlation in the superlattice [83] only broad peaks are detected at the six symmetry points in contrast to a perfectly oriented hexagonal lattice.[2] This self-organized superlattice covers the entire Ag(111) surface up to macroscopic distances, i. e. taking images at different regions of the sample by displacing the tip in the millimeter range leads to the same superstructure. Such a long-range ordered superlattice has not been observed before, even if attempts were made with Cu on Cu(111) [57, 58] and Co on Ag(111) [84].

To estimate the interaction between the Ce adatoms in the lattice, we may calculate the interaction energy for an adatom located at $\vec{r}$ surrounded by six neighbors at $\vec{r}_i$ ($i = 1 \ldots 6$) in hexagonal arrangement with an adatom-adatom distance of 3.2 nm. Using the pair interaction energy and an additional term for the interactions between three adsorbates [85] result in an interaction energy for the central atom of:

$$\Delta E_{int}(\vec{r}) \simeq \sum_{i=1}^{6} \Delta E_{pair}(|\vec{r}_i - \vec{r}|) + \sum_{i=1}^{6} \sum_{j>i}^{6} \Delta E_{triple}(\vec{r}_i, \vec{r}_j, \vec{r}) \tag{3.7}$$

[2] Higher ordered regions which show more pronounced peaks in the Fourier transformations were also found as can be seen in [60].

with ΔE_{pair} as defined in equation 3.5, and

$$\Delta E_{triple}(\vec{r}_i, \vec{r}_j, \vec{r}) \simeq -E_0 \left(\frac{(R-1)^2}{4} + R\sin^2(\delta_0^{'}) \right)^{3/2} \left(\frac{16\sqrt{2}}{\pi^{5/2}} \right) \gamma_{123} \times \frac{\sin(2k_F r_{123} + 3\theta_0 - 3\pi/4)}{(k_F r_{123})^{5/2}} \tag{3.8}$$

with the definition of θ_0 as in equation 3.6 and the shorthands

$$r_{123} = |\vec{r}_i - \vec{r}_j| + |\vec{r}_i - \vec{r}| + |\vec{r}_j - \vec{r}| \quad \text{and} \quad \gamma_{123} = 2\left(2\frac{r_{123}^{3/2}}{\sqrt{|\vec{r}_i - \vec{r}_j|\,|\vec{r}_i - \vec{r}|\,|\vec{r}_j - \vec{r}|}} \right).$$

Minimizing the interaction energy ΔE_{int} by varying the adatom-adatom distance d with a constant phase shift set to $\theta_0 = (0.37 \pm 0.05)\pi$ results in $d = 3.2 \pm 0.2$ nm, which is in excellent agreement with the observed one.[3] The corresponding energy map coded in gray levels (dark: low values, bright: high values) and a cross section is shown in figure 3.10.

Depending on the reflectivity R, the central atom sits in an energetic minimum ($\vec{r} = \vec{0}$) induced by the six next-neighbor Ce adatoms and gains an energy between 6.7 meV (for $R = 0.43$) and 31 meV (for $R = 1$) with respect to the energy at infinite position ($|\vec{r}| \to \pm\infty$). The formation of dimers is inhibited by the potential wall at $|\vec{r}| \approx 2.3$ nm. Furthermore, figure 3.10 exhibits an almost parabolic energy-position relation for small variations of $\vec{r}$ around the most stable position at $\vec{r} = \vec{0}$.

Using the statistical distribution of the variation of the adatom position between two successive scan lines at a temperature of $T = 4.8$ K, which occurs due to random jumps of the Ce adatom from one atomic position to another within the well as seen in figure 3.11 (b), we determine directly the reflectivity R by comparing to the Boltzmann distribution

$$n(\vec{r}) = n_0 \exp\left[-\frac{\Delta E_{int}^R(\vec{r}) - \Delta E_{int}^R(\vec{0})}{k_B T} \right]. \tag{3.9}$$

The result is displayed in figure 3.12 and shows a Gaussian distribution with a full width at half maximum of 0.57 ± 0.02 nm, consistent with the approximately parabolic potential well. A least square fit of equation 3.9 to the data results in a reflectivity of $R = 0.43^{+0.1}_{-0.0}$ and thereby in a superlattice confining potential of 11.8 ± 1.2 meV (see fig. 3.10)[4]. We have to note that the measured distribution was corrected to the fact that we measure changes only in one direction. It should be approximately the true adatom distribution as long as $\tau_{tip} \ll \tau_{jump} \ll \tau_{atom}$, where $\tau_{tip} \simeq 30$ ms is the time to scan over a single adatom, τ_{jump} is the temperature dependent characteristic adatom hopping time from one Ag(111) lattice

[3] Neglecting triple interactions between the adsorbates would lead to an ideal phase shift for minimal energy in a lattice with 3.2 nm adatom-adatom distance of $\theta_0 = 0.45\pi$ in contradition to the observations, while when including triple interactions the ideal phase shift becomes 0.36π. Higher order processes, i. e. interactions between 4 or more atoms have very small influence on the overall energy due to the rapid spacial decay of the wave-functions and are neglected.

[4] Surprisingly, the analysis results in the minimal possible reflectivity R that is allowed according to equation 3.6. Even if not discussed here, the interplay between the phase shift θ_0 and the reflectivity R depends strongly on the intrinsic binding of the Ce adatom to the Ag(111) surface. Since a high percentage of electrons are scattered into bulk states the adsorption seems to be dominated by the interaction with the surface state.

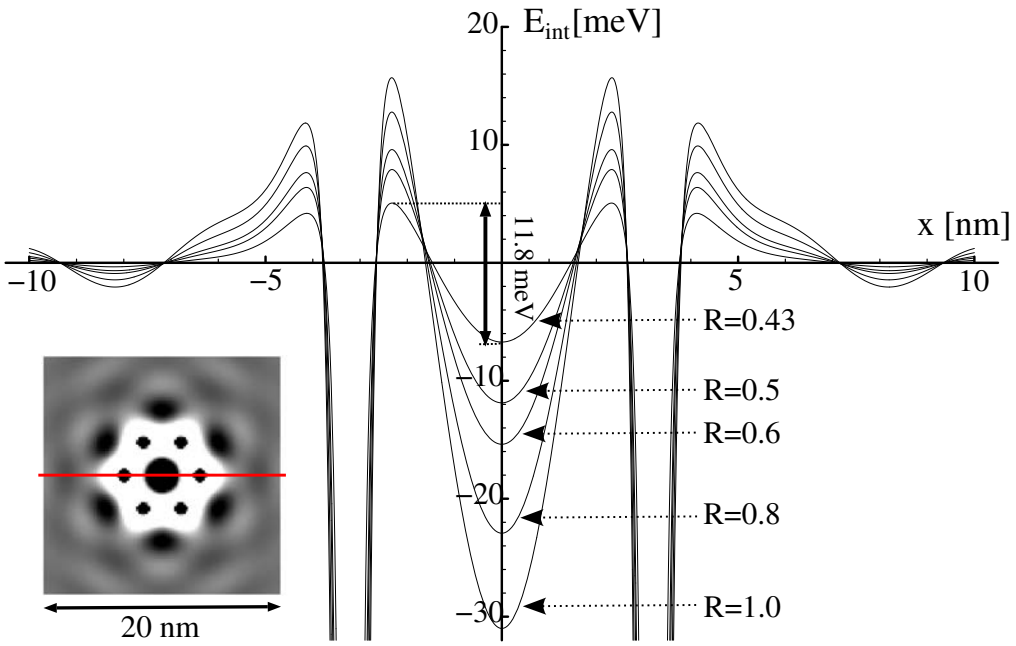

Figure 3.10: Calculated potential landscape and cross-section along the direction $\vec{r} = \binom{x}{0}$ (line) of the pair- and three-adsorbate interaction for a single adatom surrounded by 6 in hexagonal order fixed adatoms (small black spots in the intensity plot) with an adatom-adatom distance of 3.2 nm and different reflection coefficients R. For the reflectivity $R = 0.43$ the confining potential is given by 11.8 meV.

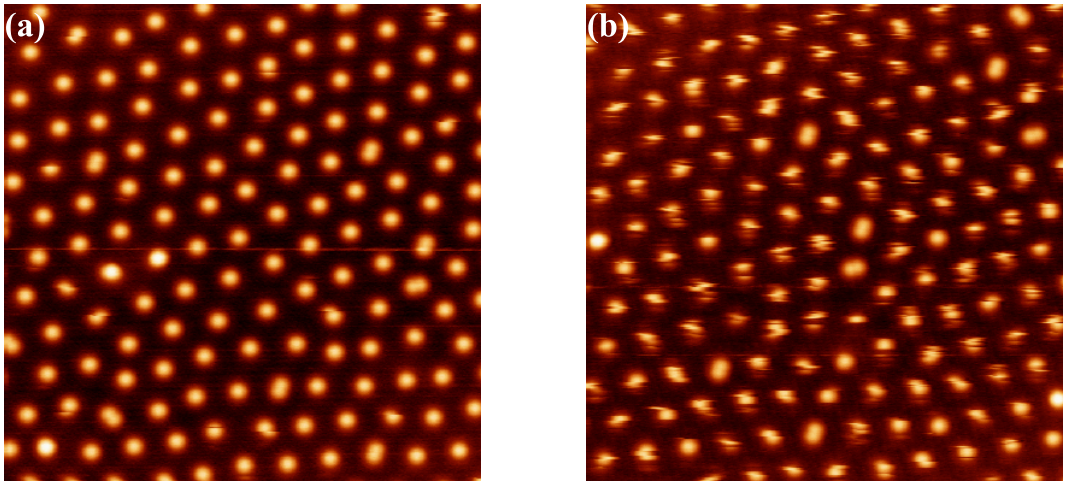

Figure 3.11: Constant-current STM images of the Ag(111) surface covered by approximately 1% of a ML of Ce obtained at a temperature of (a) 3.9 K and (b) 4.8 K with the same image-size of 35×35 nm^2 ($V_T = -100$ mV, $I_T = 20$ pA). At 3.9 K the Ce adatoms are immobile during the time of data acquisition, while they look "fuzzy" due to jumps between lattice-sites of the underlying Ag(111) surface during the scanning at the slightly elevated temperature of 4.8 K.

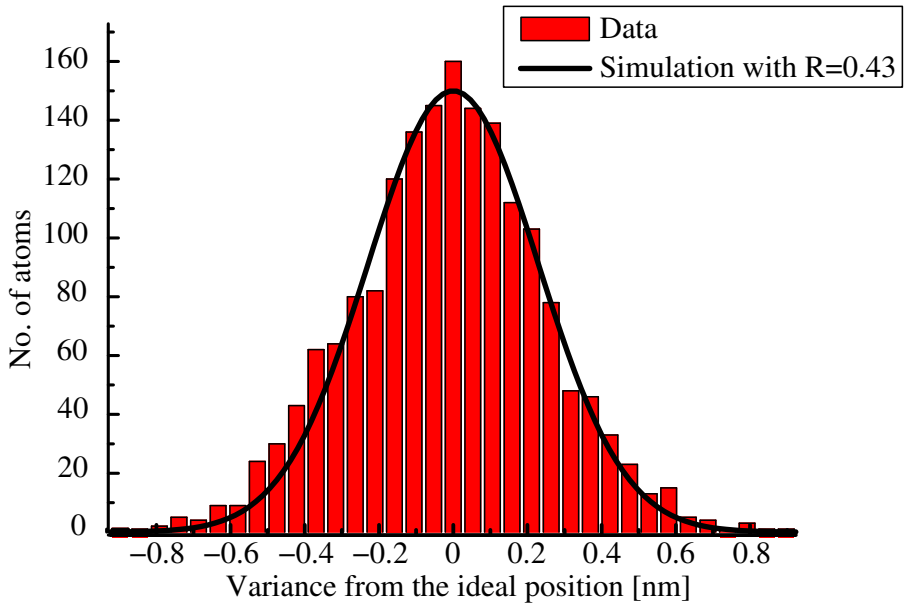

Figure 3.12: Histogram of the measured Ce adatom displacement from the ideal position of the hexagonal superlattice sites at 4.8 K (bars) and statistical analysis using the $E_{int}(r)$ relation of equation 3.7 and the Boltzmann distribution. The best agreement is obtained for an adatom reflectivity of $R = 0.43$.

site to another, and $\tau_{atom} \simeq 16$ s is the total time during which a given adatom is monitored and hopping events can be recognized. The average time between two jumps $\tau_{jump} = 300 \pm 100$ ms is estimated from the statistical probability of observing a jump during τ_{tip} and the probability of observing no jumps during the time of 1 s between successive scans over a given adatom. Non-negligible possible forward-backward jumps due to $\tau_{jump} \ll 1$ s are thereby included.

Assuming an attempt frequency of $\nu_0 = 10^{12\pm0.5}$ Hz [59] we calculate the diffusion barrier for the Ce adatom on the Ag(111) lattice to $E_{diff} = k_B T \ln(\nu_0 \tau_{jump}) = 10.9 \pm 0.7$ meV. Thus, reducing the base temperature to $T = 3.9$ K "freezes" the superlattice as seen in figure 3.11 (a) because the adatom hopping time τ_{jump} comes now in the range of several minutes. Additionally, according to equation 3.9 the variation of the adatom positions from their ideal positions is smaller, i. e. the superlattice shows a higher degree of ordering.

To summarize this section, we saw that at low Ce adatom concentration $\ll 1\%$ ML the interaction energy between two Ce adatoms creates only a shallow potential wall of 1.2 meV (see figure 3.8), not enough to trap the adatom at $T = 4.8$ K and to form an ordered structure except for small regions with locally higher adatom concentrations as seen in figure 3.7. But with higher concentration the superlattice is created because adatoms inside an ordered lattice are trapped in a sufficiently high potential wall of 11.8 meV. Additionally, the low diffusion barrier, which is of the same order of magnitude, allows the adatom to find the energetically preferred position in the superlattice, while for systems that require higher temperatures to allow adatom diffusions (as for example Cu/Cu(111) [58] or Co/Ag(111)

[59]) the long-range surface-state mediated interaction potential is too weak compared to the diffusion potential to create ordered structures on a larger scale.

Increasing the temperature and thereby increasing exponentially the mobility of the Ce adatoms results in more and more disorder in the hexagonal arrangement of the adatoms and finally causes the collapse of the superlattice at temperatures of about 10 K [61].

3.3 Modification of the surface state

The creation of the highly ordered adatom superlattice on the Ag(111) surface with its characteristic two-dimensional surface state is well described in the framework of long-range adatom-adatom interactions, as explained in detail in the previous section. But this model does not provide results for the electronic behavior of the surface state in interaction with the scattering pattern.

Thus, STS measurements were performed on the stable superlattice at a reduced base temperature of $3.3 - 3.9$ K by pumping on the liquid He bath [79] to prevent movements of the adatoms during data acquisition. The applied tunneling voltage V_T was modulated with a small sinusoidal voltage V_m and the dI/dV signal was detected with Lock-In technique as described in chapter 2.3.1.

Figure 3.13 (a) presents a close-up (7.5×7.5 nm^2) constant current STM image of the Ag(111) surface covered with approximately 0.01 ML Ce forming a well ordered hexagonal superlattice with an adatom-adatom distance of $d = 3.2$ nm. The dI/dV spectrum shown in figure 3.13 (c) (black curve) was measured in the center of the triangle formed by three Ce adatoms as marked in figure 3.13 (a). Compared to the spectrum obtained on clean Ag(111) (blue curve), the spectum has changed dramatically. Instead of a step like increase in the differential conductance at the surface state band onset of -63 meV (see section 3.1.1), two relatively broad peaks are observed at approximately 85 and 210 meV. Using the energy of the first peak as the tunneling voltage for spectroscopic mapping of the differential conductance, the image in figure 3.13 (b) is obtained revealing a maximum in the LDOS in the center of the triangles, and a minimum centered on the Ce adatoms with a finite spatial extent.

Additional site-resolved spectroscopic measurements in a slightly larger superlattice at a Ce adatom concentration of approximately 0.7% ML resulting in a superlattice spacing of $d = 3.5$ nm were performed, showing structures in the spectra that strongly depend on the spatial position, as seen in figure 3.14. On the Ce adatoms (curves $1 - 3$) the spectra are mainly flat with a broad gaplike structure between approximately -75 and $+35$ meV. When moving the tip away from the center of gravity of the adatom, a peak at an energy of approximately $+45$ meV arises which has its maximum intensity in the center position of the triangle formed by three Ce adatoms (curves $4 - 6$). The position of the peak is shifted towards lower energies compared to the measurement in the $d = 3.2$ nm superlattice (figure 3.13 (c)). Furthermore, at a bridge site position, i. e. in between two adatoms (curves $10 - 12$), the intensity of the observed peak is slightly reduced and shifted to higher energies (approximately $+60$ meV).

To get an adequate overview of the spatial location and energy of the peaks in the LDOS, 1024 spectra were measured in a raster of 32×32 points covering completely one hexagon of the superlattice. Each spectrum therefore contains 24 data points measured at a tunnel-

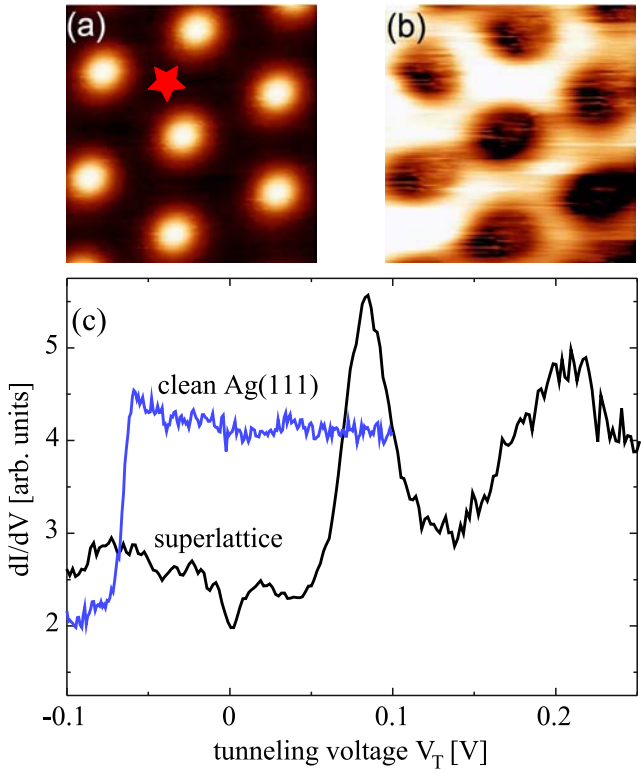

Figure 3.13: (a): STM image of a hexagonal unit cell of the superlattice of Ce adatoms on Ag(111) with an adatom-adatom distance of $d = 3.2$ nm (image size: 7.5×7.5 nm^2, $V_T = -100$ mV, $I_T = 10$ pA). The red star is not an artificial atom, but marks the point where the spectrum (c) was measured. (b): dI/dV map of the same area at $V_T = 85$ mV, corresponding to the energy eV_T of the first peak of the spectrum shown below. (c): dI/dV-measurement of the clean Ag(111) surface showing the unperturbed surface state (see section 3.1.1) in blue (set point before opening the feedback-loop: $V_T = -100$ mV, $I_T = 1$ nA, $V_m = 5$ mV) and dI/dV measurement in the center of the triangle formed by Ce adatoms in black (average of 5 spectra, $V_T = -109$ mV, $I_T = 10$ pA, $V_m = 5$ mV).

ing voltage V_T between -100 and $+130$ mV. To prevent jumps of Ce adatoms between adjacent Ag(111) lattice sites during the recording of all spectra in about 110 minutes, it was essential to reduce the base temperature to 3.3 K by pumping on the He-bath. All the data points of the 1024 spectra that correspond to a certain energy were combined into a color-coded image (color scale: blue-red-yellow corresponding to low-medium-high dI/dV signal-strength) as presented in figure 3.15. The maps at low energies of -100 and -90 meV reveal a faint higher dI/dV signal on top of the adatoms as in the region between the adatoms. Between an energy of about -60 and $+20$ meV the maps show no difference in the dI/dV signal over the whole recorded area, while at energies $eV_T \geq 40$ meV a strong dI/dV signal with a maximum at about 60 meV occurs in the region between the adatoms.

The average distance d between two Ce adatoms in the superlattice depends on the Ce coverage, and was determined experimentally to be in the range of $d = 2.3$ nm (for

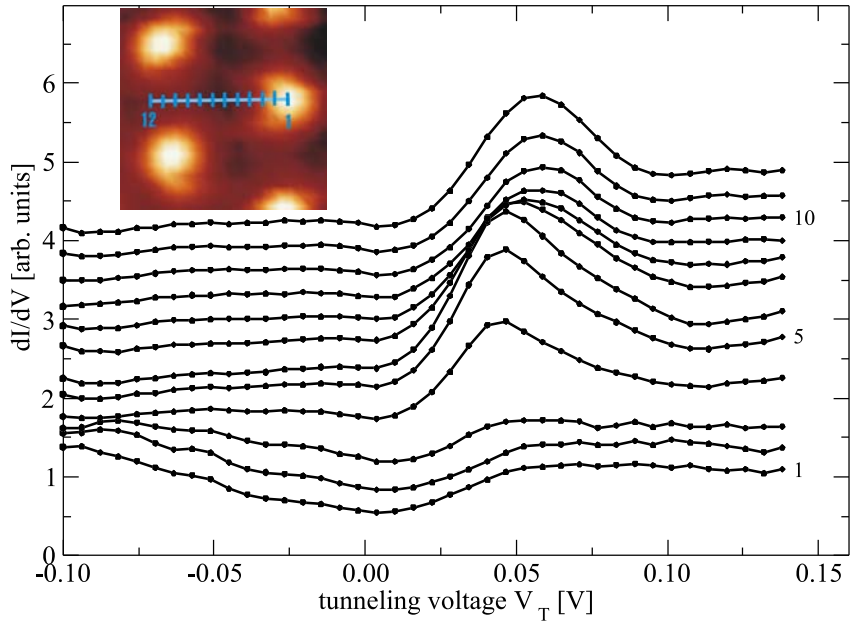

Figure 3.14: Set of dI/dV spectra measured in a hexagonal superlattice with an adatom-adatom distance of $d = 3.5$ nm from an on top position $(1-3)$ to a center position $(4-6)$ and a bridge site $(10-12)$. For illustration see the inset STM image where the positions are marked. The spectra are shifted vertically with respect to each other for better visualization. The set point before opening the feedback loop was for all spectra: $V_T = -100$ mV, $I_T = 19.5$ pA at $T = 3.3$ K and $V_m = 10$ mV.

$\approx 1.6\%$ ML) to $d = 3.5$ nm (for $\approx 0.7\%$ ML). Higher Ce coverages ($> 1.6\%$ ML) result in the formation of clusters [61] with no long-range order, while lower coverages ($< 0.7\%$ ML) lead to the formation of islands of Ce adatom superlattices with the energetically most favored interatomic distance of $d = 3.2$ nm (see figure 3.21(b)) and empty areas in between (see page 26).

The position of the first peak in the spectra recorded at the center of a triangle formed by three Ce adatoms depend critically on the adatom-adatom distance d, as shown in figure 3.16 which compares the spectra taken in superlattices with five different average adatom distances. For higher Ce concentration, i. e. smaller d, the position of the first peak shifts to higher energies. Additionally, the peaks are broadened due to the increased disorder in compressed lattices ($d < 3.2$ nm). The energy of the peak depends quadratically on the adatom-adatom distance d, as shown in figure 3.21 and discussed later.

3.3.1 The nearly free electron model

To rationalize the observed spectral features we might apply a simple, in general solid state physics well known, nearly free electron model (NFE), assuming an undisturbed, infinite 2D superlattice of regularly arranged Ce adatoms on the Ag(111) surface with a fixed adatom-adatom distance of $d = 3.2$ nm. Additionally, we assume a perfect free-electron-like surface state with parabolic band dispersion as shown in figure 3.2 and as described in equation 3.1.

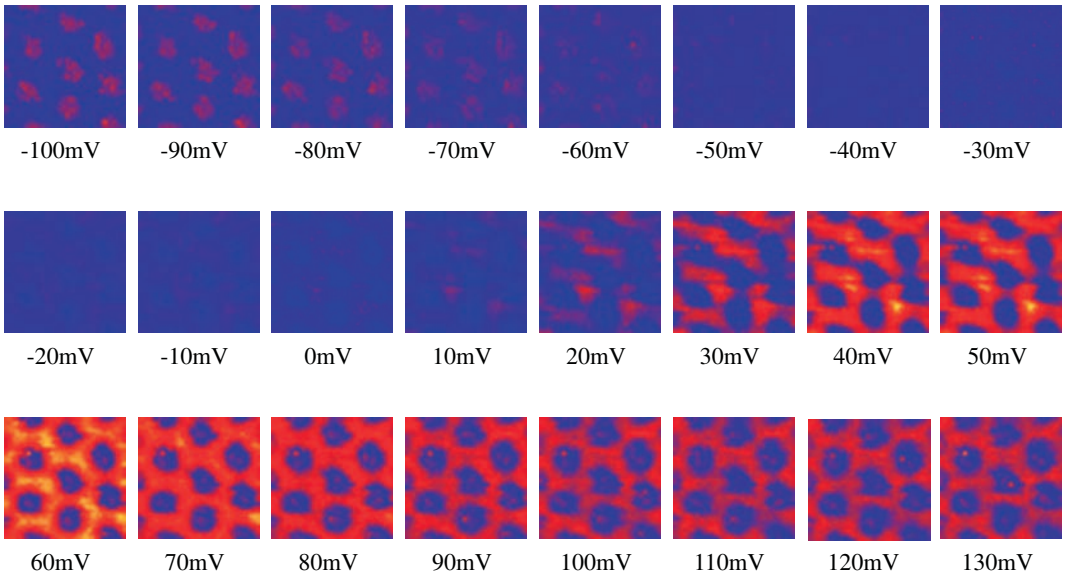

Figure 3.15: Combined images of 1024 (32×32) spectra measured in a Ce adatom superlattice with an adatom-adatom distance of $d = 3.5$ nm at a base temperature of $T = 3.3$ K. Each image corresponds to the map of the dI/dV signal of the 1024 spectra at the marked tunneling voltage V_T coded in color (blue-red-yellow: low-medium-high signal strength).

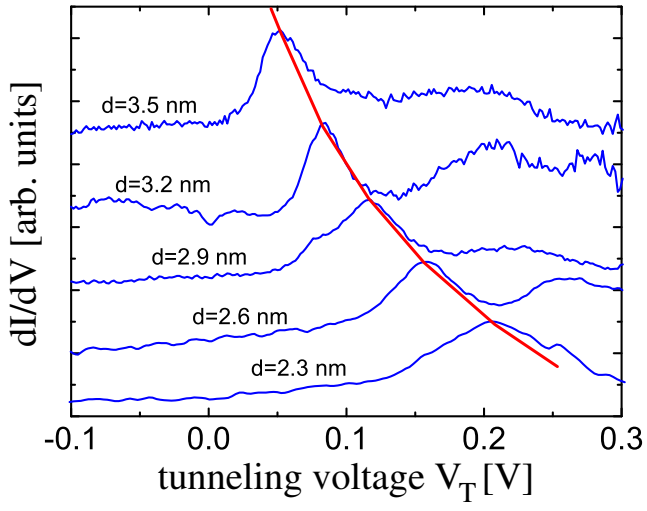

Figure 3.16: Set of spectra taken in the center of a triangle formed by 3 Ce adatoms in a hexagonal superlattice. The adatom-adatom distance d decrease from the top to the bottom spectrum due to higher Ce coverage and thereby higher superlattice compression. The red line mark the shift of the first peak in the spectra from approx. 50 meV ($d = 3.5$ nm) to approx. 200 meV ($d = 2.3$ nm). The spectra are shifted vertically in respect to each other.

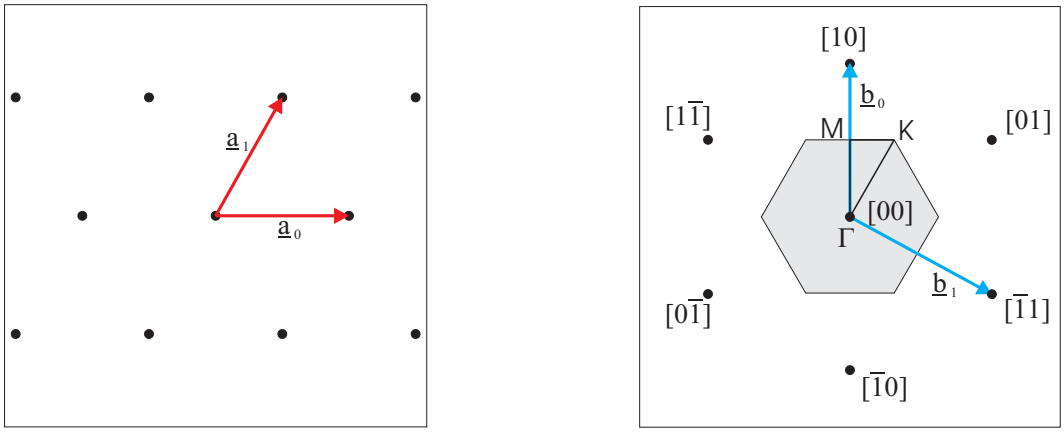

Figure 3.17: The periodic 2D superlattice is described within the vectors $\vec{a}_0$ and $\vec{a}_1$ as basis (left image). Due to the symmetry the eigenfunction of the surface state electrons can be written in the Fourier transformed reciprocal space (right image). The gray area marks the first 2D Brillouin zone where the points Γ, M, and K are found, which fulfill the Bragg condition.

Under the assumptions of a defect free superlattice, the eigenvectors $\psi_{\vec{k}}(\vec{r})$ of the surface state electrons are invariant to the translations

$$\psi_{\vec{k}}(\vec{r}) = e^{i\varphi}\,\psi_{\vec{k}}(\vec{r} + m\,\vec{a}_0 + n\,\vec{a}_1) \quad m, n \in \mathcal{Z} \tag{3.10}$$

except for the phase factor $e^{i\varphi}$, with the basis vectors of the lattice (see figure 3.17) given as:

$$\vec{a}_0 = d\begin{pmatrix}1\\0\end{pmatrix}, \quad \vec{a}_1 = d\begin{pmatrix}1/2\\\sqrt{3}/2\end{pmatrix}. \tag{3.11}$$

Due to *Bloch's* theorem [86], the eigenvectors of the surface state electrons can be described with 2D Bloch waves [72, 64]:

$$\psi_{\vec{k}}(\vec{r}) = \sum_{m,n} c_{\vec{k}-\vec{g}_{mn}} \exp\left[i(\vec{k} - \vec{g}_{mn}) \cdot \vec{r}\right]. \tag{3.12}$$

The eigenvector $\psi_{\vec{k}}(\vec{r})$ depends on the 2D in-plane vector $\vec{r}$ and on the momentum vector $\vec{k}$ parallel to the surface. The $\vec{g}_{mn}$ represent the Bloch-vectors of the hexagonal pattern weighted with prefactors ($c_{\vec{k}-\vec{g}_{mn}}$) in the sum of plane waves in equation 3.12. The Bloch vectors are written as

$$\vec{g}_{mn} = \left(m\,\vec{b}_0 + n\,\vec{b}_1\right) \quad m, n \in \mathcal{Z}, \tag{3.13}$$

with the reciprocal basis vectors given by

$$\vec{b}_0 = \frac{2\pi}{d}\begin{pmatrix}0\\2/\sqrt{3}\end{pmatrix} \quad \text{and} \quad \vec{b}_1 = \frac{2\pi}{d}\begin{pmatrix}1\\-1/\sqrt{3}\end{pmatrix} \tag{3.14}$$

to fullfill the condition $\vec{a}_i \cdot \vec{b}_i = 0$ and $\vec{a}_i \cdot \vec{b}_j = 2\pi \wedge i \neq j$. Figure 3.17 displays the two basis vectors (blue) and the construction of the first 2D Brillouin zone (gray area) with the characteristic points at Γ, M, and K.

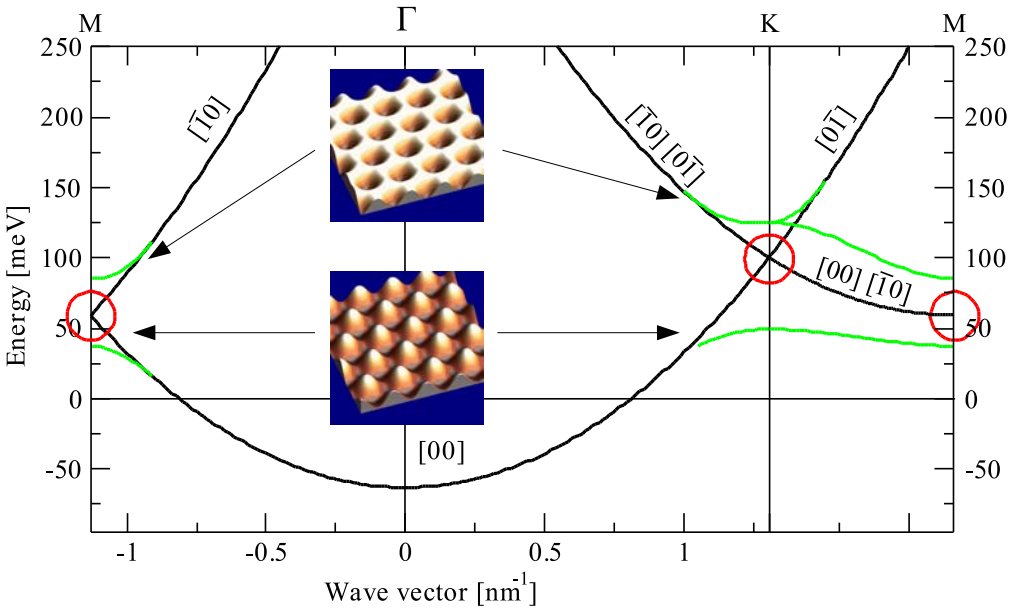

Figure 3.18: Bandstructure of the 2D electron gas in the empty lattice (black) and in the nearly free electron approximation (green). Circles mark degeneracies at high symmetry points where different bands, labeled with their corresponding band indices, have the same energy at identical wave numbers in the reduced band scheme. In the NFE model these degeneracies are removed, and close to the high symmetry points the bands are localized in real space (inset figures).

Figure 3.18 shows the folded band structure of the Ag(111) surface states along directions of high symmetry (black lines in figure 3.17 (right)). Different bands are labeled with their indices enclosed in brackets $[mn]$ having the following energy momentum relation:

$$E(\vec{k}) = \frac{\hbar^2}{2m^*}\left(\vec{k} + \vec{g}_{mn}\right)^2 - E_0, \tag{3.15}$$

where an effective electron mass of $m^* = 0.42m_0$ [73], and a surface state onset energy of $E_0 = -63$ meV [26] was used. For a superlattice spacing of $d = 3.2$ nm, the M point is localized at $\left|\vec{k}_M\right| = 2\pi/\sqrt{3}d = 1.13\ \mathrm{nm}^{-1}$ and the K point at $\left|\vec{k}_K\right| = 4\pi/3d = 1.31\ \mathrm{nm}^{-1}$. For the unperturbed electron gas this corresponds to a lowest energy of $E_M = 58$ meV and $E_K = 98$ meV. At these high symmetry points of the Brillouin zone the *Bragg* condition is fulfilled and the dispersion relation is degenerate. At the M point the $[00]$ and $[\bar{1}0]$ bands intermix, while at the K point three bands $[00]$, $[0\bar{1}]$, and $[\bar{1}0]$ cross.

The degeneracies at the K and M points are removed by including a finite periodic potential created by the Ce adatoms that affect the surface state electrons. This potential $V(\vec{r})$ can be developed in the basis of the reciprocal lattice vectors

$$V(\vec{r}) = \sum v_{mn} \exp\left[i\vec{g}_{mn} \cdot \vec{r}\right] \tag{3.16}$$

with v_{mn} as the Fourier coefficients. Since the potential $V(\vec{r})$ has to be real, and the sixfold symmetry of the superlattice implies a sixfold symmetry of the potentials[5], the first coefficients have to be equal:

$$v_{10} = v_{01} = v_{1\overline{1}} = v_{\overline{1}0} = v_{0\overline{1}} = v_{\overline{1}1} \equiv v \tag{3.17}$$

According to the perturbation theory for degenerate states [88], the eigenfunctions can be written as a weighted sum of the corresponding intermixing wave functions at the high symmetry points:

$$\psi_{\vec{k}}(\vec{r}) = \sum_i \alpha_i \psi_{\vec{k_i}}(\vec{r}) \tag{3.18}$$

It is known that the periodic potential removes the degeneracy leading to the opening of a gap in such a way that at the M point, where the $[00]$ and $[\overline{1}0]$ wave functions mix, the energy shift of the bands is[6]:

$$\Delta E_1(M) = \quad -v \qquad |\psi_1\rangle_M = \frac{1}{\sqrt{2}}\left(|\psi_{00}\rangle + |\psi_{\overline{1}0}\rangle\right) \tag{3.19}$$

$$\Delta E_2(M) = \quad +v \qquad |\psi_2\rangle_M = \frac{1}{\sqrt{2}}\left(|\psi_{00}\rangle - |\psi_{\overline{1}0}\rangle\right) \tag{3.20}$$

with $|\psi_1\rangle$ and $|\psi_2\rangle$ as the corresponding eigenvectors of the bonding and antibonding state. At the K point where three wave functions interact with the periodic potential, one has to solve the following matrix system [64]:

$$\begin{pmatrix} E(\vec{k}) & v_{\overline{1}0} & v_{0\overline{1}} \\ v_{10} & E(\vec{k}) & v_{1\overline{1}} \\ v_{01} & v_{\overline{1}1} & E(\vec{k}) \end{pmatrix} \begin{pmatrix} \alpha_1 \\ \alpha_2 \\ \alpha_3 \end{pmatrix} = 0, \tag{3.21}$$

which results, under the assumption of equation 3.17 and after a short calculation in the following energy shifts and eigenvectors:

$$\Delta E_1(K) = \quad +v \qquad |\psi_1\rangle_K = \frac{1}{\sqrt{2}}(|\psi_{\overline{1}0}\rangle - |\psi_{0\overline{1}}\rangle) \tag{3.22}$$

$$\Delta E_2(K) = \quad +v \qquad |\psi_2\rangle_K = \frac{1}{\sqrt{6}}(-2|\psi_{00}\rangle + |\psi_{\overline{1}0}\rangle + |\psi_{0\overline{1}}\rangle) \tag{3.23}$$

$$\Delta E_3(K) = \quad -2v \qquad |\psi_3\rangle_K = \frac{1}{\sqrt{3}}(|\psi_{00}\rangle + |\psi_{\overline{1}0}\rangle + |\psi_{0\overline{1}}\rangle). \tag{3.24}$$

The green curves in figure 3.18 show the results of the NFE model assuming a weak potential with fixed first Fourier components $v \approx 30$ meV. The degeneracy at the M point is removed and a symmetric gap of $2v$ width is opened, while at the K point the degeneracy is not completely removed. The $[00]$ band is shifted toward lower energies by $\Delta E = -2v$,

[5] The symmetry of the potential of the superlattice is **not** obviously sixfold. If the magnetic moment of the Ce-adatoms is taken into account, the system has an additional degree of freedom, and a 180° or a coplanar 120° symmetry (a so called *Néel*-structure) are possible solutions [87]. Nevertheless, in the following we will neglect these possibilities.

[6] To minimize confusion, all potentials are assumed to be positive, unless noted.

while the two remaining bands are shifted together toward higher energy by $\Delta E = v$ resulting in a gap width of $3v$.[7]

The Brillouin-zone of the superlattice is very small compared to the bulk. With a maximum of the absolute value of the momentum vector $|\vec{k}|$ of only 1.31 nm^{-1}, the wavelength of the eigenfunctions is relatively large ($\lambda = 2\pi/|\vec{k}|$) and thus the local distribution is accessible with STM. The probability of finding an electron with a momentum $\vec{k}$ at the real space coordinate $\vec{r}$ is the absolute square $|\psi_{\vec{k}}(\vec{r})|^2$ of the eigenfunction.

Using the results 3.20, 3.19, and 3.22–3.24 together with the definition of the Bloch-waves: $|\psi_{mn}\rangle = \exp\left[i(\vec{k}+\vec{g}_{mn})\cdot\vec{r}\right]$ (see equation 3.12) and the representation of the cosine function, $\cos(x) = \frac{1}{2}\left(e^{ix}+e^{-ix}\right)$, the transformation in real space is simply calculated to

$$\begin{aligned} |\psi_{up}|^2 &\propto 1+\cos(\vec{g}_{10}\cdot\vec{r}) \\ |\psi_{down}|^2 &\propto 1-\cos(\vec{g}_{10}\cdot\vec{r}) \end{aligned} \tag{3.25}$$

with $|\psi_{up}|^2$ as the probability density for the up-shifted (anti-bonding) bands (3.20, 3.22, 3.23) and $|\psi_{down}|^2$ as the probability density for the down-shifted (bonding) bands (3.19, 3.24).

Because of the sixfold symmetry of the system, we have to take into account the first three reciprocal basis vectors b_0, b_1, and $b_2 = b_0 - b_1$ to expand equation 3.25 to the entire 2D space:

$$\begin{aligned} |\psi_{up}(\vec{r})|^2 &\propto 3+\sum_{n=0}^{2}\cos(\vec{b}_n\cdot\vec{r}) \\ |\psi_{down}(\vec{r})|^2 &\propto 3-\sum_{n=0}^{2}\cos(\vec{b}_n\cdot\vec{r}). \end{aligned} \tag{3.26}$$

The insets in figure 3.18 show the result. States in the lower bands are concentrated close to the Ce adatoms to take advantage of the attractive potential here, while states in the upper band are concentrated at positions between the Ce adatoms. Additionally, the bands are flattened around the high symmetry points leading to an increase in the DOS (see equation 3.2 on page 23). Thus, the NFE model is able to explain accurately the observed peak at about 85 meV (Fig. 3.13 (c)) which agrees roughly with the energetic position of the flat bands. Additionally, the location of the peak between the adatom arrangement, as seen in figures 3.13 (b) and 3.15), is well understood by the spacial distribution of $|\psi_{up}(\vec{r})|$.

Nevertheless, the presented NFE model has several disadvantages as summarized in the following points:

1. The result of the model suggests a high density of states on top of the Ce adatoms at an energy of about 45 meV created by the ψ_{down} solution which is not observed.

[7] The still remaining degeneration would be removed by assuming a potential with lower symmetry (i. e. including the spin-freedom (see footnote 5). For a potential with threefold (120°) symmetry, equation 3.17 can be replaced with $v_{10} = iv$, $v_{01} = -iv$ and $v_{1\bar{1}} = iv$. Then, the bandshift energies are $\Delta E_{1,2} = \pm\sqrt{3}v$ and $\Delta E_3 = 0$, so that all bandcrossings are removed [64].

2. While we have used only the first Fourier coefficients of the potential $V(\vec{r})$ induced by the superlattice, the coverage of the potential is rather long-range ($\approx d/2$) in contradiction to supposed interactions of the Ce adatoms with only the nearest silver atoms of the supporting surface.

3. The first order interaction energy $v \approx 30$ meV is not related to any physical property of the adsorption process between Ce and the Ag(111) surface. It is rather a free guess.

4. The NFE model crucially depends on the exact periodicity of the superlattice. Imperfections cannot easily be included.

3.3.2 Tight-binding simulation

To overcome the limitations of the NFE model and to get a deeper understanding of the physics in the superlattice creation, stabilization, and in particular the changes of the LDOS of the surface state, we performed tight-binding (TB) simulations in cooperation with *Cédric Weber*[8], *Frédéric Mila*[9], and *Thierry Giamarchi*[10].

Compared to *ab initio* calculations, which are highly accurate but unfortunately at the same time highly computationally demanding and thereby even with today's available computer power still limited to systems well below 100 atoms [89], TB calculations are two or three orders of magnitude faster [90] and therefore applicable even for large systems. The TB simulations promise to be more accurate than heuristic methods (e. g. the NFE model), because the quantum mechanical nature of bonding between atoms is preserved in the calculation.

The TB method can be characterized by the following: The model approximates the exact eigenstates of the many-body Hamiltonian with a set of effectively one-particle Hamiltonians in an atomic orbital-like basis set and it replaces the exact Hamiltonian operator with parameterized Hamilton matrix elements [90]. In general, only a small number of tabulated [91] basis functions $|\psi\rangle$ are used, corresponding to the atomic orbitals in the energy range of interest. For the Ag(111) surface state which originates from the outer $5s^1$ electron of silver with its electronic structure of [Kr]$4d^1 5s^1$ only this orbital will be taken into account. The eigenstates $|\psi_\alpha\rangle$ of the system are then obtained by solving the stationary *Schrödinger* equation,

$$\hat{H}\,|\psi_\alpha\rangle = E_\alpha\,|\psi_\alpha\rangle\,. \tag{3.27}$$

For our system of metallic Ag the eigenstates can be written in a very localized base [92]:

$$\langle\psi(\vec{r})|\psi_i(\vec{r}_i)\rangle \propto e^{-|\vec{r}-\vec{r}_i|}, \tag{3.28}$$

with $\vec{r}_i$ as the position and $|\psi_i\rangle$ as the $5s^1$ electron eigenstate of the i^{th} Ag atom. The experimental findings can then be rationalized with the following TB Hamiltonian:

$$\hat{H} = -|t| \sum_{<i,j>} |\psi_i\rangle\,\langle\psi_j| + \sum_i V_i\,|\psi_i\rangle\,\langle\psi_i| + \epsilon_0, \tag{3.29}$$

[8] Institut de Recherche Romand sur les Matériaux (IRRMA), EPFL
[9] Institute of Theoretical Physics, EPFL
[10] DPMC, University of Geneva

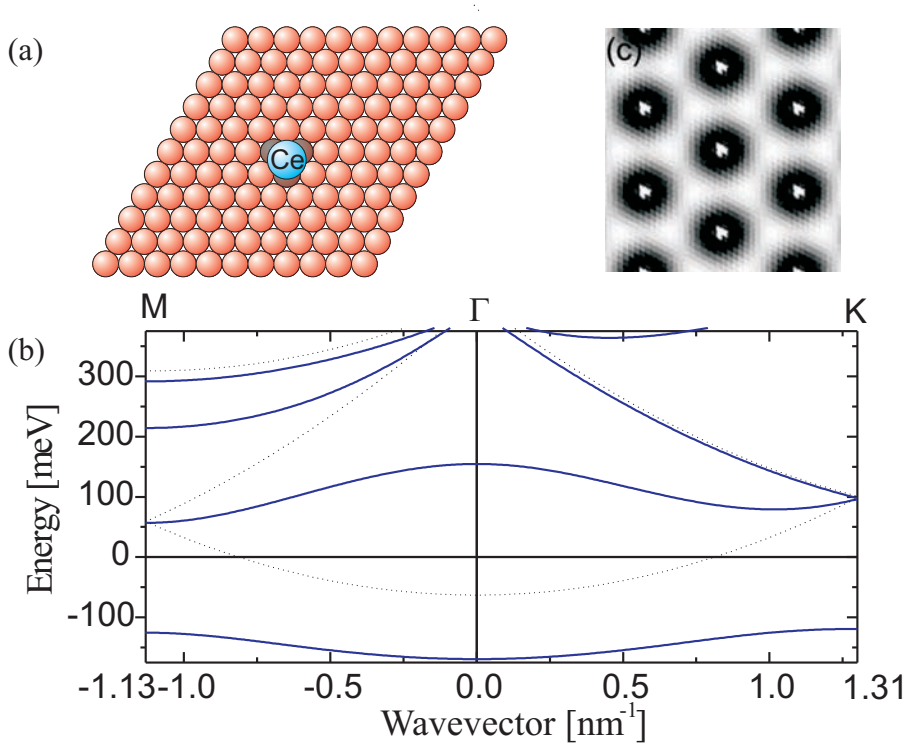

Figure 3.19: (a): $l \times l$ unit cell used for the TB calculation. The Ce adatom interacts only with the three nearest Ag neighbors (dark spheres) (b): Band structure of the 2D system for $d = 3.2$ nm. Dotted lines: folded dispersion of the unperturbed free electron in the empty lattice approximation; solid lines: TB calculation. (c): TB calculation of the spatial LDOS at an energy of 85 meV.

where the summations $< i, j >$ run over neighboring Ag sites. In the simulations, isotropic hopping integrals t are used due to the spherical symmetry of the $5s^1$ orbital. The effect of the Ce adatom on the electronic states of Ag is described by the on-site potential V_i. As long as this potential decreases fast enough with the distance from the Ce atom, the results depend very little on the actual form of the potential [92]. For simplicity, we assume that the Ce adatom stays in the middle of three neighboring Ag sites (hollow site) and that the effect of the potential induced by the Ce adatom is very local: $V_i = U$ for the three Ag atoms closest to the Ce adatom in each unit cell, and $V_i = 0$ elsewhere (see figure 3.19 (a)).

The parameters $|t|$ and ϵ_0 have been set to $|t| = 750$ meV and $\epsilon_0 = 4.437$ eV to reproduce the onset energy $E_0 = -63$ meV [26] and the effective mass $m^* = 0.42 m_0$ [73] of the unperturbed free-electron like surface state of the clean Ag(111) surface (see discussion in section 3.1.1).

A calculation of the phase shift using a TB model for a single impurity on the Ag(111) surface to reproduce the measured Friedel-like oscillations of the electron density around the adsorbate at E_F (see section 3.1.2) shows that the calculated phase shift is consistent with the experimentally observed $\theta_0 = 0.37\pi$ for an on-site potential $|U| = 1.3 \pm 0.2$ eV

in equation 3.29. The first maximum of the LDOS at E_F emerges then at a distance of $d = 3.1 \pm 0.2$ nm [92] in excellent agreement to the measured $d \approx 3.2$ nm (section 3.1.2). For the calculation, a 40×40 cluster of Ag atoms with one Ce adatom in the center and with periodic boundary conditions was used. Additionally, it was assured that finite-size effects in the calculation are negligible.

As a reference, we then calculate the band structure and LDOS assuming a periodic arrangement of the Ce adatoms. We look for the eigenstates as Bloch states of the form

$$\left|\psi_{\vec{k}}\right\rangle = \sum_{\vec{r}_i, \vec{R}_m} a(\vec{r}_i) e^{\vec{k}\cdot\vec{R}_m} \left|\vec{R}_m, \vec{r}_i\right\rangle, \tag{3.30}$$

where $\vec{R}_m$ is the position of the unit cell containing the i^{th} Ag atom, and $\vec{r}_i$ the position of the Ag atom inside the cell, which leads to a $l^2 \times l^2$ matrix (l: number of Ag atoms between two Ce adadtoms) to diagonalize for each wave vector $\vec{k}$. The resulting band structure for a system with an adatom-adatom distance of $d = 3.2$ nm, corresponding to $l = 11$, is plotted in figure 3.19 (b) with the same reciprocal basis vectors as given in equation 3.14 on page 37.

Compared to the bandstructure of the calculation done in section 3.3.1 using the NFE model (see figure 3.18) the result is quite different. At the high symmetry points K and M only the lower band is shifted towards lower energies, while the upper bands still lie on the energy of the empty lattice approximation. This asymmetric opening of an energy gap at the reduced-zone boundaries leads to peaks in the DOS due to band flattening according to equation 3.2. These peaks are also reflected in LDOS, but with different amplitudes depending on the site in the unit cell, similar to the results obtained with the NFE model. States in the lower (filled) band are concentrated close to the Ce adatoms, to take advantage of the attractive potential there, while states in the upper (empty) band are concentrated at positions between the Ce adatoms (figure 3.19 (c)). In figure 3.20 the LDOS at the center of a Ce triangle is compared to experiments. The lowest band is between -170 and -120 meV, but its contribution to the LDOS calculated at that point is very small. Apart from the tunneling region below -100 mV, the agreement is remarkably good, especially considering the fact that this is not a fit but a prediction without adjusting the microscopic parameters of the model.

Using the same parameters in the TB Hamiltonian (equation 3.29), but adjusting the size $l \times l$ of the supercell by taking for l the closest integer to d/a with $a = 289$ pm (the distance between two Ag atoms), the shift of the energy of the first peak for different superlattices is also very well reproduced by our TB calculation (see figure 3.21 (a)). This shift varies linearly with the inverse area Ω^{-1} of the triangle formed by three adsorbates with an adatom-adatom distance d, so that the first peak is localized at an Energy

$$E = E_0 + (620 \pm 10)\text{meV nm}^2 \times \frac{1}{\Omega}. \tag{3.31}$$

This behavior can be easily understood within a model of confinement in a 2D box [93]. A triangle with perfectly reflecting walls would lead to a slope of $\frac{6\sqrt{3}\pi^2\hbar^2}{m^*} = 726\,\text{meV} \times \text{nm}^2$ [11], while it is reduced in the Ce superlattices due to the the phase shift during the scattering process of the electron waves at the adatoms.

[11] The value can easily be obtained by assuming nodes in the wavefunction on the border of the triangle as boundary condition.

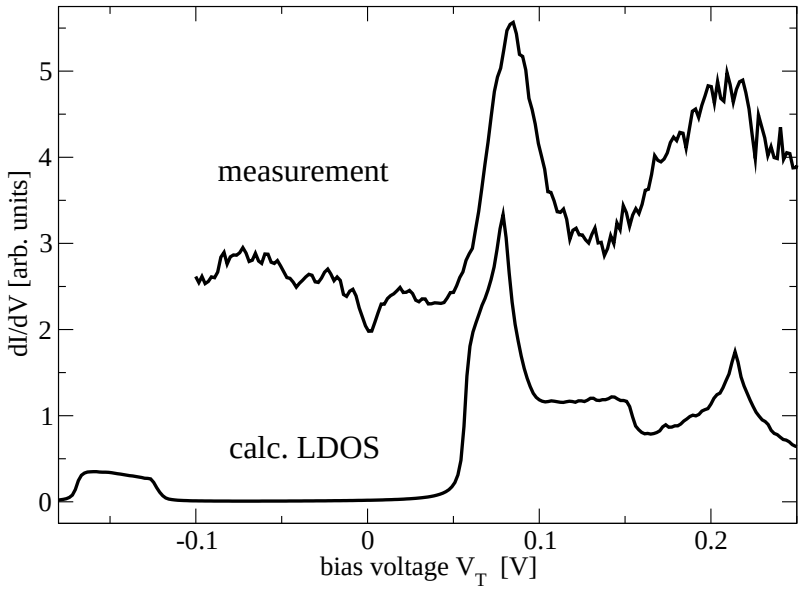

Figure 3.20: TB calculation of the LDOS and dI/dV measurement in the center of the triangle formed by Ce adatoms with an adatom spacing of $d = 3.2$ nm. The set point for the measurement before opening the feedback loop was $V_T = -109$ mV and $I_T = 5$ pA with a modulation voltage of $V_m = 2.5$ mV. The calculation, in contrast to the measurement, does not include the contribution of bulk states to the LDOS.

Additionally, the TB calculation allows us to understand why the superlattice has a "natural" periodicity of $d = 3.2$ nm. Indeed, the gap opening in the free Ag(111) band structure which is induced by the Ce potential increases the number of states below E_F and decreases their energy. Thus, we calculate the energy of the lowest band,

$$E_{\text{band}} = \int_{-\infty}^{E_F} E \times n(E) dE \tag{3.32}$$

for the clean and for the Ce covered surface. The difference between both gives directly the contribution of the Ag surface state to the gain in energy per Ce adatom for each unit cell size $l \times l$ (see figure 3.21 (b)). We find that the most favorable configuration corresponds to a Ce-Ce distance of 3.2 nm, precisely the distance realized experimentally in most cases. The energy gain remains significant for Ce-Ce distances in the range $d = 2.3 - 3.5$ nm, the distances found as a function of Ce adatom concentration. This effect is analogous to charge-density wave (CDW) formation in correlated systems [94], but the potential that stabilizes the CDW here is external (the Ce atoms) while it is self-consistently induced by correlations in a standard CDW. The optimal Ce-Ce distance agrees with that predicted by *Hyldgaard* and *Persson* [81, 85] as it was shown in section 3.2. Note, however, that the dramatic effects of the superlattice on the surface state (gap openings, LDOS singularities) cannot be accounted for by the model of *Hyldgaard* and co-workers.

Finally, we have studied the effect of local disorder with respect to perfect periodic arrangement of Ce adatoms on the LDOS. To compare with the spectra obtained on different

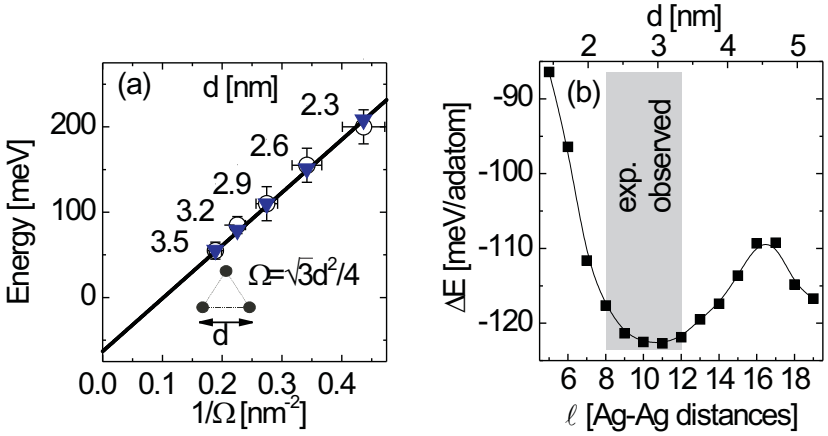

Figure 3.21: (a): Energy of the maximum of the first peak in a spectrum measured in the center of three Ce adatoms as a function of the inverse area Ω^{-1} of the triangle formed by the Ce atoms (circles: measurements; triangles: TB calculation). The increased error-bars in the experimental data for smaller adatom-adatom distances d are due to the fact that compressed lattices ($d < 3.2$ nm) spread the observed values (see also fig. 3.16). (b): Energy difference ΔE between adsorbate-covered and clean surface per Ce adatom, calculated for each unit-cell size. The solid line serves as a guide for the eye. The gray area marks the range of the adatom-adatom distances where complete superlattice formation was found.

positions in a slightly disordered superlattice, as shown in figure 3.22 (a), we reproduced the local environment around points A and B inside a 44×44 cluster of Ag atoms (figure 3.22 (b)), which was then repeated periodically to minimize finite-size effects.

To determine the degree of disorder in the local environment, the self-correlation is calculated as following

$$h(x,y) = \sum_{x'} \sum_{y'} I(x',y') \times I(x'+x, y'+y), \tag{3.33}$$

where $I(x,y)$ denotes the normalized z-height of the STM image at the position (x,y). For the results displayed in figure 3.22 (d) we used for the summations a small area ($x' \in [x_0 - 7.5\text{ nm}, x_0 + 7.5\text{ nm}]$, $y' \in [y_0 - 7.5\text{ nm}, y_0 + 7.5\text{ nm}]$) around the points $(x_0^{A(B)}, y_0^{A(B)})$ where the dI/dV spectra were taken. Any periodicity in the image will be shown as a periodic pattern, so that a perfect superlattice with no disorder $h(x,y)$ would repeat the hexagonal order. As seen in figure 3.22 (d) the ordering around point A is quite good up to three lattice distances, while around B a displacement of just two lattice distances smears out the result of the self-correlation function, indicating a much higher degree of disorder compared to the neighborhood of A.

The influence of the disorder on the dI/dV spectra is seen in figure 3.22 (c). The agreement between data and TB calculation is again very good: The broadening and the shift of the main peaks are correctly reproduced except for a small shift in energy which might be due to a small systematic error in the determination of the exact adatom positions,

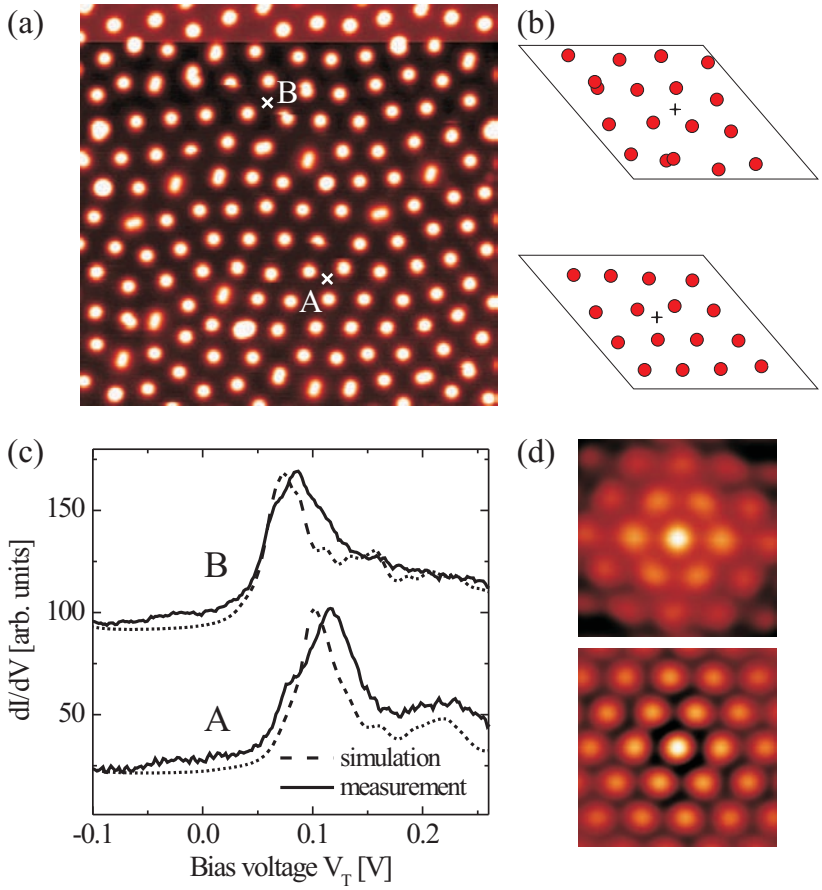

Figure 3.22: (a): STM image of a slightly disordered system (35 nm^2), $V_T = -100$ mV, $I_T = 10$ pA. (b): The local arrangement of Ce adatoms in a mesh of 44×44 Ag-atoms around the points A and B as used for the TB calculation. (c): Spectra obtained at the marked points A and B which differ by their nearest neighbor distances. The changes in peak position, intensity, and shape indicate the sensitivity of the electronic structure to local disorder. Dashed lines: TB calculation. For clarity the curves have been superimposed and curves B have been shifted vertically. (d): Self-correlation images of the area around A and B show that the region around A has a higher degree of order than the region around B.

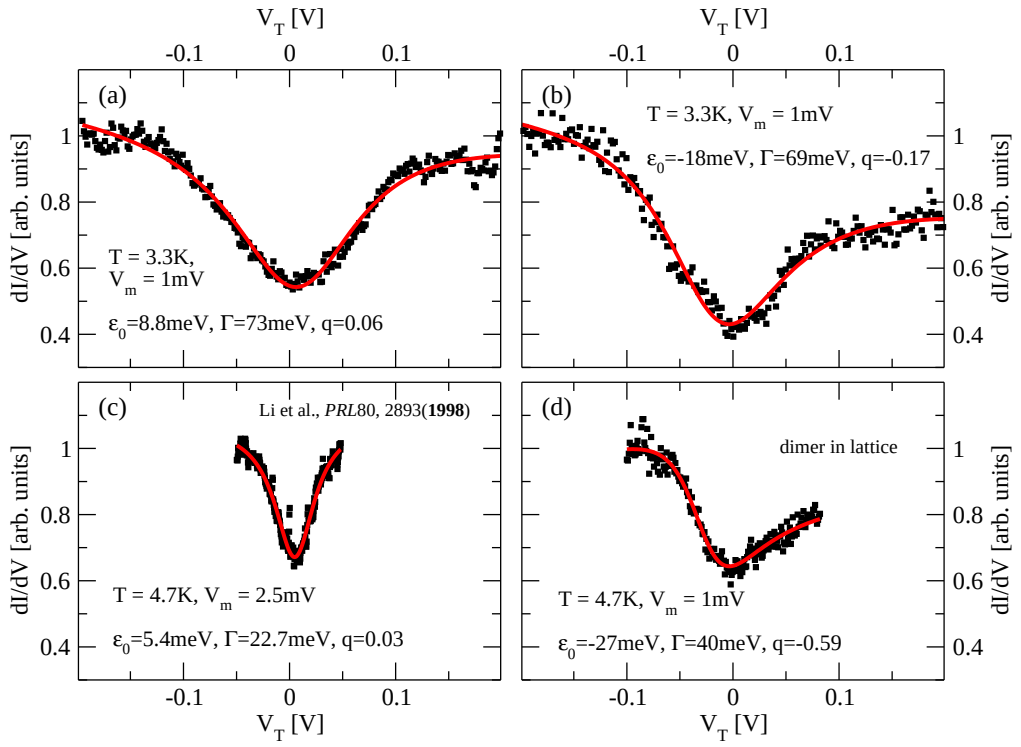

Figure 3.23: Spectra measured on Ce adatoms adsorbed on Ag(111). (a), (b): Two representative spectra obtained on top of Ce adatoms arranged in a hexagonal superlattice with an adatom-adatom spacing of $d = 3.2$ nm. A mostly symmetrical dip with respect to E_F occurs with a half-width of $\Gamma \approx 70$ meV. (c) Data taken from reference [95] (see text). (d): Spectrum taken on top of a dimer in the superlattice with much smaller half-width of $\Gamma = 40$ meV. The inset in each graph denotes the base temperature T, the modulation amplitude V_m, and the parameters of the best-fit using the *Fano* equation $\frac{dI}{dV} \propto \frac{(q+\epsilon')^2}{1+\epsilon'^2} + c$ [96], with $\epsilon' := \frac{eV_T - \epsilon_0}{\Gamma}$ (full line) (see also chapter 4.1.1 on page 51).

as well as the position of the second peak at point A and its absence at point B. Remarkably, the shifts of the main peaks agree with equation 3.32 and figure 3.21 (a) if d denotes the average distance between the 3 Ce adatoms in the triangular lattice that enclose the point A and B, respectively. Additionally, the absence of the second peak in B can be assigned to the higher degree of disorder. As seen in the TB band structure calculation (Figure 3.19 (c)), the second peak at about 200 meV is due to the flat band whose origin is in the second Brillouin zone. While the second closest adatom neighbors in B already show a sufficient amount of disorder, this band is already smeared out and therefore the formation of this peak is suppressed.

Directly over Ce adatoms the TB model predicts the onset of the lowest band near -170 meV and a band edge near -120 meV (figure 3.19 (c)), while the dI/dV spectra taken on top of the Ce adatoms and displayed in figure 3.23 (a) and (b) show a relatively wide depression in the LDOS of about 40% amplitude symmetrically around E_F, but not the expected contribution of the first band. On measurements taken in the slightly expanded

lattice with $d = 3.5$ nm a faint signal can be detected at $eV_T \approx -100$ mV which might be due to this band (see figure 3.14 and 3.15). The weakness or absence of contributions of this band can be understood by recalling that the tip is approximately 200 pm (i. e. the apparent height of one Ce adatom) further distant from the Ag(111) surface when placed above an adatom. Thus, the contribution of the disturbed surface state to the tunneling current is reduced (see chapter 2.3.4).

3.4 Summary and Outlook

In this summary I would like to point out again that the chosen system of Ce adatoms on Ag(111) is a highly interesting testbed to check theoretical predictions with real experiments, as shown in the previous sections. However, open questions still remain and additional experiments might reveal further insight into fascinating physics.

Due to the surface-state-mediated interactions between the Ce adatoms, a relatively wide 2D superlattice is created, leaving us the exciting opportunity to measure the distribution of electronic states directly inside the lattice. We have seen that the density of states varies depending on the site in the superlattice, and that at E_F the LDOS vanishes and instead a gap occurs that is essential for lattice stability. These results are surprising given the discussion at the beginning of the experimental observations where a scattering model was introduced (section 3.2) that assumes electrons at the Fermi edge are an important factor for the interatomic interaction. But as mentioned, when the superlattice is finally created, there are no surface-state electrons at the Fermi energy that could perform this interaction.

Additionally, the spectra obtained on top of the Ce adatoms lead to questions. As seen in figure 3.23, the spectra (a) and (b) which were measured in the superlattice are relatively broad, especially when compared to the spectrum (c) which was published in [95] and assigned to a *Kondo* resonance due to spin-flip processes during the scattering of electrons on the Ce adatom (see chapter 4.1.1). The result in [95] is surprising because the experiments were performed at a base temperature of $T = 5$ K where the motion of single Ce atoms inhibits spectroscopic measurements. Thus, these measurements might have been performed on dimers or small clusters which are stable at 5 K and show a smaller width in the spectrum (figure 3.23 (d)).

Although the electronic structure of the Cerium was not taken into account in this chapter, the interaction between the highly localized $4f$-state of Ce [97] and bulk or surface states electrons may not be negligible and could indeed lead to spectral features similar to the one presented in [95]. This will be discussed in detail in chapter 4.

As already mentioned (see footnote 5 on page 39) the magnetic moment of the $4f$-electron leads to an additional degree of freedom which is expected to lead to adatom-adatom interactions between the magnetic moments, the so called *Ruderman-Kittel-Kasuya-Yosida* (RKKY) exchange interaction [98, 99, 100] which has in 2D a periodicity of $\lambda_F/2$ [101, 102, 103] and a $1/r^2$ behavior, similar as the discussed adatom-adatom interaction induced by electron scattering.

This kind of ordered 2D superlattice with interacting magnetic moments could lead to interesting features including antiferromagnetic order and superconductivity [104] or to a so called *Kondo* lattice [105].

The Ce/Ag(111) system might not be the best choice for this kind of investigation be-

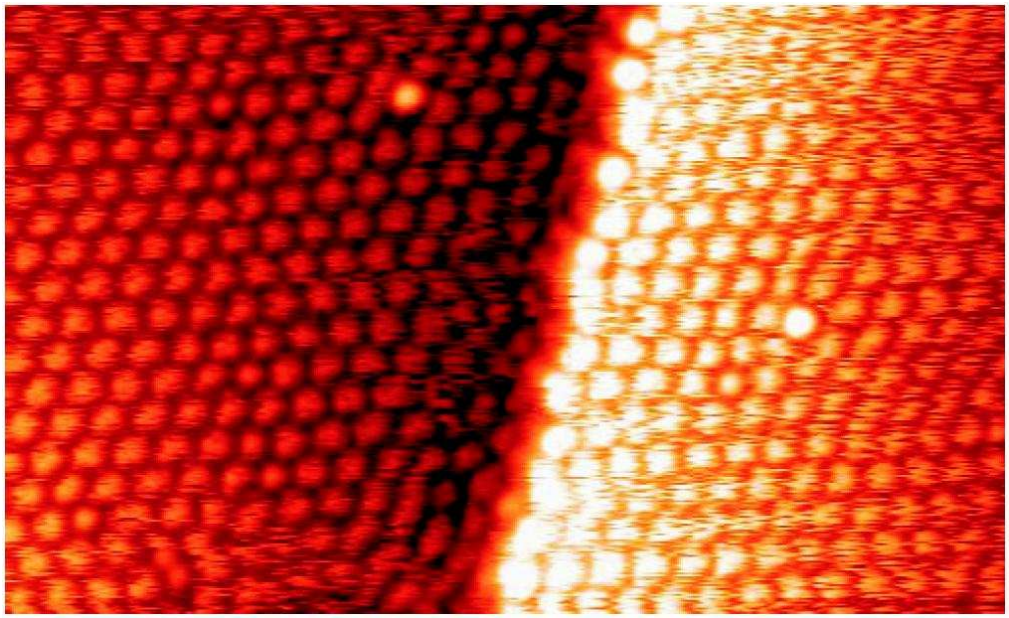

Figure 3.24: STM image of hexagonal ordered Ce adatoms on Cu(111) obtained at a base temperature of 3.3 K ($V_T = 1$ V, $I_T = 3$ pA, 36×22 nm^2). The average adatom-adatom distance is $d \approx 1.5$ nm. This is shorter then for Ag(111) due to the shorter Fermi-wavelength, $\lambda_F = 2\pi/k_F = 3.0$ nm [75], of the surface state. The two bright objects on the left and right side of the atomic step which runs vertically through the image are unknown adatoms or small Ce cluster. The fuzzy appearance of the adatoms is due to hoppings between adjacent lattice sites of the underlying Cu(111) surface even at low temperature.

cause of the relatively large adatom-adatom distance and the smaller magnetic interaction energy. Thus, we have additionally examined the superlattice formation of Ce adatoms on Cu(111) with its smaller wavelength of the surface-state at the Fermi energy of $\lambda_F = 3.0$ nm [75]. As one would expect from the above-developed models, the adatom spacing in the superlattice is clearly smaller as seen in figure 3.24. We found an average adatom-adatom distance of $d \approx 1.5$ nm, compatible with a scattering phase shift of $\theta_0 \approx 0.2\pi$. As the STM image reveals, the degree of order is high compared to the Ce superlattice on Ag(111), which can be understood by the linearity between the pair interaction energy E_{pair} and the surface-state onset energy E_0 (see equation 3.5), which for Cu(111) lies at $E_0 \approx -0.40$ eV [75].

Unfortunately, the mobility of Ce adatoms on Cu(111) is even higher than on Ag(111), so that it was impossible to perform spectroscopic measurements in the superlattice even at the lowest attainable base temperature of the STM of $T = 3.3$ K, but it could be an attractive system for STM measurements at temperatures $T \lesssim 1$ K, where the hopping rate should be sufficiently reduced.

Additionally, other systems, for example Fe/Cu(111) [106] or Mn/Cu(111) [107] may be good candidates for the detection of spin-polarized surface-state-mediated interactions between the magnetic moments of the adatoms.

Chapter 4

Spectroscopy on single Ce atoms

4.1 Introduction

With the unique potential to obtain spectroscopic results on the atomic scale, the STM opens an avenue to detailed informations about processes and interactions between single atoms or molecules and the supporting surface.

While the last chapter has discussed the interaction between an ensemble of sufficiently mobile adatoms which was moderated by the free-electron like surface state and eventally led to the formation of ordered hexagonal structures and thus allowed to measure the influence of a superlattice on the surface state, this chapter will discuss spectroscopic measurements performend directly on Ce adatoms.

Effects like vibrational excitations and the *Kondo* scattering generate clearly detectable structures in dI/dV measurements which will be the subject of a detailed analysis. As it will be shown, the determination of the physical origin of the detected features in the spectra is not allways obvious.

4.1.1 The Kondo effect

While the electrical resistance of pure metals usually decreases with decreasing temperature because the resistivity is mainly an effect of electron scattering on lattice vibrations which are evidently lowered at decreased temperature, it was already discovered in the 1930' that in some metals which have some magnetic impurities incorporated, the electrical resistivity increases below a certain temperature (see figure 1.1). The origin of this effect was longtime unsolved and only in 1964 theoretically explained by *J. Kondo* [6, 108].

He showed that the experimental observations can be sufficiently understood when considering a model including the scattering from the magnetic impurities which interact with the spins of the conduction electrons of the host metal (see figure 4.1). This behavior is nowadays called "the Kondo effect" and only arises when the defects are magnetic, meaning that the total spin of all electrons of the impurity atom is unequal to zero.

A very intuitive model to describe a single magnetic impurity embedded in a nonmagnetic metallic host was given by *P. W. Anderson* [109]. The so called "Anderson single impurity model" neglects all electronic states of the impurity except the unpaired one with spin $\left|\frac{1}{2}\right|$. This localized state might be originating from a d or f level of the magnetic impurity assuming that the impurity is a transition metal as for example cobalt (Co) with its odd

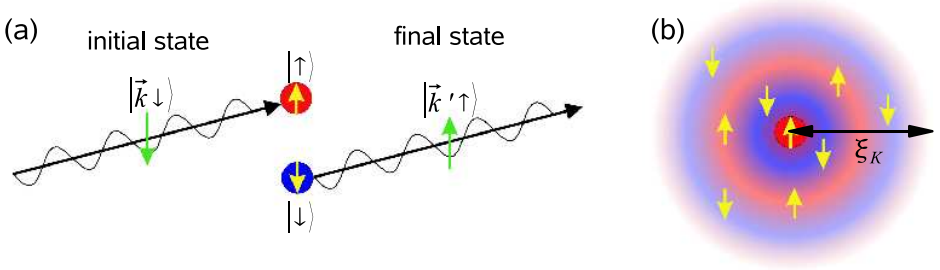

Figure 4.1: Kondo scattering on a single magnetic impurity. (a): At sufficient low temperatures an electron $\left|\vec{k}\downarrow\right\rangle$ of the host metal can be scattered at the impurity into the new state $\left|\vec{k}'\uparrow\right\rangle$ by spin-exchange with the spin moment of the magnetic atom. While in (a) the dynamic of the spin-flip process is shown, the snapshot in (b) sketches the effect of this permanent flipping. The magnetic moment of the impurity is screened over the characteristic Kondo screening length ξ_K.

number of $3d$ electrons (electronic configuration: $[\mathrm{Ar}]3d^7 4s^2$) or a rare earth metal as for example cerium (Ce) with its single $4f$ electron (electronic configuration: $[\mathrm{Xe}]4f^1 5d^1 6s^2$).

In this chapter we are mainly interested in effects arising from interactions between Ce adatoms and the supporting metallic host. Thus, for the sake of simplicity, we will describe the presented model in terms of the magnetic $4f$ electron of the Ce atom.

The singly occupied $4f$ state ($4f^1$) is located below the Fermi energy at ϵ_f and separated by the Coulomb repulsion energy U from the same $4f$ state occupied with two electrons with opposite spins ($4f^2$) as sketched in figure 4.3 (a)). Due to the hybridization between the $4f$ states and the continuum of electronic states in the metal host, the $4f$ levels are broadened by $\Delta = \rho_0 \left|V\right|^2$ with ρ_0 as the DOS at E_F of the supporting metal and V as the hybridization energy which couples the localized state with the continuum of band states.

Exchange processes can take place which flip the spin of the impurity from the "up" to the "down" state, or vice versa, as it is schematically shown in figure 4.1 (a), while simultaneously a spin-excitation state close to the Fermi energy is created. While classically an energy of at least $-\epsilon_F$ is necessary to bring the electron from the singly occupied $4f^1$ state to an empty state in the metal at E_F, in the quantum mechanical framework the Heisenberg uncertainly principle allows for a very short time of about $h/|\epsilon_f|$ this excitation [111]. Within this timescale of some attoseconds (10^{-15} s), another electron has to tunnel from the occupied Fermi sea back to the impurity. This electron, however, can be in the opposite spin state as the previous one and thus, change the spin of the impurity between initial and final state of this scattering process.

This spin exchange modifies the energy spectrum of the system. Taking many of such processes together, a new state, the so-called Kondo resonance is generated very close to the Fermi energy (see figure 4.2). This resonance is clearly a many-body phenomenon – the many-electrons of the free electron gas are decisive in the interaction with the localized state of the impurity.

The Kondo resonance has a half-width at half-maximum of Γ, which can be described

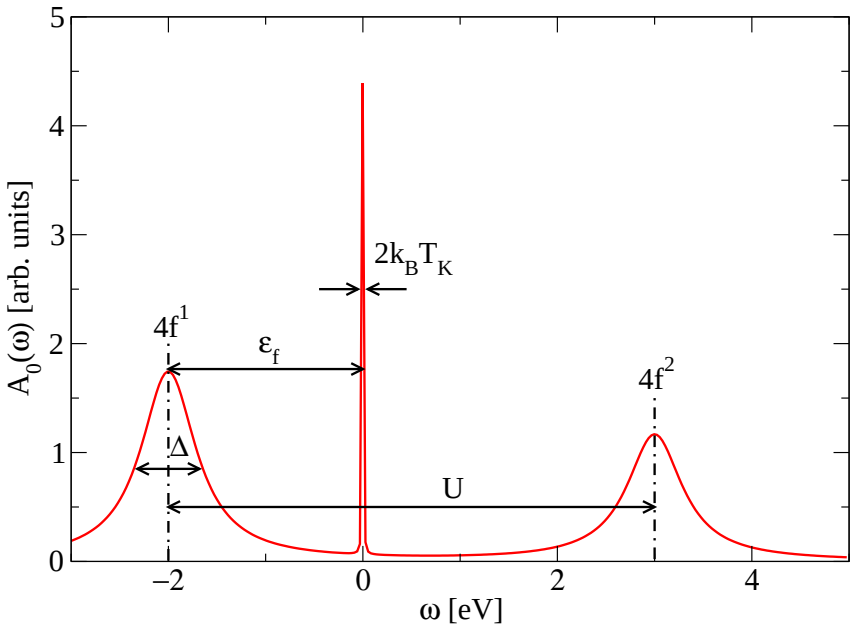

Figure 4.2: Simulation of the $4f$ spectral function $A_0(\omega)$ of a single magnetic impurity of cerium. The singly occupied $4f^1$ state lies below the Fermi energy at ϵ_f and is broadened by Δ due to hybridization with the conduction electron gas of the host. The Coulomb repulsion U separates the unoccupied $4f^2$ state from the $4f^1$ state. The Kondo resonance occurs at approximately E_F and has a half-width at half-maximum of $k_B T_K$. Used parameters for the calculation after [110]: $\epsilon_F = -2$ eV, $U = 5$ eV, and $\Delta = 0.34$ eV.

by a characteristic temperature, the so-called Kondo temperature T_K,

$$T_K = \frac{\Gamma}{k_B} \approx \Gamma \times 11.6 \frac{\mathrm{K}}{\mathrm{meV}}, \tag{4.1}$$

and is calculated by the parameters of the system to [112]:

$$\Gamma = k_B T_K \simeq \sqrt{2\Delta \frac{U}{\pi}} \exp\left[-\frac{\pi}{2\Delta} \left(\left| \frac{1}{\epsilon_f} \right| + \left| \frac{1}{\epsilon_f + U} \right| \right)^{-1} \right]. \tag{4.2}$$

While the Kondo effect and the theoretical explanation are known since a long time and have been experimentally obtained by high-resolution photoemission electron spectroscopy [113, 114] and inverse photoemission [115, 116], it was in 1998 when the Kondo effect was detected on single adatoms with STM [95, 117] and renewed the interest. While previously performed measurements always probed an ensemble of impurities due to the limited resolution, STM gave the unique opportunity to detect the Kondo effect in the entirely smallest conceivable Kondo system: A single magnetic adatom supported on top of a nonmagnetic metal.

Usually, STS measurements do not detect the peak in the spectral function close to E_F which originates from the Kondo effect, but rather a dip-like structure as it is shown in figures 4.5 and 4.6 for measurements on single cobalt adatoms on Ag(100) and Cu(111).

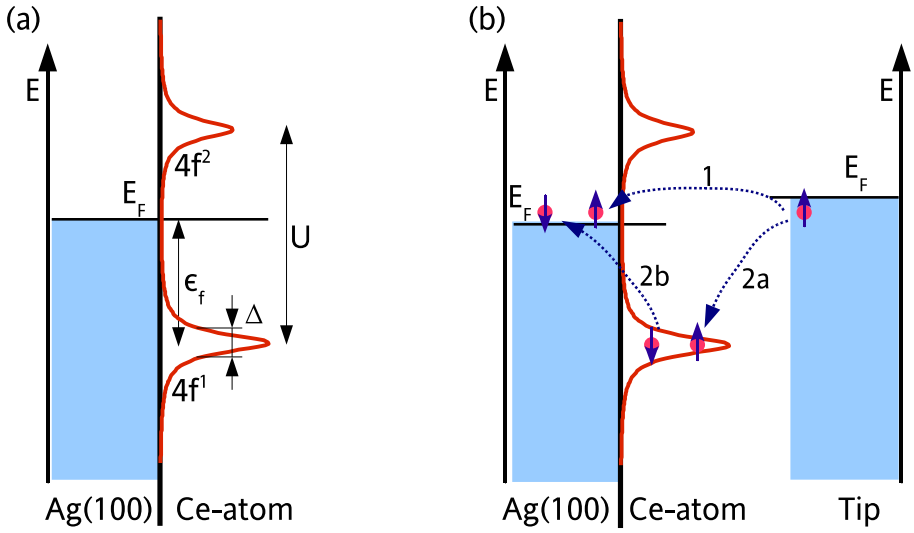

Figure 4.3: (a): Schematic drawing of the energy dependent DOS in the experimental situation of a single Ce adatom on a Ag(100) surface. (b): Electrons from the probing tip can tunnel directly into empty states of the Ag(100) bulk and conserve their spin state (1) or indirect via a spin-flip process on the magnetic adatom (2a→2b).

To understand this behavior, we want to consider a situation as outlined in figure 4.3. A magnetic adatom (Ce) is placed on top of a metal surface (in this example Ag(100)). The occupied $4f^1$ state is localized below E_F and separated by U from the $4f^2$ state as described in figure 4.2. Electrons originating from the tip have two possibilities to tunnel into the sample system. They can tunnel directly into empty bulk states above E_F of the metal sample (path 1) or indirectly via the above described spin-flip process into the hybridized and localized state of the magnetic adatom (path 2). These two different paths are chosen by the tunneling electrons with the probabilities given by the tunneling matrix elements t_1 and t_2 for the direct and indirect path, respectively. As a result, the tunneling current as a coherent quantum effect is determined by the quantum interference between both channels [118].

It was shown by *U. Fano* that such an interference process leads to a spectral feature given by the so-called Fano equation [96]:

$$\rho(E) \propto \rho_0 + \frac{\left(q + \frac{E-E_K}{\Gamma}\right)^2}{1 + \left(\frac{E-E_K}{\Gamma}\right)^2}, \tag{4.3}$$

where E_K is the position and Γ is the half-width at half-maximum of the obtained curve. The lineshape of the curve described by equation 4.3 is determined by the parameter q which results for $q \to \infty$ in a Lorentzian peak and for $q = 0$ in a Lorentzian dip. For some arbitrary values of q the resulting curves are plotted in figure 4.4.

For the tunneling processes (1) and (2a)+(2b) as sketched in figure 4.3 (b), the form

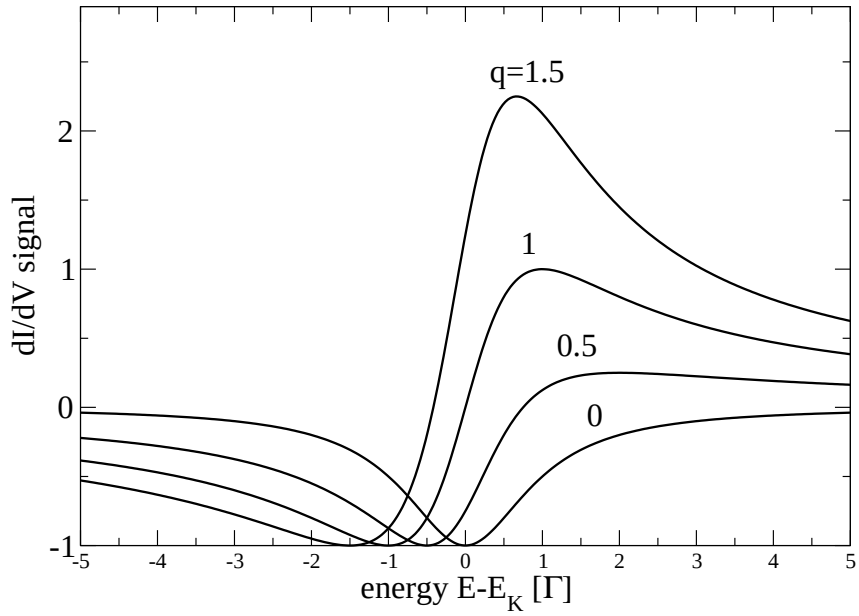

Figure 4.4: Set of curves calculated with the Fano equation 4.3 for different q values.

factor q is given by the ratio between the direct and the indirect tunneling process [118],

$$q = \frac{t_2}{2\pi\rho_0 V t_1}. \tag{4.4}$$

While the $4f$ orbitals are closely localized at the nucleus of the adatom [97], the tunneling propability t_2 for the indirect path is strongly reduced compared to the probability t_1 to tunnel directly into the more extended s- and p-orbitals of the host metal [19]. Thus, we expect for measurements on Ce values of q close to zero. This argument holds, up to a certain degree, also for the $3d$ states of the transition metals as it is seen, for example, in dI/dV measurements on single Co adatoms supported on a Ag(100) or Cu(111) surface as presented in the figures 4.5 and 4.6 with show form factors of $q = 0.6$ and 0.5, respectively.[1]

In general, the analysis of a Kondo system in STS measurements is difficult. For example, the parameters of the Fano fit for the Co/Ag(100) and Co/Ag(111) system were found to be different from values available in the literature [59, 119, 120]. The main problem is the impossibility to detect the localized $4f$ or $3d$ levels directly with STS. Thus one is restricted to the analysis of the Kondo resonance close to E_F. Unfortunately, the resonance signal has rarely a well formed Fano line-shape and the fit of equation 4.3 to the obtained data results in different parameter sets depending on the assumed background and energy window of the data taken into account for the fit (see for example the fitting to the data taken on Co/Cu(111) in ([119]).

[1] An exception from normally small q values was recently obtained in STS measurements performed on single Mn atoms supported on an ultrathin Al_2O_3 layer on a NiAl(110) surface [40]. When the coupling between the magnetic adatom and the metallic host is still strong enough to allow Kondo scattering, but the oxide layer inhibits sufficiently the direct path, a Kondo peak is obtained.

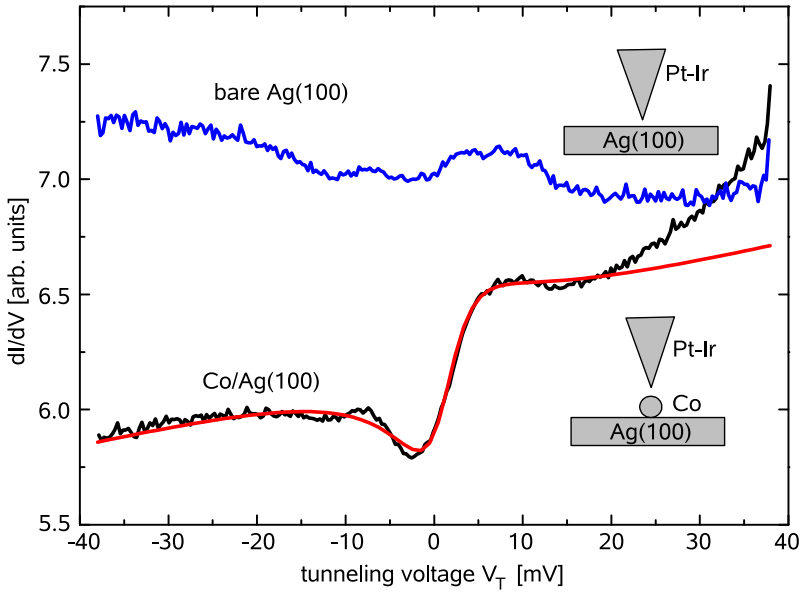

Figure 4.5: Kondo resonance detected on a single Co adatom on Ag(100) (upper curve) in comparison to the spectrum of the bare Ag(100) (lower curve). Both curves were measured with a PtIr tip. The red curve is a Fano fit to the black curve with the best fit parameters of $q = 0.60 \pm 0.05$, $\Gamma = 8 \pm 1$ meV, and $E_K = 3 \pm 2$ meV . Tunneling parameters before opening the feed-back loop: $V_T = -46$ mV, $I_T = 0.5$ nA, $V_m = 1$ mV, $T = 4.7$ K.

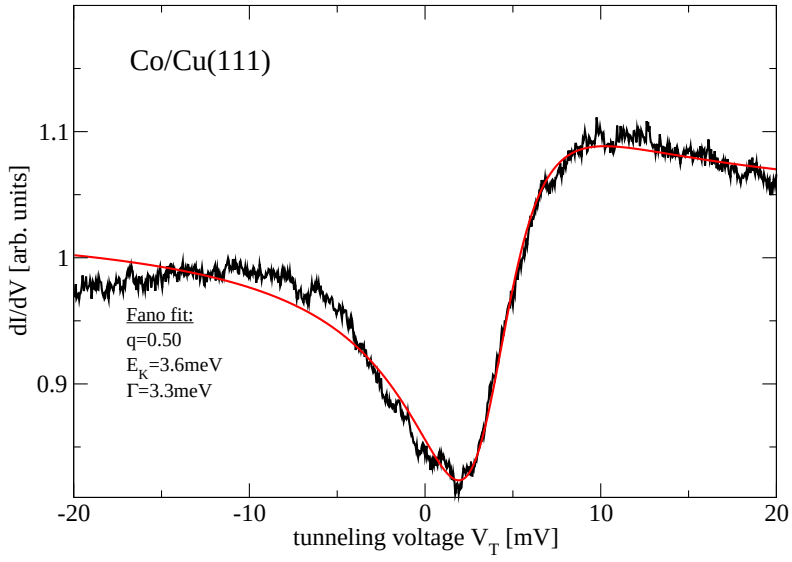

Figure 4.6: Kondo resonance measured at the IBM lab in California on a single Co adatom on Cu(111) (black curve) with an Ir tip and the corresponding Fano fit (red curve). Tunneling parameters before opening the feed-back loop: $V_T = -20$ mV, $I_T = 0.5$ nA, $V_m = 0.28$ mV at a base temperature of $T = 1.2$ K. The parameters of the fit are given in the figure.

In the analysis of the Kondo resonance, one important parameter is the average occupation number n_f for the $4f$ states of the adsorbate on the surface [112, 110]. While the adatom has an integer number of $3d$ or $4f$ electrons in the gas phase which is given by the nuclear charge and the position in the periodic table, the adatom on top of a surface can exchange charge leading to a higher average occupation number in the $3d$ or $4f$ shell. It was shown, that the position of the Kondo resonance together with its width fulfill the relation [112]:

$$E_K = \Gamma \tan\left(\frac{\pi}{2}(1 - n_f)\right). \tag{4.5}$$

The average occupation number n_f has the meaning of an extra charge which is transported from the host metal to the impurity and ranges between 0 and 1 as long as the $4f^1$ level is below and the $4f^2$ level is above the Fermi energy E_F. Furthermore, assuming a relatively small hybridization energy compared to the level energies, i. e.:

$$\Delta \ll |\epsilon_f|, \quad \Delta \ll |\epsilon_f + U|, \tag{4.6}$$

the average occupation number is calculated by the position of the $4f^1$ state and the Coulomb repulsion U [110]:

$$n_f = -\frac{\epsilon_f}{U} + \frac{1}{2}. \tag{4.7}$$

It was shown that the charge transfer, and thus the Kondo temperature (according to equations 4.7 and 4.2) can be monitored by STM. The Kondo temperature changes with the number of available next neighbors from the supporting surface. An adatom has four next neighbors available for hybridization on (100) surfaces (assuming the adatom sits in a hollow-site position), while the next neighbor number is reduced to three on top of the (111) surface [120]. Also the number of ligands, as for example CO, bound to the magnetic adatom influences the coupling of the local magnetic moment with the metallic surface and thus the Kondo temperature [121]. Additionally, metal-organic complexes are interesting objects to study because they permit to change the Kondo temperature of the magnetic atom in the center of the complex by a controlled removing of external hydrogen atoms [122].

As long as the assumptions in equation 4.6 are fulfilled, the above outlined model is sufficient to describe the Kondo effect for a wide range of different adatom-substrate systems. This is in contrast to the still ongoing theoretical discussion [123, 124, 125] to explain the STS spectra on strongly hybridized adatoms as for example Ti and Ni [126, 127]. In these, and similar systems the full impurity Green's function $G_{d,f}(\omega)$ [112]

$$G_{d,f}(\omega) = \frac{\Gamma/\Delta}{\omega - E_K + i\Gamma}, \quad |\omega| \lesssim T_K, T = 0, \tag{4.8}$$

has to be used together with the term $V^2 G_{d,f}(\omega) \equiv T_c(\omega)$ which is the T-matrix of the conduction electrons, as it follows from the Anderson Hamiltonian [110]. The complex line shape observed in tunneling experiments on Ti/Au(111) and Ti/Ag(100) [126, 127] is then due to the multiple Kondo resonances arising from the crystal-field split local orbitals of the transition metal impurity [125, 128] and can be calculated using equation 4.8 in the Dyson equation

$$G_{d,f}(\omega) = G^0_{d,f}(\omega) + G^0_{d,f}(\omega) T_c(\omega) G^0_{d,f}(\omega). \tag{4.9}$$

Finally, one has to remark that the dynamical spin-flip between the localized magnetic adatom and the electrons of the Fermi sea leads to spin-polarized electron waves (spin

waves) in the supporting metal (see figure 4.1 (b)) [129]. The characteristic length scale, the so-called Kondo screening length ξ_K, in which the impurity spin is antiferromagnetically screened, is given by [112]:

$$\xi_K = \frac{\hbar v_F}{k_B T_K}, \tag{4.10}$$

with $v_F = \sqrt{\frac{2E_F}{m^*}}$ the Fermi velocity of the electrons in the host. For typical metals as Ag and Cu with $v_F \approx 10^6$ ms^{-1} [78], and Kondo temperatures which range from $10 - 100$ K for adsorbates as for example Co, ξ_K becomes with $100 - 10$ nm relatively large. Thus, it is indeed possible that interactions between well ordered single adatoms, as for example in superlattices (see chapter 3), lead to the creation of a Kondo lattice in which the spin-flip between individual adatoms is correlated.

4.2 Ce on Ag(110)

While cerium adatoms form hexagonal superlattices on the Ag(111) and Cu(111) surface at low temperatures (see chapter 3), we do not expect such an ordered formation on the Ag(110) surface due to the absence of a surface state. Thus, dosing approximately 0.1% of a monolayer of Ce adatoms from a thoroughly degassed tungsten filament onto a well-cleaned Ag(110) surface results indeed in a random distribution of the Ce adatoms. In contrast to the high mobility of the Ce adatoms on Ag(111) at a base temperature of $T = 4.7$ K (see chapter 3.2), we detect immobile single Ce adatoms at that temperature when adsorbed on Ag(110). dI/dV spectra taken on top of these Ce adatoms reveal no difference compared to spectra taken on the clean Ag(110) surface. In particular, we do not observe a Fano-like spectral feature close to the Fermi energy which would be a sign of the Kondo effect. The detection of a Fano dip in STS measurements is limited by the base temperature and the modulation voltage (chapter 2.3.2) and results for our STM in a lower detection limit of a Kondo temperature of $T_K \approx 10$ K, i. e. a Fano dip with a half-width at half-maximum of $\Gamma \approx 1$ meV.

Apart from the absence of Kondo scattering, we detect a few objects on the surface ($<$ 1% of the adsorbates) which appear "fuzzy" in the STM image as shown in figure 4.7. The apparent height of these objects is larger (≈ 220 pm) than the height of single Ce adatoms (≈ 140 pm) when measured at a tunneling voltage of $V_T = -412$ mV. Spectroscopic measurements taken on top of these objects reveal features symmetrically to E_F. Figure 4.8 shows a typical spectrum obtained on such an unstable object. The blue $I(V)$ curve has clearly detectable voltage regions at about ± 85 mV where the differential resistance becomes negative. The numerically calculated dI/dV curve (red dots and line) reveals additional spectral features. We detect a dip symmetrically around E_F with a half-width at half-maximum of ≈ 12 meV. At slightly higher absolute tunneling voltage ($V_T \approx \pm 50$ mV), a decrease in the conductivity of about $20 - 35\%$ is seen while the already in the $I(V)$ curve visible feature at a voltage of $V_T \approx \pm 85$ mV dominates the spectrum and is identified as the result of an inelastic tunneling process with saturation (see chapter 2.3.3) which can be successfully described with equation 2.30 of page 17 (black lines).

The symmetry, the step like change in conductivity at energies of about 12 meV and 50 meV, and the negative differential conductivity at $eV_T = \pm 85$ meV let us assume that the detected structures belong to complex vibrational excitations of an unknown co-adsorbate

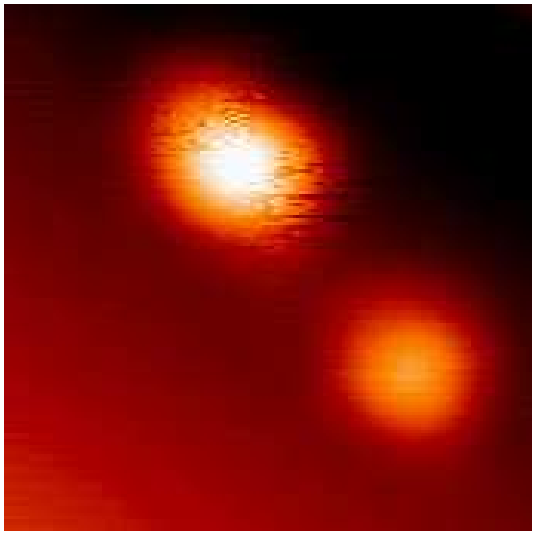

Figure 4.7: STM image of Ce adsorbates on Ag(110) observed with a PtIr tip. ($V_T = -412$ mV, $I_T = 200$ pA, $T = 4.7$ K, image size 4×4 nm^2). The object in the lower right area is a typical single Ce adsorbate in contrast to the unstable object in the upper left area which reveals complex spectral features in STS measurements.

originating from contaminations of the surface during the Ce evaporation process. Even though the exact chemical structure of this contamination can not be clarified with STM, the vibrational excitation energies give a hint of the possible molecules. The ambiguous noise (figure 4.7) and the strong negative differential resistance point to a hydrogen contamination. Recently, it was found that hydrogen on Cu (111) shows a wide variety of different vibrational resonances and two-state noise that leads to unstable tunneling conditions similar to our observation in figure 4.7 [43]. Furthermore, depending on the supporting substrate single carbon monoxide (CO) molecules show well known characteristic vibrational resonances at energies close to the energies of the spectroscopic features in our dI/dV curves [36, 37, 130, 131]. For instance, in high resolution electron energy-loss spectroscopy on CO molecules adsorbed on a W(100) surface molecular vibrations have been found at energies of 45 meV, and $70 - 80$ meV [132]. But while STS measurements on CO show [36, 133] the characteristic C–O stretching mode at an energy of about 250 meV, we do not detect any significant signal at this energy.

4.3 Ce on Ag(100)

As shown, the Kondo effect is not detectable in the spectra measured on top of single Ce adatoms supported on Ag(110), while the same experiment performed on an Ag(100) surface reveals intriguing results.

Figure 4.9 shows two different STM images of single Ce adatoms on Ag(100) measured at low temperature ($T = 4.7$ K) and exemplarily chosen from different measurement sessions. In the left image, the sample was measured at a relatively high positive tunneling

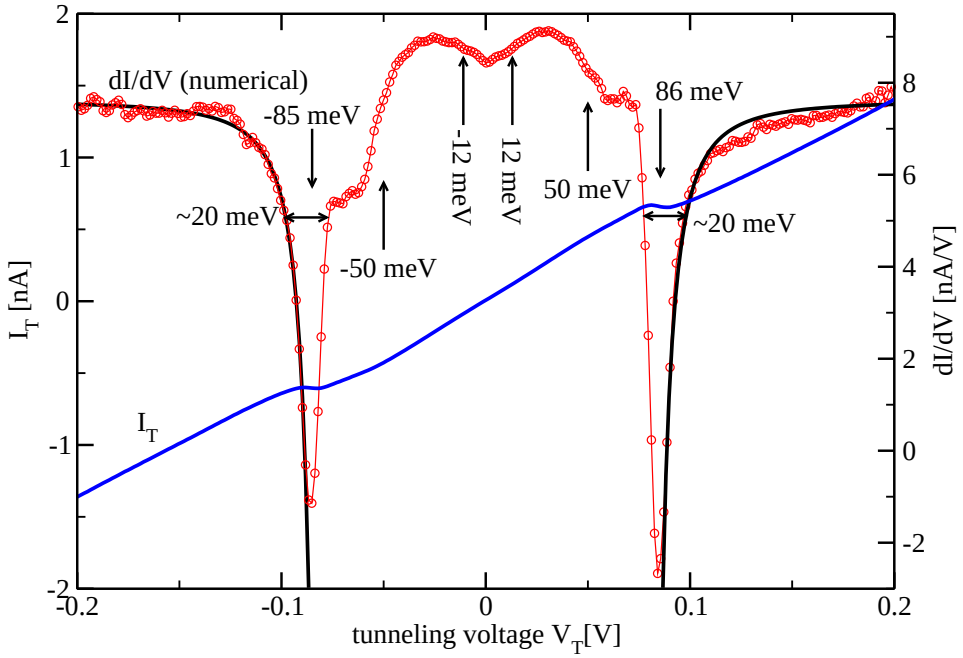

Figure 4.8: IETS spectrum obtained on top of the fuzzy object in the upper part of figure 4.7. Thick line (blue): $I(V)$ curve; Circles and thin line (red): numerically calculated dI/dV signal using the $I(V)$ data. Black lines: A least square fit to the dI/dV data using equation 2.30 of page 17 results in $A = 7.61$ nA, $B = 1.35$ nA, $\Gamma = 21$ meV, $E_i = 85.2$ meV.

voltage of $V_T = 0.5$ V with a Ce adatom concentration of about 0.007 monolayers (ML). Two different species of adsorbates are clearly distinguishable. About 85% appear as protrusions of about 230 ± 10 pm apparent height (reddish yellow dots in the image), while a minority of about 15% have a reduced apparent height of only 95 ± 10 pm (violet dots in the image). The right image of figure 4.9 was measured on a different sample at a tunneling voltage of $V_T = -90$ meV and also shows two species of adsorbates which differ by their behavior when scanned by the tip. While about 60% of the objects on the surface are stable, about 40% are switching between an initial large apparent height to a smaller one detectable by their "fuzziness" during the horizontal tip scan.

The STM image in figure 4.10 (a) shows a close-up of such an unstable object. Recorded in constant-current mode ($V_T = -80$ mV, $I_T = 500$ pA) by scanning horizontally line-by-line from bottom to top, the image reveals several reversible transitions of the object from a large apparent size to a small one and vice versa. The analysis of this transition shows that the appearance depends on the applied tunneling voltage between tip and sample. At low absolute tunneling voltage ($|V_T| < 60$ mV) the bistable adsorbates remain in their initial large appearance, while they switch to the small appearance when applying a voltage above a certain threshold. Interestingly enough, the bistable adsorbate stays in the small appearance when switched even at reduced absolute tunneling voltage until the tip is sufficiently ($\approx 0.5 - 1$ nm) laterally removed from the switching object. Thus, dI/dV spectra can be obtained from the adsorbate in both states revealing a remarkable change of the measured

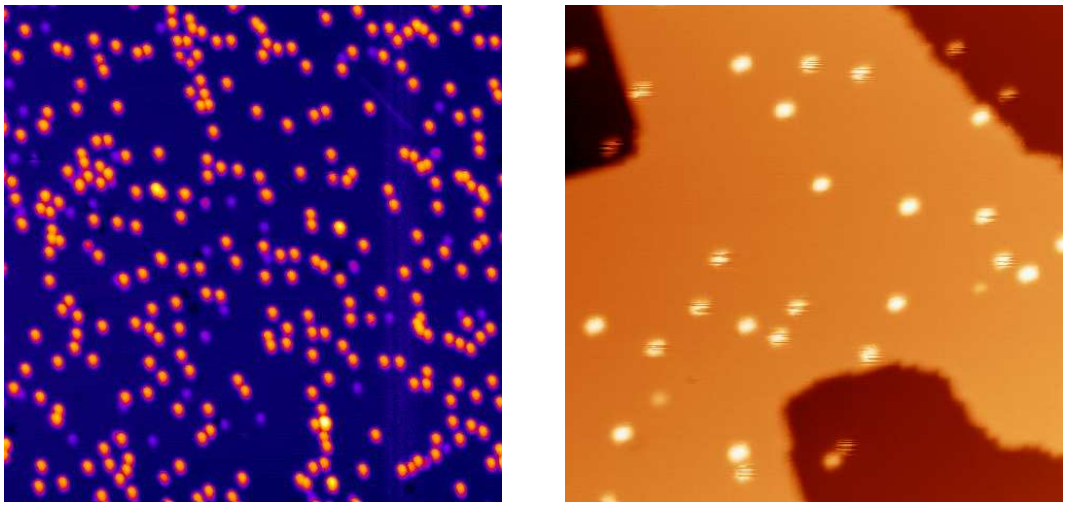

Figure 4.9: Two overview STM images of Ce adsorbates on Ag(100) observed at a base temperature of 4.7 K. Left image: 66×66 nm^2, $V_T = 0.5$ V, $I_T = 0.5$ nA; Right image: 20×20 nm^2, $V_T = -90$ mV, $I_T = 51$ pA.

dI/dV spectrum.

Figure 4.10 (b) compares the dI/dV spectra obtained on top of the adsorbate of figure 4.10 (a) in its small (red dots) and in its large manifestation (green dots). The spectrum of the adsorbate in the initial large position is featureless and almost flat in contrast to the spectrum of the same adsorbate when switched to small which reveals a decrease in the LDOS of about 20% around E_F. The obtained dip is slightly asymmetric and can be successfully described by the Fano equation 4.3 as seen in the least-square fit (blue curve). The Kondo temperature obtained from the fit is $T_K = 48 \pm 3$ K. Surprisingly, the shape of the curve leads to a small *negative* form factor of $q = -0.12 \pm 0.05$.

The voltage dependent switching behavior is plotted in detail in figure 4.11. Here, $z(V_T)$ curves are shown which were recorded on top of a switching adsorbate in constant-current mode, i. e., with closed feedback loop. Starting at $V_T = -40$ mV where the bistable object is in its large configuration, the absolute value of the tunneling voltage was increased until -153 mV, the end of each measurement. The curves show at a specific voltage (marked at each curve in red) a sudden jump in the tip height originating from the transition of the adsorbate to its small appearance. While each $z(V)$ curve is the average of about 15 measurements and the transition does not always occur at identical tunneling voltage, a steplike structure is seen especially in the measurement at $I_T = 500$ pA. Comparing the average transition voltage for different tunneling currents results in an almost logarithmic dependence as shown in the inset. While the tip-sample distance depends logarithmically on the tunneling current (see equation 2.5), we can conclude that the transition voltage mainly depends on the tip-sample separation. Furthermore, we note that the switching is independent of the applied polarization of V_T, i. e. tunneling voltages below ≈ -90 mV as well as above $\approx +90$ mV change the state of the adsorbate from large to small appearance.

Comparing the data of the adsorbates on different Ag(100) sample preparations with varying low Ce coverages (≤ 0.01 ML) and different PtIr tips, we always detect the above

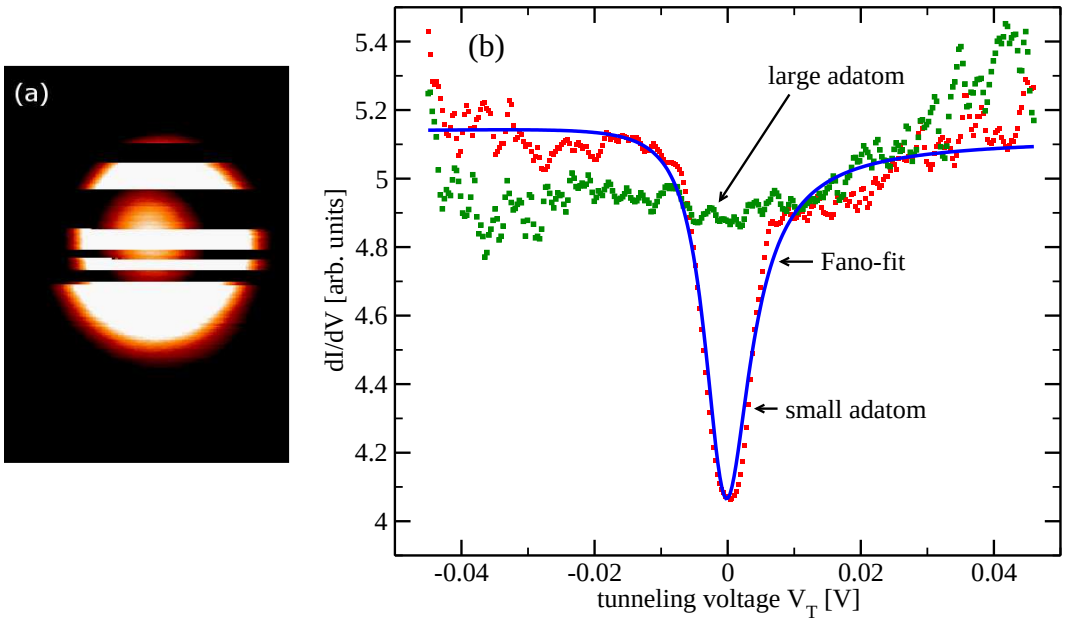

Figure 4.10: Left: STM topography of a two-state object recorded at $V_T = -80$ mV, $I_T = 500$ pA. Image size: 2.3×3.3 nm^2. Right: The dI/dV spectrum obtained on top of the bistable object in large appearance shows no characteristic feature (green dots), while the spectrum taken on the same object in small appearance an asymmetric dip around E_F is detected (red dot). A least-square Fano-fit (blue line) results in the following parameter set: $E_K = 0.9 \pm 0.1$ meV, $\Gamma = 4.2 \pm 0.3$ meV, $T_K = 48 \pm 3$ K, $q = -0.12 \pm 0.05$. Experimental settings: $T = 4.7$ K, $V_m = 1$ meV, $I_T = 500$ pA.

described behavior. Between $5 - 50\%$ of all adsorbates are bistable and reveal a dip around E_F in spectroscopic measurements when switched to the small apparent size. Additionally, results measured at a reduced base temperatures of 3.7 K by pumping on the He bath [79] are identical. A height analysis of about 700 stable and bistable adsorbated show a small difference between the extent in the z direction of the stable (z height: 230 ± 10 pm) and of the large state of the switching adsorbates (z height: 210 ± 10 pm).

To this end, the observations are reminiscent of the γ–α transition of metallic cerium. It is well known, that the electronic and magnetic properties of Ce show extreme variations with temperature and pressure which is unique among elemental solids [116]. At ambient conditions, solid Ce is in the γ-phase with a magnetic susceptibility of $\chi \approx 4.8 \times 10^{-3}$ and a Kondo temperature of $k_B T_K \approx 10$ meV [134, 135].[2] At high pressure or low temperature the γ-phase collapses into the α-phase with an isostructural[3] volume reduction of up to 17% (figure 4.12) [137]. Cerium in the α-phase looses almost its magnetic properties and has a much smaller magnetic susceptibility of $\chi \lessapprox 0.4 \times 10^{-3}$. Additionally, α-Ce has

[2] In this thesis SI units are continuously used. Thus, the unit of the magnetic susceptibility χ is converted from the cgs-system as still used in several publications with the conversion factor: $1 \frac{\text{emu}}{\text{mol}} = 4\pi \times 10^{-6} \frac{\text{m}^3}{\text{mol}} \approx 0.60$ (for γ-Ce) [136].

[3] Isostructural transition means that the crystal structure in both phases remains fcc.

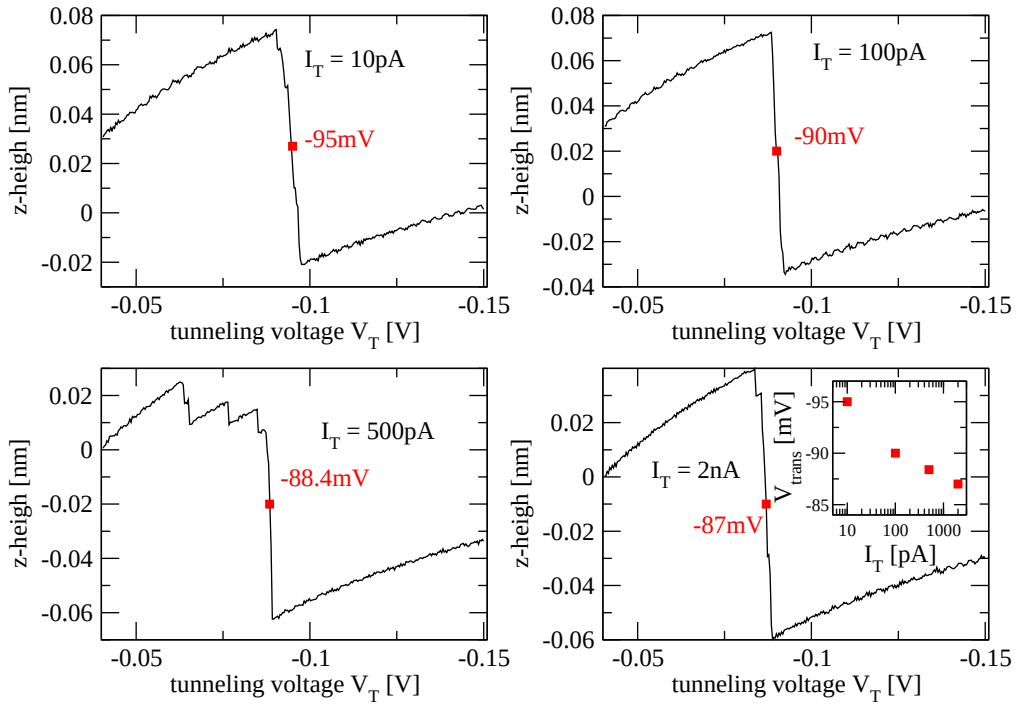

Figure 4.11: The switching of the bistable object analyzed by ramping the tunneling voltage V_T at constant current I_T and recording $z(V_T)$. Depending on the applied current I_T, the switching voltage from the large appearance to the small appearance occurs at almost the same voltage. The stairway-like steps, especially in the $I_T = 500$ pA curve, are due to an averaging over about 15 curves with occasionally large variations of the transition voltage.

an increased Kondo temperature of $k_B T_K \approx 200 - 250$ meV [139], more than an order of magnitude higher than of Ce in the γ-phase. Extensive experimental and theoretical investigations have shown that these phenomena are caused by the electronic correlations resulting from coupling of the localized $4f$ states to delocalized band states [140, 141, 142, 135, 143] which is reflected in the exceptional change of the Kondo temperature. During this transition, the occupancy of the f-level n_f changes only slightly while the hybridization with the $s-p$ band changes by a factor of about two [135] which influences the Kondo temperature exponentially (see equation 4.2). Furthermore, measurements using high-resolution photoemission electron spectroscopy (PES) on ultrathin Ce layers show reduced Kondo temperatures of $k_B T_K \approx 5$ meV and $k_B T_K \approx 26$ meV for γ-Ce and α-Ce, respectively [113, 114].

The strong reduction of the Kondo temperature in thin layers and on single atoms is observed in all Kondo systems. For instance, single Co adatoms supported on noble metal surfaces reveal a Kondo temperature of $T_K = 30 - 100$ K in STS [120] (see also figures 4.5 and 4.6) much lower than the bulk Kondo temperature of $T_K \approx 1000$ K [59] due to the subsequently reduction of the number of available neighbors in dimensionally reduced systems which leads to a decrease of hybridization of the magnetic impurity with the bulk electronic system of the supporting crystal [144].

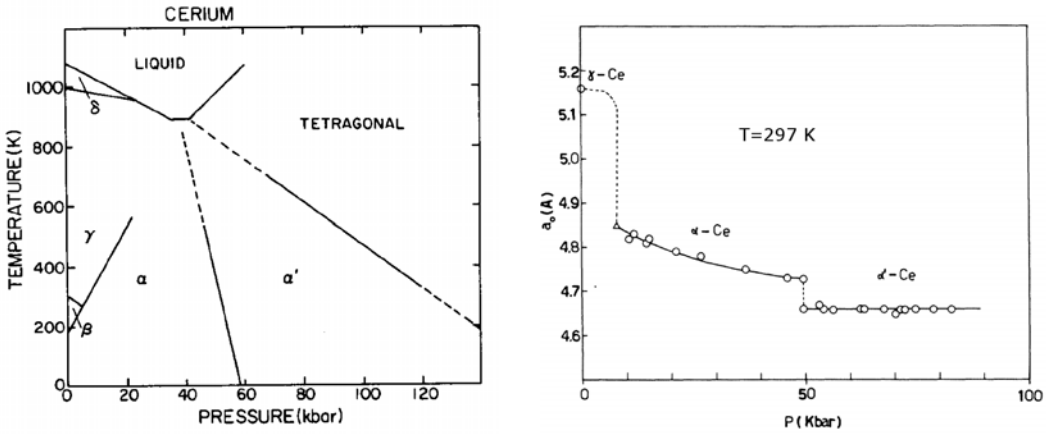

Figure 4.12: Left: The $p-T$ phase diagram of solid cerium taken from [138]. The $\gamma-\alpha$ transition appears at temperatures below ≈ 190 K at low pressure, or at high pressures at ambient temperatures. Right: Along with a change in the magnetic susceptibility, the lattice constant a_0 of the crystall changes drastically during the $\gamma-\alpha$ transition [137].

With these considerations, the observed drastic change in the spectrum on top on the bistable adsorbates might be the counterpart of the γ–α transition in bulk Ce on the single atomic scale. The tip-controlled apparent Ce height reduction of about 50% can be rationalized by considering low-energy electron diffraction (LEED) and STM investigations of the valence transition induced surface reconstruction of Sm(0001) [145, 146] which is associated with a 22% expansion of the atomic radius for the top monolayer surface Sm atoms due to the transfer of a valence electron to the $4f$ shell which effectively shields the Coulomb attraction of the nucleus. Assuming the $4f^1$ level of the Ce adatom at an energy of $\epsilon_f \approx -2$ eV and a Coulomb repulsion of $U \approx 5$ eV (see figure 4.2) [113, 114, 143], the Kondo temperature can be plotted versus the hybridization Δ using equation 4.2 as shown in figure 4.13. The occupancy is given by equation 4.7 to $n_f = 0.9$, in good agreement to earlier measurements on α-Ce of $n_f = 0.88$ [113, 114], and the calculated value using the parameters of the fit in figure 4.10 and equation 4.5 ($n_f = 0.89 \pm 0.05$). Changes of n_f caused by the transition are neglected in this simulation. The Kondo temperature of $k_B T_K \approx 4.2$ meV as observed in the small appearant state of the Ce adatom, is compatible to $\Delta \approx 0.34$ eV. Because γ-Ce is weaker hybridized than α-Ce, the corresponding Kondo temperature is below the instrumental resolution, in agreement with the featureless dI/dV spectrum on top of the bistable adsorbates in the large state.

Even though the above outlined explanation is reasonable to explain the observed height and spectroscopic differences between both states of the switchable adsorbate, several questions remain open and can lead to an alternative explanation of the observations.

In all experiments, we found only a certain amount of bistable adsorbates ($5-50\%$), while the remaining are unchangeable. Furthermore, we were able to transform bistable adsorbates into stable and vice versa by applying short voltage pulses to the adsorbates as shown in figure 4.14. But while the transformation was *always* possible from the unstable to the stable configuration, the backward direction was hindered after several switching events.

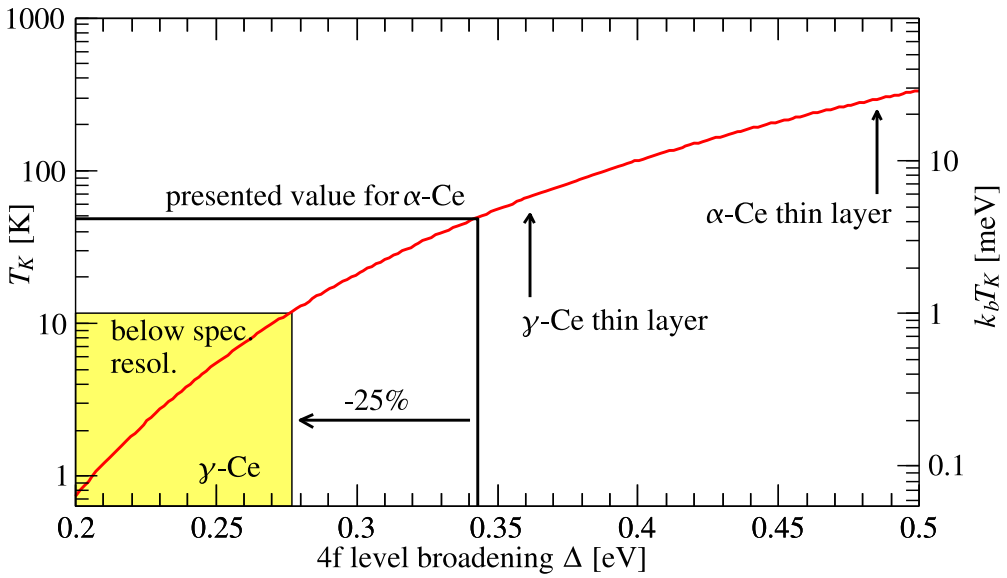

Figure 4.13: Simulation of the Kondo temperature T_K for variable $4f$ level-broadening Δ using equation 4.2 with fixed values for $U = 5$ eV, and $\epsilon_F = -2$ eV (see figure 4.2). Arrows mark the Kondo temperatures of γ- and α-Ce measured on thin films. In this framework the measured Kondo temperature of $T_K = 48$ K for α-Ce (figure 4.10) would lead to a broadening of $\Delta \approx 0.34$ eV, while the Kondo temperature for γ-Ce is below the spectroscopic resolution (yellow area).

Additionally, we found strong evidence of having co-adsorbed contaminations in several images. It is known that CO molecules and single H adsorbates on metal surfaces are detected in STM images rather as depressions than as protrusions [147, 148, 149]. Similar depressions were often found in the STM images close to the bistable adsorbate as it can be seen in figure 4.14 below the adsorbate.

Furthermore, clusters were found on the surface which reveal distinct spectra which are the result of inelastic tunneling processes, as shown in figure 4.15. Here, the spectra reveal a steplike increase (curves (a) and (b)) or decrease (curve (c)) in the differential conductance dI/dV at an energy of $|eV_T| \approx 18$ meV. The curves differ by the setpoint current and therefore by the nominal tunneling resistance R_T before opening the feedback loop and obtaining the data. The ratio between the conductivity of the ground state σ_g and the excited state σ_{ex} (see chapter 2.3.3) changes almost logarithmically as shown in figure 4.15 (d). The origin of the vibrational mode at an excitation energy of ≈ 18 meV is unknown but might be due to a complex vibration mode between co-adsorbed CO or H, the Ce adatoms, and the supporting Ag(100) surface. Remarkably, all dI/dV spectra shown in figure 4.15 reveal in addition a dip around E_F of about 5 meV half-width at half-maximum which is only marginally influenced by the tunneling resistance R_T.

Furthermore, not all spectra obtained on top of the bistable adsorbates in the small configuration reveal the typical asymmetry around E_F as shown in figure 4.10 (b) and characteristically for the Fano resonance. In Figure 4.16, such dI/dV curves are plotted for

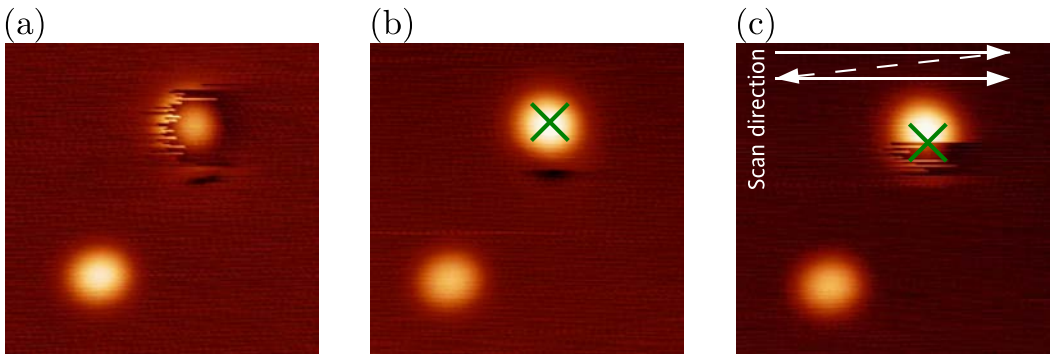

Figure 4.14: "Switching" between bistable and stable configuration by applying short (20 ms) pulses between tip and sample. (a): Initial image; (b) Image recorded after applying a $V_T = -4$ V pulse at the marked position; (c): Pulse of $V_T = +4$ V applied during the scan at the marked position. The white arrows indicate the scan direction. Tunneling parameters: $V_T = -100$ mV, $I_T = 100$ pA. Image size for all images: 5.8×5.8 nm^2.

different tunneling resistances R_T. All spectra show an identical symmetric dip within the limits of resolution. The spectra remind us of the spectrum produces by an inelastic tunneling process in the limit of $k_B T \approx E_i$ (see chapter 2.3.3 and figure 2.8)). Indeed, performing a least-square fit of the IETS equation 2.24 to the data results in a good agreement between fit and data as shown in figure 4.16 (red lines). The best fit parameters are $E_i = 3.2 \pm 0.9$ meV for the excitation energy of the inelastic process, and $T_{\text{fit}} = 6 \pm 2$ K for the temperature. The large fitting range of about $\pm 30\%$ for both parameters, i. e. the range in which the calculated curves agree with the obtained data, is due to the resolution limit in IETS of ≈ 2 meV at a base temperature of $T = 4.7$ K of the instrument (see page 15).

To determine the influence of hydrogen on the measurements, first experimental results are obtained by dosing pure H_2 gas through a microvalve into the STM chamber on the cold sample. Figure 4.17 (a) shows a STM image in pseudo 3D representation of 7.7×3.6 nm^2 size after dosing hydrogen gas. The image shows a Ce adatom of about 200 pm apparent height (labeled with I) and a small indention in the surface of about 50 pm apparent depth which is found close to the adsorbate and labeled with II. Spectroscopic measurements were performed on the hydrogen contaminated surface. The results are presented in figure 4.17 (b). The curve I was measured on top of the adsorbate and reveals a spectrum mainly identically to the one presented in the beginning of this section in figure 4.10 (b). A least-square fit using the Fano equation 4.3 results in the parameters $E_K = -0.7 \pm 0.1$ meV, $\Gamma = 3.5 \pm 0.3$ meV, and $q = -0.20 \pm 0.05$. These results are within their uncertainties identical to the earlier observations. The dI/dV spectrum measured at point II in a distance of about 1 nm from the adatom reveals a different shape which we associate mainly to a vibrational mode of the hydrogen adatom of ≈ 5 meV excitation energy. Due to the small distance to the adsorbate, it can not be excluded, that the spectrum is still influenced by the adsorbate [95, 117].

Unfortunately, further investigations have not yet been performed, so that the final answer of the origin of the observed switching and the spectral features is not yet given.

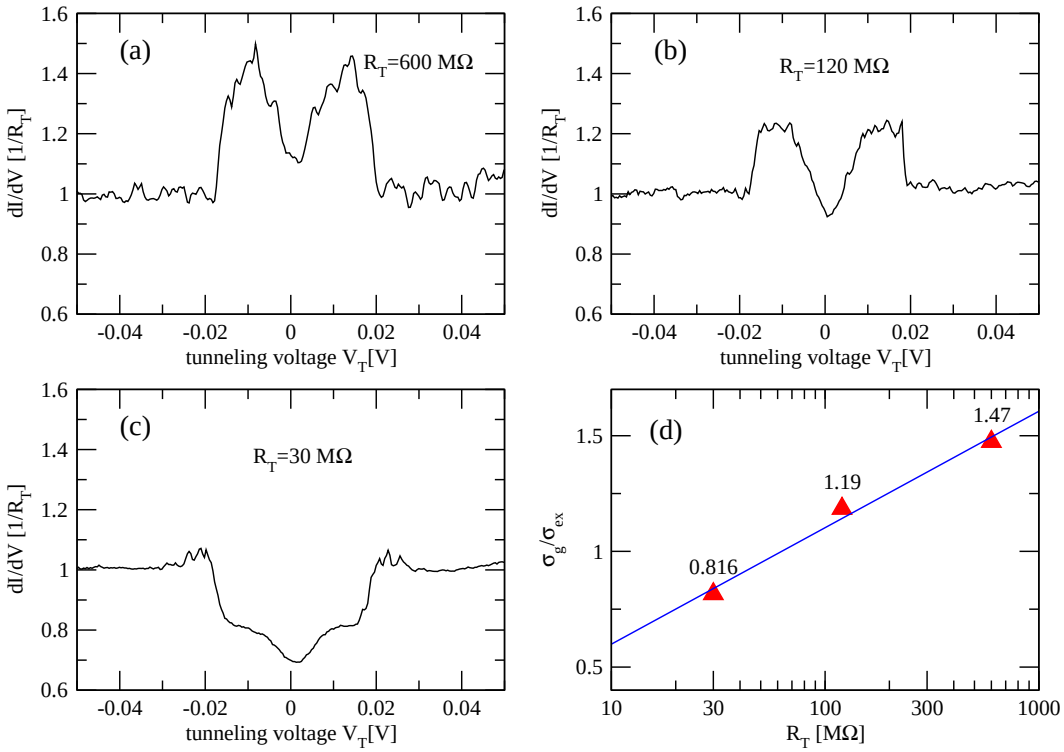

Figure 4.15: (a)-(c): Set of dI/dV curves obtained on a small Ce cluster on Ag(100) at a base temperature of $T = 4.7$ K using a modulation voltage of $V_m = 1$ mV. The spectra reveal a distinct dependence on the tunneling resistance R_T. At relatively high R_T, the ground state conductivity σ_g is higher than the excited state conductivity σ_{ex}, while the situation is inverse at lower R_T. (d): The ratio σ_g/σ_{ex} obtained from the spectra (a)–(c) shows a logarithmically dependence in R_T.

4.4 Summary

The experimental observations obtained on single Ce adatoms supported on different silver surfaces as presented in this chapter are ambiguous. In contrast to the clear manifestation of the Kondo effect in spectroscopic measurements on top of single Co atoms when supported on noble metal surfaces (figures 4.5 and 4.6) and detected by several groups [117, 47, 59, 144], the unequivocal detection of the Kondo effect originated by single Ce adatoms was not possible in this thesis.

Ce adatoms on the Ag(100) surface reveal spectroscopic features which might be partly due to the Kondo effect. Unfortunately, we are not able to exclude a co-adsorption of hydrogen which can strongly influence the Kondo temperature and show vibrational signatures in the dI/dV spectrum similar to a narrow Fano resonance. As the chapter 5.3 will address, single Co adatoms on the Cu(111) surface show no longer the characteristic Kondo scattering in the dI/dV spectrum as shown in figure 4.6 when exposed to hydrogen.

To clarify the origin of the switching and the observed spectroscopic features detected on Ce adatoms at Ag(100) it is highly recommended to perform measurements at signifi-

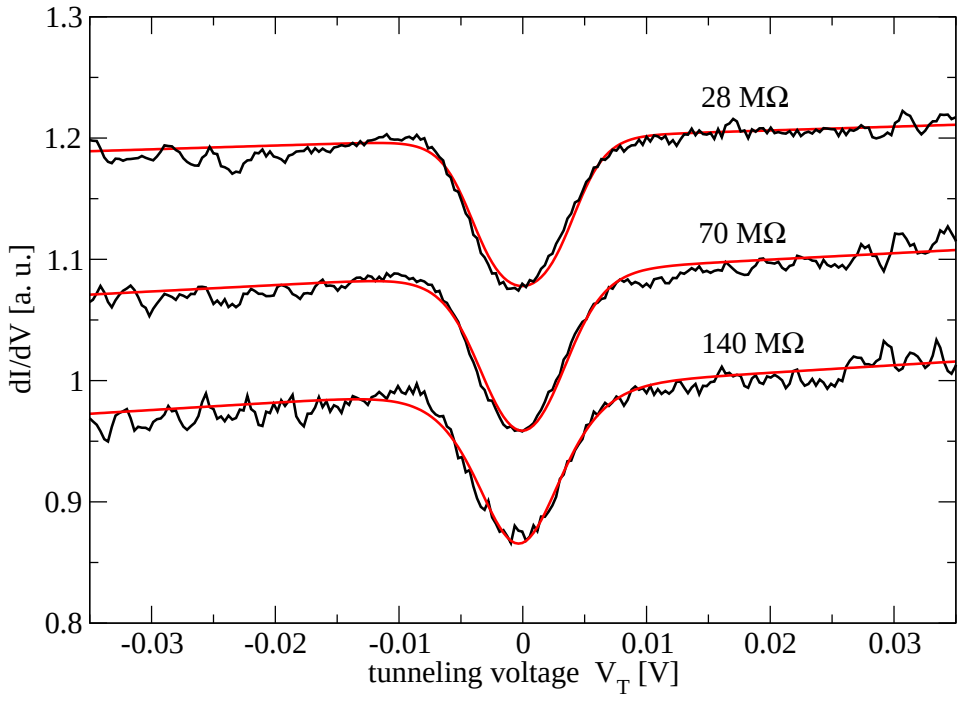

Figure 4.16: Black lines: Set of dI/dV curves measured on top of a bistable adsorbate in small configuration at different tunneling resistances. A $1/10$ voltage divider was included between the voltage supply and the junction to reduce the voltage noise and to increase the energy resolution. Additionally, a low modulation voltage of $V_m = 500$ μV was used. Red lines: Fit to the data using the IETS equation 2.24. The best fits result in: $E_i = 3.2 \pm 0.9$ meV and a temperature of $T_{\text{fit}} = 6.7 \pm 1.4$ K. The curves are shifted vertically with respect to each other by 0.1 units for better visualization.

cantly lower temperature. The base temperature of liquid helium is not sufficient to obtain an energy resolution in spectroscopic measurements to clearly distinguish between the different processes with a shape analysis of the spectra. Additionally, the contamination of the sample by hydrogen has to be ruled out. Unfortunately, hydrogen gas is always present in low-temperature measurements and due to its small mass it is only poorly pumped by the getter pumps of the STM system. Nevertheless, it might be possible to reduce the hydrogen contamination by including a non-evaporable getter pump closely to the STM in the low temperature part [150].

Such an equipment, which will be soon available in our lab, allows to contaminate the Ce/Ag(100) sample with H_2 and additionally with D_2 in a controlled manner. This experiment would help to distinguish between vibrational excitations and the Kondo effect, due to the mass-effect in IETS [35, 130, 48, 151]. Additionally, a lower base temperature would also allow to measure the spectrum of single Ce adatoms on the Ag(111) surface which is so far hindered by the mobility of single Ce adsorbates on Ag(111) or superimposed by the change in the LDOS due to the superlattice creation as discussed in chapter 3.4.

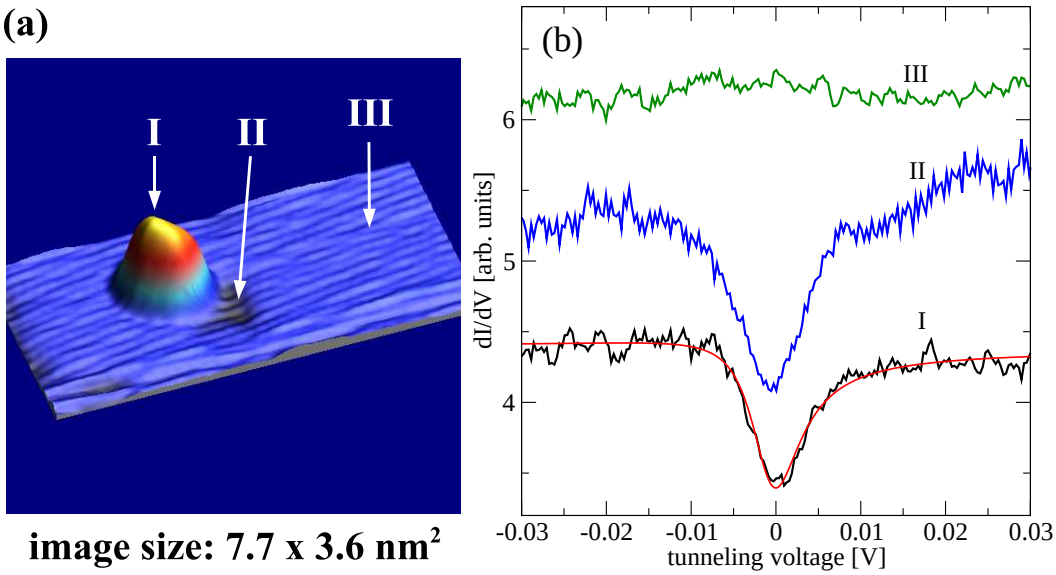

Figure 4.17: (a): Pseudo 3D representation of an STM image of an individual Ce adatom on Ag(100) after dosing H_2 on the cold sample. Tunneling parameters: $V_T = -43$ mV, $I_T = 100$ pA, $T = 4.7$ K. Image size: 7.7×3.6 nm^2. (b): Spectra obtained on three different points in the image marked with I–III by using a modulation voltage of $V_m = 1$ mV during the dI/dV measurements. The full line at I is a least-square fit using the Fano equation 4.3 and resulting in: $E_K = -0.7 \pm 0.1$ meV, $\Gamma = 3.5 \pm 0.3$ meV, and $q = -0.20 \pm 0.05$.

Chapter 5

Measurements with superconducting tips

5.1 Introduction

Experiments using superconducting materials in planar tunnel junctions for one or both electrodes have already been performed in the early 1960s [15, 152, 153, 16, 154, 155], but it is only in the last few years that superconducting tips have been successfully used in STM [156, 157, 158, 159, 160, 161].

There are several problems to solve before one can successfully use superconducting tips in STM experiments. Up to now, all published spectroscopic measurements where performed with elementary superconductors (see references above) leading to the problem that even for metals with the highest critical temperature T_C, i. e. niobium ($T_C = 9.25$ K) and lead ($T_C = 7.2$ K) [136], an essential cooling of the STM down to liquid helium temperature or lower is required. Additionally, the design of the electronic equipment, in particular the voltage generator for the tunneling voltage and the current-voltage converter, has to be selected for extremely low (voltage) noise to make spectroscopic measurements in the sub-millivolt range possible (see also chapters 2.3.2 and 2.3.5).

To overcome these complications, one could imagine using high-T_C superconductors as tip materials. Unfortunately, these materials are very brittle which makes it extremely difficult to produce a sharp tip, even though first attempts have been made to create superconducting tips made out of MgB_2 crystals [162]. Additionally, high-T_C superconductors are not yet well understood on a theoretical level which makes it difficult to interpret the obtained spectroscopic data, but might be by itself an interesting subject to explore.

In this chapter we will present data which was obtained using superconducting niobium tips. The major part of the measurements were done at the *IBM Research Division* in the STM group of *Don Eigler*[1] at the *Almaden Research Center, San Jose, California*. Here excellent conditions for STM and STS measurements are given by a ^{3}He Joule-Thomson refrigerator [48] which has the capability of cooling down the STM to a base temperature of only 0.55 K resulting in a spectroscopic energy resolution of a few μeV. Additionally, the setup has the option of applying magnetic fields between $0 - 7$ T parallel or perpendicular to the sample surface.

[1] The head of the STM group has since changed and is now *Andreas Heinrich*.

The experiments can be divided into two categories. As discussed in chapter 2.3.5, superconducting tips can be used to boost the resolution of STS measurements below the limit of their normal-conducting counterpart, which was used to measure excitations of very low energy (section 5.3). Additionally, tunneling between two superconductors reveals by itself very exciting physics of multiple *Andreev* reflections [163, 164], as we will discuss in section 5.4 [165], and of *Josephson* supercurrent [166], which will be the subject of section 5.6.

Furthermore, in section 5.5, the interaction between two superconducting electrodes (i. e. tip and sample) and a magnetic adatom will be presented, giving an outlook on the interesting physics and opportunities that measurements with superconducting tips open.

5.1.1 Preparing superconducting tips

For the preparation of superconducting Nb tips two different techniques were used in this work. To produce sharp and stable *normal*-conducting tips, electrochemical etched tungsten wires are widely used [17]. This etching process was applied to Nb where we used the following procedure [167, 168]: A purified (99.99%) polycrystalline Nb wire of 0.25 mm diameter was degreased with isopropyl and immersed approximately $1.5 - 2$ mm deep in a solution of 25% HCl in water. The electrochemical etching was then performed by applying a 50 Hz ac voltage of approximately $24\mathrm{V}_{\mathrm{rms}}$ between the wire and a graphite block used as counter-electrode. The ac current was recorded during the etching and showed a slow, almost linear decrease until a certain point at which the current dropped much faster, marking the endpoint of the etching process for sharp tips. Such tips are covered with a thick layer of different insulating oxides like NbO, NbO_2, and Nb_2O_5. These tips were afterwards transfered into the preparation chamber where the oxide layer was removed by Ar ion sputtering. After this procedure, the tips are able to image the sample surface with atomic resolution.

The second method used by us was, in a way, a more “brute force” technique. While the exchange of tips in the STM at the *IBM* lab is difficult to perform and can only be done by breaking the vacuum, we attached a Nb microcrystal on a normal-conducting Ir tip. Therefore, a Nb(110) single crystal sample was cleaned by successive cycles of heating and Ar-ion sputtering until we resolved a flat surface (see figure 5.1 (a)) [169]. By indenting the Ir tip between $1 - 20$ μm into the Nb sample, we attached a Nb microcrystal on the apex of the tip as schematically drawn in figure 5.1 (b), resulting in a superconducting gap ranging from 21% - 86% of the bulk Nb value, i. e. $\Delta = 0.31 - 1.27$ meV.

Superconducting tips produced with this method show an unexpected stability. Without mechanically destroying the tip, measurements with tunneling currents up to $I_T = 500$ nA and tunneling resistances down to $R_T = 8$ kΩ were performed. Additionally, the tips were sharp enough to resolve atomic resolution as seen in figure 5.1 (a).

5.1.2 The BCS model of superconductivity

The sudden disappearance of conductivity below a critical temperature, which was already detected in several materials at the beginning of the 20th century starting with the early measurements of *H. K. Onnes* [2] (see figure 1.1 on page 2), is surely the most known characteristic of superconductivity. At that time, when the quantum mechanical revolution

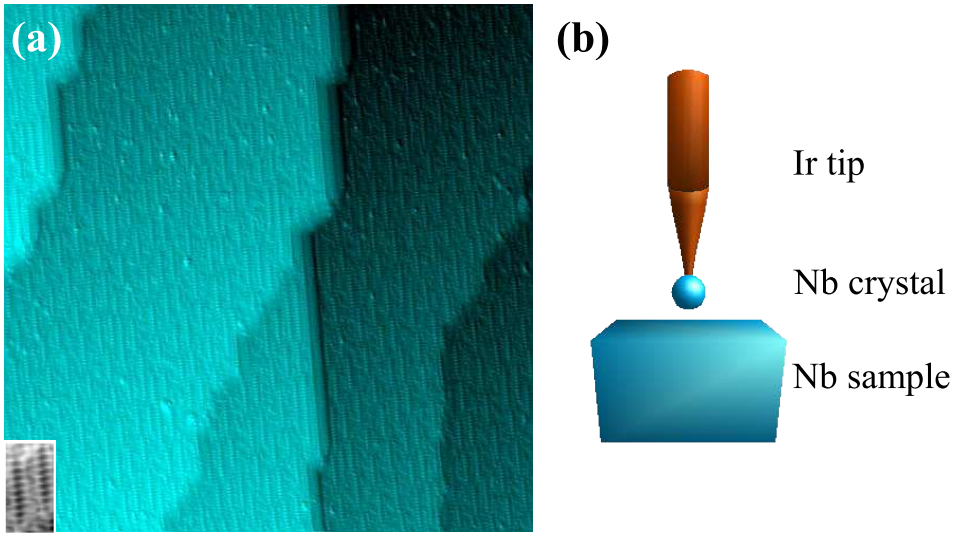

Figure 5.1: (a): Image of the Nb(110) surface (50×50 nm^2, $V_T = 50$ mV, $I_T = 1$ nA) observed with a superconducting tip. Bottom left inset: 2.4×4.1 nm^2 detail revealing atomic resolution (b): Schematic of the superconducting tip used. A microcrystal of Nb was attached to a normal-conducting Ir tip by indenting the tip into the Nb(110) crystal.

has not yet started, it was impossible to explain the effect adequately. Additionally, with the observation of the perfect diamagnetism of superconductors by *W. Meissner* and *R. Ochsenfeld* [170], it became clear that superconductivity is more than the simple loss of electrical resistivity in certain materials.

It took more than 40 years until superconductivity was successfully put in a quantum mechanical framework, the so called BCS model, after *J. Bardeen*, *L. N. Cooper*, and *J. R. Schrieffer* [5]. This section gives the outline of this theory with the emphasis on the topics necessary for the interpretion of tunneling measurements. The BCS theory is based on an assumption that under certain conditions an attractive interaction can exist between electrons near the Fermi surface of a metal. These interactions were first proposed by *H. Fröhlich* [171] and independently by *J. Bardeen* [172]. They showed that such an interaction can occur by the exchange of virtual phonons.

This attractive interaction may arise when an electron with momentum $\vec{k}_1$ polarises a lattice of positive ions to such an extent that it is overscreened, resulting in an attractive force on a second electron with the initial momentum $\vec{k}_2$ (see figure 5.2). The overscreening can only occur when the difference in energy between initial and final states is smaller than the energy of lattice vibrations, and thus the exchanged phonon is a virtual one [173, 174]. The maximum momentum exchange $\vec{q}$ between the two interacting electrons is limited. The scattering process takes place only from an occupied state into an empty state. Therefore, all scattering events have to occur in a narrow energy range around E_F of width $\pm\hbar\omega_D$, with ω_D as the *Debye* frequency of the lattice which characterizes the cut off of the phonon spectrum in the crystal.

By using this positive electron-electron interaction, *Cooper* considered in 1956 [175] what would happen to two electrons added to a Fermi sea at $T = 0$. The electrons were

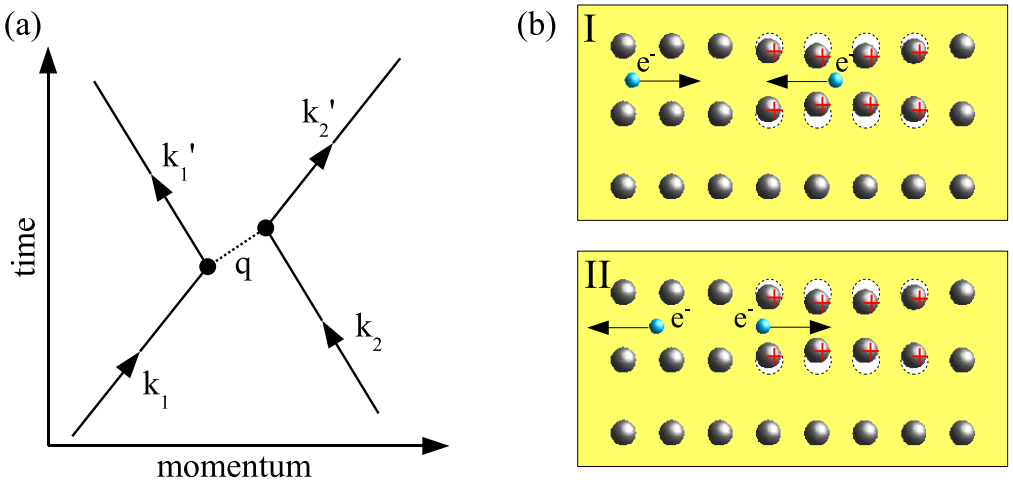

Figure 5.2: (a): Interaction between two electrons by exchange of a virtual phonon. An electron with the momentum $\vec{k}_1$ interacts with one with momentum $\vec{k}_2$. Conservation of momentum requires $\vec{k}_1' = \vec{k}_1 - \vec{q}$ and $\vec{k}_2' = \vec{k}_2 + \vec{q}$. (b): The interaction can be understood by assuming an overscreened response of the positive lattice ions initialized by a passing electron (I). The local positive charge than attracts a second electron (II).

only allowed to interact with each other via the above described interaction, but not with the electrons of the Fermi sea except by Pauli exclusion, which excludes them from already occupied states, i. e. from states below the Fermi energy. He showed that the lowest energy state is reached when the momenta of the two electrons are opposite, i. e. $\vec{k}_2 = -\vec{k}_1$, so that pairs with a total momentum of zero are energetically most favored. To additionally satisfy the Pauli exclusion principle and the indistinguishability of the electrons in the pair, the total wavefunction of the two-electron system has to be antisymmetric for the permutation of the electrons, meaning that the electrons themself have to be in an antisymmetric singlet spin state with oppositely directed spins,[2] so that the two-particle wavefunction can be written as:

$$\phi_{2e^-} = \frac{1}{\sqrt{2}}\Big(|\uparrow\rangle_1 |\downarrow\rangle_2 - |\downarrow\rangle_1 |\uparrow\rangle_2 \Big), \tag{5.1}$$

with $|\uparrow\rangle_i$ as the i-th electron in spin up and $|\downarrow\rangle_i$ as the i-th electron in spin down state.

As a consequence of the positive interaction, all electrons will pair and thus go into this new state as long as the gain in energy is greater than zero. The new ground state of the Fermi sea, which results from the pairing of the electrons, is determinated by a complex interplay between the electrons. The paired electrons are called Cooper pairs in honor of his introduction of this concept. Because of the opposite spin of the two electrons, the Cooper pairs have a sum spin of zero and act more like bosons which can condense according to the *Bose-Einstein* statistic into the same energy level.

The pair $(\vec{k}\uparrow, -\vec{k}\downarrow)$ can be occupied or unoccupied so that we can choose the following

[2] This might not be the case in high-T_C superconductors, where symmetric triplet spin interactions is in discussion.

representation for the wavefunction:

$$|\psi\rangle_{\vec{k}} = u_{\vec{k}}\,|0\rangle_{\vec{k}} + v_{\vec{k}}\,|1\rangle_{\vec{k}}\,, \tag{5.2}$$

where $|1\rangle_{\vec{k}}$ and $|0\rangle_{\vec{k}}$ are the wavefunctions for the pair $(\vec{k}\uparrow, -\vec{k}\downarrow)$ in occupied and unoccupied states, respectively. We note that $|1\rangle_{\vec{k}}$ and $|0\rangle_{\vec{k}}$ are orthogonal to each other. $w_{\vec{k}} = v_{\vec{k}}^2$ is now the probability of finding the electron pair occupied, and $1 - w_{\vec{k}} = u_{\vec{k}}^2$ the probability of finding it unoccupied. The BCS ground state of the superconductor is approximatively the product of all pair states [173]:

$$|\phi_{\mathrm{BCS}}\rangle \simeq \prod_{\forall \vec{k}} \left(u_{\vec{k}}\,|0\rangle_{\vec{k}} + v_{\vec{k}}\,|1\rangle_{\vec{k}}\right). \tag{5.3}$$

The equation 5.3 can be rewritten in second quantization as:

$$|\phi_{\mathrm{BCS}}\rangle \simeq \prod_{\forall \vec{k}} \left(u_{\vec{k}} + v_{\vec{k}} b_{\vec{k}}^*\right)|0\rangle_{\vec{k}}\,, \tag{5.4}$$

with $b_{\vec{k}}^* = c_{\vec{k},\uparrow}^* c_{-\vec{k},\downarrow}^*$ as the operator for the combined creation of two electrons in the Cooper pair state $(\vec{k}\uparrow, -\vec{k}\downarrow)$.

While $v_{\vec{k}}$ and $u_{\vec{k}}$ obey the relation $v_{\vec{k}}^2 + u_{\vec{k}}^2 = 1$, one can rewrite the prefactors by using only one variable $v_{\vec{k}} = \cos\theta_{\vec{k}}$ and $u_{\vec{k}} = \sin\theta_{\vec{k}}$. The fraction of occupation for the BCS ground-state at $T = 0$ is than calculated as (see for example [72] or [173]):

$$w_{\vec{k}} = v_{\vec{k}}^2 = \frac{1}{2}\left(1 - \frac{E}{\sqrt{E^2 + \Delta^2}}\right), \tag{5.5}$$

with Δ as the gap energy of the superconductor. The function, plotted in figure 5.3, reminds one of the Fermi-Dirac distribution at the critical temperature $T_C = \frac{1}{1.76 k_B}\Delta$ of the superconductor[3]. Of course we have to keep in mind that w_k is only described with equation 5.5 inside the small energy window $E_F \pm \hbar\omega_D$ in which the interaction energy between the paired electrons is positive.

In most tunneling experiments, we are not interested in w_k but in the so called quasiparticle excitation spectrum. To excite a single electron in the superconductor from an occupied state below E_F to an empty state above, an energy of at least 2Δ is necessary to break a Cooper pair leading to a gap of 2Δ width around the Fermi energy. The exact form of the quasiparticle excitation spectrum is plotted in figure 5.3 and calculated in the framework of the BCS theory as:

$$\rho(E) = \Re\left\{\frac{E - i\delta}{\sqrt{(E - i\delta)^2 - \Delta^2}}\right\}, \tag{5.6}$$

where, in addition to the BCS theory, a small imaginary part $i\delta$ is added to the energy to account for the finite lifetime of the quasiparticles at the gap edge [176]. δ is usually relatively small, within a few percent of the gap energy Δ.

In figure 5.4 we outline schematically the tunneling between a superconductor and a normal conducting metal. The top curves (ρ_t) are drawn using the quasiparticle excitation

[3] Here we see clearly that we do no longer have a single electron statistics. w_k is similar to the Fermi-Dirac distribution at T_C even if we have plotted the curve for a temperature of $T = 0$.

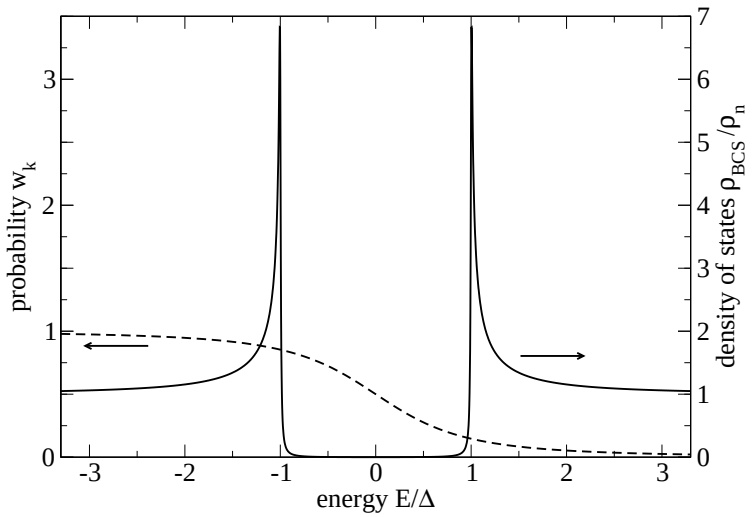

Figure 5.3: Dashed line: Plot of the fraction of occupation for the BCS ground state at $T = 0$ (equation 5.5). The cut-off at $E_F \pm \hbar\omega_D$ is not shown. Full line: Quasiparticle excitation spectra (equation 5.6) with δ set to 0.01Δ. The energy for both plots is given relatively to the Fermi energy E_F in units of the superconducting gap Δ.

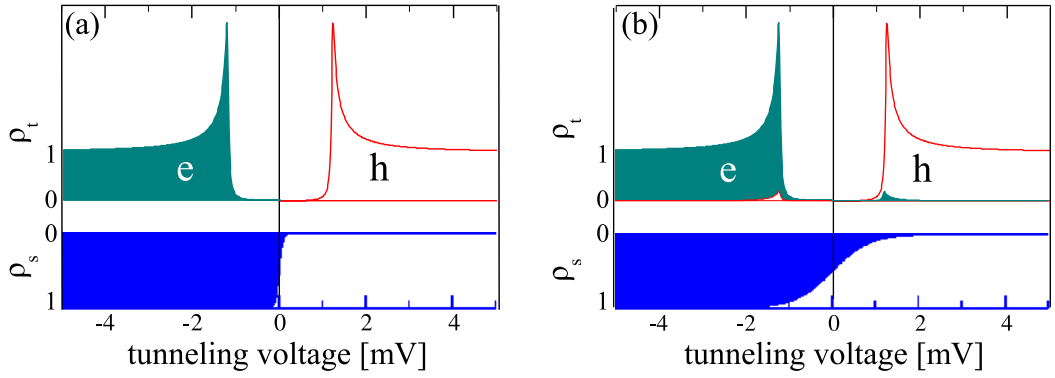

Figure 5.4: Quasiparticle excitation spectra for a Nb superconductor with $\Delta = 1.47$meV (ρ_t), and density of states for a normal metal (ρ_s). (a): At $T = 0.5$ K almost no electron-like states above E_F, and hole-like states below E_F exist in the superconductor. The Fermi-Dirac distribution for the normal conducting electrode has a sharp edge at E_F. (b): At $T = 5$ K some electron-like states above E_F, and some hole-like states below E_F exist in ρ_t, while the Fermi-Dirac distribution in ρ_s is smeared out around E_F.

spectrum of equation 5.6. They are divided into two parts labeled "e" and "h" to account for occupied (electron) states and unoccupied (hole) states. This is similar to the band notation in semiconductors and in some cases is very helpful as we will see below. Nevertheless, we must be aware that the situation in a superconductor is quite different from a semiconductor and that these notations should not lead to the assumption that the physics of superconductors are similar and applicable to models used in semiconductor physics. The difference between the plots in figure 5.4 (a) and (b) is the temperature of the system. In (a) we have assumed $T = 0.5$ K which is far below the critical temperature of $T_C = 9.2$ K for a Nb superconductor with $\Delta = 1.47$ meV. The electron states are filled up to $E_F - \Delta$, while the occupied hole states only exist at $E > E_F + \Delta$. The electron density ρ_S of the metallic electrode shows a sharp, step-like decrease at E_F.

The situation is different in (b) where the temperature $T = 5$ K is elevated compared to (a) and the thermal energy $k_B T = 0.43$ meV $\simeq 0.3\Delta$ is of the same order as the superconducting gap energy. At once, one remarks the influence of the higher temperature on the electron density ρ_s. In the metallic electrode, the occupation of electrons is smeared out in a range of about $4k_B T$ around E_F (see also chapter 2.3.2), but the quasiparticle excitation spectrum of the superconducting electrode remains mostly unchanged.[4] The only difference from the low temperature curve is that a small part of electrons have enough energy to overcome the gap and thus fill states above the Fermi energy leaving the same quantity of hole states below E_F.

5.1.3 Andreev reflections

To describe tunneling between two superconductors, equation 5.6 has to be used for the ρ_t in the tip as well as for the ρ_s in the sample. Using equation 2.9, the convolution of ρ_t and ρ_s leads to a dI/dV spectrum which has a gap of $\pm(\Delta_1 + \Delta_2)$ width around E_F. Here Δ_1 and Δ_2 are the superconducting gap energies of the tip and the sample, respectively. Assuming a finite temperature and thus some electronic excitations above E_F as displayed in figure 5.4 (b), additional peaks are detected in the dI/dV spectrum at $\pm|\Delta_1 - \Delta_2|$ as shown in figure 5.5. These features diminish when $k_B T \ll \Delta_{1,2}$.

As we will see in section 5.4, the above described structure of the dI/dV spectrum of the superconductor-insulator-superconductor tunneling is only valid if the coupling between both superconductors is weak, i. e. the tunneling resistance is high ($R_T \gtrapprox 1$ MΩ).

In stronger coupled tunneling junctions new features occur inside the gap due to Andreev reflection processes. This mechanism was first pointed out by *A. F. Andreev* in 1964 [178] and is schematically presented in figure 5.6 following the description of *G. E. Blonder, M. Tinkham,* and *T. M. Klapwijk* [163, 164].

In this figure, a voltage $2\Delta > |eV_T| > \Delta$ is applied between two equal superconductors.[5] We assume now that an electron (1a) moves from a state below $E_{F1} - \Delta$ in the left superconductor 1 into the right superconductor 2. While in superconductor 2 no electron-like empty states are available for the incoming electron, this process can only occur if the electron is backscattered into a hole (1b) which tunnels in the opposite direction back to the

[4] Δ is a function of temperature, but as long as T is sufficiently smaller than T_C it decreases only slightly. At $T \approx 0.5T_C$ it is still a good approximation to set $\Delta(T) = \Delta(T = 0)$.

[5] It is not necessary to have equal superconductors as we will see in section 5.4. $\Delta_1 = \Delta_2$ is only chosen to simplify the derivation outlined in this section.

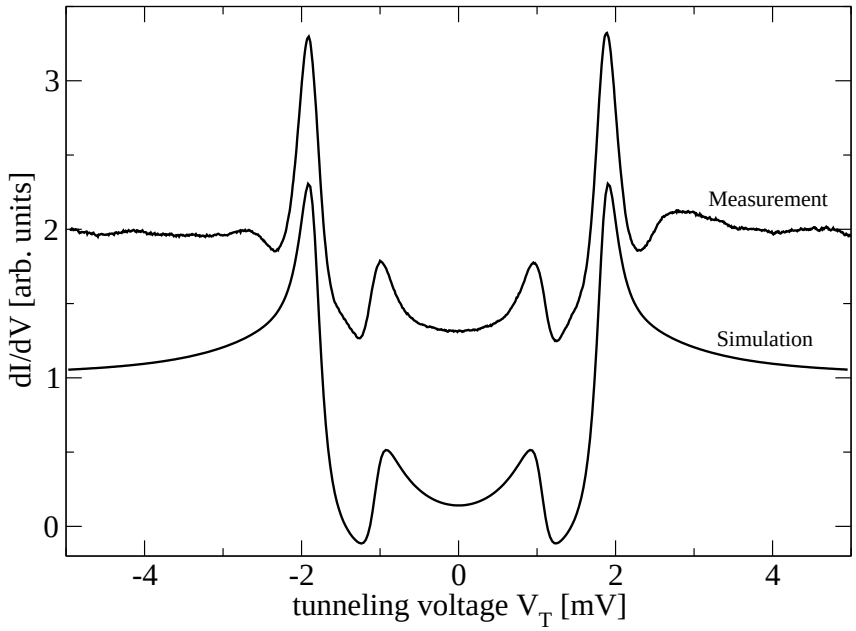

Figure 5.5: Upper curve: dI/dV spectrum between a superconducting sample with $\Delta_1 = 1.47$ meV and a superconducting tip with $\Delta_2 = 0.4$ meV at $T = 4.2$ K ($R_T = 5\,\mathrm{M}\Omega$, $V_m = 28\ \mu$V). Peaks are visible at $eV_T = \pm(\Delta_1 + \Delta_2)$ and at $\pm(\Delta_1 - \Delta_2)$ due to quasiparticle tunneling (spectrum is shifted by one unit for better visibility). Lower curve: Simulation using equation 5.6 to describe the excitation spectra in tip and sample. The dI/dV spectrum was then calculated with equation 2.9. The difference between simulation and measurement at $|V_T| \gg 2$ mV is caused by phonon excitations in Nb [177] which are not included in the simulation.

left electrode where empty hole-states are available.

The electron (1a) is "mirrored" on the Fermi energy of the right superconductor 2 during this Andreev reflection process. The incoming electron $(\vec{k}, \uparrow)$ with an energy E_{1a} is reflected into a hole $(-\vec{k}, \downarrow)$ with opposite energy $E_{1b} = -E_{1a}$ in respect to E_{F2}. After this process, two electron charges are transported across the junction from left to right, creating a Cooper pair inside the gap of the right superconductor.

To calculate the probability $|a|^2$ of the occurrence of an Andreev reflection process, we write the incident electron wave function as:

$$\psi_{\mathrm{inc}} = \begin{pmatrix} 1 \\ 0 \end{pmatrix} e^{i\vec{k}\vec{x}}, \tag{5.7}$$

the reflected hole-like wave function as

$$\psi_{\mathrm{refl}} = \begin{pmatrix} 0 \\ 1 \end{pmatrix} e^{-i\vec{k}\vec{x}}, \tag{5.8}$$

and the transmitted wave function as

$$\psi_{\mathrm{trans}} = \begin{pmatrix} u \\ v \end{pmatrix} e^{i\vec{k}\vec{x}}. \tag{5.9}$$

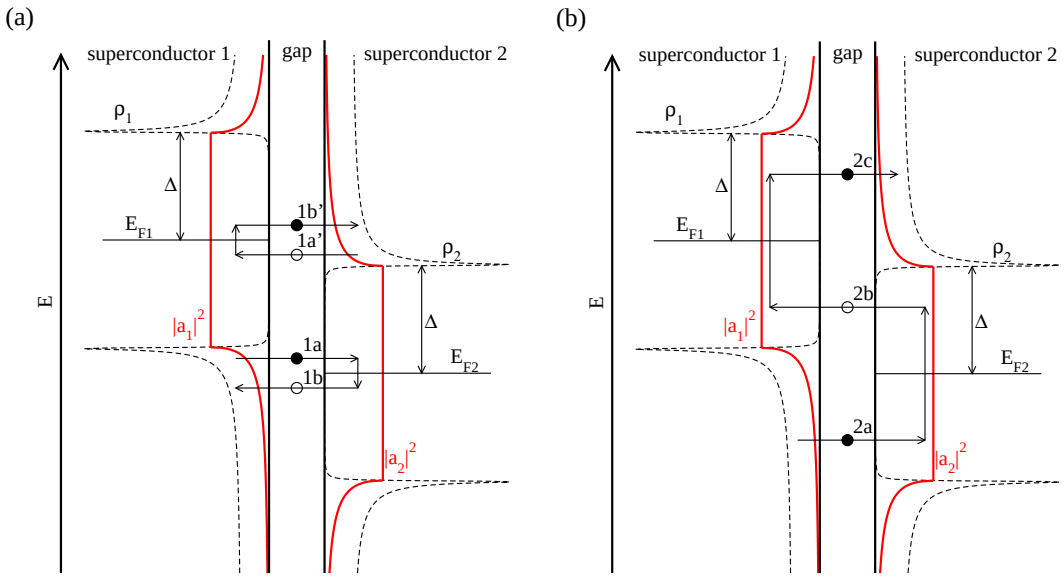

Figure 5.6: Sketch of the Andreev reflection process between two superconductors. Dashed lines: Quasiparticle excitation spectrum for the left and right superconductor. Red lines: Square of the Andreev reflection amplitudes $|a(E)|^2$. Arrows indicate second order (1a→1b, 1a'→1b') (figure (a)) and third order (2a→2b→2c) processes (figure (b)). For details see text.

Matching the amplitude and derivative at the boundary, we find the Andreev reflection coefficient to be [164]:

$$|a|^2 = \begin{cases} 1 & , \quad |E| < \Delta \\ \dfrac{v^2}{u^2} = \dfrac{|E| - \sqrt{E^2 - \Delta^2}}{|E| + \sqrt{E^2 - \Delta^2}} & , \quad |E| \geq \Delta \end{cases} \tag{5.10}$$

Whereby the quasiparticle wave function is phase shifted at each Andreev reflection process by:

$$\phi = \arctan\left(-\frac{\sqrt{\Delta^2 - E^2}}{|E|}\right). \tag{5.11}$$

As we see in equation 5.10, all electrons with $|E| < \Delta$ are completely reflected as a hole, while the Andreev reflection coefficient $|a|^2$ diminishes rapidly for quasiparticles with energies $|E| > \Delta$ (see red lines in figure 5.6).

A similar process is possible that involves an incident hole-like quasiparticle (1a') from the right superconductor 2, which is Andreev reflected into an electron-like quasiparticle (1b') by annihilating a Cooper-pair in superconductor 1. In the sum, the 1a'→1b' process is equivalent to the 1a→1b one. Both transport two elementary charges across the junction. Higher ordered processes involving more than one Andreev reflection are possible. In figure 5.6 the 2a→2b→2c transport is drawn as an example of such a higher order process. Here, three quasiparticles are involved (two electrons and one hole) transferring three elementary charges across the junction from the left to the right superconductor.

The threshhold voltage for the n-th order process, where n is the number of elementary charges that are transported over the junction involving $n-1$ Andreev reflections is given by:

$$eV_T \geq \frac{2\Delta}{n}, \tag{5.12}$$

as it can be easily deduced graphically from figures like 5.6 or 5.23 (page 100).

5.1.4 Supercurrent and Andreev bound-states

It was in 1962 when *B. D. Josephson* pointed out that between two superconducting electrodes not only quasiparticle tunneling is possible, but additionally Cooper pairs should be able to tunnel across the barrier leaving the quasiparticle distribution unchanged [166, 179]. The tunneling of Cooper pairs leads to a supercurrent, which can flow even in unbiased junctions.

This macroscopic quantum phenomenon is called Josephson effect: the supercurrent is driven by the phase difference δ between the wavefunctions of the Cooper pair condensates of the two superconductors. While the Cooper pairs in the two superconducting electrodes are all in the same state, δ is a collective variable coupling the quantum mechanic observable directly with macroscopic electric quantities. Josephson showed that the effect is described by two equations

$$I = I_0 \sin(\delta), \tag{5.13}$$

$$V = \varphi_0 \frac{d\delta}{dt}, \tag{5.14}$$

where I and V are the current and voltage of the tunnel junction, I_0 is the critical current and $\varphi_0 = \hbar/2e = 3.291 \times 10^{-16}$ Vs is the reduced flux quantum.

Together, these two equations, are able to describe a wide range of experimental results and observations. They can be understood easily in the following way: Equation 5.13 describes the dc-Josephson effect, i. e. the phenomena that a current flows between two superconductors without voltage drop. The supercurrent depends therefore only on the phase difference δ between both superconductors and the critical supercurrent I_0, which is given for a temperature T and equal gaps Δ in both tunneling electrodes by [166]

$$I_0 = \frac{\pi\Delta}{2R_T} \tanh\left(\frac{\Delta}{k_B T}\right), \tag{5.15}$$

with R_T as the junction resistance in the normal conducting state. For unequal superconductors with $\Delta_1(T) \geq \Delta_2(T)$, *V. Ambegaokar* and *A. Baratoff* showed that the supercurrent is calculated as [180]

$$I_0 = \frac{1}{R_T}\Delta_2(T) K\left(\sqrt{1 - \frac{\Delta_2(T)^2}{\Delta_1(T)^2}}\right) \tanh\left(\frac{\Delta_2}{k_B T}\right), \tag{5.16}$$

with T as the temperature and $K(x)$ as Jacobi's complete elliptic integral of the first kind.

Shortly after the publication of Josephson's theoretical assumptions, the experimental evidence of the proposed zero-voltage supercurrent was discovered in thin film measurements [181] and in greater detail in point contacts [182]. Today, experiments are mainly

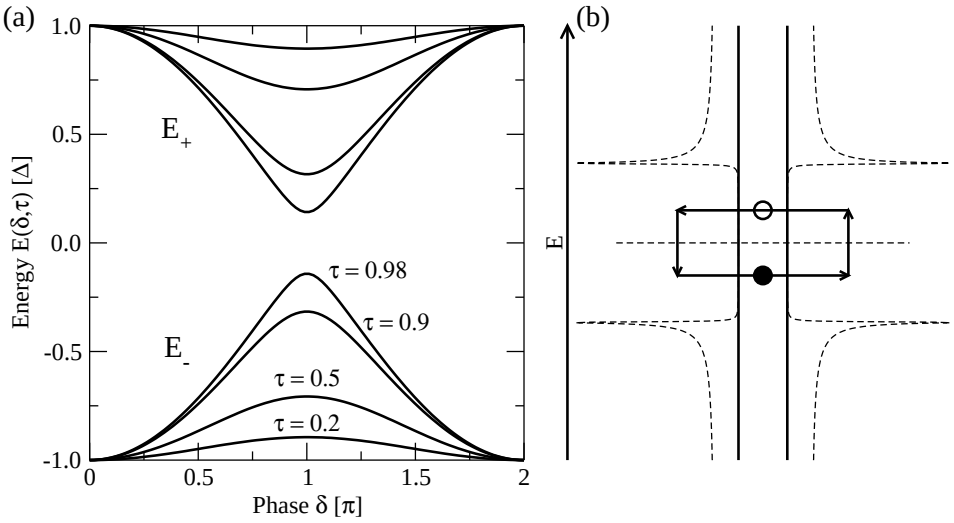

Figure 5.7: (a): Andreev bound-states energies $E_{\pm}$ for different transmission coefficients τ and phase shifts δ between the two equal superconducting electrodes. (b): Sketch of the Andreev reflection process between two superconductors. The bound states lead to a closed cycle of quasiparticle tunneling, Andreev reflections, and the annihilation and creation of Cooper pairs. During this process, charge is transported in $2e$ quantities across the junction at zero voltage.

done in break junction experiments [183, 184] due to their ability to achieve single contacts between both superconductors. Additionally, experiments using STM have been performed [185, 186]. Based on these earlier works, we will present new data with intriguingly high energy resolution and probably new effects in section 5.6.

Equation 5.14 describes the so called ac-Josephson effect. Here, the phase between the two superconductors δ is no longer fixed. The time derivative $d\delta/dt$ is directly proportional to the voltage across the junction. Thus, an applied small voltage produces an alternating supercurrent with a frequency of $f = \frac{V}{2\pi\varphi_0} = 483.5979$ MHz/μV.[6] The first experimental observation of the ac-Josephson current was done by applying microwaves to the junction. Sharp steps in the recorded $I - V$ curves were found when the applied voltage crossed multiples of $2\pi\varphi_0 f$ [188, 189, 190]. These steps are called *Shapiro* steps in honor of *S. Shapiro* who first discovered them [188]. These steps exist due to photon induced tunneling. The probability of the tunneling increases when the injected electromagnetic wave is in resonance to the Josephon ac-current. Additionally, the direct microwave emission of superconducting junctions was detected [191].

The current transport can be understood within the framework of Andreev reflections (section 5.1.3). Figure 5.7 (b) shows the principle: An electron tunnels from the left superconductor to the right one and is Andreev reflected into a hole which travels back to the left

[6] The exact conversion of the applied voltage to an ac-current with a conversion factor that only uses physical constants (equation 5.14) is the basis for ultra-high precision voltage references. While the second is a SI-unit based on the transition between the two hyperfine levels of the ground state of the cesium 133 atom, frequencies can be generated with a relative error of $\approx 10^{-14}$ and thus voltage generators that have sub-nanovolt resolution in a -1 V $- +1$ V range are available using the ac-Josephson effect [187].

superconductor where it is again reflected into the same energy level as the first one. During each cycle two quasiparticles are transported across the junction which create a Cooper pair in the right and annihilate one in the left superconductor. Matching the phase shift (equation 5.11) at each Andreev reflection process for arbitrary short junctions, the result for coherent tunneling, i. e. for tunneling in which the overall phase shift in one cycle is $n \times 2\pi$, leads to the following Andreev bound-states in symmetric junctions [192, 193] (see figure 5.7 (a)):

$$E_{\pm}(\delta, \tau) = \pm\Delta\sqrt{1 - \tau \sin^2\left(\frac{\delta}{2}\right)}, \tag{5.17}$$

with τ as the transmission coefficient of the junction,

$$\tau = \frac{h}{2e^2}\frac{1}{R_T} = 12.906\ \mathrm{k\Omega}\frac{1}{R_T}. \tag{5.18}$$

The current can flow over these two Andreev bound-states in both directions and is given by the derivative of the bound state energy with respect to the phase difference between both superconductors:

$$I_{\pm}(\delta, \tau) = \varphi_0^{-1}\frac{dE_{\pm}(\delta, \tau)}{d\delta}. \tag{5.19}$$

The net supercurrent results from the imbalance of the population of the bound states which is driven by the external voltage source. For small transmission coefficients τ, the result for the supercurrent using equation 5.19 is the same as the equation Josephson found in weakly coupled superconductors (equation 5.13). Especially, the maximal current is given at the same phase shift ($\delta = \pm\pi/2$), while for $\tau \to 1$ the maximal supercurrent is reached at a phase shift $\delta = \pi$ between the electrodes (see figure 5.8).

5.2 First attempts of spin-selective measurements

Triggered by the results of the superlattice formation of the magnetic Ce adatoms on the Ag(111) surface (chapter 3) and the open question of magnetic interactions therein (see page 48), together with the effects we have observed in the previous chapter like the switching of single atoms (page 59 and following) and the Kondo effect (page 51 and following), we became interested in spin selective measurements.

Measurements which are able to detect the magnetic moment at the level of single atoms are of considerable general interest because they provide an additional channel of information which promises to give new insight into local magnetic interaction.

In STM measurements, the first attempts to detect magnetism on the nanometer scale were performed by detecting the polarization of the light emitted from the tunneling junction between a ferromagnetic Ni tip and a GaAs(110) surface [194] and by the use of CrO_2 coated ferromagnetic tips to detect the antiferromagnetic order of Cr(001) terraces [195]. Meanwhile, spin-polarized STM (SP-STM) measurements using ferromagnetic tips to detect magnetic structures were regularly performed by coating a nonmagnetic tip with a thin layer of Fe [196, 197, 198, 199] or Gd [200, 201]. While ferromagnetic tips have the disadvantage of influencing the sample by their stray field [196], tips coated with antiferromagnetic Cr are able to overcome this limitation [202, 203].

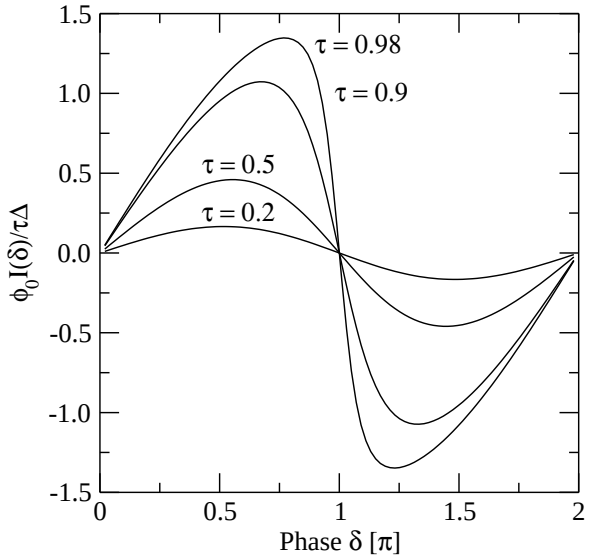

Figure 5.8: Current-phase relation for different transmissions τ. For relatively weak coupled junctions $\tau \lessapprox 0.5$ the relation is given by equation 5.14 and has its maximum at $\delta = \pi/2$. For $\tau \to 1$ the maximum shifts toward $\delta = \pi$.

Nevertheless, the spin signal is very small and not sufficient to detect the magnetic moment of single atoms. A different approach to get magnetic information relies on the strong influence of magnetism on superconductivity. It is well known that even small amounts of magnetic impurities can significantly reduce the critical temperature of a superconductor and even destroy superconductivity [204, 173], while non-magnetic impurities do not influence the superconductivity in a classical s-wave superconductor much [205].[7] Experiments using a Nb(110) sample and a normal conducting tip have indeed shown different spectral features when the data were taken on top of magnetic Mn and Gd adatoms while the spectrum remained unchanged on top of non-magnetic Ag adatoms [157]. The results could be understood by assuming an exchange interaction between the localized spin of the adatom and the conduction electrons of the sample which leads to spin-polarized scattering states in the gap [206].

5.2.1 Direct influence on the superconducting gap

A more interesting method than the one mentioned above is to exchange sample and tip. The use of a superconducting tip as probe for magnetic atoms on a non-magnetic surface is promising as we pointed out in the beginning of this section. First measurements of Gd trimers on Cu(100) with a Nb tip show indeed an influence of the adsorbate on the spectrum [159].

In the experiments presented here, we used a Nb tip prepared by etching (described in section 5.1.1) which showed a BCS-like gap when measured at $T = 4.7$ K against a

[7] In high-T_C superconductors with their complex crystal structure even small amounts of nonmagnetic impurities can drastically change the superconducting order parameter.

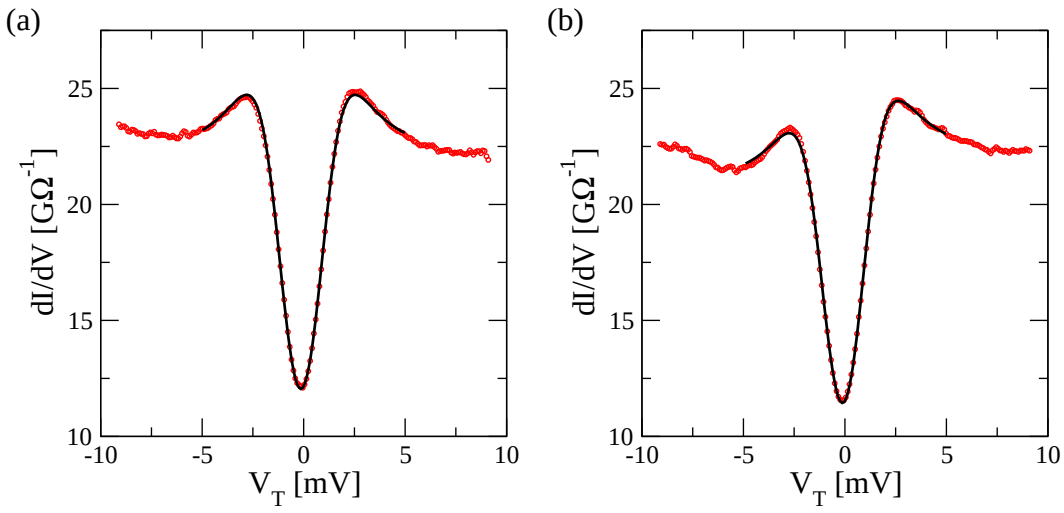

Figure 5.9: (a): Spectrum of the Nb tip measured on the bare Ag(100) surface (dots) at $T = 4.7$ K and $R_T = 45$ MΩ. The black line is a least-square fit using the BCS-equation including broadening due to the temperature and modulation. The results of the fit are $T = 4.74$ K, $\Delta = 1.24$ meV, and $\delta = 5$ μeV (b): Spectrum obtained with the same tip on top of a Co adatom on Ag(100) (dots). The black line is a least-square fit to the convolution of BCS and Fano function including broadening effects and resulting in $T = 4.71$ K, $\Delta = 1.20$ meV, $\delta = 5$ μeV, $q = 1.2$, $E_K = 1.78$ meV, and $\Gamma = 3.25$ meV. The modulation voltage was $V_m = 0.25$ meV for both measurements.

Ag(100) sample as plotted with red dots in figure 5.9 (a). The black line is a least-square fit using equation 2.9 (page 8) with ρ_s as constant and ρ_t given by the quasiparticle excitation spectrum of equation 5.6. The best-fit results in a BCS gap of $\Delta = 1.24$ meV, $\delta = 5$ μeV, and a temperature of $T = 4.74$ K which is in excellent agreement with the temperature of $T = 4.7$ K, measured with a rhodium-iron (Rh-Fe) resistor thermometer in a four-terminal measurement configuration.

After dosing some Co adatoms from a thoroughly degassed tungsten filament on the cold Ag(100) sample, we were able to compare the above spectrum with one taken on top of a single Co adatom on the Ag(100) surface. We ensured that the probed Co atoms had at least a next neighbor distance of 10 nm and thus do not interact with each other by using only a very low coverage.

The spectra measured on top of the Co adatoms show an asymmetry in the peak height at the superconducting gap edges ($eV_T \approx \pm\Delta$) as plotted in figure 5.9 (b) (red dots). Since it is known that single Co adatoms on Ag(100) show a Fano-like dip around E_F due to the Kondo-effect [120] (see figure 4.5 in chapter 4.1.1), we performed a least-square fit using the convolution of equation 5.6 for the LDOS of the tip and the Fano equation 4.3 of chapter 4.1.1 for the LDOS of the Co/Ag(100) sample system to describe the obtained spectrum following equation 2.9. The results of the homemade fitting routine, which included broadening due to the finite temperature as well as the modulation voltage (see chapter 2.6), are plotted as a black line in figure 5.9 (b). The Kondo temperature (see equation 4.1) of our fit results in $T_K = 38 \pm 5$ K, which is in good agreement with the value of 41 ± 5 K observed

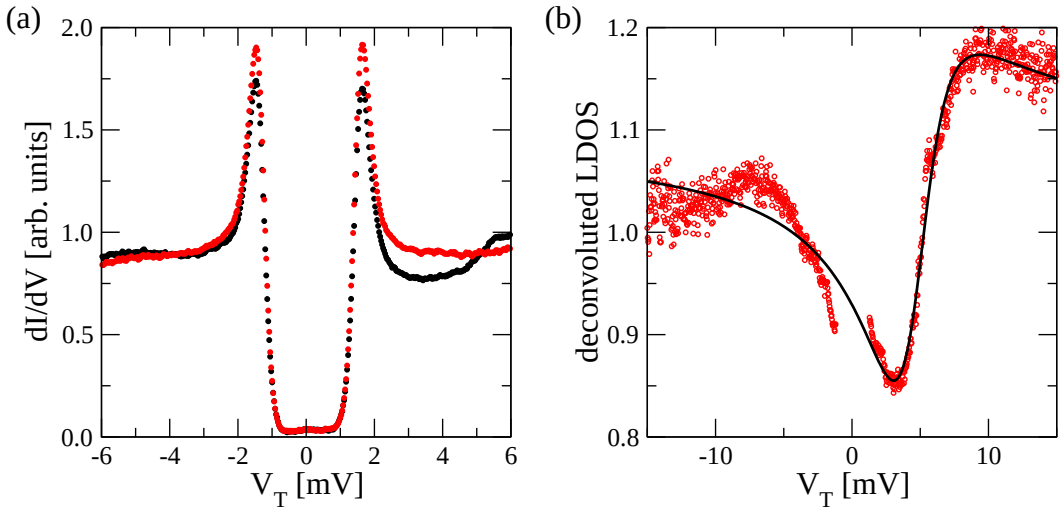

Figure 5.10: (a): Spectra of the Nb tip measured on the bare Cu(111) surface (red dots) and on top of an adsorbed Co adatom (black dots) at $T = 0.6$ K, $I_T = 3$ nA, and $V_m = 71$ μV. (b): After deconvolution an asymmetric dip is detected in the spectrum (red dots) which was successfully fitted with the Fano function using the parameters $q = 0.60$, $E_K = 4.7$ meV, and $\Gamma = 2.8$ meV in good agreement with [47, 59]. The discontinuity around E_F is due to limitations of the deconvolution inside the gap.

in earlier measurements [120].

Additionally, we detect a slight decrease of approximatively -3% in the quasiparticle gap width on top of the Co adatom compared to the bare Ag(100) surface ($\Delta = 1.20$ meV compared to $\Delta = 1.24$ meV) which might be due to a direct interaction between the magnetic moment of the single Co adatom and the pairing energy of the superconducting tip.

Unfortunately, this change in the gap width of the fitting results is not significant at a base temperature of $T = 5$ K, i. e. $k_B T = 0.43$ meV. Therefore, to answer the question whether the magnetic moment of the single Co adatom has influenced the superconductivity of the Nb tip, measurements at lower temperature are necessary.

We repeated the experiment at the IBM lab at a base temperature of only $T = 0.6$ K with single Co adatoms on a Cu(111) surface and a superconducting tip by attaching a Nb microcrystal on an Ir tip (see section 5.1.1). The results, plotted in figure 5.10 (a), show a much higher resolution due to the lower temperature (0.6 K compared to 4.7 K) and the smaller modulation voltage. The red curve is a BCS-like dI/dV spectrum of the tip measured on the clean Cu(111) surface showing a quasiparticle gap width of $\Delta = 1.27$ meV. Placing the same tip over an isolated Co adatom the black curve is recorded revealing a similar asymmetry as that seen in figure 5.9 (b) and a change of the LDOS in the quasiparticle spectum at $eV > E_F + \Delta$. We calculate the LDOS of the Co/Cu(111) sample by performing a deconvolution using the pure BCS-like spectrum (red dots in figure 5.10 (a)) and the Co/Cu(111) spectrum obtained with the Nb tip (black dots). The result is plotted in figure 5.10 (b) (red dots) and shows an asymmetric dip around E_F. A least-square fit (black line) using the Fano equation 4.3 yields a form factor of $q = 0.60$ and a Kondo-temperature of $T_K = 32 \pm 5$ K. Even if the obtained T_K is lower than the one detected in previous measure-

ments [47, 59], the overall form of the spectrum agrees well with the structure found in the literature and the data presented in chapter 4.1.1 (Figure 4.6). Furthermore, we do not detect any influence of the presence of the Co adatom on the gap width in the superconducting tip.

Similar results were obtained for all tunneling currents in the range of $I_T = 50$ pA to $I_T = 30$ nA (i. e. $670\,\text{k}\Omega \leq R_T \leq 400\,\text{M}\Omega$), whereas STS could not be obtained at higher currents due to tip induced motions of the Co adatom [147, 50]. In particular, no reduction of the superconducting gap width was detected even when the coupling between the wavefunctions of tip and sample was increased, i. e. at higher tunneling current.

To summarize, compared to previous measurements on Mn trimers on Ag(100) [159], the magnetic moment of a single Co adatom hosted on Ag(100) or Cu(111) does not change the gap in a superconducting tip and the previously observed small change in Δ might be due to limitations in the fitting procedure. The reason why this influence is undetectable might be due to the fact that the magnetic moment of the Co adatom is screened by the electrons of the metal which is manifested in the observed Kondo-resonance around E_F. Thus, the relatively weak-coupled tip is not affected by the atomic moment. Indeed, as it will be shown later in this chapter (section 5.5), Co adatoms directly supported on a superconducting surface show a strong influence on the gap structure.

5.2.2 Spin polarized tunneling with superconducting tips

A different approach for performing spin selective measurements with superconducting tips was proposed by *R. Meservey* [207]. His idea is based on the experimentally found splitting of the quasiparticle excitation spectum in thin film measurements between superconducting aluminum and a normal conducting metal separated by a very thin Al_2O_3 layer when a magnetic field is applied [208, 209, 210, 211]. While in the absence of a magnetic field the quasiparticle excitation spectrum is given by equation 5.6, a magnetic field will act on the spins of the electrons as well as on their orbits. If the superconducting film in thin film measurements is thin enough, the effect of the field on the electron orbits will be negligible compared with the effect on the electron spins if the spin-orbit coupling is sufficiently small [208]. In this case, the quasiparticle spectrum will be split for spin-up and spin-down electrons by an energy of twice the *Zeeman* energy, $E = g\mu_B B$, with $g \approx 2$ as the gyromagnetic factor of the free electron, $\mu_B = e\hbar/2m_e = 9.28 \times 10^{-24}$ J/T$= 57.9$ μeV/T as the Bohr magneton, and B as the applied field. The composed spectrum has thus a theoretical form as shown in figure 5.11 (a), revealing the possibility of getting pure spin-selective currents.

Indeed, it was shown that the tunneling probabilities for spin-up and spin-down electrons are not equal when the second electrode is made of a ferromagnetic material such as Ni, Fe, Co, or Gd [209, 210] and that in these cases, electrons with the spin direction of the majority charge carriers in the ferromagnet dominate the tunneling current.

Unfortunately, strong spin-orbit coupling inhibits spin selective measurements with Nb tips, as seen in the measurements taken on a clean Cu(111) surface and shown in figure 5.11 (b), where dI/dV curves at different magnetic fields applied in plane to the sample surface and ranging from $B = 0 - 4$ T are plotted.[8] A spin-splitting, as schematically

[8] Remarkably, the Nb microcrystal shows a critical magnetic field of $B_C \approx 4$ T, much higher than the bulk value of $B_C = 198$ mT [136]. This enormous increase can be understood by the confinement of the superconducting phase into a very small region at the apex of the tip.

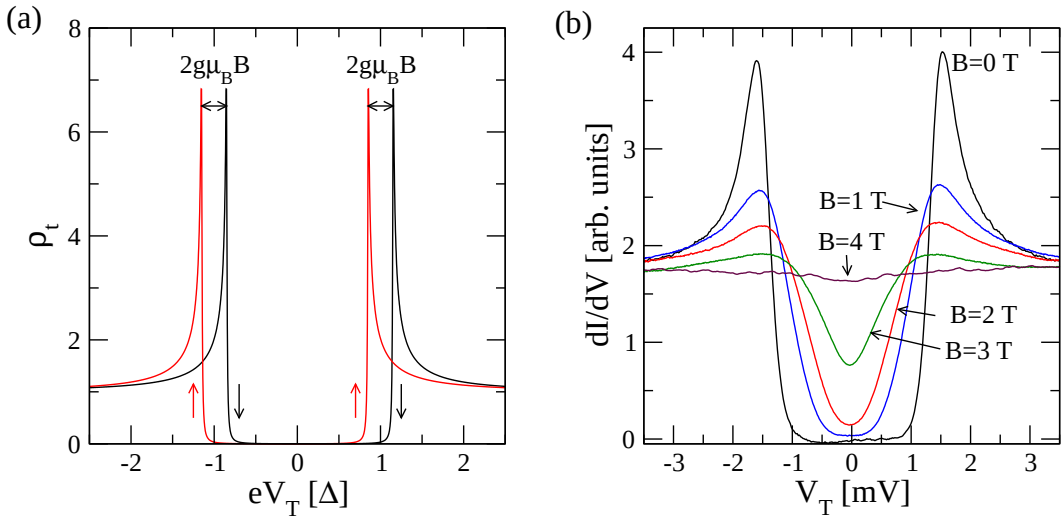

Figure 5.11: (a): Theoretical spectra for the spin up and spin down quasiparticles of a superconducting tip in a magnetic field B without spin-orbit coupling in the zero temperature limit. The degeneration of the spin is removed leading to two curves for each spin direction separated by an energy of $2\mu_B B$. (b): Spectra of a superconducting Nb tip in a magnetic field of $B = 0 - 4$ T measured at $T = 0.6$ K, $I_T = 2$ nA, and $V_m = 71$ μV. Due to spin-orbit coupling the quasiparticle spectrum is not simply split. The interaction between the orbital and spin moment in the magnetic field leads to a broadening of the spectrum.

drawn in figure 5.11 (a), is not obtained but instead an overall broadening that cannot be assigned to the different spin directions.

This result can be understood by referring to the theory of *A. A. Abrikosov* and *L. P. Gor'kov*. They suggested that spin-orbit coupling should increase approximately as Z^4, where Z is the atomic number of the superconducting element [212, 211]. Thus, Nb with its relatively high atomic number of $Z = 41$ (compared to Al, $Z = 13$) is not a good candidate for these kind of measurements. But Al, which was intensively used in thin film measurements as shown before, is difficult to use as tip material because of its softness which is in conflict with the need for sharp and stable tips in STM experiments. Additionally, the critical temperature of bulk Al is only 1.1 K, which is only by a factor of two higher than the minimal attainable temperature of the STM used and would therefore lead to significant broadening due to thermally excited quasiparticle tunneling similar to the results of Nb at $T = 4.7$ K (see figure 5.10 (a)). It might be possible to overcome these limitations by using stable normal conducting tips coated with an ultra-thin layer of aluminum which has an increased critical temperature of about $T_C \approx 2.5$ K for a layer thickness of 4 nm [207].

Other materials with lower spin-orbit coupling are being discussed for use in STM. Vanadium, with a critical temperature of $T_C = 5.4$ K [136], and its compounds, for example VN, VTi, V_3Ga, and V_3Si, might be good candidates [207]. V and VN ($T_C = 8.2$ K [213]) should show significantly reduced spin-orbit coupling due to their smaller atomic numbers (vanadium: $Z = 23$, nitrogen: $Z = 7$) and were found to show spin splitting in magnetic fields [214]. Experiments using V_3Si as tip material might also be interesting. V_3Si is

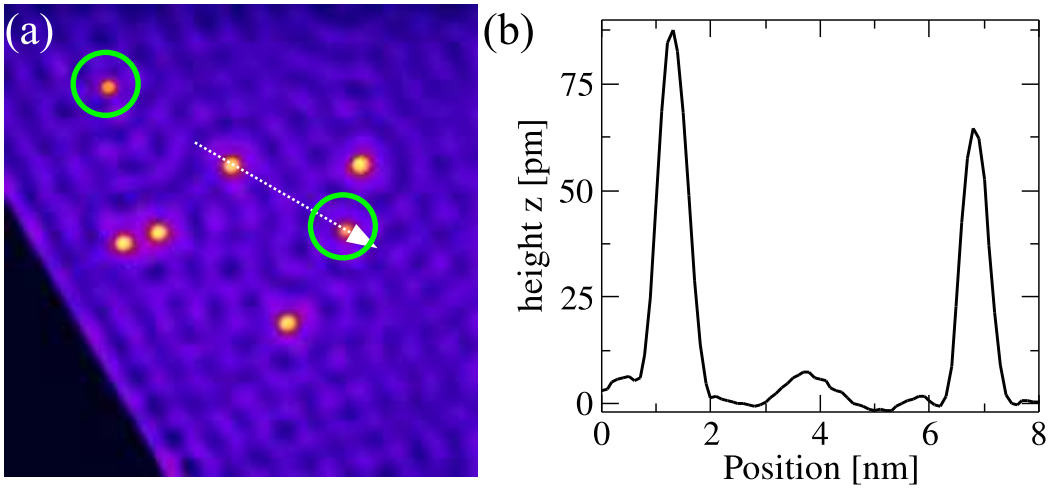

Figure 5.12: (a): Image of individual Co adatoms (bright spots) on top of a Cu(111) surface after dosing of hydrogen on the cold sample. Image parameters: 20×20 nm^2, $V_T = -20$ mV, $I_T = 1$ nA, $T = 0.6$ K. (b): The height profile along the arrow in (a) show that two different species (marked with circles) with different apparent heights are observed.

known to be a material with a relatively high critical temperature of 17.5 K [213], and thus would allow to perform measurements even at 5 K.

5.3 Influence of hydrogen on single Co atoms

In this section we will discuss the enormous change in the dI/dV spectrum of single Co adatoms supported on a clean Cu(111) surface when additionally hydrogen is dosed and attached to the Co adatoms.

Using a clean Cu(111) sample on which a low quantity of Co adatom were deposited, we dosed atomic and molecular hydrogen from a heated tungsten filament. The filament, which was previously used in a Mn evaporator, had a direct view onto the cold sample surface. By placing the filament directly over a mass spectrometer we checked that the Mn source was exhausted and that indeed only hydrogen, which originate from hydrogen incorporations in the tungsten wire, was evaporated.

A constant-current topographic image of the Cu(111) surface after dosing hydrogen with the filament is shown in figure 5.12 (a). On top of the 20×20 nm^2 large detail of the Cu(111) surface, seven adsorbates are visible as protrusions. While the unchanged Co adatoms have an apparent height of about 90 pm, two objects in the image, which are indicated by green circles, have a lower apparent height of only ≈ 65 pm as seen in the line profile (figure 5.12 (b)), which was taken along the arrow in figure 5.12 (a). Additional visible periodic height modulations of a few pm amplitude are due to interferences between surface state electrons, which are reflected at the step edge, and at the adsorbates, leading to standing wave patterns and modulations in the LDOS (see chapter 3.1.2).

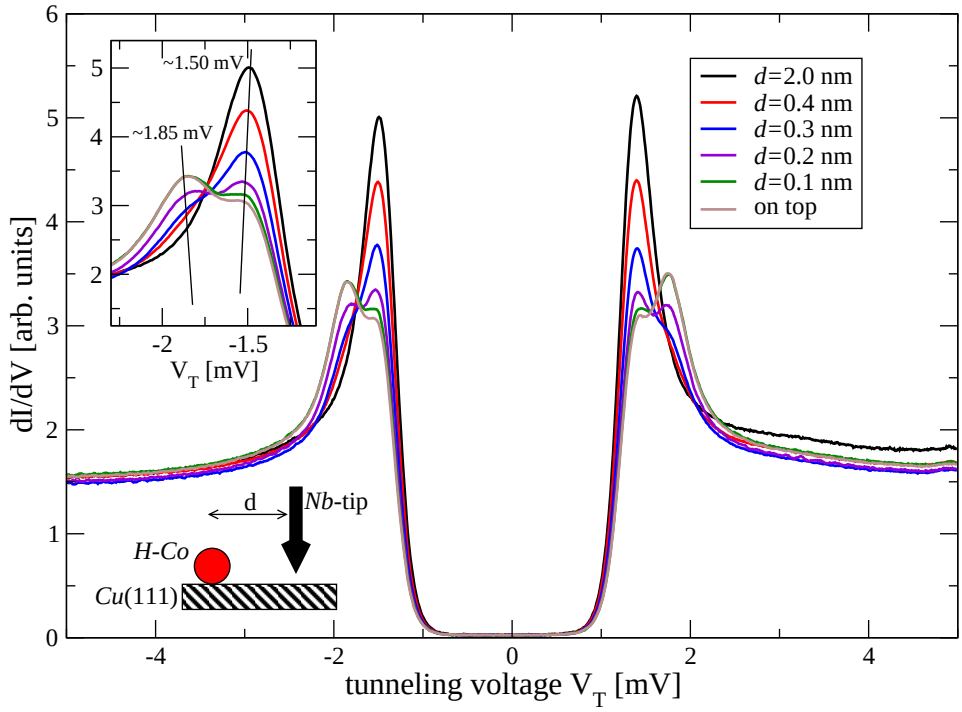

Figure 5.13: Spectra taken at $T = 0.6$ K and $B = 0$ using a superconducting Nb tip placed at different lateral distances d from the hydrogen-attached Co adatom on Cu(111) (see lower inset). The upper inset shows an enlargement of the left edge of the quasiparticle excitation spectra and reveals two distinct peaks at $\approx$ 1.50 and $\approx$ 1.85 meV. Setpoint parameters before performing the dI/dV measurements: $V_T = -5$ mV, $I_T = 2$ nA, $V_m = 71$ μV.

Using the superconducting Nb tip as probe in spectroscopic measurements on the objects with higher apparent height reveals spectra similar to the one displayed with black dots in figure 5.10 (a) which allows us to identify them as single Co adatoms. Surprisingly, spectra obtained on the lower species found in figure 5.12 have a completely different structure. Typical dI/dV spectra of these, presumably with hydrogen-attached Co adatoms, are displayed in figure 5.13. They do not show the characteristic asymmetry of the signal strength at the quasiparticle gap edge, which was identified by deconvolution (see figure 5.10 (b)) to have its origin in a Fano dip around E_F due to spin-flip scattering of the Cu(111) electrons on the magnetic moment of the 3d electron of the Co adatom.

Instead of a Fano dip, we detect a splitting of the superconducting quasiparticle excitation spectrum similar to the expected splitting in a magnetic field as discussed in section 5.2.2 and schematically shown in figure 5.11 (a).[9] The effect is strongly localized on top of the adsorbate and diminishes rapidly when the distance between the point where the spectrum is obtained and the center of gravity of the adsorbate is increased. Already at a lateral distance of 0.4 nm from the center of the adatom, the unperturbed quasiparticle spectrum of the superconducting tip is mainly recovered.

[9] But here we have to be reminded that the externally applied magnetic field was set to zero, although an external magnetic field is the essential condition for the Zeeman splitting described in section 5.2.2.

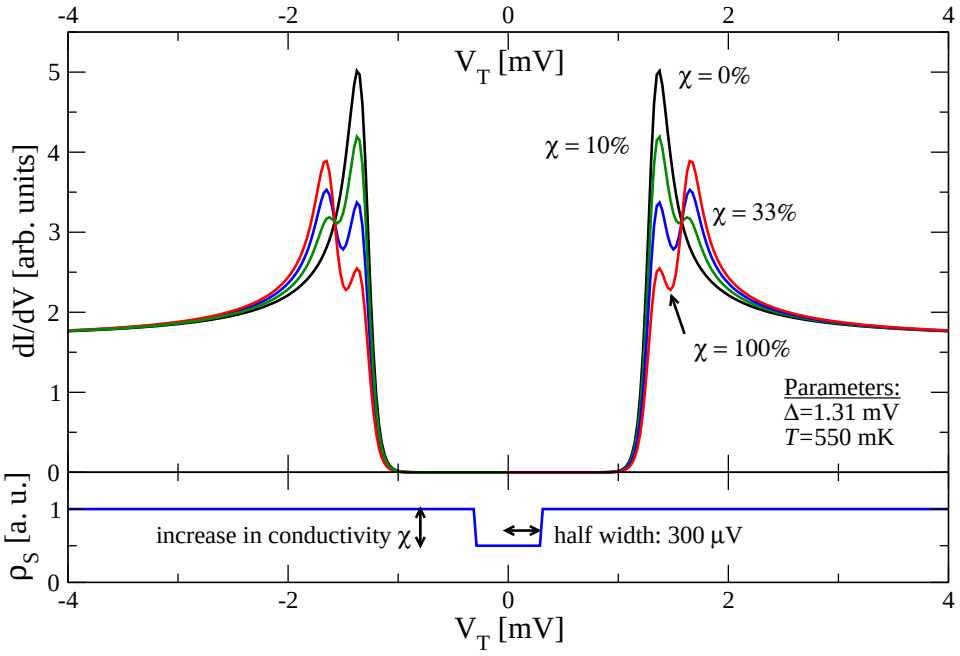

Figure 5.14: Simulation of spectra at $T = 550$ mK assuming tunneling between a superconducting tip ($\Delta = 1.31$ meV) and a sample with a vibrational state at an energy of 300 μeV resulting in a ρ_s as seen in the lower part (see chapter 2.3.3). Depending on the dip depth χ the spectrum of figure 5.13 can be reproduced.

The observed spectra can be understood by assuming an inelastic tunneling channel on the sample side of the tunneling junction. As pointed out in chapter 2.3.3, this additional channel induces a step like increase in the differential conductance when the kinetic energy of the tunneling electrons exceeds the threshhold given by the mode energy of the inelastic process, i. e. $|eV_T| \geq E_i$, and thus the electrons can tunnel elastically as well as inelastically.

A simulation between a superconducting tip and a sample system with an inelastic tunneling channel which has its excitation energy at $E_i = 300$ μeV is shown in figure 5.14. The calculated spectra show the same splitting as observed in the experiment. A detailed analysis on several hydrogen-attached Co adatoms results in an energy where the inelastic contribution begins of $E_i = 325 \pm 50$ μeV.[10] The increase in conductivity χ at energies greater than E_i due to the additional inelastic channel is, with approximately 40%, relatively large.

To get further insight into the physical process originating in the observed spectral feature, we performed spectroscopic measurements by varying the tunneling current in a large range, from 50 pA to 10 nA, corresponding to a tunneling resistance between 100 MΩ and 500 kΩ. The different spectra show, apart from reduced noise at higher I_T, no change in the splitting, i. e. in the mode energy E_i or in the depth χ, as seen in figure 5.15. Spectra

[10] Here we want to emphasize the high energy resolution of the superconducting tip. Even at $T = 0.6K$ and a modulation voltage of $V_m = 71$ μV resulting in a broadening of ≈ 280 μV due to the temperature and ≈ 160 μV due to the modulation (see chapter 2.3.3) the IETS is clearly detected showing the advantage in using superconducting tips as discussed in chapter 2.3.5

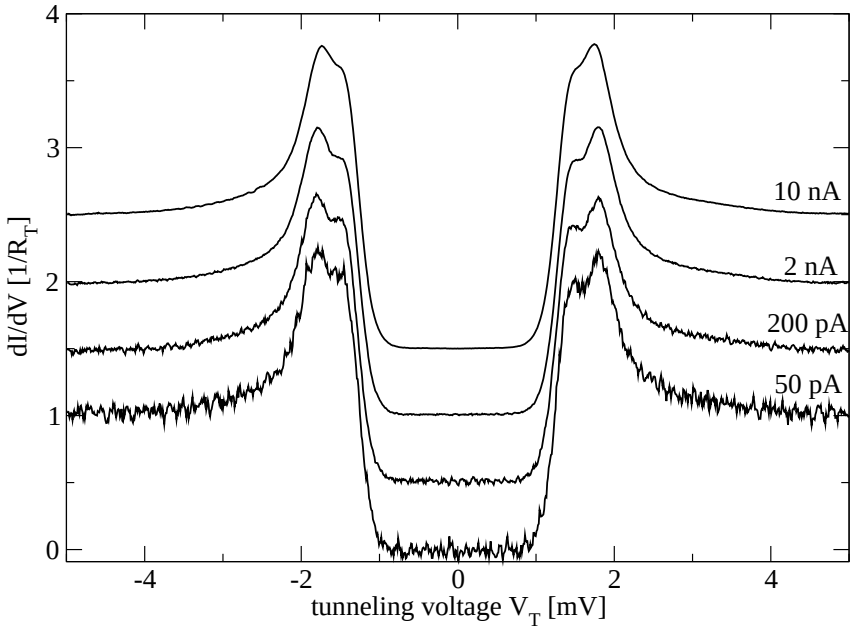

Figure 5.15: Spectra measured on top of a hydrogen-attached Co adatom obtained at different setpoint currents I_T before the feedback loop was opened. The curves are rescaled to $1/R_T$ with R_T as the tunneling resistivity V_T/I_T determined outside the gap at $V_T = -5$ mV. They are additionally vertically displaced in respect to each other for better visualization.

at higher tunneling current could not be measured because a further decrease of the tunneling resistance results in tip induced movements of the adatom [147, 50]. By performing such movements we were always able to transform the object back to ordinary Co adatoms which then recovered the initial apparent height and spectrum, as discussed in the beginning of the section. This observation can be interpreted as a tip-induced detachment of the hydrogen similar to experiments using acetylene on Cu(001) [215] or cobalt phthalocyanine on Au(111) [122].

To ensure that the spectral features are indeed due to an inelastic tunneling channel, we applied a magnetic field in plane to the sample surface to drive the tip into the normal conducting region. A field of at least $B = 4$ T has to be used to suppress the superconductivity in the Nb microcrystal of the tip as shown in figure 5.11 (b). Thus, spectra were measured with an applied magnetic field in the range of $B = 4 - 7$ T, which are plotted in figure 5.16. A step-like increase in the dI/dV signal, broadened by the finite temperature and the modulation voltage, is observed when the tunneling voltage exceeds $\pm E_i/e$ as expected for an inelastic tunneling process. A fit to the obtained data using equation 2.24 of chapter 2.3.3 results in excellent agreeing curves shown as black lines. The fitting results are listed in the table on page 94 and plotted in figure 5.18. They show a surprising linear dependence of the excitation energy E_i with the applied magnetic field.

To this end, we performed local tunneling spectroscopy only with a superconducting Nb tip and a metallic filament as hydrogen source. In an additionally performed control

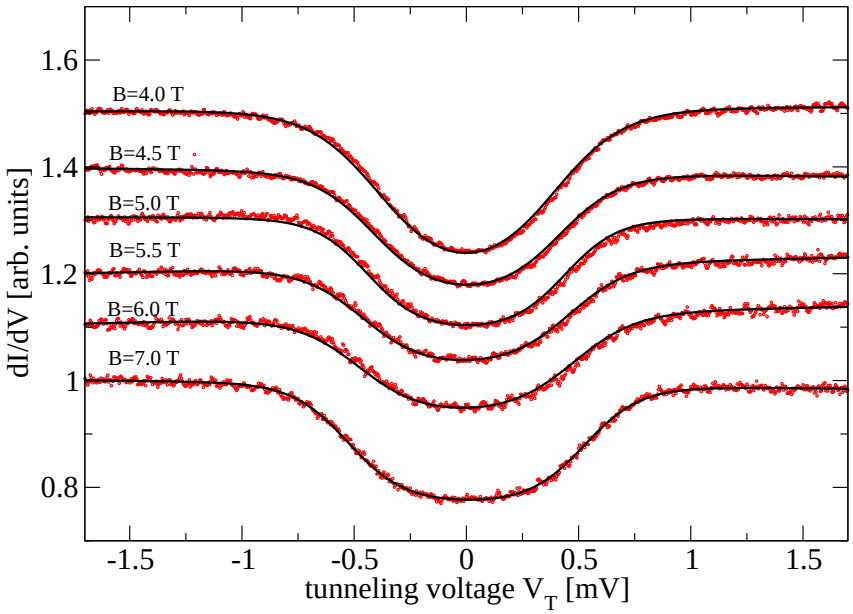

Figure 5.16: Spectra taken on top of a hydrogen-attached Co adatom on Cu(111) measured with a Nb tip which was driven into the normal conducting state by applying a magnetic field of $B = 4 - 7$ T thereby exceeding the critical field of the Nb microcrystal ($V_T = -2$ mV, $I_T = 1$ nA, $V_m = 28$ μV, $T = 0.55$ K). The IETS equation 2.24 of chapter 2.3.3 can be fitted (lines) in excellent agreement to the data (dots).

experiment, we have found similar results using H_2 gas as a hydrogen source and a normal conducting tip. We used a newly cleaned Cu(111) sample onto which a low coverage of Co adatoms were dosed. Then, we induced pure H_2 gas in the room temperature UHV chamber by a microvalve leading to a partial pressure of $p \approx 1 \times 10^{-7}$ mbar for about 40 minutes. The shutter to the low temperature stage was opened during this time to allow the H_2 to arrive at the sample surface. STM images measured with a normal conducting Ir tip after the exposure show clear signs of hydrogen contamination. We detect ubiquitous noise which appears in images taken at higher tunneling voltages, similar to recent measurements [43], and a halo-like shape around the Co adatoms as seen in figure 5.17 (a).

Similar to the experiment described above where a filament was used as a hydrogen source, we detected that a small quantity of the Co adatoms onto which hydrogen was bound appear as protrusions in STM images with lower apparent height compared to the pure Co adatoms. The hydrogen could be detached from the Co adatom by tunneling with a high current exactly as in the earlier experiment. Tunneling spectra obtained on top of the hydrogen-attached Co adatoms reveal the same IETS features as observed with the superconducting tip in high magnetic fields, as seen in figure 5.17 (right). The results of a least-square fit using equation 2.24 for for the spectra here and for the experiments are summarized in table 5.3 and in figure 5.18.

The resulting values for E_i show a non negligible dependence on the applied external magnetic field. These observations lead to the assumption that the inelastic tunneling channel has its origin in a spin-flip process. As it was recently shown, single spin-flip spec-

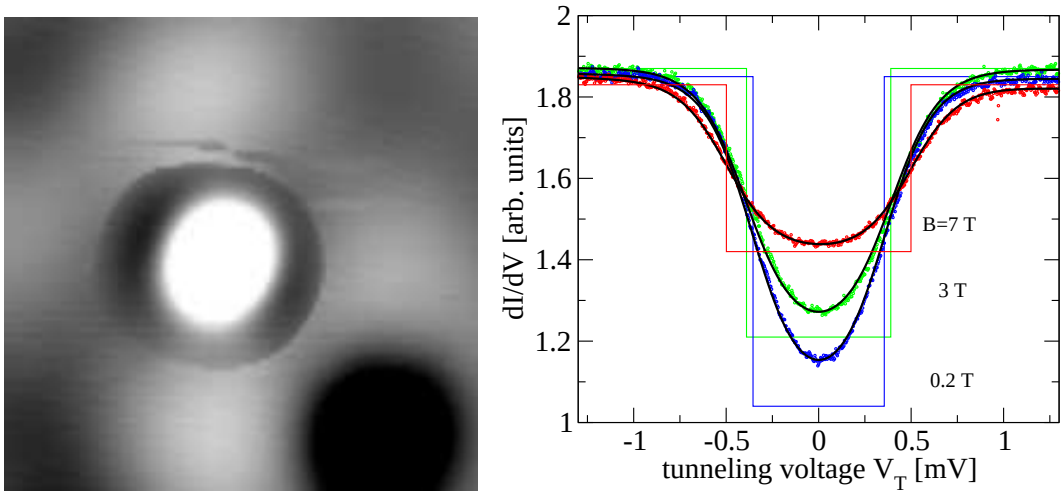

Figure 5.17: Left: Image of a single Co adatom (bright spot) on a Cu(111) surface after dosing H_2. A sombrero like circular structure is visible around the adatom (image size: 3×3 nm^2, $V_T = 5$ mV, $I_T = 1$ nA). Right: Spectra obtained with a normal conducting Ir tip on top of a hydrogen-attached Co adatom at different magnetic fields ($V_T = -2$ mV, $I_T = 1$ nA, $V_m = 28$ μV, $T = 0.55$ K). The lines are fits to the data (dots) using equation 2.24. The full colored lines are representations of the IETS gap idealized for $T = 0$ K and no lifetime broadening.

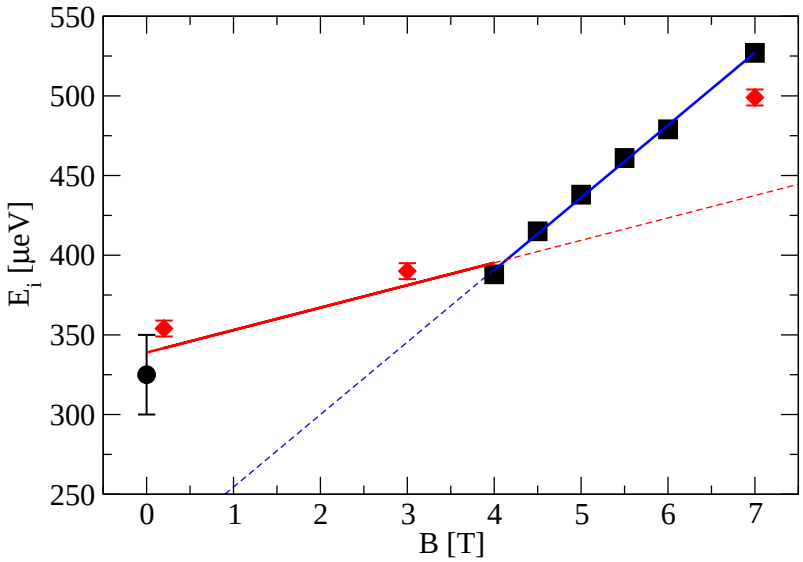

Figure 5.18: Graphical representation of the observed E_i. Circle: averaged value from measurements as shown in figure 5.13; squares: data taken from figure 5.16; diamonds: data taken from figure 5.17. Blue line: linear regression using data from figure 5.16 ($B \geq 4$ T); red line: linear regression using all values with $B \leq 4$ T.

B [T]	E_i [μeV]*	χ	T_{fit} [K]	
0.0	325 ± 25	$\approx 40\%$	–	superconducting tip, see figure 5.13
4.0	388 ± 5	32%	0.63 ± 0.10	superconducting tip, see figure 5.16
4.5	415 ± 5	23%	0.54 ± 0.10	
5.0	438 ± 5	19%	0.50 ± 0.10	
5.5	461 ± 5	19%	0.54 ± 0.10	
6.0	479 ± 5	19%	0.58 ± 0.10	
7.0	527 ± 5	22%	0.50 ± 0.10	
0.2	354 ± 5	78%	0.52 ± 0.10	normal tip, see figure 5.17 (right)
3.0	390 ± 5	55%	0.53 ± 0.10	
7.0	499 ± 5	28%	0.51 ± 0.10	

* The uncertainty in the determination of E_i is mainly due to the finite stability of the voltage generator for the tunneling voltage V_T. Except for the first line, the error of the fitting is only about ± 2 μeV.

Table 5.1: Summary of the data obtained on with hydrogen attached Co adatom on Cu(111).

troscopy can be performed with STM resulting in spectra similar to the presented ones [40]. The spin-flip process can therefore only occur if the tunneling electrons overcome the Zeeman splitting energy with their kinetic energy and exchange their spin momentum with one 3d electron of the Co adatom leaving it in an excited spin state.

Taking only the data obtained with the superconducting tip at fields ≥ 4T, as shown in figure 5.16, and performing a linear regression of the form:

$$E_i = E_0 + g\mu_B B_{\mathrm{ext}}, \tag{5.20}$$

with B_{ext} as the externally applied magnetic field, g as the gyromagnetic factor, and μ_B as the Bohr magneton, results in $g = 0.79 \pm 0.02$ and $E_0 = (209 \pm 8)$ μeV (blue line in figure 5.18). The form of the function is uncommon, because the Zeeman energy, $E_Z = g\mu_B B_{\mathrm{ext}}$, increases linearly with the applied field without having a zero field splitting term E_0. Additionally, the result of E_0 does not match with the splitting observed in measurements at $B = 0$ (figure 5.13 and blue curve in 5.17). For the data obtained at $B \leq 4$ T, a least-square fit using equation 5.20 results in $g' = 0.24 \pm 0.08$ and $E_0' = (339 \pm 12)$ μeV which is shown as a red line in figure 5.18.

The results of the above presented experiments are ambiguous. As we have seen, the dI/dV spectra of hydrogen-attached single Co adatoms differ drastically from the spectra obtained on pure Co adatoms. While the latter show a well known Fano-like lineshape due to the Kondo screening of the magnetic moment, the hydrogen-attached Co adatoms show a IETS-like gap feature with an energy in zero field of $E_i \approx 340$ μeV.[11]

[11] One could imagine that this dip is due to the Kondo effect with a strongly reduced Kondo temperature T_K and a symmetrical Lorentz profile, i. e. a Fano factor of $q = 0$. But an additionally performed fit on the data at $B = 0.2$ T (figure 5.17) using the Voigt function: $y = a_0 \int \frac{\exp(-t^2)}{a_3^2 + ((x-a_1)/a_2) - t)^2} dt / \int \frac{\exp(-t^2)}{a_3^2 + t^2} dt$, to take into account the thermal broadening and the Lorentzian of the Kondo resonance, results in a higher discordance with the data than the IETS fit and in an Lorentzian width of almost zero (≤ 1 neV !).

This energy is very small compared to vibronic excitation energies, which are usually at least one order of magnitude higher. Additionally, the increase in the differential conductance at $|eV_T| \geq E_i$ is, with 40% and 78% (see table 5.3), much higher than for vibronic excitations where χ reaches usually only a view tenth of a percent [42, 35, 36].

Applying a magnetic field yields an increase of the characteristic energy E_i, reminiscent of spin-flip spectroscopy. As long as the magnetic field is relative small ($B \leq 4$ T) the corresponding slope, i. e. the g factor, is very small. For higher magnetic fields, the slope increases resulting in a g factor of 0.79 ± 0.02, much smaller than the gyromagnetic factor for the free electron of $g_0 = 2.0023$. The small value might be due to influences originating from the local environment. In planar tunneling junctions, factors of $g = 1.1$ and $g = 2.6$ have been found [216] and were shown to reflect a complex interaction between Zeeman spin-flip scattering as well as Kondo screening. In the measurements with a magnetic field of $B \geq 4$ T, the observed jump in the conductivity at $\pm E_i$ is with $\chi \approx 20\%$ (see table 5.3) similar to the increase in spin-flip measurements on single Mn adatoms [40].

The edges of the step in the dI/dV signal are broadened due to the modulation voltage, the temperature, and the finite lifetime of the excited spin-state. The results of T_{fit} as listed in table 5.3 have an average value of $\overline{T}_{\mathrm{fit}} = 0.54$ K, which agrees essentially with the base temperature of $T = 0.55$ K, and limits the finite lifetime broadening to $\Delta E_{\mathrm{lifetime}} \lessapprox 0.1\ \mathrm{K}/k_B$. Thus, we find a lower limit for the lifetime of spin-flip excitation of $\tau \geq 80$ fs.

To summarize, we have to admit that the origin of the observed effect is unclear. It might be a superposition of at least two different effects which are necessary to explain the curve shown in figure 5.18. The role of the hydrogen is therefore mostly unknown, except that its presence strongly influences the magnetic attributes of the Co adatoms which are reflected in the spectroscopic measurements. Further measurements are recommended to analyze the system in greater detail which was not possible due to the time limitations of the three months stay at IBM.

5.4 Novel subgap structure in asymmetric superconducting tunnel junctions

For more than 40 years the subgap structure of superconducting–insulating–superconducting (SIS) tunnel junctions has been in the focus of experimental and theoretical investigations [217, 218]. Due to the difficulties of planar junctions to clearly manifest Andreev reflections, break-junction experiments were used extensively [183, 219, 220, 221]. In break-junction experiments, the coupling between both superconductors is varied continuously, a necessity for a thorough understanding of Andreev reflections [222, 223, 224, 225] and Josephson supercurrent [166]. However, break-junctions are thus far limited to *symmetric* tunnel junctions, in which the superconductors have equal gap energies.

On the other hand, *asymmetric* tunnel junctions are of interest because they are predicted to show new spectroscopic features due to the loss and the opening of new Andreev reflection processes [226, 227]. Asymmetric tunnel junctions can be realized by STM techniques by using different gaps in the tip and sample, and the coupling between the superconductors can be varied by changing the tip-sample distance [185, 160, 186]. STM techniques have the additional advantage that they may be extended to study *locally* how the presence of magnetic structures as small as a magnetic adatom in the SIS junction influences the multi-

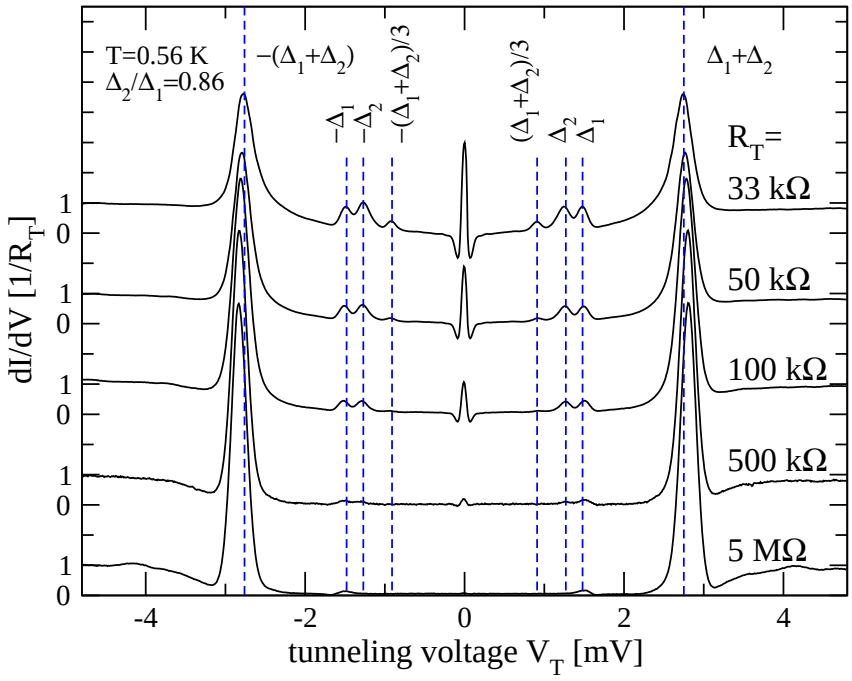

Figure 5.19: dI/dV spectra observed at $T = 0.56$ K between a superconducting sample and tip with nearly equal gaps ($\Delta_1 = 1.47$ meV, $\Delta_2 = 1.27$ meV) showing Andreev reflections for different junction resistances. The peak evolving at $V_T = 0$ is due to the Josephson supercurrent. The dotted lines are a guide for the eye marking characteristic features in the spectra. The spectra are shifted vertically with respect to each other for better visibility.

ple Andreev reflections [228] as we will discuss in section 5.5. So far, however, STM has only been used to detect Andreev reflections in symmetric tunnel junctions [156, 186].

Here we present SIS measurements on asymmetric niobium tunnel junctions made by controlling the size of a superconducting microcrystal attached to a normal conducting tip as described in section 5.1.1. Due to finite size effects [229, 230] of the tip-attached microcrystal, its superconducting energy gap is reduced with respect to the bulk sample value. Novel peaks in the dI/dV spectra at energies of $\pm|\Delta_1 - \Delta_2|$ arise at low junction resistances when the difference between Δ_1 and Δ_2 is sufficiently large. This surprising spectral feature is not due to thermal excitations of the quasi-particles but is explained within the framework of Andreev scattering (see section 5.1.3) and the concept of full counting statistics [231, 232].

Figure 5.19 shows a set of dI/dV measurements using a tip with a superconducting gap of $\Delta_2 = 1.27$ meV at $T = 0.56$ K and different values of the nominal junction resistance, R_T, which were determined outside the gap at $V_T = 5$ mV. By successively reducing the resistance and thereby increasing the coupling between the two superconductors, we observe the evolution of subgap conductance peaks at characteristic energies of $\pm\Delta_1$, $\pm\Delta_2$ and $\pm(\Delta_1 + \Delta_2)/3$. Also observed is the peak at $V \approx 0$ corresponding to the Josephson supercurrent, which will be discussed in more detail in section 5.6. These are the first observations of Andreev reflections in asymmetric superconducting tunnel junctions, which are predicted to occur at energies $\pm\Delta_1/n$, $\pm\Delta_2/n$ and $\pm(\Delta_1 + \Delta_2)/(2n + 1)$, where n is

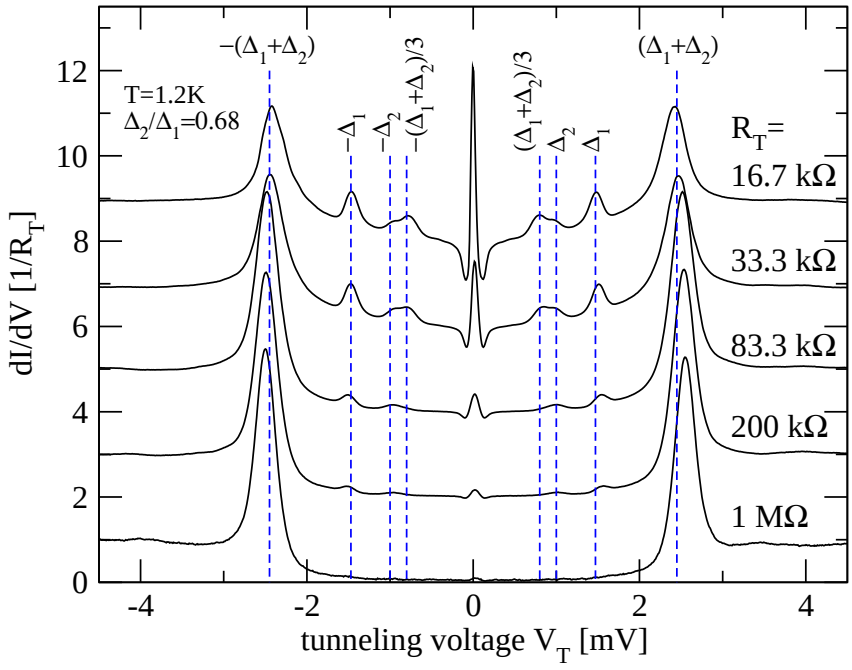

Figure 5.20: dI/dV spectra similar to the measurements shown in figure 5.19, but observed at slightly higher temperature of 1.2 K and with a gap of the tip of $\Delta_2 = 1.00$ meV, i. e. a ratio of $\Delta_2/\Delta_1 = 0.68$. Due to the higher temperature the subgap features are broader than in figure 5.19. The spectra are shifted vertically by two units with respect to each other for better visibility.

an integer [226]. The Andreev reflections representing the observed subgap peaks ($n = 1$) are represented schematically in figure 5.23 (a)(i-iii).

Figure 5.20 shows a similar set of dI/dV measurements using a tip with slightly smaller superconducting gap of $\Delta_2 = 1.00$ meV and a base temperature of 1.2 K which is about two times higher than the above described measurements. Similar to the data in figure 5.19, we detect conductance peaks at the energies $\pm\Delta_1$, $\pm\Delta_2$, and $\pm(\Delta_1 + \Delta_2)/3$. Compared to the measurements of figure 5.19, the peak intensity is decreased, especially for the curves at lower junction resistances R_T. Additionally, the peaks are broaden which is a direct consequence of the increased temperature.

In figure 5.21, the subgap structure observed for a tip with a gap $\Delta_2 = 0.32\,\text{meV} \approx 0.21 \times \Delta_1$ is substantially different. While the peaks at $\pm\Delta_1$ and $\pm\Delta_2$ are still present, the peaks at $\pm(\Delta_1 + \Delta_2)/3$, corresponding to an energy of about ± 0.60 meV, are barely visible. Surprisingly, peaks at $\pm(\Delta_1 - \Delta_2)$, corresponding to ± 1.15 meV, appear at lower junction resistances. These new features are not present in junctions with a gap ratio closer to one (figure 5.19 and 5.20). Notice that $eV_T = \Delta_1 - \Delta_2$ does not correspond to any threshold voltage of a multiple Andreev reflection process, and thus the nature of these peaks must be different from the peaks discussed above.

In order to clarify the origin of this novel spectral feature, we measured the temperature dependence at constant junction resistance, which is shown in figure 5.22 (a). As the temper-

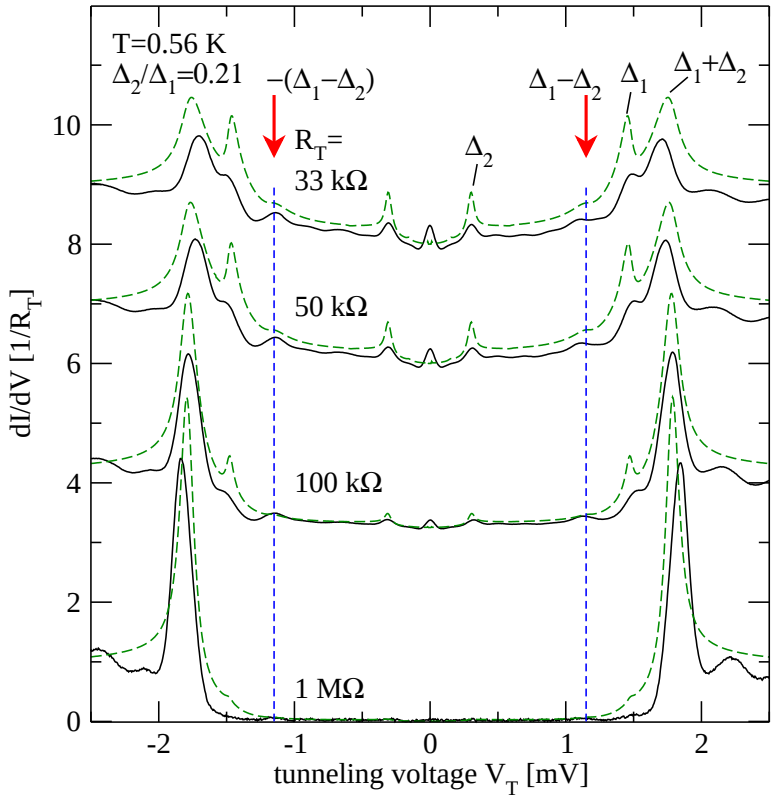

Figure 5.21: Full lines: dI/dV spectra measured between a Nb sample ($\Delta_1 = 1.47$ meV) and a tip with a small gap ($\Delta_2 = 0.32$ meV) at 0.56 K and different junction resistances. Dashed lines: Results of the single-channel multiple Andreev reflection theory of reference [225]. The transmission coefficient τ is determined by the corresponding R_T. Vertical lines and arrows: A guide for the eye to mark a new feature at $\pm(\Delta_1 - \Delta_2)$.

ature increases, all features smear out and the supercurrent peak as well as the peaks at Δ_1 and Δ_2 diminish. Above approximately 1.5 K, the height of the peak at $\Delta_1 - \Delta_2$ increases significantly due to thermally activated tunneling of single quasiparticles [173, 174], while below 1.5 K the intensity of the peak stays constant indicating that at low temperatures the novel peak is not due to thermal excitation of quasiparticles. The structure of the dI/dV spectrum with the characteristic peak at $eV = \Delta_1 + \Delta_2$ is still visible at a temperature of 3 K in contradiction to a critical temperature of $T_C = 2.1$ K for a BCS superconductor with $\Delta = 0.32$ meV. Figure 5.22 (d) shows the unusual temperature behavior of Δ_2, which is presumably due to the small size of the microcrystal [233]. In spite of this anomalous behavior, the dI/dV spectra of the tips measured against a Cu(111) sample could be well described by the standard tunnel formula assuming a bulk BCS density of states for the tip. An example is shown in figure 5.22 (c) for a tip with a gap of 0.41 meV at $T = 0.56$ K.

Using the known gaps Δ_1 and Δ_2 from sample and tip, the temperature, and the junction resistance as parameters, we have calculated the conductance using the single-channel

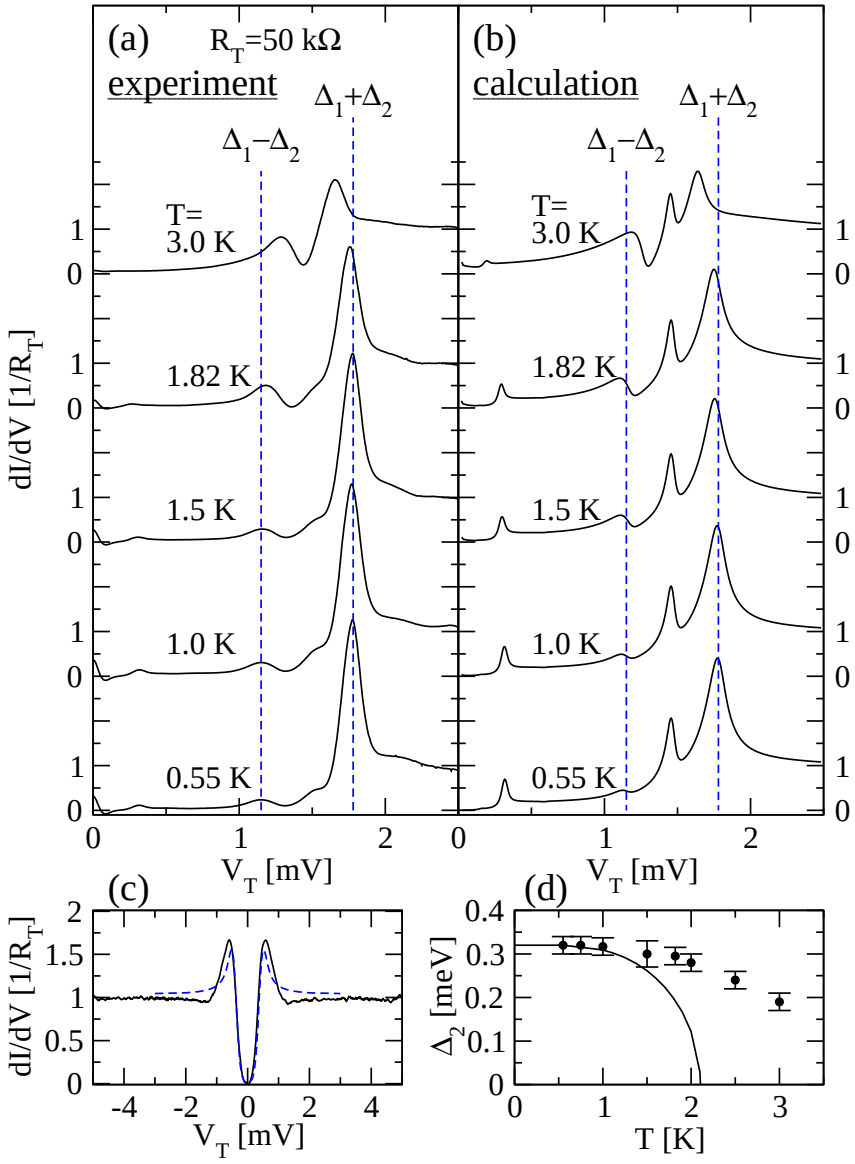

Figure 5.22: (a): Temperature dependent dI/dV spectra observed at $R_T = 50$ kΩ between tip and sample as in figure 5.21. (b): Results of the full counting statistic theory with $\tau = 0.26$. Vertical lines: A guide for the eye marking the $\Delta_1 \pm \Delta_2$ positions at 0 K. (c): Spectrum of the superconducting tip measured against a normal conducting Cu(111) sample at 0.56 K with $V_{mod} = 70$ μV (full line) and BCS simulation using equation 5.6 with the parameters $\Delta = 0.41$ meV, $T = 0.6$ K (dashed line). (d): Dots: Temperature dependence of the superconducting tip gap Δ_2. Full line: BCS calculation.

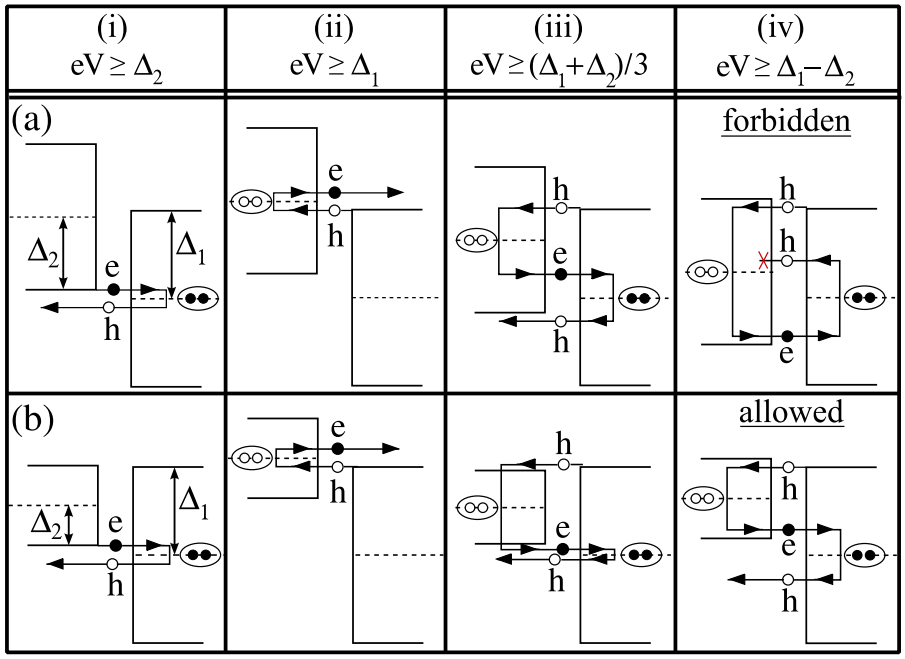

Figure 5.23: Schematic representation of the most pronounced multiple Andreev reflections in asymmetric superconductor-insulator-superconductor tunnel junctions [(a): $\Delta_2/\Delta_1 \approx 0.8$, (b): $\Delta_2/\Delta_1 \approx 0.4$] and their threshold: (i): At $eV \geq \Delta_2$ an electron (e) tunnels from the left superconductor into the right superconductor and is reflected into a hole (h) by creating a Cooper pair in the right superconductor. (ii): At $eV \geq \Delta_1$ a hole tunnels from the right superconductor into the left superconductor and is reflected into an electron annihilating a Cooper pair in the left superconductor. (iii): Two-step process at $eV \geq (\Delta_1 + \Delta_2)/3$ involving the tunneling of 3 particles and the creation of a Cooper pair in the right and the annihilation in the left superconductor. (iv): Special case of the two-step process shown in (iii), where the left Andreev reflection takes place just inside the gap of the left superconductor. This case is only possible in junctions with $\Delta_2/\Delta_1 \leq 0.5$.

multiple Andreev reflection theory of reference [225] (Figure 5.21 dashed curves).[12] In the calculation we only consider the dissipative current, and therefore the supercurrent peak does not appear in the simulation. Moreover, for the figures 5.21 and 5.22 we have used a small imaginary part of the energy ($\delta = 0.01\Delta_1$) to simulate the voltage modulation of the experiment and the finite lifetime of the quasiparticles (see equation 5.6). Notice that the theory reproduces the peak structure of the data and specifically the feature at $\Delta_1 - \Delta_2$. However, most of the peaks appear to be more pronounced in the calculation, which we attribute in part to the fact that the Nb microcrystal attached to the tip is not a perfect BCS superconductor, as we assume in the theory (see for instance the difference between measurement and BCS-fit in figure 5.22 (c) and (d)). On the other hand, following reference [219], we have performed fits including several conduction channels, but in this case it did not improve the quality of the agreement.

[12] This was done in collaboration with *J. C. Cuevas*, University of Karlsruhe.

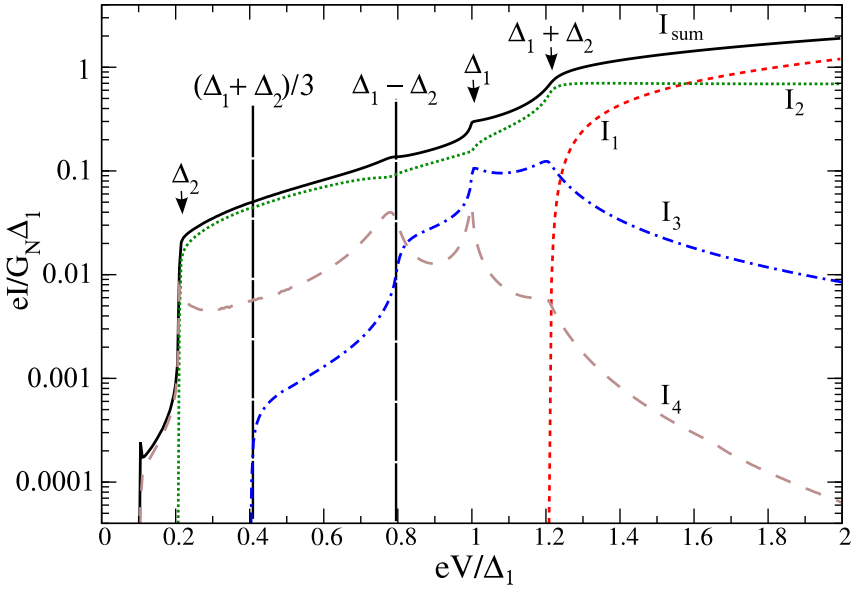

Figure 5.24: Calculated current contributions I_n to the overall tunneling current I_{sum} (full line) of multiple Andreev reflections at n-th order in a junction with $\Delta_2/\Delta_1 = 0.21$ and a transmission coefficient of $\tau = 0.2$ at a temperature of 0 K using a full counting statistics simulation. The arrows and the vertical lines mark energies where peaks in the spectrum occur.

For the simulation in figure 5.22 (b) we calculate the dI/dV spectra with a BCS-like spectrum of the superconducting sample and the measured $\Delta_2(T)$ (figure 5.22 (d)) for the tip. There is a good overall agreement, although the peak at Δ_1 is clearly much higher in the theory.

To get a deeper understanding of the origin of the new peak at $\Delta_1 - \Delta_2$ we use the concept of full counting statistics . As shown in reference [231], the total current, I_{sum}, can be written as a sum of the individual contributions of the Andreev reflections of different order, i.e.

$$I_{sum} = \sum_n I_n. \tag{5.21}$$

Here, I_n is the current contribution of a tunneling process involving the transfer of n electron charges and the occurrence of $n-1$ Andreev reflections, and it can be expressed as

$$I_n(V) = \frac{2e}{h} \int_0^{eV_T} nP_n(V,E)\, dE, \tag{5.22}$$

where $P_n(V,E)$ is the probability of the n-order Andreev reflection process. The probabilities can be obtained by means of a generalization to the asymmetric case of the recipe described in reference [231]. In figure 5.24 we plot the total current and the main contributions I_n for a junction with a gap ratio $\Delta_2/\Delta_1 = 0.21$. We assume zero temperature and a transmission coefficient of $\tau = 0.2$, which corresponds to a junction resistance $R_T = \frac{h}{2e^2}\frac{1}{\tau} = 64.5\ \text{k}\Omega$, with $\frac{h}{2e^2} = G_0^{-1} = 12906\ \Omega$ as the inverse of the quantum conductance. The peak at $\Delta_1 - \Delta_2$ originates mainly from the large increase of I_3 at this voltage.

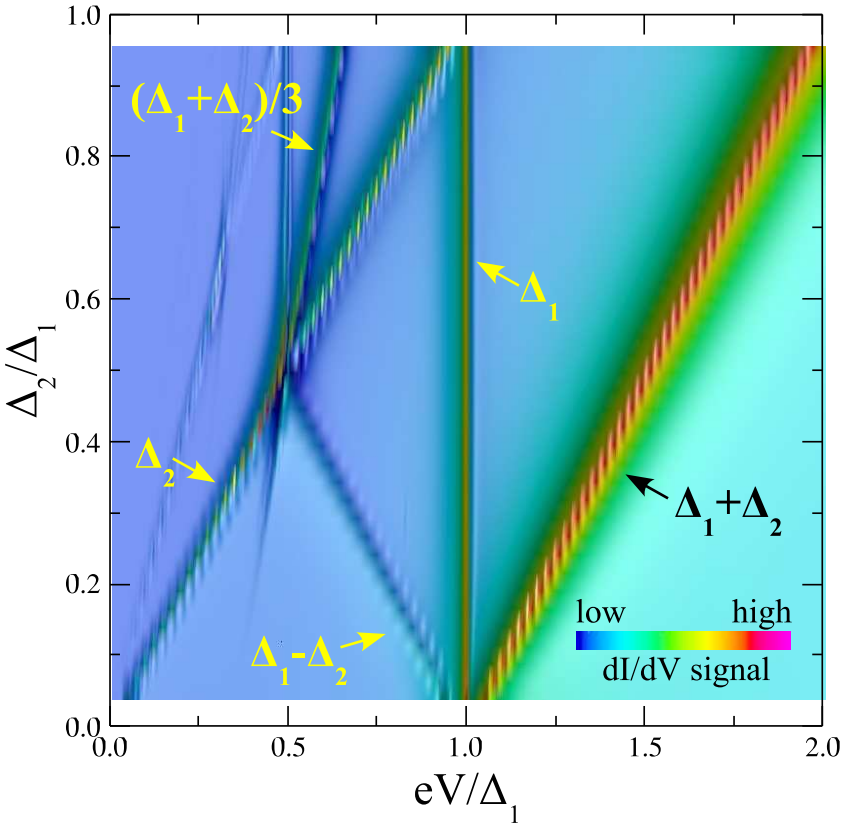

Figure 5.25: Full counting statistics calculation of the dI/dV-signal in an energy range between $0 \leq eV \leq 2\Delta_1$ between two superconductors with different gap ratios Δ_2/Δ_1 at a temperature of $T = 0$ K and a transmission coefficient of the junction of $\tau = 0.25$. The intensity is coded in color (see inset). Peaks at Δ_1, Δ_2, and $\Delta_1 + \Delta_2$ are visible for all gap ratios, while the peak at $\Delta_1 - \Delta_2$ only exists for a ratio $\Delta_2/\Delta_1 \leq 0.5$ and the peak at $(\Delta_1 + \Delta_2)/3$ diminishes for a ratio $\Delta_2/\Delta_1 < 0.3$.

As illustrated in figure 5.23 (b)(iv), such an increase is due to the fact that for $eV \geq \Delta_1 - \Delta_2$ the two Andreev reflections involved in this process can occur inside the gaps, which implies an enhancement of their probability (see figure 5.6, section 5.1.3). Order 4 processes also contribute strongly to the feature at $\Delta_1 - \Delta_2$: The peak in I_4 evident in figure 5.24 results in a marked change in the lineshape of the dI/dV peak at $\Delta_1 - \Delta_2$. So in short, we propose that the peak at $\Delta_1 - \Delta_2$ is due to the enhancement of the probability of a multiple Andreev reflection of order 3, which transfers 3 electron charges and involves two Andreev reflections [165].

On the other hand, in contrast to the data shown in figures 5.19 and 5.20, where the ratio between the gaps is nearly equal, none of the I_n produces a significant feature at $(\Delta_1 + \Delta_2)/3$. In particular, the jump in I_3 is only about $10^{-2} \times I_{sum}$, because at the onset of this process one of the two Andreev reflections takes place outside the gap, which makes this process quite unlikely (see figure 5.23 (b)(iii)).

Figure 5.25 presents in a color coded map the calculated Andreev reflections (dI/dV maxima) for a superconducting-insulating-superconducting tunnel junction of transmission coefficient $\tau = 0.25$ as a function of normalized junction voltage for gap ratios Δ_2/Δ_1 between $0.05 - 0.95$. At an energy of Δ_1, Δ_2, and $\Delta_1 + \Delta_2$ Andreev reflections are developed at all ratios. For a ratio ≥ 0.3 a maximum at $(\Delta_1 + \Delta_2)/3$ is clearly detectable, while it diminishes for smaller ratios. A maximum at $\Delta_1 - \Delta_2$ occurs for all $\Delta_2/\Delta_1 \leq 0.5$ and vanishes completely when the gap ratio exceeds 0.5. This calculation is in excellent agreement with our observed spectral features presented in figures 5.19, 5.20, and 5.21. For the first two with a ratio of $\Delta_2/\Delta_1 = 0.86$ and 0.68, three peaks inside the gap are located at Δ_1, Δ_2, and $(\Delta_1 + \Delta_2)/3$, while the peak at $\Delta_1 - \Delta_2$ does not exist. For the latter, we observe the $\Delta_1 - \Delta_2$ peak, while the peak at $(\Delta_1 + \Delta_2)/3$ is very weak.

To summarize, using a low-temperature STM for the creation and characterization of asymmetric superconducting tunnel junctions we gained new insight into the physics of Andreev reflections by analyzing in detail the observed subgap structure. In particular, for junctions with a relatively small gap ratio $\Delta_2/\Delta_1 < 0.5$ we observe novel peaks at $eV = \pm(\Delta_1 - \Delta_2)$, which are not due to the thermal excitation of quasiparticles. All observed subgap features can be understood as Andreev reflections within a full counting statistics model.

5.5 Magnetic impurities in superconducting tunnel junctions

Measurements using a superconducting tip to probe single magnetic impurities on normal conducting samples show only a convolution between the quasiparticle excitation spectrum of the tip and the LDOS of the sample adatom system, as we have shown in section 5.2.2. In particular, no influence on the superconducting gap was detected.

Nevertheless, interactions between the magnetic moment of a single atom and the superconducting phase are expected and were detected in spectra taken on top of adatoms hosted on a Nb sample which is a classical superconductor [157] and on top of Zn impurities on a high-T_C superconductor [234] by probing with normal conducting tips. In both works midgap states inside the superconducting energy gap were detected localized at the position of the magnetic atoms.

5.5.1 A Single Co atom attached to a superconducting tip

Here we present first results of a similar experiment using a superconducting tip on which a single Co atom was attached to the apex by using atomic manipulation techniques [147]. These measurements are in a way the mirror experiments of the work of *A. Yazdani et al.* [157] and were originally proposed by [206].

Figure 5.26(a) shows dI/dV spectra of the superconducting Nb tip prepared with a single Co atom picked up onto the apex measured against a clean Cu(111) surface at a base temperature of $T = 0.6$ K. The spectra were taken at different tunneling currents between 1 nA and 20 nA which corresponds to tunneling resistances between $R_T = 250$ k$\Omega - 5$ MΩ. They reveal three subgap peaks at energies of approximately -0.5, 0.0, and $+0.45$ meV. The amplitude and the position of the peaks as well as the overall form of the spectra are identical for all curves showing that the physical process which produces the midgap states is only negligibly influenced by the coupling strength of the tunneling process.

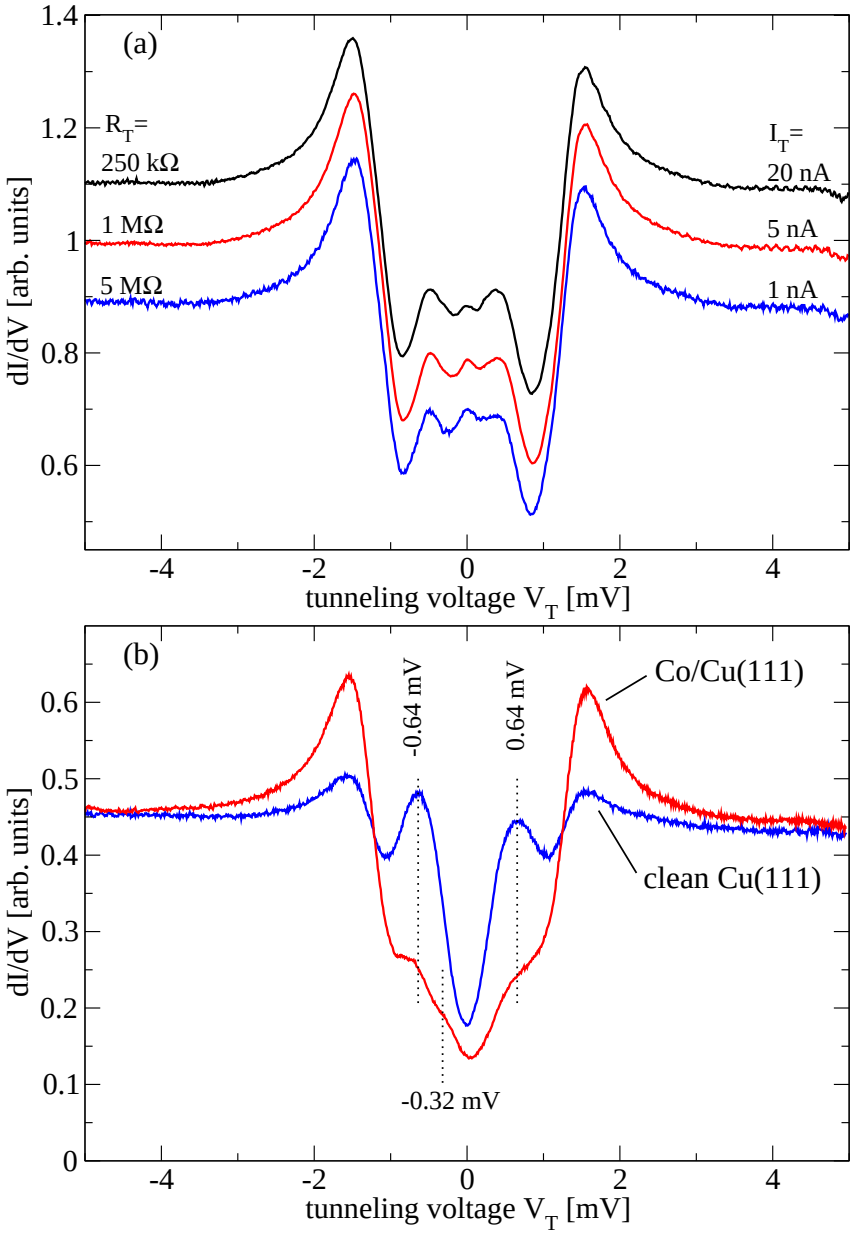

Figure 5.26: dI/dV spectra taken with a superconducting tip ($\Delta = 1.27$ meV) on which a Co adatom was attached at the apex. (a): Curves obtained at different setpoint currents I_T against a clean Cu(111) surface. (b): Spectrum of the same tip at $I_T = 1$ nA after the change of the position of the attached Co adatom reveals strong peaks originating from midgap states at an energy of$\pm\Delta/2$ (blue curve). The intensity of the midgap states are drastically reduced when the Co/Nb tip is placed over a second Co atom which is adsorbed on the Cu(111) surface (red curve). Tunneling parameters: $V_T = -5$ mV, $V_m = 71$ μV, $T = 0.6$ K

While the stability of the tip with an attached Co atom is quite good and allows one to perform measurements using tunneling resistances down to a few hundred kΩ, the exact position of the Co atom and the local environment on the apex remains unknown. Different sites of the Co adatom on the tip apex result in strongly changed spectra. This is clearly seen in figure 5.26 (b) where the spectrum of a similar tip is plotted as a blue curve. This tip shows much stronger peaks at ± 0.64 meV, while at $V_T = 0$ a dip is detected instead of a peak as seen in the spectra of figure 5.26 (a).

While in the previous measurements of [157] the subgap peak structure was only seen when subtracting the unperturbed BCS-like spectrum of the tip from the measured data, the spectra of both tips in figure 5.26 reveal clearly detectable midgap states directly in the dI/dV curves without further manipulation. We attribute the stronger pronouncing partly to the much lower temperature used in the presented work.

Using the model described in [206], we can assign the symmetrical appearance of the midgap peaks to two spin-polarized states localized at

$$\epsilon_{1,2} = \pm \frac{\alpha \Delta}{\sqrt{1+\alpha^2}}, \tag{5.23}$$

with $\epsilon_{1,2} = \pm 0.64$ meV as the position of the midgap states resulting in an $\alpha = 0.577$ for a superconducting tip with $\Delta = 1.27$ meV. The splitting is the result of an exchange coupling between the magnetic moment of the adatom and the paired quasiparticles [235, 236].

J. Šmakov et al. could simulate the results of the earlier experiment [157] by characterizing the exchange interaction W between the impurity and the conduction electrons of the host Nb sample and the on-site potential U, whereby both energies determine the parameter α [206]. Here, we have not performed this analysis due to the unreproducibility of the tip spectrum.

The appearance of the spin-polarized states can be additionally explained by introducting a spin-mixing angle Θ which describes the rotation of the quasiparticle spin at the magnetic adatom [228]. Within this description, the position of the midgap states are given by

$$\epsilon_{1,2} = \pm \Delta \cos\left(\frac{\Theta}{2}\right), \tag{5.24}$$

leading to a spin-mixing angle of $\Theta = \frac{2}{3}\pi$ for the presented data of figure 5.26 (b).

There exists another interesting result: Using the tip with the attached Co atom to measure the dI/dV spectum on top of a *second* single Co adatom supported on the Cu(111) surface reveals strongly suppressed midgap states (see red curve in figure 5.26 (b)). This result is surprising considering the obtained spectrum of Co on Cu(111) using a *clean* superconducting Nb tip in which the Kondo resonance was clearly detected (see figure 5.10 in section 5.2.1). The reduced intensity of the midgap states at $\epsilon_{1,2}$ can be understood by assuming similar spin-polarized states in the sample as in the apex of tip and a *antiferromagnetic* coupling between the two Co adatoms. Thus, the formation of the midgap states is suppressed.

5.5.2 Localized states in a superconducting junction induced by a Co atom

While the reproducibility is not given in the case of superconducting tips with an attached magnetic adatom, but magnetic atoms in superconducting junctions are of interest for the

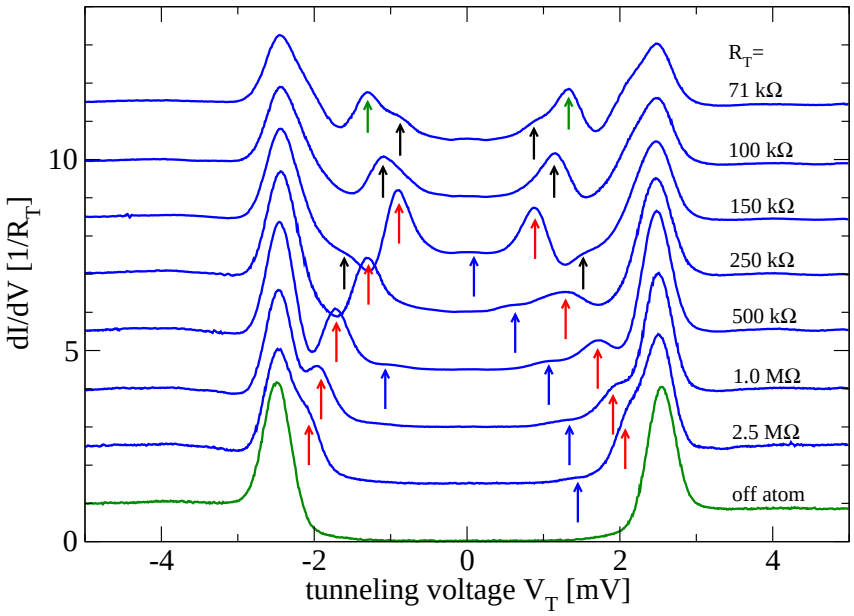

Figure 5.27: Set of dI/dV spectra measured with a superconducting tip on top of a Co adatom supported by a superconducting Nb(110) sample. The tunneling resistance R_T is changed between the different curves. The green (bottom) curve gives a reference of a superconducting– insulating–superconducting spectrum observed on the clean Nb. For clarity, all curves are shifted vertically with respect to each other. The arrows mark midgap states inside the gap.

understanding of the interactions between superconductivity and localized magnetic moments, we performed measurements between a superconducting Nb sample on which a low quantity of Co adatoms were dosed and a superconducting tip.

The spectra obtained in such superconducting–magnetic adatom–vacuum–superconducting (SMIS) junctions are presented in figure 5.27. The bottom curve, plotted in green, is measured at a lateral distance of at least 2 nm from any Co-adatoms at a relatively high tunneling resistance of $R_T = 2.5$ MΩ. It reveals the quasiparticle gap of $2(\Delta_1 + \Delta_2)$ width and strong peaks at $\pm(\Delta_1 + \Delta_2)$ due to the convolution between the quasiparticle excitation spectra (equation 5.6) of tip ($\Delta_1 = 1.47$ meV) and sample ($\Delta_2 = (0.95 \pm 0.05)$ meV) as discussed in section 5.1.3.

The set of blue curves are taken on top of a Co adatom at successively reduced tunneling resistances R_T. They reveal a sequence of peaks located inside the gap. Increasing the coupling between the tip and the sample, i. e. reducing R_T, shifts the peak energies closer to zero while new peaks occur (see colored arrows). All peaks appear symmetrically around E_F but with variable intensities. This is especially given for the peaks closest to E_F marked with blue arrows which are barely visible at negative tunneling voltages. The peak position scales thereby almost linear with the transmission coefficient, $\tau = \frac{1}{G_0 R_T}$ (see figure 5.28 (a)).

To rationalize the observations, we will focus on the curve taken at $R_T = 2.5$ MΩ at first. At this tunneling resistance the two superconductors are only weakly coupled,

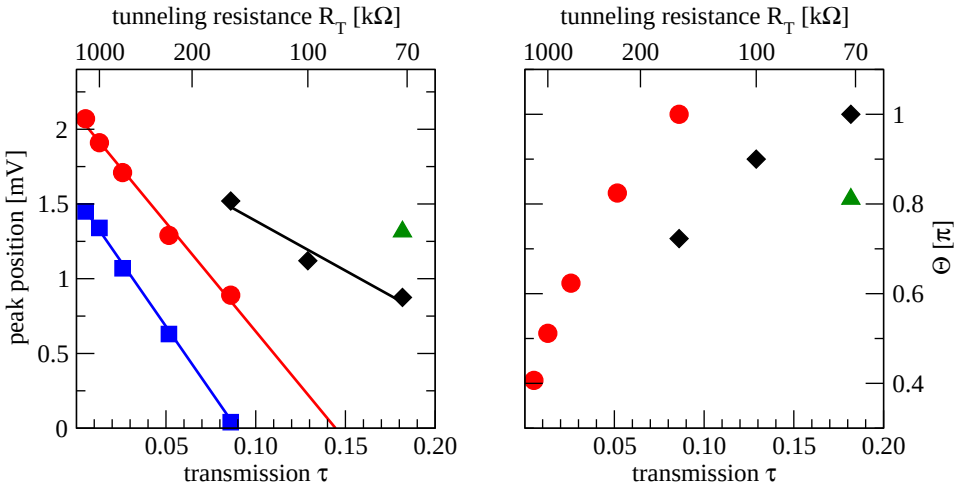

Figure 5.28: (a): Energy of the peaks found in figure 5.27. The lines mark the linearity with the transmission of the junction τ. (b): Calculated spin-mixing angle Θ for the data in (a) except for the low energetic square points.

and two shoulders are detected at an energy of ± 2.07 meV. These energies correspond approximatively to the positions one would expect if the Co adatom on the Nb sample produced a spectum similar to the one shown in figure 5.26 with midgap states located at $\epsilon \approx E_F \pm 1$ meV and a BCS-like spectrum of the tip. Due to the convolution of the LDOS of the tip and the sample (see equation 2.9 on page 8) peaks at $\pm(\Delta_2 + \epsilon) \approx \pm 2$ meV should appear. But while the spectra in the measurements with a normal conductor as one electrode stayed unchanged at higher setpoint current (see figure 5.26 (a)), the peak positions in the SMIS measurements change remarkably at lower tunneling resistances, i. e. increased tunneling current, as shown in figure 5.27. Especially, the observation of peaks at energies with an absolute value *smaller* than the superconducting gap energy of the probing tip (see blue arrows in figure 5.27) clarifies that the underlying process must be an interaction including *both* superconductors.[13]

Remarkably, the previously detected appearance of peaks in superconducting–insulating–superconducting junctions due to Andreev reflections processes at the fixed energies given by $\pm\Delta_1/n$, $\pm\Delta_2/n$, and $\pm(\Delta_1 + \Delta_2)/(2n+1)$ (see section 5.4) are not observed. Additionally, no supercurrent peak arises at low tunneling resistances. These observations clearly indicate that the magnetic Co adatom has a strong influence on the interaction between both superconductors.

While it is possible to calculate the spin-mixing angle Θ with equation 5.24 for the peaks at energies outsite the gap width Δ_2, when assuming the above mentioned assumption of a simple convolution of the quasiparticle spectrum of tip with midgap states in the sample (see figure 5.28 (b)), this model can not explain the weak peaks marked with blue arrows in figure 5.27. Additionally, notice that the low energy peaks are not explainable with an

[13] As long as the tip is only a probe for the sample states there can not exist any dI/dV signal in an energy range $\pm\Delta_2$. This is for example seen in the simulation of the IETS signal in section 5.3 and illustrated in figure 5.14.

Andreev scattering model which includes the additional spin-selective states induced by the Co adatom leading to subgap states at $(\Delta_2 + \epsilon)/n$, $(\Delta_1 + \epsilon)/n$, and $2\epsilon/n$ ($n \in \mathcal{Z}$) [228].

Nevertheless, the observed spin-mixing angle Θ for the most pronounced peaks points towards a variable $0 \rightarrow \pi$ transition of the magnetic adatom depending only on the coupling between both superconductors [237, 228].

5.6 Analyzing the supercurrent

As discussed in the theoretical part for superconducting-insulating-superconducting tunneling (see section 5.1.4), not only quasiparticles but additionally Cooper pairs can cross the junction leading to a Josephson supercurrent. In dI/dV measurements, the supercurrent is detected as a sharp peak at zero voltage. This feature is clearly visible in the subgap structure of figures 5.19–5.21 (section 5.4), especially in the curves obtained at low tunneling resistances.

5.6.1 Experimental findings

To get a deeper insight into this phenomenon, we performed high resolution spectroscopic measurements between a superconducting tip with a gap width of $\Delta_2 = 1.27$ meV and the Nb sample ($\Delta_1 = 1.47$ meV). To achieve energy resolutions of a few μeV, all experiments were done with a setup that eliminated all sources of electronically and thermally generated noise as far as possible. Thus, the experiments where performed at the lowest attainable base temperature of $T = 0.55$ K and by recording directly the $I-V$ curves without a modulation voltage added to the applied tunneling voltage. Additionally, all electrical instruments and devices which were not essential to perform the experiment and data acquisition were switched off, disconnected from the power-line, and removed from the STM. With this preparation the influences of magnetic and electric stray-fields on the obtained data were minimized.

The electrical wiring, together with the output impedance R_B of the voltage generator, the input impedance R_C of the $I-V$ converter, and the HF-filters between the tip and sample on one side, and the voltage generator and $I-V$ converter on the other side results in an overall serial dc-resistivity of $R_S = 4.3 \pm 0.1$ kΩ (see the simplified circuit diagram of the electrical set-up in figure 5.29 (a)). To eliminate the voltage drop on R_S, the raw data points (V_B, I_T) have been corrected to obtain the true junction voltage V_J using the equation

$$V_J = V_B - R_S I_T(V_B).^{14} \tag{5.25}$$

Figure 5.30 shows a set of $I-V$ curves taken at different tunneling resistances R_T. For each value of R_T the forward and backward pass of the voltage sweep from -1.5 mV to $+1.5$ mV are shown. Slightly different forward and backward curves at the lowest tunneling resistances and at higher voltages are due to small drifts in the tip sample distance.

[14] Usually, this voltage drop is automatically corrected by the data acquisition software (using the so called "smart" mode) by applying a slightly higher voltage to the junction depending on the actually measured tunneling current I_T. This clever correction must fail when the differential junction conductivity dI/dV approaches infinite values as it is possible in Josephson junctions.

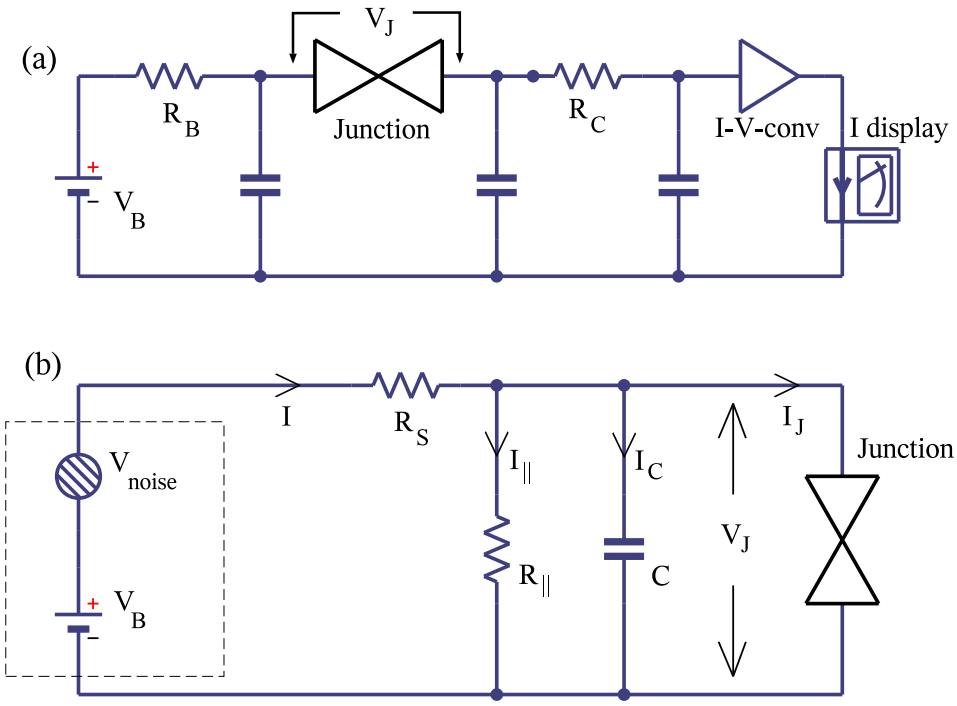

Figure 5.29: (a): A Josephson tunnel junction represented by the ⋈ symbol in a simplified electronic set-up of the STM. A voltage V_B is applied over a RC network to one electrode (for example the sample), while the current is detected on the second electrode (for example tip) and processed in a current-voltage converter to a voltage proportional to the initial tunneling current I_T. (b): Simplified electromagnetic resistively shunted junction (RSJ)-model of the environment in which the Josephson junction is embedded and which is used in the simulations.

These small changes of less than 3% during the acquisition time of about 1 minute mean a variation of the tip sample distance of approximatively 1 pm (see equation 2.1 on page 4). This variation is very small and is a proof of the extraordinary stability of the apparatus as well as of the superconducting tip. The tunneling resistivity R_T was calculated by using the setpoint current at an applied voltage of $V_B = -5$ mV before opening the feedback loop and performing the sweep. The internal resistance R_S was taken into account for this calculation.

All curves are symmetrical to the origin. With the exception of the data set obtained at $R_T = 4600\ \Omega$, all spectra show characteristic steps at the voltages $V_J \approx \pm 0.9$ mV and $V_J \approx \pm 1.25$ mV which correspond to the threshold energies of a multiple Andreev reflection process at $\pm\Delta_2$ and $\pm(\Delta_1 + \Delta_2)/3$ (see chapter 5.1.3). The absence of these features in the curves with the lowest junction resistance and the almost linear slope (except for the supercurrent branch) which corresponds to the adjusted R_T, indicates that the tip during this recording was no longer in tunneling distance but in electrical contact with the surface. Nevertheless, the junction still shows tunneling behavior at $R_T = 8200\ \Omega$ which is sufficiently smaller than the lowest resistance for which a single channel atomic junction is

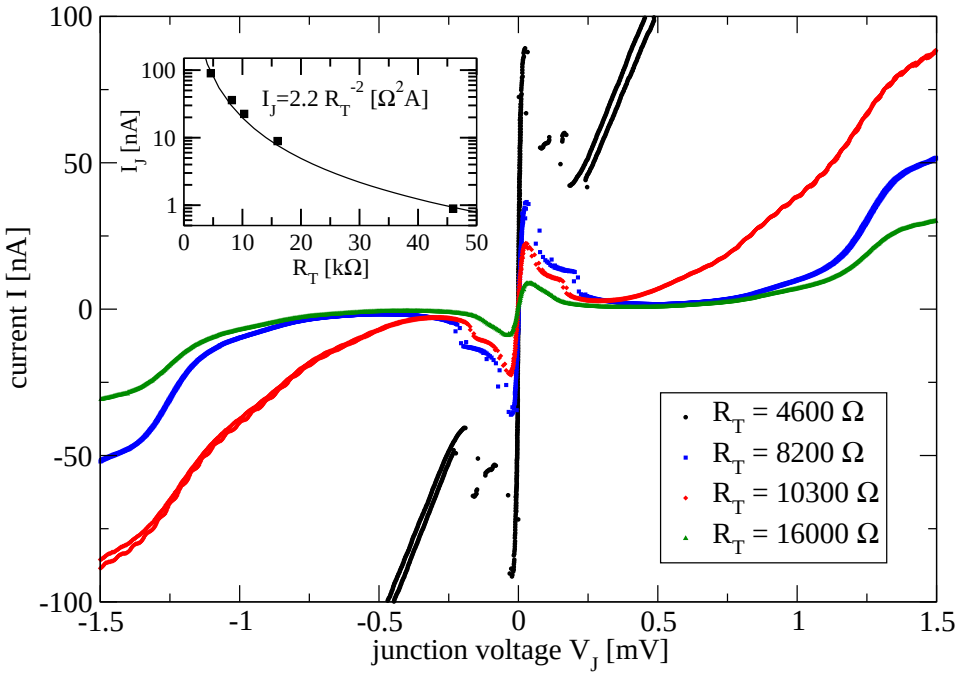

Figure 5.30: $I-V$ curves of a superconducting-insulator-superconducting junction at different setpoint resistivities R_T. All spectra are recorded at $T = 0.55$ K. Inset: The maximal dc-supercurrent over junction resistivity shows a R^{-2} behavior. (The curve corresponding to $R_T = 46$ kΩ is not shown.)

still in the vacuum tunneling regime and which is given approximatively by the inverse of the quantum conductance $G_0^{-1} = \left(\frac{2e^2}{h}\right)^{-1} = 12906\ \Omega$ [219]. Thus, we have to assume that the atomic tunneling contact between both Nb electrodes has at least $2-3$ channels which contribute to the tunneling current. This assumption is in agreement with break-junction measurements [221].

As expected, all curves show a zero-voltage current which reaches a maximum value $I_{\max}$ before it switches to the dissipative branch. The maximal dc-supercurrent can be calculated from the junction resistance with the empirical equation

$$I_{\max} = (2.2 \pm 0.2) \times R_T^{-2.04\pm0.08}\ \left[\Omega^{2.04\mp0.08}\mathrm{A}\right] \tag{5.26}$$

in good agreement to the data as shown in the inset of figure 5.30. The obtained maximal supercurrents are much smaller than the critical supercurrent I_0 calculated with the Ambegaokar equation 5.16 (for a comparison see table 5.2 on page 117). Additionally, equation 5.16 predicts a maximal supercurrent which scales with R_T^{-1} and not with the experimentally obtained R_T^{-2}. These findings can only be explained in a junction model which includes the electromagnetic environment of the STM and the finite temperature (section 5.6.2).

Figures 5.37, 5.38, and 5.39 (pages 121–123) exhibit blow-ups of the positive supercurrent branches for junction resistances of 8.2 kΩ, 10.3 kΩ, and 16 kΩ, respectively. The

top panels of the figures show the raw data as they were obtained by the experiments, i. e. without the correction of R_S. Starting from the origin by increasing the voltage, a linear progression of the current with a slope $dI/dV = 1/R_S$ is detected which reaches its maximum and drops than suddenly to smaller values (black dots). A similar jump occurs again at slightly higher bias voltage. While this double step structure is clearly visible in the measurements with $R_T = 8.0$ kΩ and $R_T = 10.2$ kΩ, it is barely detectable in the curve taken at a junction resistance of $R_T = 16$ kΩ.

This double step structure is also detected in the backward sweep (red dots), but it appears at different energies leading to a hysteresis loop which is clearly visible in figures 5.37 and 5.38, but only slightly evolved in figure 5.39.

The curves shown in the lower panels are obtained after correcting the data with equation 5.25. The appearance of the first step is easily understood by the load-line of the voltage generator together with the serial resistor R_S and the negative differential resistance regime which follows the maximal current. Figure 5.31 shows a simulated supercurrent curve using an equation of the form;

$$I(V) = A \frac{V}{V^2 + V_P^2}, \tag{5.27}$$

which was used to describe the supercurrent in STM experiments with Pb–vacuum–Pb junctions [185, 238]. We obtain a curve similar to the one measured at $R_T = 8$ kΩ (figure 5.37) with the empirical parameters $A = 2.31$ μAV and $V_P = 32$ μV. For the explanation of the load-line induced jump in the supercurrent the meaning and derivation of equation 5.27 is not crucial and will be addressed in section 5.6.2.

Whereas for each applied bias voltage V_B infinite pairs of junction voltage V_J, and current I values are available which fullfill equation 5.25, and which are located on the load-line as shown in figure 5.31 (black lines), there exist points of instability in the system. Approaching the origin from negative bias voltage, such a point of instability is reached in the example at $V_B = -0.227$ mV. Increasing V_B above this point leads to an abrupt jump of the current I and the junction voltage V_J (arrow in figure 5.31). At the positive $I - V$ branch a jump occurs too, but here at $V_B = 0.255$ mV, i. e. at slightly higher absolute value.

To conclude, the first jump and the hysteresis, which are visible in all raw data, are effects of the finite serial resistance R_S. Some scattered data points in the lower part of figures 5.37–5.39 which are visible after the correction are due to the relatively long response time of the current detection system and are artifacts. A perfect voltage generator together with a serial resistor $R_S \to 0$ would lead to jumpless curves without hysteresis. Nevertheless, only the first jump is understood with the model presented here. The simple equation 5.27 together with the load-line argument is not adequate to describe the appearance of the second jump.

Additionally, it is important to mention that in break-junction experiments the junction is usually driven in constant current mode which hinders the observation of the detailed $I - V$ curves close to zero voltage presented here (see figure 5.32). Especially, to my knowledge there is no literature available that has observed jumps whose positions scale with the inverse junction resistance as detected in the lower panel of figures 5.37–5.39. The observation of a step in $I - V$ traces of Pb-PbO-Pb point-junctions [182] might have the same origin as in our observations, but was not discussed by the authors.

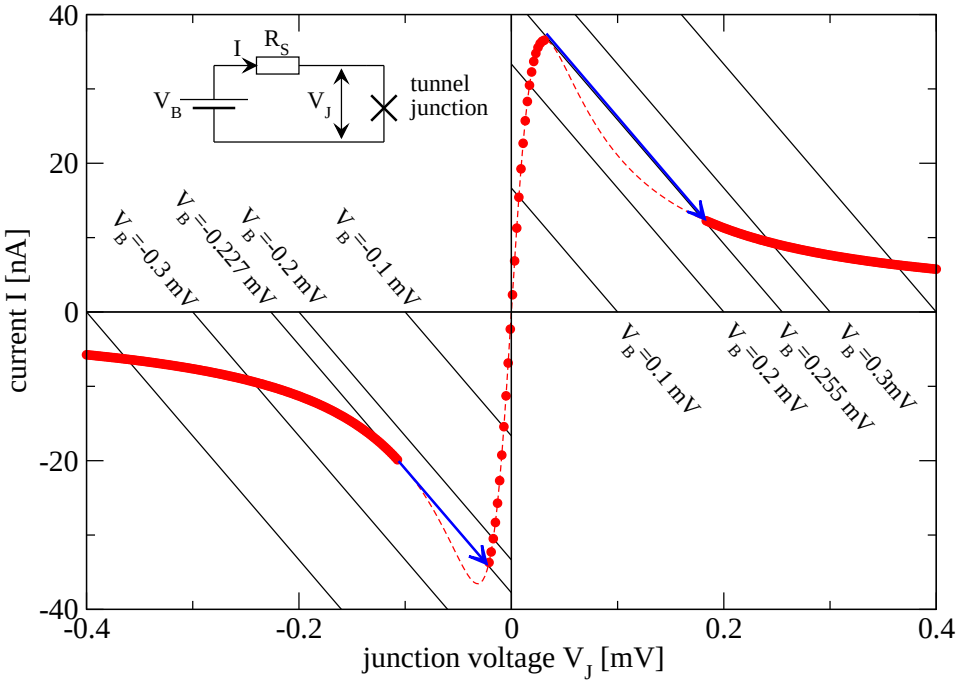

Figure 5.31: Simulation of the supercurrent in a Josephson junction using the equation $I(V) = A\frac{V}{V^2+V_P^2}$ [185, 238] with $A = 2.32\ \mu$AV and $V_P = 32\ \mu$V to obtain a curve similar to the data shown in figure 5.37 Due to the serial resistor R_S which determines the load-line of the voltage source some points on the $I-V$ curve are unstable. For each applied V_B, pairs of (I, V_J) exist which fulfill equation 5.25(black lines). If the slope of the supercurrent curve exceeds the slope of the load-line jumps occur which are indicated by blue arrows.

5.6.2 Theoretical model

To include the electromagnetic environment, the resistively and capacitively shunted junction model (RCSJ-model) [239, 240], has been adapted to STM measurements following the idea in [241].

The starting point is the simplified junction model drawn in figure 5.29 (b). It includes an ideal voltage generator V_B and a noise source V_{noise} in which all thermally (*Nyquist* noise of the resistors) and electronically generated noises are summarized. The complex multipoles of the electrical environment is simplified by a RC combination parallel to the Josephson junction, while the voltage drop is taken into account by the serial resistor R_S. According to *Kirchhoff*'s law, the current I can be written as the sum of the partial currents:

$$I = I_{||} + I_C + I_J = \frac{V_J}{R_{||}} + C\frac{dV_J}{dt} + I_0 \sin\delta. \tag{5.28}$$

Using equation 5.14, which describes the ac-Josephson effect, the voltage V_J can be elimi-

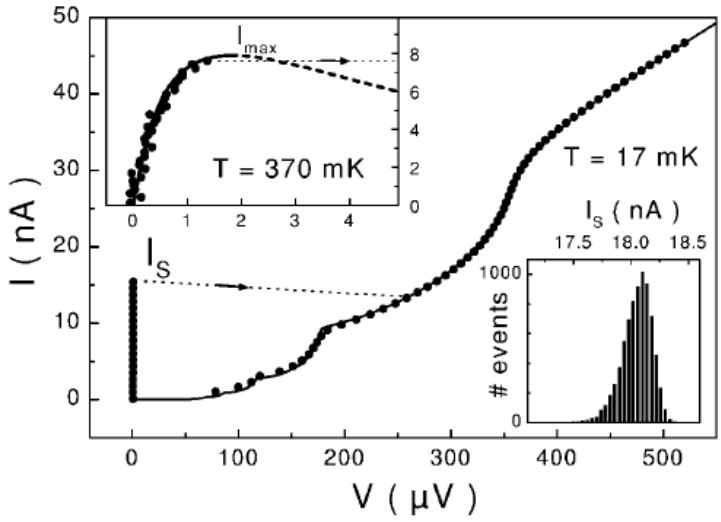

Figure 5.32: Typical $I-V$ curve measured in an Al break-junction experiment. The data (dots) were obtained at $T = 17$ mK (inset at $T = 370$ mK) in constant current configuration and show a large hysteresis. The system switches from the supercurrent branch at $V \approx 0$ to the dissipative branch to a relatively high $V \approx 270$ μV (dotted line with arrow). The full line is a fit using full counting statistics with 3 independent tunneling channels and transmission coefficients of $\tau_{1...3} = 0.52, 0.26, 0.26$. The critical supercurrent is calculated to $I_0 = 25.3 \pm 0.4$ nA. Figure and data are taken from [184].

nated leading to a differential equation of second order:

$$I = \varphi_0 C \frac{d^2\delta}{dt^2} + \frac{\varphi_0}{R_{||}} \frac{d\delta}{dt} + I_0 \sin\delta. \tag{5.29}$$

For small phase amplitudes $\delta \bmod 2\pi \ll 1$ the Josephson junction can be seen as a linear inductance $L = \varphi_0/I_0$ and equation 5.29 has the same structure as the well known harmonic oscillator with damping:[15]

$$\frac{I}{I_0} = LC \frac{d^2\delta}{dt^2} + \frac{L}{R_{||}} \frac{d\delta}{dt} + \sin\delta. \tag{5.30}$$

The resonance frequency

$$\omega_0^\gamma = \frac{1}{\sqrt{LC}} = \ = \frac{2e}{\hbar}\sqrt{E_J E_C}, \tag{5.31}$$

and the quality factor

$$Q = R_{||}\sqrt{\frac{C}{L}} = G_0 R_{||}\sqrt{\frac{E_J}{2E_C}} \tag{5.32}$$

[15]The analogy to an inductance is of course limited. One has to keep in mind that for an electrical inductance the characteristic equation $V_{\rm ind} = L\frac{dI}{dt}$ connects the induced voltage with the time derivative of the current while the analogy presented here links the voltage with the time derivative $d\delta/dt$ of the superconducting phase difference.

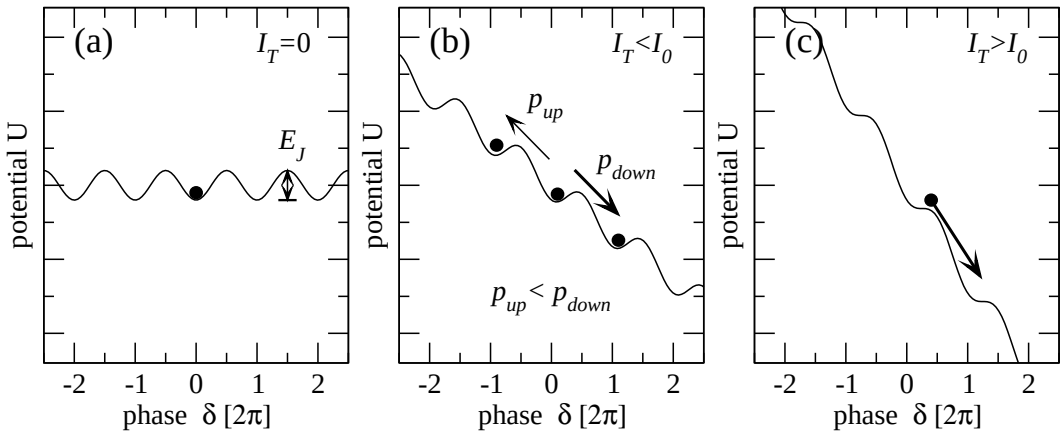

Figure 5.33: The "tilted washboard model" of a Josephson junction. (a): At $I = 0$ the "particle" has its stable configuration at $\delta \bmod 2\pi = 0$. (b): For $0 < I < I_0$ the particle which might gain some thermal energy has a higher probability to move downhill than uphill. (c): When the current I exceeds the critical current I_0 the particle can run downhill only damped by the viscosity of the medium.

determines the Josephson junction. The ratios between the Josephson binding energy $E_J = \frac{\hbar}{2e^2} I_0$, the electrostatic charging energy $E_C = \frac{e^2}{2} C^{-1}$, and the thermal energy $k_B T$ are governing the dynamics at finite temperature.

The Josephson binding energy E_J gives thereby an energy scale for the coupling between the different phases of the two superconducting electrodes. It depends linearly on the maximal supercurrent I_0 (equation 5.16) and is directly related to the superconducting order parmeters $\Delta_{1,2}$ of the two superconductors and the junction normal state resistance R_T [180].

The electrostatic charging energy E_C is the necessary energy to change the number of electrons on the capacitor C by one. This capacity is very low in the case of small junctions such as those given in STM between the tip and the sample. For a junction with an internal $C \approx 2$ fF the charging energy $E_C \approx 50$ μeV is of the order of $k_B T$ with T as the temperature of the experiment.[16]

A different analogy can be drawn between the description of the Josephson junction as in equation 5.30 and a particle of "mass" $\frac{\hbar^2}{4e^2} C$, moving in a potential landscape that reminds one of a tilted washboard [242, 173] with:

$$U(\delta) = -E_J \cos\delta - \frac{\hbar I}{2e}\delta. \tag{5.33}$$

The particle is hindered by a "viscosity" proportional to $\frac{\hbar^2}{4e^2} R_{||}^{-1}$ and can perform *Brownian* motion due to statistical excitation given by the noise source in figure 5.29(b).

When only a small current I is applied, i. e. the washboard is only slightly tilted (figure 5.33 (b)), the system stays mainly in one well of the potential landscape with an average δ

[16]Note that the capacities of the external filter RC-networks (see figure 5.29 (a)) are not part of this capacity because they are only weakly coupled to the junction in the frequency range $\omega_0^\gamma \approx 10^{10}$ Hz in which the charging and discharging of the junction takes place.

given by the Josephson equation $I = I_0 \sin\delta$ (equation 5.13). Due to the noise term, statistical fluctuation exist which lead the particle to move in a preferred direction and produces an average voltage $\langle V\rangle = \varphi_0 \left\langle \frac{d\delta}{dt}\right\rangle \neq 0$.[17]

By increasing the current I over the critical supercurrent I_0 , the system will be in the so called "running state" (figure 5.33). The current is still governed by the average $I_0 \langle\sin\delta\rangle$ whereby the voltage $\langle V\rangle$ determines the average speed of the particle.

To calculate the dynamic behavior of the junction including the noise term is difficult and only analytically solvable under restricted assumptions. As it was shown by *P. Joyez et al.* in [241], this can be done by assuming the following simplifications:

- While E_J and E_C are of the same order of magnitude, the electromagnetic environment provided by the leads presents an impedance of the order of the vacuum impedance, i. e $R_{||} \lessapprox Z_0 = \sqrt{\frac{\mu_0}{\epsilon_0}} \cong 377\ \Omega \ll G_0^{-1}$. Thus, the quality factor is $Q \ll 1$, i. e. the junction is at the plasma frequency ω_0^γ highly damped.

- Coulomb Blockade effects are irrelevant because the environment can charge the capacitance much faster than the Josephson current.

- The capacitance C (figure 5.29 (b)) is very small, so that the first term in equation 5.29 can be neglected (resistively shunted junction (RSJ) limit).

- The noise source can be described with an effective temperature T_{eff} originating from perfectly randomized Nyquist noise in the resistor $R_{||}$ and thus obeys the relation $\langle V_{\text{noise}}(t) V_{\text{noise}}(t')\rangle = 2k_B T_{\text{eff}} R_{||} \delta(t-t')$, where $\delta(t)$ is here the delta distribution and not the phase difference.

- The detected voltage V_J is heavily damped so that the junction is in the adiabatic limit and the dynamic of δ can be solved assuming $V_J = \langle V_J\rangle$.

The results in [241] were calculated for break-junction experiments in which the system is usually driven in constant-current mode. For our needs of a mainly constant-voltage driven junction, the equations for the detected current I and voltage V_J are slightly adapted and result in:

$$I(\xi) = I_0 \langle\sin\delta\rangle = I_0 \Im\left[\frac{\mathcal{I}_{1-i\eta}\left(\frac{E_J}{k_B T_{\text{eff}}}\right)}{\mathcal{I}_{-i\eta}\left(\frac{E_J}{k_B T_{\text{eff}}}\right)}\right], \tag{5.34}$$

$$V_J(\xi) = R_{||}\left(I(\xi) - \xi\right). \tag{5.35}$$

With the shorthand

$$\eta = \frac{E_J}{k_B T_{\text{eff}}}\xi, \tag{5.36}$$

$\Im(x)$ as the imaginary part of x, and $\mathcal{I}_\alpha(\beta)$ as the modified Bessel function of first kind and of the complex order α taken at β.

[17] $\langle\ldots\rangle$ has here the meaning of a time average.

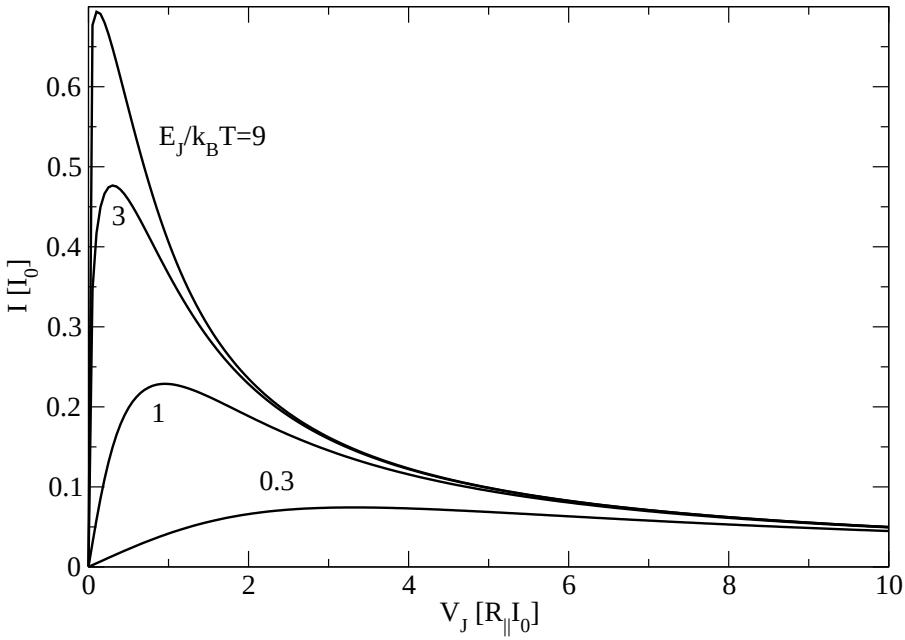

Figure 5.34: Simulated $I-V$ curves for different $\frac{E_J}{k_B T_{\text{eff}}}$ values using the equations 5.34 and 5.35 of the resistively shunted junction model.

In the limit $E_J \ll k_B T_{\text{eff}}$ the equations 5.34 and 5.35 can be reduced to the more simple form [243, 244]:

$$I(V_J) = \frac{1}{2} I_0^2 R_{||} \frac{V_J}{V_J^2 + \left(\frac{2e}{\hbar} R_{||} k_B T_{\text{eff}}\right)^2}, \tag{5.37}$$

which we have already introduced in section 5.6.1 (equation 5.27). Here, the use of this approximation is not recommended because in our experiments $E_J \gtrsim k_B T_{\text{eff}}$.

Figure 5.34 shows $I-V$ curves calculated by using equations 5.34 and 5.35 for different $\frac{E_J}{k_B T_{\text{eff}}}$ values. The critical current I_0 is only achieved in the limit $\frac{E_J}{k_B T_{\text{eff}}} \to \infty$, while the maximal current diminishes rapidly with increasing T_{eff}.

This set of equations allows us to perform least-square fits to the measured data when including an additional current I_{ind} given by:

$$I_{\text{ind}}(V_J) = \begin{cases} \alpha G_0 V_J, & V_J \leq V_{\text{jump}} \\ 0, & V_J > V_{\text{jump}} \end{cases} \tag{5.38}$$

to incorporate the detected second jump. While the fit was not stable when letting the position of V_{jump} also be a variable parameter, this value was fixed at the observed position, while the remaining parameters were varied using a fitting routine.

For each experimentally measured data point (V_J, I), the routine searches iteratively ξ until $V_J(\xi)$ of equation 5.35 corresponds to the junction voltage at this point and than calculates $I(\xi)$. Performing this procedure for all data points, we get calculated (V_J, I) data for a set of parameters, which were than be optimized to reach maximal agreement with the experimental data.

	tunneling resistance R_T		
	8.2 ± 0.1 kΩ	10.3 ± 0.1 kΩ	16.0 ± 0.1 kΩ
I_0 (calc.)	287 ± 6 nA	229 ± 4 nA	148 ± 3 nA
$I_{\max}$ (exp.)	36.5 ± 0.5 nA	26.5 ± 0.5 nA	8.8 ± 0.2 nA
$I_0' = \frac{1}{3} I_0$ (calc.)	96 ± 2 nA	76.5 ± 1.4 nA	49.3 ± 0.9 nA
I_0^{fit}	95.7 nA	76.2 nA	55 nA
$E_J' = \frac{\hbar}{2e^2} I_0'$ (calc.)	197 ± 4 μeV	157 ± 3 μeV	101 ± 2 μeV
$E_J^{\text{fit}} = \frac{\hbar}{2e^2} I_0^{\text{fit}}$	196.6 μeV	156.5 μeV	113 μeV
eV_{jump} (exp.)	197 ± 3 μeV	156 ± 5 μeV	110 ± 10 μeV
$\tau^* = \frac{1}{3} R_T^{-1} G_0^{-1}$ (calc.)	0.52	0.42	0.27
α (fit)	0.43	0.35	0.20
$R_{\|\|}$ (fit)	242 Ω	246 Ω	245 Ω
T_{eff} (fit)	1.2 K	1.4 K	2.0 K

Table 5.2: Calculated data from the experimental settings and parameters obtained by a least-square fit of the superconducting-insulating-superconducting $I - V$ curves.

The results of the best fits for the experiments with junction resistivities of $R_T = 8.2$ kΩ, 10.3 kΩ, and 16 kΩ are displayed as blue lines in the figures 5.37, 5.38, and 5.39. The best parameter set can be found in table 5.2.

As already mentioned, the observed maximal supercurrent $I_{\max}$ is much smaller than the I_0 calculated with equation 5.16. Even if we assume an increased effective temperature in our apparatus, the experimentally observed data and the obtained fit parameters can not be brought to agree with each other. But when assuming that the junction contains three identical tunneling channels which is in agreement to findings in break-junction experiments [221] and thus using a critical supercurrent of $I_0' = \frac{1}{3} I_0$, the obtained parameter for the best fit of I_0^{fit} agrees very well with the calculated I_0'. Additionally, the results of the fit for T_{eff} and $R_{||}$ agree with the model. As discussed above, $R_{||}$ should be of the order of the vacuum impedance ($Z_0 \approx 377$ Ω) which was the case ($R_{||} \approx 0.65 \times Z_0$). The effective temperature T_{eff} is with $1.2 - 2$ K only slightly higher than the base temperature of the apparatus and suggests an overall noise factor of $F = \frac{T_{\text{eff}}}{T_{\text{base}}} = 2 - 3$ which is quite acceptable compared to similar measurements where the noise factor was $F \approx 3.5$ [185].

Using I_0' and calculating E_J lead to a remarkable coincidence between the jump position and the Josephson energy. In the two measurements with a tunneling resistance $R_T = 8.2$ kΩ, and 10.3 kΩ they agree with each other within an error of $< 1\%$, while a difference of about 10% is found in the measurement with $R_T = 16$ kΩ, mainly due to the difficulty to determine the exact position of V_{jump}. Remarkably, the error between both values is reduced to $\approx 3\%$ when using the fitted value of I_0^{fit} to calculate E_J^{fit}.

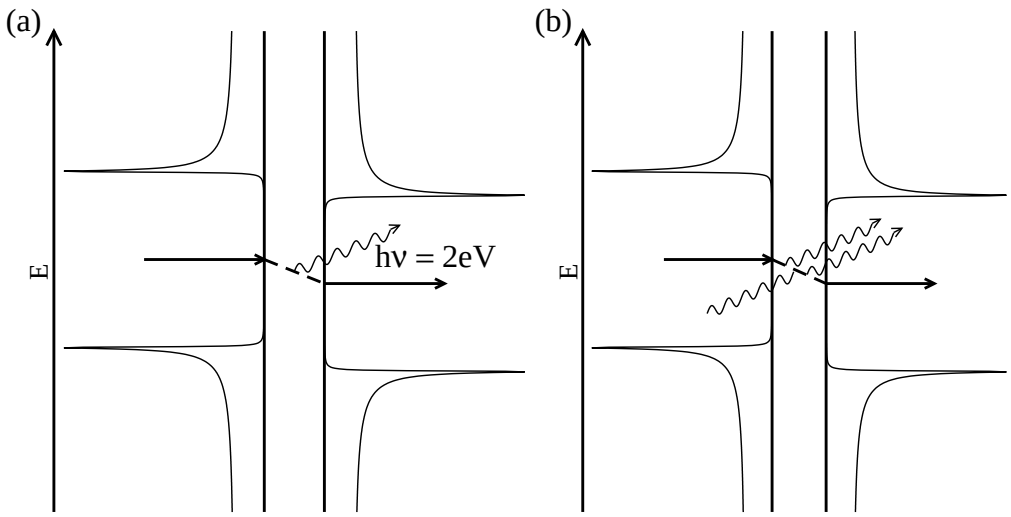

Figure 5.35: A Cooper pair which crosses the tunnel junction at an applied voltage emits a photon of an energy $\hbar\omega = 2eV$ (a). The same photon can induce a second transition of a Cooper pair from the left to the right electrode (b).

While the underlying physical process stays unclear and up to now similar results were to my knowledge never reported, we can only present some ideas about the origin of this additional current and its sharp drop at E_J. The following observations should be reflected:

- The presumably linear dependence of I_{ind} on the junction voltage with a slope of $\alpha \approx \tau^*$, i. e. the additional channel acts like an ohmic channel parallel to the junction with a transmissivity of the same order as the major channel.
- The drop in current at junction voltages $|eV_J| \geq E_J$.

Self-induced tunneling

Since early measurements on superconducting tunnel junctions it has been known that Cooper pairs which tunnel across a biased junction emit microwaves at $\omega = 2eV_J/\hbar$ (figure 5.35 (a)) [191, 179]. Additionally, it is well known and proven by several experiments that an externally applied HF-field leads to Shapiro steps in the $I - V$ curve due to microwave induced tunneling [188, 189, 190]. Thus it might be possible, that the observed extra current is due to self-induced tunneling (see figure 5.35 (b))

To be more precise, the applied junction voltage V_J induces an oscillation of the system variable δ (the phase difference between the two superconducting states), resulting in an ac-current with a frequency of the phase oscillation. This alternating current is the source of an emitted electromagnetic wave with the same frequency. In the model outlined in figure 5.33 the average speed of the "particle" determines the photon energy. Similar to the situation given in a Laser device, the photon can now be absorbed by the junction or stimulate the coherent emission of a second photon [179]. The absorption of a photon with an energy of $E = 2eV$ results in a reduction of the current due to the tunneling of a Cooper pair in opposite direction to the applied junction voltage; i. e. the "particle" in figure 5.33 (b) is

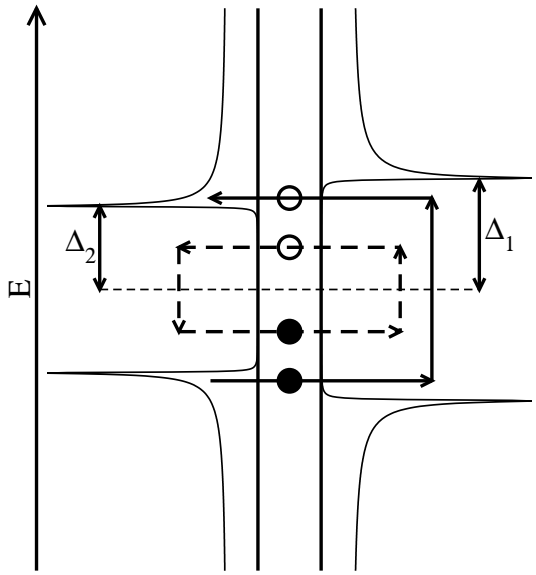

Figure 5.36: Schematic view of an asymmetric junction at low bias. Supercurrent can not only be transported over Andreev bound-states (dashed lines) but additionally by Andreev scattering of electrons originating from continuum states at $-\Delta_2 \geq E \geq -\Delta_1$ (full lines).

moved by 2π uphill, while the stimulated emission of a second photon leads to an additional dc-current which is superimposed to the current originating from RSJ-model.

To get more incidents of stimulated emission than of absorption, it is known that "population inversion" is a necessary condition, i. e. a greater occupancy in the upper than in the lower level of the system. In the experiments presented here, the current I transports Cooper pairs to the energetically higher left superconductor in figure 5.35, leading to a population invertion.

At a junction voltage $eV_J \geq E_J$ the photon energy is higher than the coupling energy between both superconductors. Thus, we expect that the two superconductors are no longer firmly coupled and self-emission processes are inhibited leading to the sharp drop in I_{ind}.

Andreev reflected continuum states

In section 5.1.4 the charge transport which leads to the supercurrent was discussed in terms of Andreev bound-states. While for *symmetric* junctions a supercurrent at $V_J \approx 0$ can only be transported via Andreev reflection processes between the Andreev bound-states as illustrated in figure 5.7, the situation in *asymmetric* junctions is different.

Figure 5.36 sketches the possible transports in a tunnel junction with $\Delta_2 < \Delta_1$. Not only reflection processes into Andreev bound-states contribute to the overall current but additionally quasiparticles originating from occupied states between the energy interval $-\Delta_1 < E < -\Delta_2$ which are reflected at the boundary can lead to an non negligible current contribution [245, 246, 247].

Unfortunately, this additional channel closes for voltages higher than the difference between the two superconducting gaps, i. e. at $|eV_J| = \Delta_2 - \Delta_1$. Nevertheless, it cannot

be completely ruled out that the gap in the microcrystal changes for different tunneling resistances and that it is only by coincidence that the closing appears at approximatively E_J.

Interestingly, break-junction measurements have so far never reported similar jumps. Break-junctions are usually driven by applying a constant-current to the junction and recording the junction voltage in a four-terminal measurement configuration to eliminate errors due to the voltage drop along the wiring. During the rising current sweep ($I_J = 0 \rightarrow \pm I$) and after exceeding the maximal supercurrent the system jumps from almost zero voltage to a point relatively far on the dissipative branch (see figure 5.32). At opposite sweep direction ($I_J = \pm I \rightarrow 0$) an increase in the current can principally not be detected. Thus, the observed jump at E_J might be detectable in break-junctions when performing measurements in constant-voltage mode.

5.6.3 Summary

To summarize, the presented $I - V$ measurements between two unequal superconductors are in general well reproduced by the RSJ-model except for the second jump in the raw data. While the first jump and the hysteresis originates from the experimental setup which lead to an unavoidable serial resistor, and thus to a no longer completely voltage-driven measurement, the second jump has a different origin which is not yet well understood. Additionally, the RSJ-model only works well if it is assumed that the junction contains several transport channels in which the major channel has a transmissivity of exactly $1/3$ of the sum of all transmission coefficients.

While we cannot completely exclude that the observed second jump has its origin in external sources of error not controlled by our experiment, we want to state that we have observed these jumps in all measurements when the junction resistivity was set to sufficiently low values with at least three differently prepared superconducting tips.

Further investigations are recommended, because the jump occurs surprisingly at an energy which is identified as the Josephson coupling energy, the energy which characterizes the Josephson effect between both superconductors.

Evidently, the extra current I_{ind} (equation 5.38) we introduced "ad hoc" is only a sufficient approximation to describe the data as long as $E_J \gg k_B T_{\mathrm{eff}}$. In the $I - V$ curves obtained at $R_T = 16\ \mathrm{k}\Omega$ (figure 5.39) where $E_J \approx k_B T_{\mathrm{eff}}$ this approximation is obviously no longer a good one.

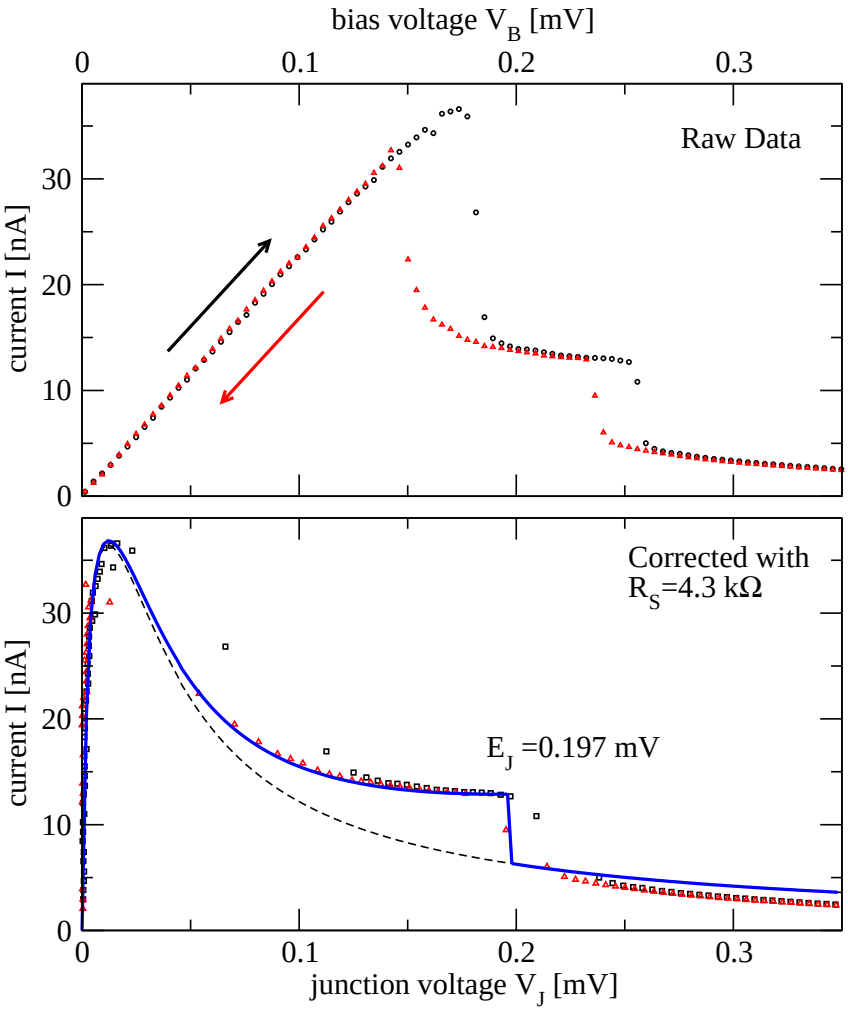

Figure 5.37: Blow-up of the forward (circles) and backward (triangles) $I - V$ curves obtained at a tunneling resistance of $R_T = 8200\ \Omega$. The top panel shows the uncorrected raw data in which two jumps are clearly visible. These two jumps occur at different bias voltages V_B for the forward and backward sweep leading to hysteresis loops. After correcting the data using equation 5.25 to compensate the voltage drop on the serial resistance R_S, the spectra shown in the lower panel are obtained. Here, the first jump can be explained by the load line of the voltage source, while the origin of the second jump which occurs approximately at the Josephson energy E_J stays unclear. The data can reproduced with a fit using the RSJ-model (dashed line) plus an additional linear term presumably due to stimulated tunneling which abruptly stops at E_J (full line). For details see text.

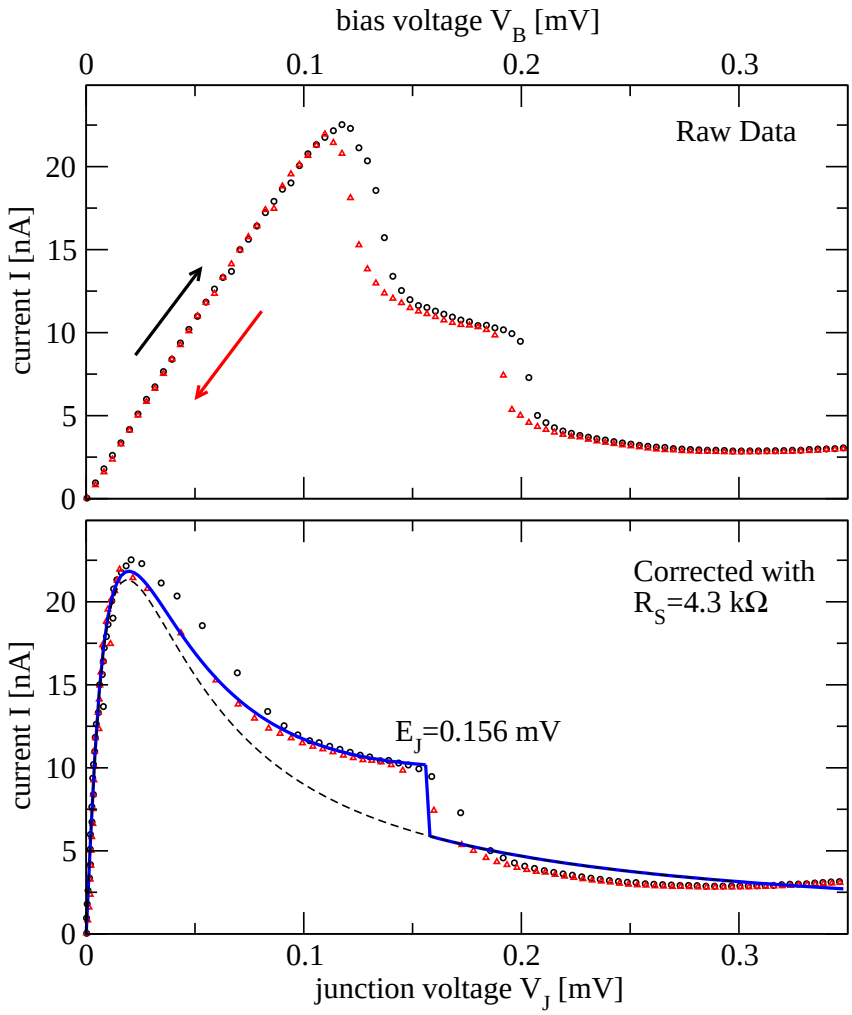

Figure 5.38: Same graphic as in figure 5.37 but for a junction resistivity of $R_T = 10.3\ \mathrm{k}\Omega$.

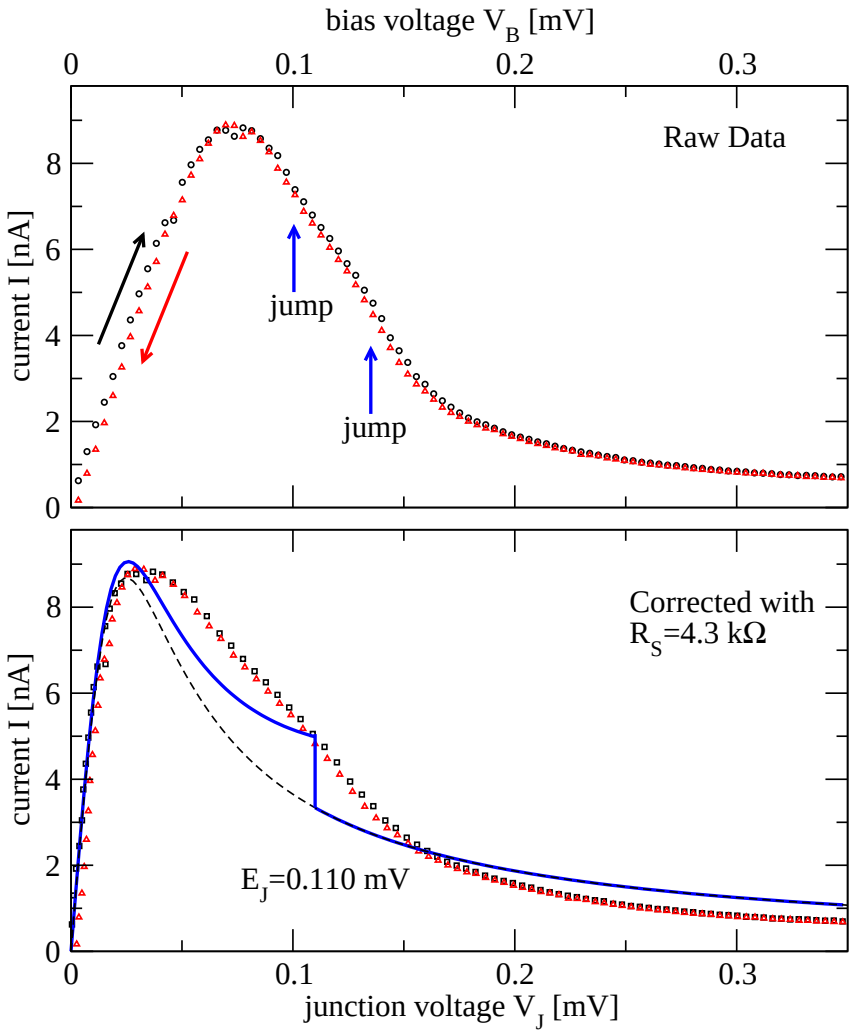

Figure 5.39: Same graphic as in figure 5.37 but for a junction resistivity of $R_T = 16.0\,\mathrm{k}\Omega$. The jumps and the hysteresis loop are only faintly visible due to an effective temperature higher than the Josephson coupling energy ($k_B T_{\mathrm{eff}} > E_J$). For details, see text.

Acknowledgments

Without the help and contribution of many people during the last four years it would have been impossible for me to perform the experiments and to get the profound knowledge in the underlying physical concepts which were thoroughly necessary to write this thesis in the extent as presented here. Mainly my forgetfulness and partly the limitation in space does not allow me to express my appreciation to all of them here, and I can only apologize to any whose name might have been forgotten.

First and foremost I would like to thank my advisor, Prof. Wolf-Dieter Schneider, for giving me the opportunity to perform this challenging research and for all the discussions we had in an atmosphere which allowed me to find my own ideas and which were based on the belief that physics has to be developed by "dreaming on a scientific base" which means that one has to explore new paths and that there is no disgrace if one formulates ideas even without having completely analyzed every part in detail.

I am very happy that I had the chance to meet Prof. Jonathan P. Pelz from the University of Columbus in Ohio who stayed in Lausanne for his sabbatical year in the beginning of my thesis. The discussions with him about STM techniques and the origin of the superlattice creation were a great pleasure and an enormous help for me.

Special thanks go to Prof. Frédéric Mila and Cédric Weber for the fruitful cooperation which finally led to a profound understanding of the superlattice electronic structure. I am also glad that Frédéric accepted to be referee in my thesis commission as well as Dr. Andreas Heinrich, Prof. Harald Brune, and Prof. Christoph Renner.

In particular, I would like to thank very much Andreas Heinrich who invited me for a three months period to the IBM labs in Almaden, California. As chapter 5 in this thesis reflects, this period was scientificly extremely fruitful. But it were not only the excellent experimental conditions which allowed me to explore new fields of research, but much more the extraordinary pleasant and admirable atmosphere in the lab created by Andreas, Don Eigler, Chris Lutz, and Cyrus Hirjibehedin. From the very first day I felt accepted and at home in this group, and I will never forget the trust Andreas had in me letting me operate his "baby", the 0.5 K STM, already after three weeks completely alone and additionally to lend me his car during his absence so that I had the great chance also to explore California. I have to mention that the presented results and explanations were only possible with the help of Chris Lutz and Cyrus Hirjibehedin.

For the deeper understanding of the physics of multiple Andreev reflections I am grateful for all the help Juan Carlos Cuevas from the University of Karlsruhe provided me with. His Fortran code and much more his explanations given in numerous mails and during my short stay in Karlsruhe gave me a basic understanding in the complex physics behind this process.

Furthermore, I would like to thank Prof. Hans Kroha from the University of Bonn with whom I had long discussions about the origin of the Kondo effect and which finally lead to a comment on a theoretical paper in PRL.

I am very thankful for the help I got from the members of the LPS during my thesis. In particular, I would like to thank Dr. François Patthey for all the support in preparing samples and driving the instrument, and to Monsieur Rittner from the electronic workshop who supported me and built the crosstalk compensation units.

My colleagues Marie Christine Blüm, Elizabetha Ćavar, and Hans-Christoph Ploigt will always be remembered. We had a great time together and I am very happy for all the uncountable coffee-breaks with discussion sometimes about physics and mostly about more important “real” life questions. I am sure that we will stay in contact even if we are spread around the world.

Finally, I would like to thank Vincent and Gwendoline Lam and their families which helped me a lot to feel home in Switzerland, especially in the beginning. I am grateful to Lee Nicol, Hans-Christoph Ploigt and Jessen Page for reading and correcting my thesis and for their friendship as well as Laura Bamert for taking care of me. Addionally, I would like to thank my family and all the friends which supported me in great many ways and who stayed by me.

Curriculum vitae

Markus Ternes

Date of birth: May 13, 1972 in Rheinhausen (Duisburg), Germany
Nationality: German

Education:

- 1994–2001: Technische Universität Berlin, Germany. Degree as “Diplom-Physiker”. Title of the diploma thesis: “Aufbau eines Rastertunnelmikroskops und Untersuchungen an Querschnittsflächen von Halbleiterstrukturen” in the group of Prof. Mario Dähne.

Professional experience:

- 1997-2000: Student assistant responsible for the electronic equipment in the group of Prof. Peter Heide, TU-Berlin
- 2001: Research assistant in the group of Prof. Mario Dähne, TU Berlin.
- since December 2001: Reseach and teaching assistant in the group of Prof. Wolf-Dieter Schneider, Université de Lausanne; Since Oct. 1, 2003: École Polytechnique Fédérale de Lausanne.

List of publications during this thesis:

- F. Silly, M. Pivetta, M. Ternes, F. Patthey, J. P. Pelz, and W.-D. Schneider. Creation of an Atomic Superlattice by Immersing Metallic Adatoms in a Two-Dimensional Electron Sea. Phys. Rev. Lett. **92**, 016101 (2004).
- F. Silly, M. Pivetta, M. Ternes, F. Patthey, J. P. Pelz, and W.-D. Schneider. Coverage-dependent self-organization: from individual adatoms to adatom superlattices. New J. Phys. **6**, 14 (2004).
- M. Ternes, C. Weber, M. Pivetta, F. Patthey, J. P. Pelz, T. Giamarchi, F. Mila, and W.-D. Schneider. Scanning-Tunneling Spectroscopy of Surface-State Electrons Scattered by a Slightly Disordered Two-Dimensional Dilute “Solid”: Ce on Ag(111). Phys. Rev. Lett. **93**, 146805 (2004).
- Ch. Kolf, J. Kroha, M. Ternes, and W.-D. Schneider. Comment on “Fano Resonance for Anderson Impurity Systems”. Phys. Rev. Lett., **96**, 019701 (2006).

- M. Ternes, W.-D. Schneider, J. C. Cuevas, C. P. Lutz, C. F. Hirjibehedin, and A. J. Heinrich. Novel Subgap Structure in Asymmetric Superconducting Tunnel Junctions. Phys. Rev. Lett., submitted.

Teaching experience:

- 1996-2000: Student assistant for the experimental training of undergrade students ("Projektlabor"), Prof. Peter Heide, TU Berlin
- 2002-2004: Teaching assistant: Experimental exercises I and IV (TP)

Languages:

German (mother tongue), English (fluent), French (advanced).

Bibliography

[1] A. Einstein. Elementare Betrachtungen über die thermische Molekularbewegung in festen Körpern. *Ann. d. Phys.*, 35:679, 1911.

[2] H. K. Onnes. The disappearance of the resistivity of mercury. *Comm. Leiden*, 122(b), 1911.

[3] J. P. Franck, F. D. Manchester, and D. L. Martin. The Specific Heat of Pure Copper and of Some Dilute Copper+Iron Alloys Showing a Minimum in the Electrical Resistance at Low Temperatures. *Proc. R. Soc. Lond. A*, 263:494, 1961.

[4] J. G. Bednorz and K. A. Müller. Possible high-T_C superconductivity in the Ba-La-Cu-O system. *Z. Phys. B*, 64:189, 1986.

[5] J. Bardeen, L. N. Cooper, and J. R. Schrieffer. Theory of Superconductivity. *Phys. Rev.*, 108:1175, 1957.

[6] J. Kondo. Resistance Minimum in Dilute Magnetic Alloys. *Prog. Theor. Phys.*, 32:37, 1964.

[7] G. Binnig, H. Rohrer, Ch. Gerber, and E. Weibel. Tunneling through a controllable vacuum gap. *Appl. Phys. Lett.*, 40:178, 1982.

[8] G. Binnig, H. Rohrer, Ch. Gerber, and E. Weibel. Surface studies by scanning tunneling microscopy. *Phys. Rev. Lett.*, 49:57, 1982.

[9] G. Binnig, H. Rohrer, Ch. Gerber, and E. Weibel. 7×7 reconstruction on Si(111) resolved in real space. *Phys. Rev. Lett.*, 50:120, 1983.

[10] G. Binnig, C. F. Quate, and Ch. Gerber. Atomic Force Microscope. *Phys. Rev. Lett.*, 56:930, 1984.

[11] D. W. Pohl, W. Denk, and M. Lanz. Optical stethoscopy: Image recording with resolution $\lambda/20$. *Appl. Phys. Lett.*, 44:651, 1984.

[12] Y. Martin and H. K. Wickramasinghe. Magnetic imaging by force microscopy with 1000 A resolution. *Appl. Phys. Lett.*, 50:1455, 1987.

[13] W. J. Kaiser and L. D. Bell. Direct investigation of subsurface interface electronic structure by ballistic-electron-emission microscopy. *Phys. Rev. Lett.*, 60:1406, 1988.

[14] J. Frenkel. On the electrical resistance of contacts between solid conductors. *Phys. Rev.*, 36:1604, 1930.

[15] I. Giaever. Energy Gap in Superconductors Measured by Electron Tunneling. *Phys. Rev. Lett.*, 5:147, 1960.

[16] J. C. Fisher and I. Giaever. Tunneling Through Thin Insulating Layers. *J. Appl. Phys.*, 32:172, 1961.

[17] C. J. Chen. *Introduction to Scanning Tunneling Microscopy*. Oxford University Press, New York, Oxford, 1993.

[18] H. B. Michaelson. The work function of the elements and its periodicity. *J. Appl. Phys.*, 48:4729, 1977.

[19] N. D. Lang. Spectroscopy of single atoms in the scanning tunneling microscope. *Phys. Rev. B*, 34:5947, 1986.

[20] Y. Kuk, P. J. Silverman, and H. Q. Nguyen. Study of metal surfaces by scanning tunneling microscopy with field ion microscopy. *J. Vac. Sci. Technol. A*, 6:524, 1988.

[21] J. Bardeen. Tunnelling from a Many-Particle Point of View. *Phys. Rev. Lett.*, 6:57, 1961.

[22] J. Tersoff and D.R. Hamann. Theory and Application for the Scanning Tunneling Microscope. *Phys. Rev. Lett.*, 50:1998, 1983.

[23] J. Tersoff and D. R. Hamann. Theory of the scanning tunneling microscope. *Phys. Rev. B*, 31:805, 1985.

[24] R. M. Feenstra, J. A. Stroscio, J. Tersoff, and A. P. Fein. Atom-selective imaging of the GaAs(110) surface. *Phys. Rev. Lett.*, 58:1192, 1987.

[25] G. Binnig and H. Rohrer. Scanning tunneling microscopy. *Surf. Sci.*, 126:236, 1983.

[26] M. Pivetta, F. Silly, F. Patthey, J. P. Pelz, and W.-D. Schneider. Reading the ripples of confined surface-state electrons: Profiles of constant integrated local density of states. *Phys. Rev. B*, 67:193402, 2003.

[27] J. Klein, A. Léger, M. Belin, and D. Défourneau. Inelastic-Electron-Tunneling Spectroscopy of Metal-Insulator-Metal Junctions. *Phys. Rev. B*, 7:2336, 1973.

[28] J. T. Li, W.-D. Schneider, R. Berndt, O. R. Bryant, and S. Crampin. Surface-State Lifetime Measured by Scanning Tunneling Spectroscopy. *Phys. Rev. Lett.*, 81:4464, 1998.

[29] J. A. Støvneng and P. Lipavský. Thermopower in scanning-tunneling-microscope experiments. *Phys. Rev. B*, 42:9214, 1990.

[30] M. A. Schneider, M. Wenderoth, K. J. Engel, M. A. Rosentreter, A. J. Heinrich, and R. G. Ulbrich. Local electronic structure at steps on Au(111) investigated by the thermovoltage in scanning tunneling microscopy. *Appl. Phys. A*, 66:S161, 1998.

[31] R. C. Jaklevic and J. Lambe. Molecular Vibration Spectra by Electron Tunneling. *Phys. Rev. Lett.*, 17:1139, 1966.

[32] J. Klein and A. Leger. Tunneling measurement of phonon spectrum in granular A1. *Phys. Lett. A*, 28:134, 1968.

[33] J. M. Rowell, W. L. McMillan, and W. L. Feldmann. Phonon Emission and Self-Energy Effects in Normal-Metal Tunneling. *Phys. Rev.*, 180:658, 1968.

[34] D. P. E. Smith, G. Binnig, and C. F. Quate. Detection of phonons with a scanning tunneling microscope. *Appl. Phys. Lett.*, 49:1641, 1986.

[35] B. C. Stipe, M. A. Rezaei, and W. Ho. Single-Molecule Vibrational Spectroscopy and Microscopy. *Science*, 280:1732, 1998.

[36] L. J. Lauhon and W. Ho. Single-molecule vibrational spectroscopy and microscopy: CO on Cu(001)and Cu(110). *Phys. Rev. B*, 60:R8525, 1999.

[37] F. Moresco, G. Meyer, and K.-H. Rieder. Vibrational Spectroscopy of CO/Cu(211) with a CO terminated tip. *Mod. Phys. Lett. B*, 13:709.

[38] J. R. Hahn, H. J. Lee, and W. Ho. Electronic Resonance and Symmetry in Single-Molecule Inelastic Electron Tunneling. *Phys. Rev. Lett.*, 85:1914, 2000.

[39] J. I. Pascual, J. J. Jackiw, Z. Song, P. S. Weiss, H. Conrad, and H.-P. Rust. Adsorbate-Substrate Vibrational Modes of Benzene on Ag(110) Resolved with Scanning Tunneling Spectroscopy. *Phys. Rev. Lett.*, 86:1050, 2001.

[40] A. J. Heinrich, J. A. Gupta, C. P. Lutz, and D. M. Eigler. Single-Atom Spin-Flip Spectroscopy. *Science*, 306:466, 2004.

[41] J. Lambe and R. C. Jaklevic. Molecular Vibration Spectra by Inelastic Electron Tunneling. *Phys. Rev.*, 165:821, 1968.

[42] B. N. J. Persson. Inelastic Vacuum Tunneling. *Phys. Scr.*, 38:282, 1988.

[43] J. A. Gupta, C. P. Lutz, A. J. Heinrich, and D. M. Eigler. Strongly coverage-dependent excitations of adsorbed molecular hydrogen. *Phys. Rev. B*, 71:115416, 2005.

[44] J. Gaudioso, L. J. Lauhon, and W. Ho. Vibrationally Mediated Negative Differential Resistance in a Single Molecule. *Phys. Rev. Lett.*, 85:1918, 2000.

[45] J. T. Li, W.-D. Schneider, and R. Berndt. Analysis of spectroscopic scanning tunneling microscope images. *Appl. Phys. A*, 66:S167, 1998.

[46] D. M. Eigler and E. K. Schweizer. Positioning single atoms with a scanning tunnelling microscope. *Nature*, 344:524, 1990.

[47] H. C. Manoharan, C. P. Lutz, and D. M. Eigler. Quantum mirages formed by coherent projection of electronic structure. *Nature*, 403:512, 2000.

[48] A. J. Heinrich, C. P. Lutz, J. A. Gupta, and D. M. Eigler. Molecule Cascades. *Science*, 298:1381, 2002.

[49] N. Nilius, T. M. Wallis, and W. Ho. Development of One-Dimensional Band Structure in Artificial Gold Chains. *Science*, 297:1853, 2002.

[50] J. A. Stroscio and R. J. Celotta. Controlling the Dynamics of a Single Atom in Lateral Atom Manipulation. *Science*, 306:242, 2004.

[51] G. M. Whitesides and B. Grzybowski. Self-Assembly at All Scales. *Science*, 295:2418, 2002.

[52] H. Zeng, J. Li, J. P. Liu, Z. L. Wang, and S. Sun. Exchange-coupled nanocomposite magnets by nanoparticle self-assembly. *Nature*, 420:395, 2002.

[53] C. T. Black, C. B. Murray, R. L. Sandstrom, and S. Sun. Spin-Dependent Tunneling in Self-Assembled Cobalt-Nanocrystal Superlattices. *Science*, 290:5494, 2000.

[54] M.-C. Blüm, E. Ćavar, M. Pivetta, F. Patthey, and W.-D. Schneider. Conservation of Chirality in a Hierarchical Supramolecular Self-Assembled Structure with Pentagonal Symmetry. *Angew. Chem.*, 44:5334, 2005.

[55] K. H. Lau and W. Kohn. Indirect long-range oscillatory interaction between adsorbed atoms. *Surf. Sci.*, 75:69, 1978.

[56] T. T. Tsong. Field-Ion Microscope Observations of Indirect Interaction between Adatoms on Metal Surfaces. *Phys. Rev. Lett.*, 31:1207, 1973.

[57] E. Wahlström, I. Ekvall, H. Olin, and L. Walldén. Long-range interaction between adatoms at the Cu(111) surface imaged by scanning tunnelling microscopy. *Appl. Phys. A*, 66:S1107, 1998.

[58] J. Repp, F. Moresco, G. Meyer, K.-H. Rieder, P. Hyldgaard, and M. Persson. Substrate Mediated Long-Range Oscillatory Interaction between Adatoms: Cu/Cu(111). *Phys. Rev. Lett.*, 85:2981, 2000.

[59] N. Knorr, M. A. Schneider, L. Diekhöner, P. Wahl, and K. Kern. Kondo Effect of Single Co Adatoms on Cu Surfaces. *Phys. Rev. Lett.*, 88:096804, 2002.

[60] F. Silly, M. Pivetta, M. Ternes, F. Patthey, J. P. Pelz, and W.-D. Schneider. Creation of an Atomic Superlattice by Immersing Metallic Adatoms in a Two-Dimensional Electron Sea. *Phys. Rev. Lett.*, 92(1):016101, 2004.

[61] F. Silly, M. Pivetta, M. Ternes, F. Patthey, J. P. Pelz, and W.-D. Schneider. Coverage-dependent self-organization: from individual adatoms to adatom superlattices. *New J. Phys.*, 6:16, 2004.

[62] Marina Pivetta. PhD thesis, École Polytechnique Fédérale de Lausanne, 2004.

[63] M. Ternes, C. Weber, M. Pivetta, F. Patthey, J. P. Pelz, T. Giamarchi, F. Mila, and W.-D. Schneider. Scanning-Tunneling Spectroscopy of Surface-State Electrons Scattered by a Slightly Disordered Two-Dimensional Dilute "Solid": Ce on Ag(111). *Phys. Rev. Lett.*, 93:146805, 2004.

[64] W. Sacks, D. Roditchev, and J. Klein. Voltage-depend STM image of a charge density wave. *Phys. Rev. B*, 57:13118, 1998.

[65] N. Mott. Metals, non-metals and metal-non-metal transitions: some recollections. *Rep. Prog. Phys.*, 47:909, 1984.

[66] N. Mott. *Metal-Insulator Transitions*. Taylor and Francis, London, New York, 2nd edition, 1990.

[67] P. W. Anderson. Absence of Diffusion in Certain Random Lattices. *Phys. Rev.*, 109:1492, 1958.

[68] E. Abrahams, P. W. Anderson, D. C. Licciardello, and T. V. Ramakrishnan. Scaling theory of localization: Absence of quantum diffusion in two dimensions. *Phys. Rev. Lett.*, 42:673, 1979.

[69] R. W. G. Wyckoff. *Crystal Structures*. John Wiley and Sons, New York, 2nd edition, 1963.

[70] W. Shockley. On the surface states associated with a periodic potential. *Phys. Rev.*, 56:317, 1939.

[71] A. Zangwill. *Physics at Surfaces*. Cambridge University Press, Cambridge, 1988.

[72] Ibach and Lüth. *Festkörperphysik*. Springer, Berlin, 4th. edition, 1995.

[73] J. T. Li, W.-D. Schneider, and R. Berndt. Local density of states from spectroscopic scanning-tunneling-microscope images: Ag(111). *Phys. Rev. B*, 56:7656, 1997.

[74] L. C. Davis, M. P. Everson, and R. C. Jaklevic. Theory of the local density of surface states on a metal: Comparison with scanning tunneling spectroscopy of a Au(111) surface. *Phys. Rev. B*, 43:3821, 1991.

[75] M. F. Crommie, C. P. Lutz, and D. M. Eigler. Imaging standing waves in a 2-dimensional electron gas. *Nature*, 363:524, 1993.

[76] Y. Hasegawa and Ph. Avouris. Direct observation of standing wave formation at surface steps using scanning tunneling spectroscopy. *Phys. Rev. Lett.*, 71:1071, 1993.

[77] J. Friedel. Metallic alloys. *Nuovo Cim. Suppl.*, 7:287, 1958.

[78] N. W. Ashcroft and N. D. Mermin. *Solid State Physics*. HRW, Philadephia, 1976.

[79] R. Gaisch, J. K. Gimzewski, B. Reihl, R. R. Schlittler, and M. Tschudy. Low-temperature ultra-high-vacuum scanning tunneling microscope. *Ultramicroscopy*, 42:1621, 1992.

[80] J. Harris. Simplified method for calculating the energy of weakly interacting fragments. *Phys. Rev. B*, 31:1770, 1985.

[81] P. Hyldgaard and M. Persson. Long-ranged adsorbate-adsorbate interactions mediated by a surface-state band. *J. Phys.: Condens. Matter*, 12:L13, 2000.

[82] V. S. Stepanyuk, A. N. Baranov, D. V. Tsivlin, W. Hergert, P. Bruno, N. Knorr, M. A. Schneider, and K. Kern. Quantum interference and long-range adsorbate-adsorbate interactions. *Phys. Rev. B*, 68:205410, 2003.

[83] T. Giamarchi and P. Le Doussal. Statics and Dynamics of Disordered Elastic Systems. *cond-mat*, page 9705096, 1997.

[84] N. Knorr, H. Brune, M. Epple, A. Hirstein, M. A. Schneider, and K. Kern. Long-range adsorbate interactions mediated by a two-dimensional electron gas. *Phys. Rev. B*, 65:115420, 2002.

[85] P. Hyldgaard and T. L. Einstein. Surface-state-mediated three-adsorbate interaction. *Europhys. Lett.*, 59:265, 2002.

[86] F. Bloch. *Z. für Phys.*, 52:555, 1928.

[87] D. Wortmann, S. Heinze, Ph. Kurz, G. Bihlmayer, and S. Blügel. Resolving Complex Atomic-Scale Spin Structures by Spin-Polarized Scanning Tunneling Microscopy. *Phys. Rev. Lett.*, 86:4132, 2001.

[88] M.C. Desjonquêres and D. Spanjaard. *Concepts in Surface Physics*. Springer, Berlin, 1993.

[89] A. Groß. *Theoretical Surface Science*. Springer, Berlin, Heidelberg, 2003.

[90] C. M. Goringe, D. R. Bowler, and E. Hernàndez. Tight-binding modelling of materials. *Rep. Prog. Phys.*, 60:1447, 1997.

[91] J. C. Slater and G. F. Koster. Simplified LCAO Method for the Periodic Potential Problem. *Phys. Rev.*, 94:1498, 1954.

[92] C. Weber. Rapport Ce/Ag(111). Technical report, Lausanne, 2004.

[93] J. T. Li, W.-D. Schneider, R. Berndt, O.R. Bryant, and S. Crampin. Electron Confinement to Nanoscale Ag Islands on Ag(111): A Quantitative Study. *Phys. Rev. Lett.*, 80:3332, 1998.

[94] L. R. Gor'kov and G. Grüner, editors. *Charge Density Waves in Solids*. Elsevier, Amsterdam, 1989.

[95] J. T. Li, W.-D. Schneider, R. Berndt, and B. Delley. Kondo Scattering Observed at a Single Magnetic Impurity. *Phys. Rev. Lett.*, 80:2893, 1998.

[96] U. Fano. Effects of Configuration Interaction on Intensities and Phase Shifts. *Phys. Rev.*, 124:1866, 1961.

[97] B. N. Harmon and A. J. Freeman. Spin-polarized energy-band structure, conduction-electron polarization, spin densities, and the neutron magnetic form factor of ferromagnetic gadolinium. *Phys. Rev. B*, 10:1979, 1974.

[98] M. A. Ruderman and C. Kittel. Indirect Exchange Coupling of Nuclear Magnetic Moments by Conduction Electrons. *Phys. Rev.*, 96:99, 1954.

[99] T. Kasuya. *Prog. Theor. Phys. (Kyoto)*, 16:45, 1956.

[100] K. Yosida. Magnetic Properties of Cu-Mn Alloys. *Phys. Rev.*, 106:893, 1957.

[101] B. Fischer and M. W. Klein. Magnetic and nonmagnetic impurities in two-dimensional metals. *Phys. Rev. B*, 11:2025, 1975.

[102] M. T. Béal Monod. Ruderman-Kittel-Kasuya-Yosida indirect interaction in two dimensions. *Phys. Rev. B*, 36:8835, 1987.

[103] V. I. Litvinov and V. K. Dugaev. RKKY interaction in one- and two-dimensional electron gases. *Phys. Rev. B*, 58:3584, 1998.

[104] C. Weber, A. Laeuchli, F. Mila, and T. Giamarchi. Magnetism and superconductivity of strongly correlated electrons on the triangular lattice. *cond-mat*, page 0509520, 2005.

[105] H. Tsunetsugu, M. Sigrist, and K. Ueda. The ground-state phase diagram of the one-dimensional Kondo lattice model. *Rev. Mod. Phys.*, 69:809, 1997.

[106] V. S. Stepanyuk, L. Niebergall, R. C. Longo, W. Hergert, and P. Bruno. Magnetic nanostructures stabilized by surface-state electrons. *Phys. Rev. B*, 70:075414, 2004.

[107] C. F. Hirjibehedin and C. P. Lutz. private communication.

[108] J. Kondo. Effect of Ordinary Scattering on Exchange Scattering from Magnetic Impurity in Metals. *Phys. Rev.*, 169:437, 1968.

[109] P. W. Anderson. Localized Magnetic States in Metals. *Phys. Rev.*, 124:41, 1961.

[110] O. Újsághy, J. Kroha, L. Szunyogh, and A. Zawadowski. Theory of the Fano Resonance in the STM Tunneling Density of States due to a Single Kondo Impurity. *Phys. Rev. Lett.*, 85:2557, 2000.

[111] L. Kouwenhoven and L. Glazman. Revival of the Kondo effect. *Physics World*, (January):33, 2001.

[112] A.C. Hewson. *The Kondo problem to heavy fermions*. Cambridge University Press, Cambridge, 1993.

[113] F. Patthey, B. Delley, W.-D. Schneider, and Y. Baer. Low-Energy Excitations in α- and γ-Ce Observed by Photoemission. *Phys. Rev. Lett.*, 55:1518, 1985.

[114] F. Patthey, J.-M. Imer, W.-D. Schneider, H. Beck, and Y. Baer. High-resolution photoemission study of the low-energy excitations in $4f$-electron system. *Phys. Rev. B*, 42:8864, 1990.

[115] E. Wuilloud, H. R. Moser, W.-D. Schneider, and Y. Baer. Electronic structure of *gamma*- and *alpha*-Ce. *Phys. Rev. B*, 28:7354, 1983.

[116] K. A. Gschneidner and L. Eyring. *Handbook on the Physics and Chemistry of the Rare Earths*. North-Holland, Amsterdam, 1987.

[117] V. Madhavan, W. Chen, T. Jamneala, M. F. Crommie, and N. S. Wingreen. Tunneling into a Single Magnetic Atom: Spectroscopic Evidence of the Kondo Resonance. *Science*, 280:567, 1998.

[118] M. Plihal and J. W. Gadzuk. Nonequilibrium theory of scanning tunneling spectroscopy via adsorbate resonances: Nonmagnetic and Kondo impurities. *Phys. Rev. B*, 63:085404, 2001.

[119] M. A. Schneider, L. Vitali, N. Knorr, and K. Kern. Observing the scattering phase shift of isolated Kondo impurities at surfaces. *Phys. Rev. B*, 65:121406, 2002.

[120] P. Wahl, L. Diekhöner, M. A. Schneider, L. Vitali, G. Wittich, and K. Kern. Kondo Temperature of Magnetic Impurities at Surfaces. *Phys. Rev. Lett.*, 93:176603, 2004.

[121] P. Wahl, L. Diekhöner, G. Wittich, L. Vitali, M. A. Schneider, and K. Kern. Kondo effect of molecular complexes at surfaces: Ligand control of the local spin coupling. *Phys. Rev. Lett.*, 95:166601, 2005.

[122] A. Zhao, Q. Li, L. Chen, H. Xiang, W. Wang, S. Pan, B. Wang, X. Xiao, J. Yang, J. G. Hou, and Q. Zhu. Controlling the Kondo Effect of an Adsorbed Magnetic Ion Through Its Chemical Bonding. *Science*, 309:1542, 2005.

[123] H. G. Luo, T. Xiang, X. Q. Wang, Z. B. Su, and L. Yu. Fano Resonance for Anderson Impurity Systems. *Phys. Rev. Lett.*, 92:256602, 2004.

[124] Ch. Kolf, J. Kroha, M. Ternes, and W.-D. Schneider. Comment on "Fano Resonance for Anderson Impurity Systems". *Phys. Rev. Lett.*, 96:019701, 2006.

[125] H. G. Luo, T. Xiang, X. Q. Wang, Z. B. Su, and L. Yu. Reply to "Comment on 'Fano resonance for Anderson Impurity Systems' ". *Phys. Rev. Lett.*, 96:019702, 2006.

[126] K. Nagaoka, T. Jamneala, M. Grobis, and M. F. Crommie. Temperature Dependence of a Single Kondo Impurity. *Phys. Rev. Lett.*, 88:077205, 2002.

[127] T. Jamneala, V. Madhavan, W. Chen, and M.F. Crommie. Scanning tunneling spectroscopy of transition-metal impurities at the surface of gold. *Phys. Rev. B*, 61:9990, 2000.

[128] J. Kroha. private communication.

[129] I. Affleck and P. Simon. Detecting the Kondo Screening Cloud Around a Quantum Dot. *Phys. Rev. Lett.*, 86:2854, 2001.

[130] H. J. Lee and W. Ho. Single-Bond Formation and Characterization with a Scanning Tunneling Microscope. *Science*, 286:1719, 1999.

[131] G. Witte. Low frequency vibrational modes of adsorbates. *Surf. Sci.*, 502:405, 2002.

[132] H. Froitzheim, H. Ibach, and S. Lehwald. Surface vibrations of CO on W(100). *Surf. Sci.*, 63:56, 1977.

[133] N. Lorente and H. Ueba. CO dynamics induced by tunneling electrons: differences on Cu(110) and Ag(110). *Eur. Phys. J. D*, 35:341, 2005.

[134] C. Stassis, T. Gould, O. D. McMasters, K. A. Gschneidner, and R. M. Nicklow. Lattice and spin dynamics of γ-Ce. *Phys. Rev. B*, 19:5746, 1979.

[135] L. Z. Liu, J. W. Allen, O. Gunnarsson, N. E. Christensen, and O. K. Anderson. $\alpha - \gamma$ transition in Ce: A detailed analysis of electron spectroscopy. *Phys. Rev. B*, 45:8934, 1992.

[136] David R. Lide, editor. *Handbook of Chemistry and Physics*. CRC Press LCC, Boca Raton, Florida, 90th. edition, 1999.

[137] E. Franceschi and G. L. Olcese. A New Allotropic form of Cerium Due to its Transition Under Pressure to the Tetravalent State. *Phys. Rev. Lett.*, 22:1299, 1969.

[138] M. E. Eberhart. Molecular-Orbital Models of the $\alpha - \gamma$ Transformation of cerium. *Solid State Commun.*, 54:187, 1985.

[139] R. M. Galera, D. Givord, J. Pierre, A. P. Murani, J. Schweizer, C. Vettier, and K. R. A. Ziebeck. Polarized neutron scattering in Kondo or intermediate valence compounds. *J. Mag. Mag. Mat.*, 52:103, 1985.

[140] J. W. Allen and M. Martin. Kondo Volume Collapse and the $\gamma - \alpha$ Transition in Cerium. *Phys. Rev. Lett.*, 49:1106, 1982.

[141] M. Lavagna, C. Lacroix, and M. Cyrot. Volume collapse in the Kondo lattice. *Phys. Lett. A*, 90:210, 1982.

[142] M. Lavagna, C. Lacroix, and M. Cyrot. The $\gamma - \alpha$ transition in cerium compounds. *J. Phys. F*, 13:1007, 1983.

[143] J. W. Allen and L. Z. Liu. $\alpha - \gamma$ transition in Ce. II. A detailed analysis of the Kondo volume-collapse model. *Phys. Rev. B*, 46:5047, 1992.

[144] M. A. Schneider, L. Vitali, P. Wahl, N. Knorr, L. Diekhöner, G. Wittich, M. Vogelgesang, and K. Kern. Kondo state of Co impurities at noble metal surfaces. *Appl. Phys. A*, 80:937, 2005.

[145] A. Stenborg, J. N. Andersen, O. Björneholm, A. Nilsson, and N. Mårtesson. Valence-Transition-Induced 5×5 Surface Reconstruction of Sm(0001). *Phys. Rev. Lett.*, 63:187, 1989.

[146] E. Lundgren, J. N. Andersen, R. Nyholm, X. Torrelles, J. Rius, A. Delin, A. Grechnev, O. Eriksson, C. Konvicka, M. Schmid, and P. Varga. Geometry of the Valence Transition Induced Surface Reconstruction of Sm(0001). *Phys. Rev. Lett.*, 88:136102, 2002.

[147] J. A. Stroscio and D. M. Eigler. Atomic and Molecular Manipulation with the Scanning Tunneling Microscope. *Science*, 254:1319, 1991.

[148] L. Bartels, G. Meyer, and K.-H. Rieder. Controlled vertical manipulation of single CO molecules with the scanning tunneling microscope: A route to chemical contrast. *Appl. Phys. Lett.*, 213:213, 1997.

[149] L. J. Lauhon and W. Ho. Direct Observation of the Quantum Tunneling of Single Hydrogen Atoms with a Scanning Tunneling Microscope. *Phys. Rev. Lett.*, 85:4566, 2000.

[150] C. Benvenuti, J. M. Cazeneuve, P. Chiggiato, F. Cicoira, A. E. Santana, V. Johanek, V. Ruzinov, and J. Fraxedas. A novel route to extreme vacua: the non-evaporable getter thin film coatings. *Vacuum*, 53:219, 1999.

[151] J. I. Pascual, N. Lorente, Z. Song, H. Conrad, and H.-P. Rust. Selectivity in vibrationally mediated single-molecule chemistry. *Nature*, 423:525, 2003.

[152] I. Giaever. Electron Tunneling Between Two Superconductors. *Phys. Rev. Lett.*, 5:464, 1960.

[153] J. Nicol, S. Shapiro, and P. H. Smith. Direct Measurement of the Superconducting Energy Gap. *Phys. Rev. Lett.*, 5:461, 1960.

[154] I. Giaever and K. Megerle. Study of Superconductors by Electron Tunneling. *Phys. Rev.*, 122:1101, 1961.

[155] M. D. Sherrill and H. H. Edwards. Superconducting Tunneling on Bulk Niobium. *Phys. Rev. Lett.*, 6:460, 1961.

[156] N. Agraït, J. G. Rodrigo, and S. Vieira. Transition from the tunneling regime to point contact and proximity-induced Josephson effect in lead-normal-metal nanojunctions. *Phys. Rev. B*, 46:5814, 1992.

[157] A. Yazdani, B. A. Jones, C. P. Lutz, M. F. Crommie, and D. M. Eigler. Probing the Local Effects of Magnetic Impurities on Superconductivity. *Science*, 275:1767, 1997.

[158] S.H. Pan, E.W. Hudson, and J.C. Davis. Vaccum tunneling of superconducting quasiparticles from atomically sharp scanning tunneling microscope tips. *Appl. Phys. Lett.*, 73:2992, 1998.

[159] L. Bürgi. *Scanning Tunneling Microscopy as local probe of electron density, dynamics, and transport at metall surface*. PhD thesis, École Polytechnique Fédérale de Lausanne, 1999.

[160] J. G. Rodrigo, H. Suderow, and S. Vieira. On the use of STM superconducting tips at very low temperatures. *Eur. Phys. J. B*, 40:483, 2004.

[161] J. Wiebe, A. Wachowiak, F. Meier, D. Haude, T. Foster, M. Morgenstern, and R. Wiesendanger. A 300 mK ultra-high vacuum scanning tunneling microscope for spin-resolved spectroscopy at high energy resolution. *Rev. Sci. Instr.*, 75:4871, 2004.

[162] M. Xu, Y. Takano, M. Kitahara, and D. Fujita. The fabrication of MgB_2 superconducting STM tips. *Physica C*, 388:117, 2003.

[163] G. E. Blonder, M. Tinkham, and T. M. Klapwijk. Transition from metallic to tunneling regimes in superconduction microconstrictions: Excess current, charge imbalance, and supercurrent conversion. *Phys. Rev. B*, 25:4515, 1982.

[164] T. M. Klapwijk, G. E. Blonder, and M. Tinkham. Explanation of subharmonic energy gap structure in superconducting contacts. *Physica*, 109:1657, 1982.

[165] M. Ternes, W.-D. Schneider, J. C. Cuevas, C. P. Lutz, C. F. Hirjibehedin, and A. J. Heinrich. Novel Subgap Structure in Asymmetric Superconducting Tunnel Junctions. *Phys. Rev. Lett.* submitted.

[166] B. D. Josephson. Possible new effects in superconductive tunnelling. *Phys. Lett.*, 1:251, 1962.

[167] Y. Uehara, T. Fujita, M. Iwami, and S. Ushioda. Superconducting niobium tip for scanning tunneling microscope light emission spectroscopy. *Rev. Sci. Instr.*, 72:2097, 2001.

[168] G. Petzow. *Metallographisches Ätzen*. Gebrüder Borntraeger, Berlin, Stuttgart, 6th edition, 1994.

[169] C. Sürgers, M. Schöck, and H. v. Löhneysen. Oxygen-induced surface structure of Nb(110). *Surf. Sci.*, 471:209, 2001.

[170] W. Meissner and R. Ochsenfeld. Ein neuer Effekt beim Eintritt der Supraleitfähigkeit. *Die Naturwissenschaften*, 21:787, 1933.

[171] H. Fröhlich. Theory of the Superconducting State. I. The Ground State at the Absolute Zero of Temperature. *Phys. Rev.*, 79:845, 1950.

[172] J. Bardeen. Wave Functions for Superconducting Electrons. *Phys. Rev.*, 80:567, 1950.

[173] M. Tinkham. *Introduction to Superconductivity*. McGraw-Hill, New York, 1985.

[174] W. Buckel. *Supraleitung*. VCH Verlagsgesellschaft, Weinheim, Germany, 4th edition, 1990.

[175] L. N. Cooper. Bound Electron Pairs in a Degenerate Fermi Gas. *Phys. Rev.*, 104:1189, 1956.

[176] R. C. Dynes, N. Narayanamurti, and J. P. Garno. Direct Measurement of Quasiparticle-Lifetime Broadening in a Strong-Coupled Superconductor. *Phys. Rev. Lett.*, 41:1509, 1978.

[177] H. Suderow, E. Bascones, A. Izquierdo, F. Guinea, and S. Vieira. Proximity effect and strong-coupling superconductivity in nanostructures built with an STM. *Phys. Rev. B*, 65:100519, 2002.

[178] A. F. Andreev. *Sov. Phys. JETP*, 19:1228, 1964.

[179] B. D. Josephson. Coupled Superconductors. *Rev. Mod. Phys.*, 36:216, 1964.

[180] V. Ambegaokar and A. Baratoff. Tunneling Between Superconductors. *Phys. Rev. Lett.*, 10:486, 1963.

[181] P. W. Anderson and J. M. Rowell. Probable Observation of the Josephson Superconducting Tunneling Effect. *Phys. Rev. Lett.*, 10:230, 1963.

[182] S. A. Buckner, J. T. Chen, and D. N. Langenberg. Current-Voltage Characteristics of Small Josephson Tunnel Junctions. *Phys. Rev. Lett.*, 25:738, 1970.

[183] N. van der Post, E. T. Peters, I. K. Yanson, and J. M. van Ruitenbeek. Subgap Structure as Function of the Barrier in Atom-Size Superconducting Tunnel Junctions. *Phys. Rev. Lett.*, 73:2611, 1994.

[184] M. F. Goffman, R. Cron, A. L. Yeyati, P. Joyez, M. H. Devoret, D. Esteve, and C. Urbina. Supercurrent in Atomic Point Contacts and Andreev States. *Phys. Rev. Lett.*, 85:170, 2000.

[185] O. Naaman, W. Teizer, and R. C. Dynes. Fluctuation Dominated Josephson Tunneling with a Scanning Tunneling Microscope. *Phys. Rev. Lett.*, 87:097004, 2001.

[186] O. Naaman and R. C. Dynes. Subharmonic gap structure in superconducting scanning tunneling microscope junctions. *Solid State Commun.*, 129:299, 2004.

[187] S. P. Benz, C. A. Hamilton, C. J. Burroughs, and T. E. Harvey. Stable 1 volt programmable voltage standard. *Appl. Phys. Lett.*, 71:1866, 1997.

[188] S. Shapiro. Josephson Currents in Superconducting Tunneling: The Effect of Microwaves and Other Observations. *Phys. Rev. Lett.*, 11:80, 1963.

[189] D. D. Coon and M. D. Fiske. Josephson ac and Step Structure in the Supercurrent Tunneling Characteristic. *Phys. Rev.*, 138:A744, 1965.

[190] K. W. Lehnert, N. Argaman, H.-R. Blank, K. C. Wong, S. J. Allen, E. L. Hu, and H. Kroemer. Nonequilibrium ac Josephson Effect in Mesoscopic Nb-InAs-Nb Junctions. *Phys. Rev. Lett.*, 82:1265, 1999.

[191] D. N. Langenberg, D. J. Scalapino, B. N. Taylor, and R. E. Eck. Investigation of Microwave Radiation Emitted by Josephson Junctions. *Phys. Rev. Lett.*, 15:294, 1965.

[192] A. Furusaki and M. Tsukada. Dc Josephson effect and Andreev reflection. *Solid State Commun.*, 299:299, 1991.

[193] C. W. J. Beenakker and H. van Houten. Josephson current through a superconducting quantum point contact shorter than the coherence length. *Phys. Rev. Lett.*, 66:3056, 1991.

[194] S. F. Alvarado and P. Renaud. Observation of spin-polarized-electron tunneling from a ferromagnet into GaAs. *Phys. Rev. Lett.*, 68:1387, 1992.

[195] R. Wiesendanger, H.-J. Gütherodt, G. Güntherodt, R. J. Gambino, and R. Ruf. Observation of vacuum tunneling of spin-polarized electrons with the scanning tunneling microscope. *Phys. Rev. Lett.*, 65:247, 1990.

[196] M. Bode, M. Getzlaff, and R. Wiesendanger. Spin-Polarized Vacuum Tunneling into the Exchange-Split Surface State of Gd(0001). *Phys. Rev. Lett.*, 81:4256, 1998.

[197] M. Bode, M. Getzlaff, and R. Wiesendanger. Quantitative aspects of spin-polarized scanning tunneling spectroscopy of Gd(0001). *J. Vac. Sci. Technol. A*, 17:2228, 1999.

[198] M. Kleiber, M. Bode, R. Ravlić, and R. Wiesendanger. Topology-Induced Spin Frustrations at the Cr(001) Surface Studied by Spin-Polarized Scanning Tunneling Spectroscopy. *Phys. Rev. Lett.*, 85:4606, 2000.

[199] H. Yang, A. R. Smith, M. Prikhodko, and W. R. L. Lambrecht. Atomic-Scale Spin-Polarized Scanning Tunneling Microscopy Applied to $Mn_3N_2(010)$. *Phys. Rev. Lett.*, 89:226101, 2002.

[200] O. Pietzsch, A. Kubetzka, M. Bode, and R. Wiesendanger. Real-Space Observation of Dipolar Antiferromagnetism in Magnetic Nanowires by Spin-Polarized Scanning Tunneling Spectroscopy. *Phys. Rev. Lett.*, 84:5212, 2000.

[201] A. Kubetzka, O. Pietzsch, M. Bode, and R. Wiesendanger. Magnetism of nanoscale Fe islands studied by spin-polarized scanning tunneling spectroscopy. *Phys. Rev. B*, 63:140407, 2001.

[202] A. Wachowiak, J. Wiebe, M. Bode, O. Pietzsch, M. Morgenstern, and R. Wiesendanger. Direct Observation of Internal Spin Structure of Magnetic Vortex Cores. *Science*, 298:577, 2002.

[203] A. Kubetzka, M. Bode, O. Pietzsch, and R. Wiesendanger. Spin-Polarized Scanning Tunneling Microscopy with Antiferromagnetic Probe Tips. *Phys. Rev. Lett.*, 88(5):57201, 2002.

[204] L. Solymar. *Superconductive Tunneling and Applications*. Chapman and Hall Ltd, London, 1972.

[205] P. W. Anderson. Theory of dirty superconductors. *J. Phys. Chem. Solids*, 11:26, 1959.

[206] J. Šmakov, I. Martin, and A.V. Balatsky. Theory of Scanning Tunneling Microscopy Measurement of Single Spin Decoherence in a Superconductor. *Phys. Rev. Lett.*, 88:037003, 2002.

[207] R. Meservey. Tunneling in a magnetic field with spin-polarized electrons. *Phys. Scr.*, 38:272, 1988.

[208] R. Meservey and P. M. Tedrow. Magnetic Field Splitting of the Quasiparticle States in Superconducting Aluminum Films. *Phys. Rev. Lett.*, 25:1270, 1970.

[209] P. M. Tedrow and R. Meservey. Spin-Dependent Tunneling into ferromagnetic nickel. *Phys. Rev. Lett.*, 26:192, 1971.

[210] P. M. Tedrow and R. Meservey. Spin polarization of electrons tunneling from films of Fe, Co, Ni, and Gd. *Phys. Rev. B*, 7:318, 1973.

[211] R. Meservey and P. M. Tedrow. Spin-polarized electron tunneling. *Phys. Rep.*, 238:173, 1994.

[212] A. A. Abrikosov and L. P. Gor'kov. *Sov. Phys. JETP*, 15:1088, 1962.

[213] G. F. Hardy and J. K. Hulm. The superconductivity of some transition metal compounds. *Phys. Rev.*, 93:1004, 1953.

[214] G. A. Gibson and R. Meservey. Evidence for spin fluctuations in vanadium from a tunneling study of Fermi-liquid effects. *Phys. Rev. B*, 40:8705, 1989.

[215] L. J. Lauhon and W. Ho. Control and Characterization of a Multistep Unimolecular Reaction. *Phys. Rev. Lett.*, 84:1527, 2000.

[216] L. Y. L. Shen and J. M. Rowell. Zero-Bias Tunneling Anomalies-Temperature, Voltage, and Magnetic Field Dependence. *Phys. Rev.*, 165:566, 1968.

[217] B. N. Taylor and E. Burstein. Excess Current in Electron Tunneling Between Superconductors. *Phys. Rev. Lett.*, 10:14, 1963.

[218] J. R. Schrieffer and J. W. Wilkins. Two-Particle Tunneling Processes Between Superconductors. *Phys. Rev. Lett.*, 10:17, 1963.

[219] E. Scheer, P. Joyez, D. Esteve, C. Urbina, and M. H. Devoret. Conduction Channel Transmissions of Atomic-Size Aluminum Contacts. *Phys. Rev. Lett.*, 78:3535, 1997.

[220] E. Scheer, N. Agraït, J. C. Cuevas, A. L. Yeyati, B. Ludoph, A. Martin Rodero, G. R. Bollinger, J. M. van Ruitenbeek, and C. Urbina. The signature of chemical valence in the electrical conduction through a single-atom contact. *Nature*, 394:154, 1998.

[221] B. Ludoph, N. van der Post, E. N. Bratus, E. V. Bezuglyi, V. S. Shumeiko, G. Wendin, and J. M. van Ruitenbeek. Multiple Andreev reflection in single-atom niobium junctions. *Phys. Rev. B*, 61:8561, 2000.

[222] M. Octavio, M. Tinkham, G. E. Blonder, and T. M. Klapwijk. Subharmonic energy-gap structure in superconducting constrictions. *Phys. Rev. B*, 27:6739, 1983.

[223] E. N. Bratus, V. S. Shumeiko, and G. Wendin. Theory of Subharmonic Gap Structures in Superconductiong Mesoscopic Tunnel Contacts. *Phys. Rev. Lett.*, 74:2110, 1995.

[224] D. Averin and A. Bardas. ac Josephson Effect in a Single Quantum Channel. *Phys. Rev. Lett.*, 75:1831, 1995.

[225] J. C. Cuevas, A. Martin Rodero, and A. L. Yeyati. Hamiltonian approach to the transport properties of superconducting quantum point contacts. *Phys. Rev. B*, 54:7366, 1996.

[226] M. Hurd, S. Datta, and P. F. Bagwell. Current-voltage relation for asymmetric ballistic superconducting junctions. *Phys. Rev. B*, 54:6557, 1996.

[227] M. Hurd, S. Datta, and P. F. Bagwell. ac Josephson effect for asymmetric superconducting junctions. *Phys. Rev. B*, 56:11232, 1997.

[228] M. Andersson, J. C. Cuevas, and M. Fogelström. Transport through superconductor/magnetic dot/superconductor structures. *Phys. C*, 367:117, 2002.

[229] Y. Guo, Y.-F. Zhang, X.-Y. Bao, T.-Z. Tang, L.-X. Zhang, W.-G. Zhu, E. G. Wang, Q. Niu, Z. Q. Qiu, J.-F. Jia, Z.-X. Zhao, and Q.-K. Xue. Superconductivity Modulated by Quantum Size Effects. *Science*, 306:1915, 2004.

[230] S. Bose, P. Raychaudhuri, R. Banerjee, P. Vasa, and P. Ayyub. Mechanism of the Size Dependence of the Superconducting Transition of Nanostructured Nb. *Phys. Rev. Lett.*, 95:147003, 2005.

[231] J. C. Cuevas and W. Belzig. Full Counting Statistics of Multiple Andreev Reflections. *Phys. Rev. Lett.*, 91:187001, 2003.

[232] J. C. Cuevas and W. Belzig. Dc transport in superconducting point contacts: A full-counting-statistics view. *Phys. Rev. B*, 70:214512, 2004.

[233] R. Rossignoli, J. P. Zagorodny, and N. Canosa. Parity and finite size effects in the thermodynamics of small superconductors. *Phys. Lett. A*, 258:188, 1999.

[234] S. H. Pan, E. W. Hudson, K. M. Lang, H. Eisaki, S. Uchida, and J. C. Davis. Imaging the effects of individual zinc impurity atoms on superconductivity in $Bi_2Sr_2CaCu_2O_{8+\delta}$. *Nature*, 403:746, 2000.

[235] M. I. Salkola, A. V. Balatsky, and J. R. Schrieffer. Spectral properties of quasiparticle excitations induced by magnetic moments in superconductors. *Phys. Rev. B*, 55:12648, 1997.

[236] M. E. Flatté and J. M. Byers. Local Electronic Structure of a Single Magnetic Impurity in a Superconductor. *Phys. Rev. Lett.*, 78:3761, 1997.

[237] M. Fogelström. Josephson currents through spin-active interfaces. *Phys. Rev. B*, 62:11812, 2000.

[238] O. Naaman. *Josephson Scanning Tunneling Microscope-A Local Probe of the Superconducting Pair Amplitude*. PhD thesis, University of California, San Diego, CA, 2003.

[239] J. M. Martinis and R. L. Kautz. Classical phase diffusion in small hysteretic Josephson junctions. *Phys. Rev. Lett.*, 89:1507, 1989.

[240] R. L. Kautz and J. M. Martinis. Noise-affected $I - V$ curves in small hysteretic Josephson junctions. *Phys. Rev. B*, 42, 1990.

[241] P. Joyez, D. Vion, M. Götz, M. H. Devoret, and D. Esteve. The Josephson Effect in Nanoscale Tunnel Junctions. *J. Supercond.*, 12:757, 1999.

[242] V. Ambegaokar and B. I. Halperin. Voltage Due to Thermal Noise in the dc Josephson Effect. *Phys. Rev. Lett.*, 22:1364, 1969.

[243] G.-L. Ingold and H. Grabert. Cooper-pair current through ultrasmall Josephson junctions. *Phys. Rev. B*, 50:395, 1994.

[244] Y. Harada, H. Takayanagi, and A. A. Odintsov. Cooper-pair tunneling in small junctions with tunable Josephson coupling. *Phys. Rev. B*, 54:6608, 1996.

[245] L.-F. Chang and P. F. Bagwell. Ballistic Josephson-current flow through an asymmetric superconductor-normal-metal-superconductor junction. *Phys. Rev. B*, 49:15853, 1994.

[246] A. Furusaki. Josephson current carried by Andreev levels in superconducting quantum point contacts. *Superlatt. Microstruct.*, 25:809, 1999.

[247] S.-T. Wu and S. K. Yip. ac Josephson effect in asymmetric superconducting quantum point contacts. *Phys. Rev. B*, 70:104511, 2004.

Index